# 2005
## Annual Progress Report

# HEAVY VEHICLE SYSTEMS OPTIMIZATION PROGRAM

*Less dependence on foreign oil, and eventual transition to an emissions-free, petroleum-free vehicle*

FREEDOMCAR AND VEHICLE TECHNOLOGIES PROGRAM

U.S. Department of Energy
Energy Efficiency and Renewable Energy
Bringing you a prosperous future where energy is clean, abundant, reliable, and affordable

FreedomCAR & Fuel Partnership

21st CENTURY TRUCK PARTNERSHIP

## Acknowledgement

We would like to express our sincere appreciation to Argonne National Laboratory for its technical and artistic contributions in preparing and publishing this report.

In addition, we would like to thank all the participants for their contributions to the programs and all the authors who prepared the project abstracts that comprise this report.

**U.S. Department of Energy**
**Office of FreedomCAR and Vehicle Technologies**
**1000 Independence Avenue S.W.**
**Washington, D.C. 20585-0121**

# FY 2005

## Annual Progress Report for Heavy Vehicle Systems Optimization Program

**Energy Efficiency and Renewable Energy**
**FreedomCAR and Vehicle Technologies Program**

**Lee Slezak**
**Technology Development Manager**

**January 2006**

# Contents

**Foreword** ..... 1

**I. Aerodynamic Drag Reduction** ..... 3

A. DOE Project on Heavy Vehicle Aerodynamic Drag
Lawrence Livermore National Laboratory, R.C. McCallen ..... 3

B. Computational Fluid Dynamics Simulations of Heavy Vehicle Drag Reduction Devices
Lawrence Livermore National Laboratory, K. Salari, et al. ..... 8

C. Computational Modeling of Spray Dispersion in Heavy Vehicle and Tire Assembly Wakes
Lawrence Livermore National Laboratory, K. Salari, et al. ..... 16

D. Experimental Measurement of the Flow-field of Heavy Trucks
University of Southern California, F. Browand ..... 21

E. Detailed Experimental Results of Drag-Reduction Concepts on a Generic Tractor-Trailer
NASA/AerospaceComputing, Inc., B.L. Storms ..... 30

F. Commercial CFD Code Validation for External Aerodynamics Simulations of Realistic Heavy-Vehicle Configurations
Argonne National Laboratory, W.D. Pointer ..... 49

G. Test, Evaluation, and Demonstration of Practical Devices/Systems to Reduce Aerodynamic Drag of Tractor/Semitrailer Combination-Unit Trucks
Truck Manufacturers Association, R.M. Clarke ..... 59

**II. Thermal Management** ..... 69

A. Cooling Fan and System Performance and Efficiency Improvements
Caterpillar, Inc., R.L. Dupree, et al. ..... 69

B. Efficient Cooling in Engines with Nucleate Boiling
Argonne National Laboratory, J.R. Hull ..... 74

C. Nanofluids for Thermal Control Applications
Argonne National Laboratory, S.U.S. Choi ..... 81

D. Evaporative Cooling
Argonne National Laboratory, S.U.S. Choi ..... 88

E. Erosion of Materials in Nanofluids
Argonne National Laboratory, J.L. Routbort ..... 93

# Contents (Cont.)

F. Thermal Analysis of an Off-Road Machine Engine with Combined Use of 1-D Network Flow and 3-D CFD Simulation Techniques
Argonne National Laboratory, T. Sofu, et al. ..... 97

**III. Friction and Wear** ..... 105

A. Boundary Lubrication Mechanisms
Argonne National Laboratory, O.O. Ajayi, et al. ..... 105

B. Parasitic Engine Loss
Argonne National Laboratory, G. Fenske, et al. ..... 111

C. Efficiency Improvement Through Reduction of Friction and Wear in Powertrain Systems
Eaton Corporation, B. Lisowsky ..... 119

**IV. Fuel Reformer Systems** ..... 129

A. Diesel Fuel Reformer Technology
Argonne National Laboratory, M. Krumpelt. ..... 129

B. Onboard Plasmatron Hydrogen Production for Improved Vehicles
Plasma Science and Fusion Center, D.R. Cohn, et al. ..... 133

**V. Electromagnetic (EM) Regenerative Shocks** ..... 139

A. Regenerative Shock Absorbers and Tires
Argonne National Laboratory, J.R. Hull ..... 139

**VI. Analysis** ..... 145

A. Systems Analysis for Heavy Vehicles
Argonne National Laboratory, L. Gaines ..... 145

**VII. Off-Highway** ..... 153

A. Hybrid Energy Storage and Fuel Optimization
GE Global Research, L. Salasoo, et al. ..... 153

B. Advanced Hybrid Propulsion and Energy Management System for High-Efficiency, Off-Highway, 320-Ton-Class, Diesel Electric Haul Trucks
GE Global Research, T. Richter ..... 159

**VIII. Brake Systems** ..... 165

A. Advanced Brake Systems for Heavy-Duty Vehicles
Pacific Northwest National Laboratory, G. Grant ..... 165

# Contents (Cont.)

**IX. Efficiency Improvements for Heavy Vehicles** ..... 177

A. Truck Essential Power Systems Efficiency Improvements for Medium-Duty Trucks
Caterpillar Inc., L.M. Slone ..... 177

B. Advanced Electric Systems and Aerodynamics for Efficiency Improvements in Heavy-Duty Trucks
Caterpillar Inc., K.W. Johnson ..... 182

**X. Ultralight Transit Bus System** ..... 189

A. The Vehicle System Optimization of a Lightweight Stainless Steel Bus
Autokinetics Inc., J.B. Emmons ..... 189

# Forward

Dr. Sidney Diamond at the Mid-America Trucking Show (2003)

The FY2005 Heavy Vehicle (HV) Systems Annual Report is dedicated to Dr. Sidney Diamond, whose untimely death in August 2005 created a void in the program that cannot be filled. Sid started the HV program, and under his guidance, it thrived and produced amazing results that pointed in the direction of improving fuel efficiency of long-haul heavy vehicles by almost one-third. Several technologies initiated by Sid are now commercially available. It is fair to say that Sid was loved, admired, and respected by all of his colleagues. His intellect, curiosity, highly animated enthusiasm for science and technology was an inspiration to all of his colleagues, especially those who have contributed to this report. Dr. Sid, you will be missed, but the work you started, and its lofty goals to reduce the U.S. dependence on imported petroleum, will continue, with you always in mind.

# I. AERODYNAMIC DRAG REDUCTION

## I.A. DOE Project on Heavy Vehicle Aerodynamic Drag

*Project Principal Investigator: R. C. McCallen*
*Lawrence Livermore National Laboratory*
*P.O. Box 808, Livermore, CA 94551-0808*
*(925) 423-0958, e-mail: mccallen1@llnl.gov*

*Principal Investigator: K. Salari*
*Co-Investigators: J. Ortega, P. Castellucci, C. Eastwood, J. Paschkewitz*
*Lawrence Livermore National Laboratory*
*P.O. Box 808, Livermore, CA 94551-0808*
*(925) 424-4635, e-mail: salari1@llnl.gov*

*Principal Investigator: W. D. Pointer*
*Argonne National Laboratory*
*9700 S. Cass Avenue, NE-208, Argonne, IL 60439*
*(630) 252-1052, e-mail: dpointer@anl.gov*

*Principal Investigator: L. J. DeChant*
*Co-Investigators: B. Hassan*
*Sandia National Laboratories*
*P.O. Box 5800, MS 0825, Albuquerque, NM 87185-0825*
*(505) 844-4250, e-mail: ljdecha@sandia.gov*

*Principal Investigator: F. Browand*
*Co-Investigators: C. Radovich, T. Merzel, D. Plocher*
*Aerospace & Mechanical Engineering, University of Southern California*
*RRB 203, Los Angeles CA 90089-1191*
*(213) 740-5359, e-mail: browand@spock.usc.edu*

*Principal Investigator: J. Ross*
*Co-Investigators: B. Storms, J.T. Heineck, S. Walker*
*NASA Ames Research Center*
*MS 260-1, Moffett Field, CA 94035*
*(650) 604-6722, e-mail: jcross@mail.arc.nasa.gov*

*Principal Investigator: C. J. Roy*
*Auburn University*
*211 Aerospace Engineering Building*
*Auburn University, AL 36849-5338*
*(334) 844-5187, e-mail: cjroy@eng.auburn.edu*

*Technology Development Managers: Sid Diamond and Lee Slezak*
*(202) 586-2335, e-mail: Lee.Slezak@hq.doe.gov*
*Technical Program Manager: Jules Routbort*
*(630) 252-5065, e-mail: routbort@anl.gov*

---

*Contractor: Lawrence Livermore National Laboratory, Sandia National Laboratories, Argonne National Laboratory, NASA Ames Research Center*
*Contract No.: W-7405-ENG-48, DE-AC04-94AL85000, W-31-109-ENG-38, DE-AI01-99EE50559*

---

## In Memory

## Dr. Sidney ('Sid') Diamond

This document is dedicated to our DOE Program Manager, supporter, and dear friend Dr. Sid Diamond. This Consortium effort would not exist without Sid's vision, dedication, perseverance, and passion. His enthusiasm for this project, with his wonderful gusto for life, was contagious and pushed our effort forward. He will be dearly missed.

## Objectives

Class 8 tractor-trailers consume 11–12% of the total U.S. petroleum use. At highway speeds, 65% of the energy expenditure for a Class 8 truck is in overcoming aerodynamic drag. The project objective is to improve fuel economy of Class 8 tractor-trailers by providing guidance on methods of reducing drag by at least 25%. A 25% reduction in drag would result in a 12% improvement in fuel economy at highway speeds, equivalent to about 130 midsize tanker ships per year. Specific goals include:

- Provide guidance to industry in the reduction of aerodynamic drag of heavy truck vehicles.
- Establish a database of experimental, computational, and conceptual design information, and demonstrate the potential of new drag-reduction devices.

## Approach

- Develop and demonstrate the ability to simulate and analyze aerodynamic flow around heavy truck vehicles using existing and advanced computational fluid dynamics (CFD) tools.
- Generate an experimental database for code validation through an extensive experimental effort.
- Validate computations using experimental database.
- Provide industry with design guidance and insight into flow phenomena from experiments and computations.
- Investigate aero devices (e.g., base flaps, tractor-trailer gap stabilizers, underbody skirts and wedges, blowing and acoustic devices), provide industry with conceptual designs of drag reducing devices, and demonstrate the full-scale fuel economy potential of these devices.

## Accomplishments

A multi-laboratory, multi-university consortium has constructed a multi-year program plan with industry. The consortium has leveraged Advanced Strategic Computing Initiative (ASCI) funds, utilized results of complementary laboratory, university and National Aeronautics and Space Administration (NASA) internal supported efforts, in addition to buy-in, collaboration, and communications with truck industries and organizations. The program has

- Demonstrated several concepts and devices which meet the 25% drag reduction goal and represent a savings of 4,200 million gals per year. This is equivalent to 130 midsize tanker ships per year!
- Provided clear guidance to industry on reliable, predictable experimental techniques based on insight from experiments and experimental database.
- Provided clear guidance and caution warnings on the use of steady Reynolds-averaged Navier Stokes (RANS) models for CFD simulations based on computational results.

## Future Direction

- Get devices on roads
  - Develop less obtrusive and optimized device concepts from understanding of key flow mechanisms.
  - Apply results from demonstration wind tunnel, track, and road tests by leveraging work with DANA/Oak Ridge National Laboratory (ORNL), National Research Council of Canada, and Truck Manufacturers Association (TMA)/Department of Energy (DOE), and seek collaborative demonstrations with fleet owners and operators.
- Conduct economic/duty cycle evaluation with Powertrain System Analysis Toolkit (PSAT) (Argonne National Laboratory's system model):
  - Provide mechanistic data: strong variation in drag per yaw, speed, geometry/devices, environment, etc.
  - Review road/track test plans, and provide needed assistance in calibration/evaluation to DANA/ORNL.

- Develop and transfer technology and information to industry:
  - Collaborate with DOE Industrial Consortium who will be conducting fleet tests of advanced aerodynamic drag reduction devices. Schedule industry meetings to share findings and encourage consideration of effective design concepts for road testing.
  - Continue experimental data reduction and analysis for the generic conventional model (GCM).
  - Continue computations of flow around GCM, compare to experimental data, perform analyses, and provide guidance to industry on use of unsteady RANS and hybrid RANS/Large-Eddy Simulation (LES) methods.
- Address consequences with aerodynamic drag reduction and use of devices:
  - Contouring the tractor hood reduces the grille area, also reducing coolant flow. Include underhood flow in aerodynamic drag computations to provide insight into the coupled flow phenomena. In addition, modify underhood exhaust gas recirculation to meet EPA 2007 regulations, which require more underhood cooling.
  - Continue our investigation of air flow around rotating tires for improved brake cooling, as well as drag reduction. Aerodynamic devices reduce moving resistance increasing braking distance and require more braking down hill, encouraging bake overheating. Underbody and near wheel aerodynamic devices can also restrict critical brake air cooling.
  - Trailer base devices and side skirts appear to enhance air upwash which is likely to enhance splash and spray. Per industry encouragement, we will continue our investigation of device and wheel aero related to splash and spray from tires and devices, pursuing ways to minimize this road safety hazard.
- Leverage program work and seek funding from other agencies.

---

## Introduction

Class 8 tractor-trailers consume 11–12% of the total US petroleum use. A modern Class 8 tractor-trailer can weigh up to 80,000 pounds and has a wind-averaged drag coefficient ($C_D$) around $C_D = 0.6$. The drag coefficient is defined as the drag/(dynamic pressure × projected area). The higher the speed the more energy consumed in overcoming aerodynamic drag. At 70 miles per hour (mph), a common highway speed today, overcoming aerodynamic drag represents about 65% of the total energy expenditure for a typical heavy truck vehicle. Reduced fuel consumption for heavy vehicles can be achieved by altering truck shapes to decrease the aerodynamic resistance (drag). Reducing aerodynamic drag by 25% improves fuel economy by about 12% at highway speeds. This would result in a savings of over 4,000 million gallons per year or up to 130 midsize tanker ships per year.

The project goal is to develop and demonstrate the ability to simulate and analyze aerodynamic flow around heavy truck vehicles using existing and advanced computational fluid dynamics (CFD) tools. Activities also include an extensive experimental effort to generate data for code validation and a design effort for developing drag reducing devices. The final products are specific device concepts that can significantly reduce aerodynamic drag, and thus improve fuel efficiency, in addition to an experimental data base and validated CFD tools. The objective is to provide industry with clear guidance on methods of computational simulation and experimental modeling techniques that work for predicting the flow phenomena around a heavy vehicle and add-on drag reducing devices. Development of effective drag reducing devices is also a major goal.

The following reports on the findings and accomplishments for fiscal year 2005 in the project's three focus areas

- Drag reduction devices
- Experimental testing
- Computational modeling

Detailed reports from each participating organization are provided in Sections I.B through I.G. Included are experimental results by the National Aeronautics and Space Administration (NASA) and the University of Southern California (USC), and complementary computations by Lawrence Livermore National Laboratory (LLNL), and Argonne National Laboratory (ANL). The computational results from LLNL, ANL, and Sandia

National Laboratory (SNL)/Auburn University for the integrated tractor-trailer benchmark geometry called the Ground Transportation System (GTS) model and Generic Conventional Model (GCM) are used for the trailer wake and tractor-trailer gap flow investigations, turbulence model development, and benchmark simulations being investigated. Auburn University's task involves performing Detached Eddy Simulation (DES) computations on the GTS geometry. This effort is an extension of a Fiscal Year 2004 task which involved DES simulations on a truncated version of the GTS model. The FY04 computations were found to have mesh quality issues, and thus, a new mesh of the full geometry has been generated. DES simulations for both 15 million cell and 30 million cell meshes are running on 72 processors and final results will be presented in the next Annual Report. USC provides wind tunnel test results for variable angle tractor side extenders and a novel tire splash/spray device in Section I.C., and LLNL presents vehicle and wheel computational results for splash and spray in section I.B.

## Drag Reduction Devices and Future Plans

There are three areas identified for aero drag reduction and several drag reduction devices have been investigated

- **Tractor-Trailer Gap**
  Stabilizing devices, cab extenders
- **Wheels/Underbody**
  Skirts/wedge and lowboy trailer
- **Trailer Base**
  Boattail plates, base flaps, rounded edges, and pneumatics

Over 12% increase in fuel economy is possible, e.g.,

> 4% trailer base-flaps
> 6% trailer skirts
> 2% gap splitter plate
> 12% Total

Unfortunately, these devices have operational and maintenance issues. With our understanding of the key flow mechanisms, we are developing less obtrusive and optimized innovative design concepts using computational fluid dynamics and experiments. In addition, to get devices on the road, consequences of aerodynamic improvements need to be addressed.

Contouring the tractor hood reduces the grille area, also reducing coolant flow. In addition, underhood exhaust gas recirculation added to meet EPA 2007 emissions regulations requires more underhood cooling. With industry encouragement, we are including underhood flow in aerodynamic drag computations to provide insight into the coupled flow phenomena.

Aerodynamic devices reduce moving resistance, which increases braking distance and requires more downhill braking, encouraging brake overheating. Underbody and near-wheel aerodynamic devices can also restrict critical brake air cooling. We will continue our investigation of air flow around rotating tires for improved brake cooling, as well as drag reduction.

Trailer base devices and side skirts appear to enhance air upwash which is likely to enhance splash and spray. Per industry encouragement, we will continue our investigation of device and wheel aero related to splash and spray from tires and devices, pursuing ways to minimize this road safety hazard.

Addressing these consequences of aerodynamic improvements is an important task in getting devices on the road. Fortunately, the task overlaps with our efforts in device optimization. In addition, these issues are of interest to other government agencies (e.g., U.S. Department of Transportation [DOT] and U.S. Environmental Protection Agency [EPA]) and industry (i.e., Michelin is providing partial support for experiments at USC). The splash and spray effort will continue to receive complimentary support from industry and we will actively seek joint government funding.

# I.B. Computational Fluid Dynamics Simulations of Heavy Vehicle Drag Reduction Devices

*Kambiz Salari, Rose McCallen, Jason Ortega, Craig Eastwood, John S. Paschkewitz, Paul Castelucci*
*Lawrence Livermore National Laboratory*
*7000 East Ave, L-098, Livermore, CA 94551*
*(925) 423-0958, fax: (925) 422-3389, e-mail: mccallen1@llnl.gov*

*Technology Development Managers: Sid Diamond and Lee Slezak*
*(202) 586-2335, e-mail: Lee.Slezak@hq.doe.gov*

*Technical Program Manager: Jules Routbort*
*(630) 252-5065, e-mail: routbort@anl.gov*

---

*Contractor: Lawrence Livermore National Laboratory*
*Contract No.: W-7405-ENG-48*

---

Lawrence Livermore National Laboratory's (LLNL's) effort consists of two experimental and computational focus areas:

- Improve fuel economy through innovative, effective conceptual design of aerodynamic drag reduction devices utilizing computational studies of devices for a trailer underbody, gap, and base
- Get devices on the road by addressing consequences of aerodynamic drag reduction related to brake performance and splash/spray through computational studies of tire aerodynamics and spray dispersion in tire and heavy vehicle flow fields.

The following describes the objective, approach, accomplishments, and future directions for each of these focus areas.

---

## Objectives

- Evaluate the performance of heavy vehicle drag reduction devices applied to the tractor-trailer gap, trailer underbody, and trailer base.
- Determine if computational modeling can replicate the performance of drag reduction devices seen experimentally.
- Understand how the drag reduction devices alter the flow field about a heavy vehicle.

## Approach

- Perform computational fluid dynamics (CFD) simulations of heavy vehicle geometries at both wind-tunnel and full-scale operating conditions.
- Model the drag reduction performance of add-on devices placed in the gap between the tractor and trailer (splitter plate), on the trailer base (base flaps), and beneath the trailer (wedge-shaped skirt).
- Compare the simulated results with experimental data.
- Analyze the computed velocity and pressure fields to yield a deeper insight into how the drag reduction devices function.

## Accomplishments

- Assessed the performance of add-on drag reduction devices using CFD.
  - At lab-scale Reynolds numbers, both the tractor cab extenders and the trailer splitter plate produce a 5% drag reduction at large gap lengths.
  - At full-scale Reynolds numbers, the addition of a trailer splitter plate decreases vehicle drag by 1% while maintaining vehicle side force.
  - At full-scale Reynolds numbers, base flaps decrease the drag coefficient by 8–14%.
  - At full-scale Reynolds numbers, the wedge-shaped skirt decreases the drag coefficient by 2%.
- Observed that at full-scale Reynolds numbers, the increased vertical flow in the gap between the tractor and trailer alters the gap flow structures.
- Determined that base flaps function by increasing the pressure on the trailer base through the elimination of a recirculation zone on the trailer base.
- Investigated the sensitivity of the drag coefficient reduction of the wedge-shaped skirt and base flaps to both grid refinement and steady versus unsteady simulations.

## Future Directions

- Investigate the effect of varying the splitter plate size and gap length on drag reduction.
- Utilize a trailer splitter plate in combination with compact tractor cab extenders, base flaps, and a wedge-shaped skirt on a heavy vehicle.
- Investigate design modifications of the base flaps to further enhance their performance.
- Evaluate the performance of drag reduction devices at finite yaw angles.
- Design and simulate alternate drag reduction concepts that alleviate the recirculation zone on the trailer base.

---

## Introduction

Computational fluid dynamics (CFD) simulations are used to determine whether or not the drag reduction from add-on devices can be replicated with computer modeling. Additionally, CFD simulations provide three-dimensional data on pertinent flow quantities, such as velocity, pressure, vorticity, turbulent kinetic energy, and dissipation, which are not readily accessible about the entire vehicle using experimental measurements. This added information gives a deeper insight into how the devices modify the flow about a heavy vehicle and identifies the means by which the devices can be further optimized. The targeted areas for drag reduction are the gap between the tractor and trailer, the trailer base, and the trailer underbody, all of which have been shown previously (Cooper 2003) to contribute significantly to the overall heavy vehicle drag.

Base flaps (Figure 1a) are selected to alleviate the trailer base drag, a wedge-shaped skirt (Figure1b) for the trailer underbody drag, and a gap splitter plate (Figure 1c) and cab extenders (Figure 1d) for the gap drag. The base flaps are comprised of four angled, flat plates, which can be folded against the trailer sides, allowing access to the trailer cargo area. Previous studies (Cooper 2003, Ortega et al. 2004, Storms et al. 2004) have shown that the base flaps provide a relatively constant drag reduction, $\Delta C_d$, on the order of $0.04 \leq \Delta C_d \leq 0.1$ with respect to the vehicle yaw angle. Recent full-scale tests (Browand 2004) demonstrated that the base flaps provide over a 4% improvement in fuel economy. The wedge-shaped skirt is formed from two flat plates that are suspended from the trailer underside. The advantage of the wedge-shaped skirt over conventional side skirts is that it does not limit driver access to the trailer underside. Small-scale wind tunnel tests at the National Aeronautics and

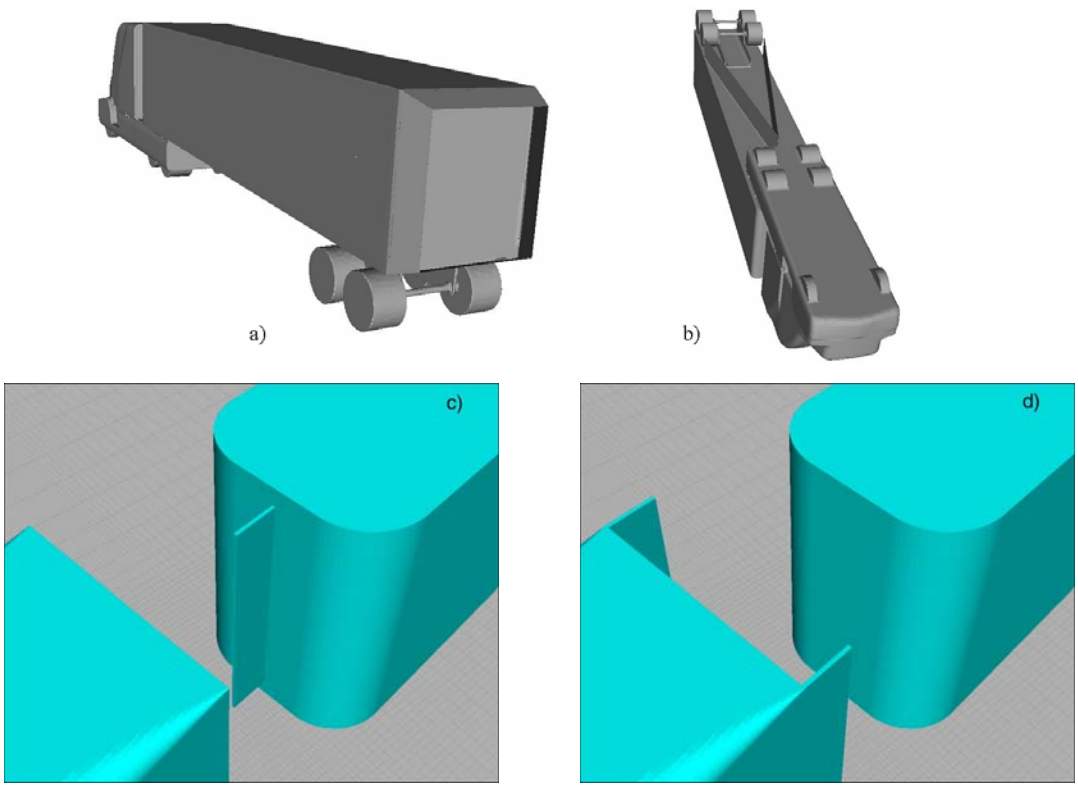


**Figure 1.** a) Base flaps b) Wedge-shaped skirt c) Splitter plate d) Cab extenders

Space Administration (NASA) Ames Research Center (Ortega et al. 2004) showed that the wedge-shaped skirt is capable of reducing the wind-averaged drag coefficient by approximately 2%. Recent experiments utilizing a gap splitter plate on the front trailer face have shown that the plate reduces the separated flow entrained into the tractor-trailer gap and makes the flow distribution more symmetric across the gap. As part of the U.S. Department of Energy's (DOE's) Heavy Vehicle Aerodynamics Consortium, the University of Southern California (USC) has compiled body force and flow field wind-tunnel data for a simplified tractor-trailer at varying yaw angles and gap lengths. Preliminary experimental results indicate that a single trailer splitter plate may be as effective as tractor cab extenders in reducing aerodynamic drag at yaw without increasing side force substantially.

## Computational Setup

To evaluate the base flaps and the wedge-shaped skirt, the GCM heavy vehicle model (Storms et al. 2004) (Figure 2) is used as a platform for the simulations. A freestream velocity and a moving

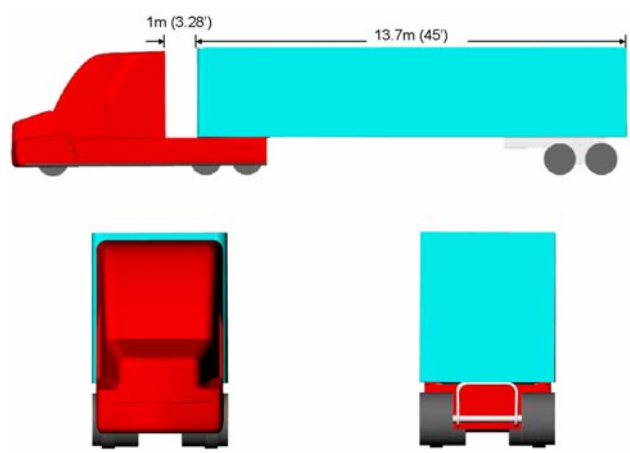


**Figure 2.** Generic conventional model (GCM) used in the CFD simulations.

ground plane of 65 mph are specified upstream and beneath the Generic Conventional Model (GCM), respectively. The deflection angle for the base flaps is chosen to be 20°, which Storms et al. (2004) showed to be the optimum angle for the GCM geometry at full-scale Reynolds numbers. The turbulent flow about the GCM is modeled using both the steady and unsteady Reynolds-averaged Navier-Stokes (RANS) approach. The simulations are

performed with the CFD code, STAR-CD, on the parallel supercomputers at LLNL with multiple computational meshes ranging in size from 1.4 to 10.0 million cells.

The drag reduction devices employed in the tractor-trailer gap are modeled on a simplified heavy vehicle geometry referred to as the MGTS (Figure 3). The simulations of the gap devices are performed with NASA's OVERFLOW code, a compressible, control-volume based code using overset grids (Hariharan et al. 1997). Based on prior experience (Salari et al. 2004), the two-equation, Menter SST, steady RANS turbulence model (Menter 1994) is used for all simulations. To ensure proper turbulence model performance, all surface grids are extruded such that off-the-wall y+ values are less than unity. The computational domain extends 15 vehicle widths upstream, 30 widths downstream, and 10 above and to the sides of the model. All walls, with the exception of the ground plane, are assigned slip wall boundary conditions. This is done to mimic the blockage experienced in the 3-foot by 4-foot Dryden wind tunnel at USC (Browand et al. 2005); however, no attempt is made to model the tunnel sides or ceiling. In addition, the four posts that support the model above the tunnel floor are omitted from computations. Furthermore, the incoming boundary layer is eliminated in the experiment by applying suction through the test section floor. This effect is reproduced computationally by applying a fixed velocity boundary condition to the ground plane.

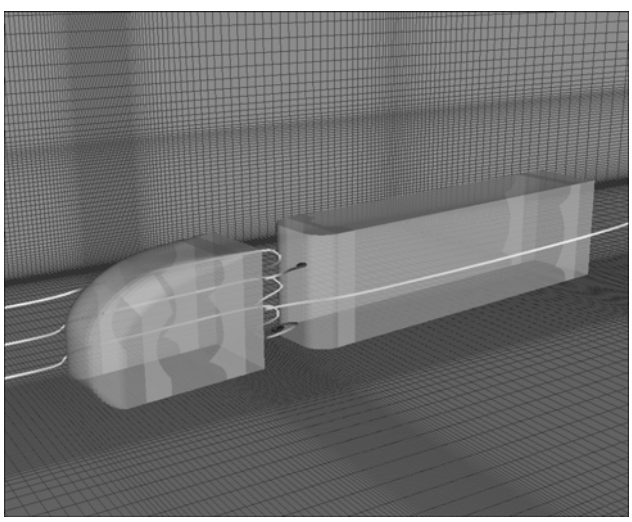

**Figure 3.** Simplified heavy vehicle geometry (MGTS) at 6° yaw with velocity-colored streamtraces

## Results and Discussion

The resulting drag reduction of the base flaps and wedge-shaped skirt are shown in Figure 4. Although there is some sensitivity to the level of grid confinement, a comparison of the values of section drag coefficient ($C_d$) between similar-sized grids indicates that the simulations predict levels of drag reduction comparable to those seen experimentally. Another important observation from this plot is that the unsteady RANS simulations, which require a substantial amount of central processing unit (CPU) power and storage space, predict nearly the same drag coefficient as that seen in the steady RANS simulations. This result could be of interest to tractor-trailer manufacturers, who are concerned about accurately predicting $C_d$, but do not have the computational capability to perform high resolution, unsteady simulations.

The simulations also highlight the manner in which the devices alter the flow field about the heavy vehicle. As can be seen in the velocity streamlines (Figure 5), the wedge-shaped skirt increases the upwash beneath the trailer. The base flaps produce an appreciable downwash, which has the effect of transporting high momentum fluid from the freestream into the trailer wake and reducing the overall wake size. Furthermore, it is evident that the base flaps reduce both the size and strength of the swirling flow structure on the bottom half of the trailer wake. As can be seen in Figure 6, this

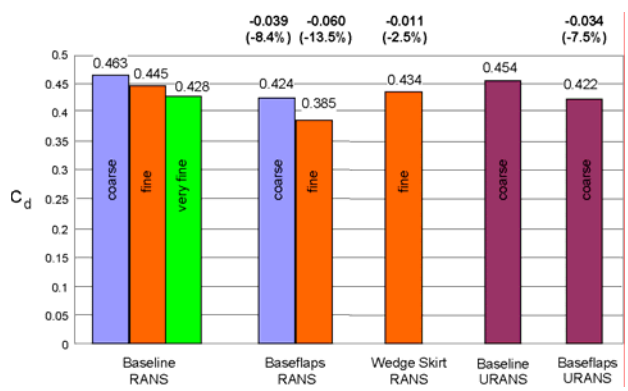


**Figure 4.** Drag coefficient for the baseline GCM with and without the drag reduction devices. The labels "coarse," "fine," and "very fine" refer to the level of grid refinement. The bold numbers at the top of the plot are the reductions in $C_d$ with respect to the baseline configuration, and the numbers in parenthesis are the percent reduction in $C_d$.

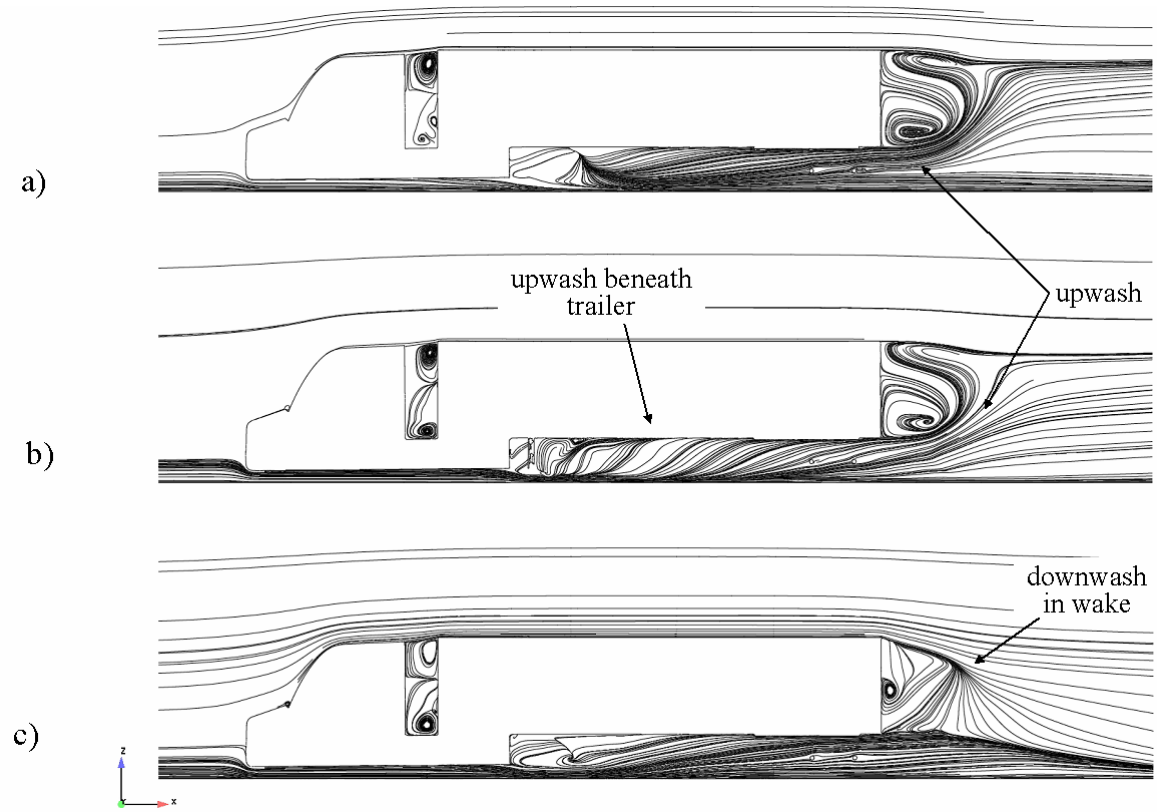


**Figure 5.** Velocity streamlines at the centerplane of the a) baseline GCM, b) GCM with the wedge-shaped skirt, and c) GCM with base flaps

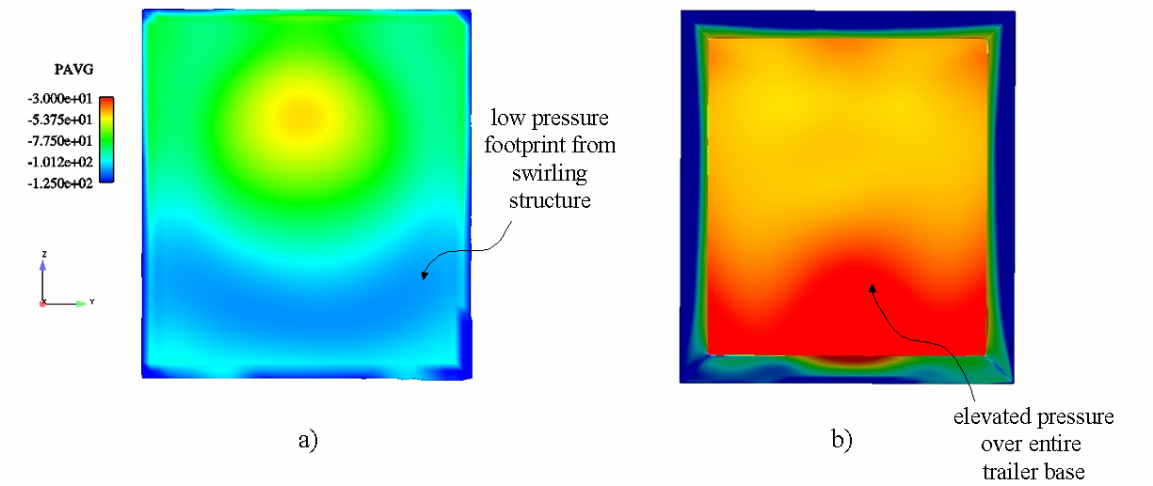


**Figure 6.** Pressure distribution over the trailer base of the a) baseline GCM and b) GCM with base flaps

swirling flow structure is source of the low pressure region on the trailer base. By eliminating this structure, the base flaps remove the low pressure footprint, increase the pressure over the trailer base, and reduce the overall vehicle drag.

The baseline MGTS simulations at lab-scale Reynolds number and 6° yaw compare favorably to experiment for both body forces and flow structure, see Figures 7 and 8. These results add confidence in the use of overset grids with steady RANS turbulence models for predicting the flow around a simplified tractor-trailer with drag-reducing devices. The trailer splitter plate is nearly as effective as tractor cab extenders in reducing drag at relatively low, lab-scale Reynolds numbers. Both devices appear to suffer from increases in vehicle side force, although the splitter plate to a lesser extent. In addition, each device is found to be most effective at reducing drag on the part of the vehicle to which it is mounted. Furthermore, the splitter plate is most effective at larger gap lengths, where more flow is entrained into the gap and interacts with the trailer face. A summary of each device's performance at two gap lengths is plotted in Figures 9 and 10.

At a full-scale Reynolds number of 7 million, tractor cab extenders remain the more effective of the devices at reducing gap drag, but due mostly to the benefit received by the trailer. At larger gap lengths, one would expect the tractor cab extenders to lose

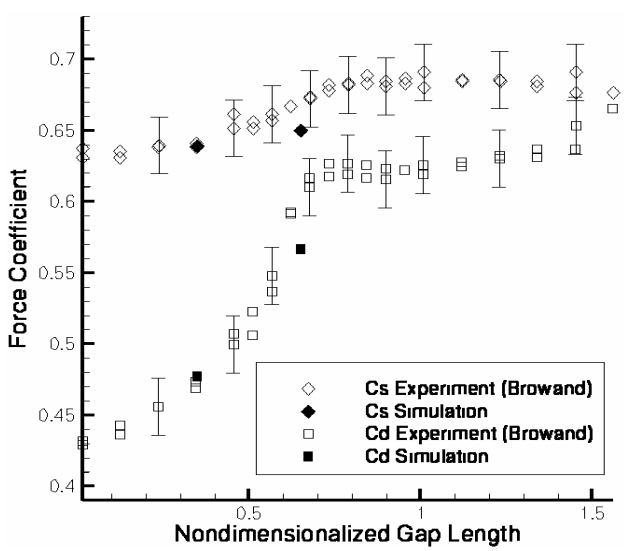


**Figure 7.** MGTS body force coefficients at 6° yaw and Re = 340,000

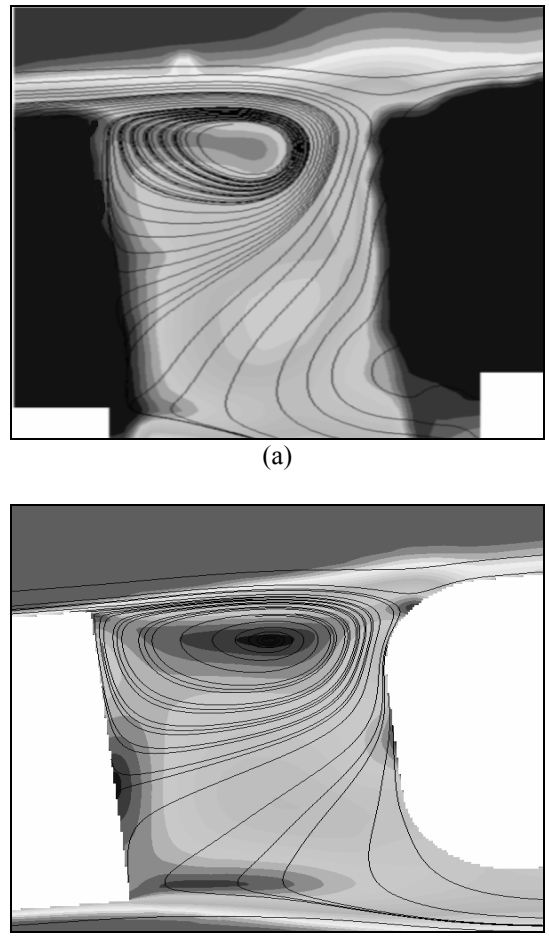


**Figure 8.** Mid-height streamtraces and velocity magnitude contours for a) Experiment (Browand et al. 2005) and b) Simulation at 6° yaw and Re = 340,000

some of their advantage to a trailer splitter plate in redirecting gap flow near the trailer. The fact that the addition of a trailer splitter plate is shown to simultaneously reduce both drag and side force, raises the question of vertical flow effects in the tractor-trailer gap. Unfortunately, no experimental data are available for MGTS lift, and any results would surely be sensitive to floor boundary layer reproduction. Regardless, for all simulations, the trailer splitter plate consistently reduces vehicle drag without a significant increase in side force. A summary of each device's performance is plotted in Figure 11.

Of the gap devices tested, the splitter plate is not as effective as cab extenders in reducing drag at lab or

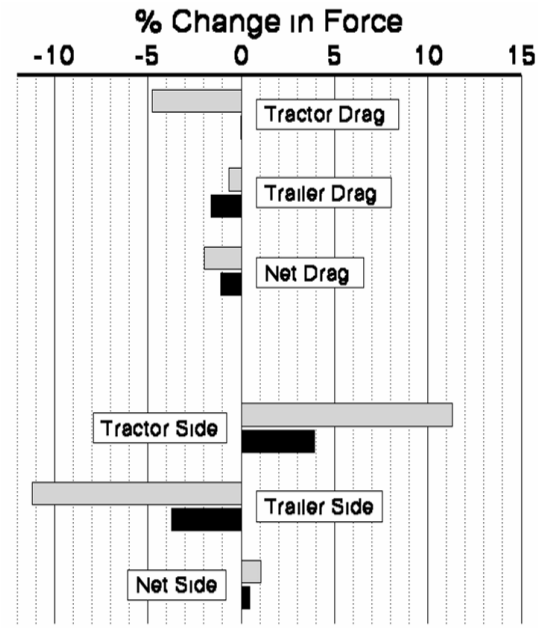


**Figure 9.** MGTS body force modification at 0.35 length gap, Re = 340,000: Cab extenders — Gray, Splitter plate — Black

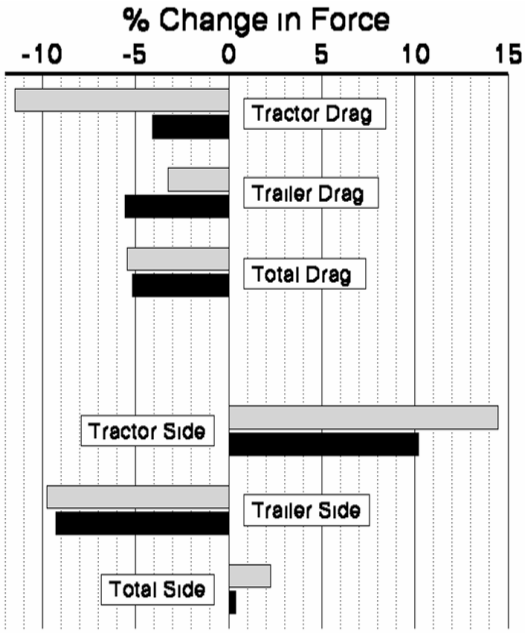


**Figure 10.** MGTS body force modification at 0.65 length gap, Re = 340,000: Cab extenders — Gray, Splitter plate — Black

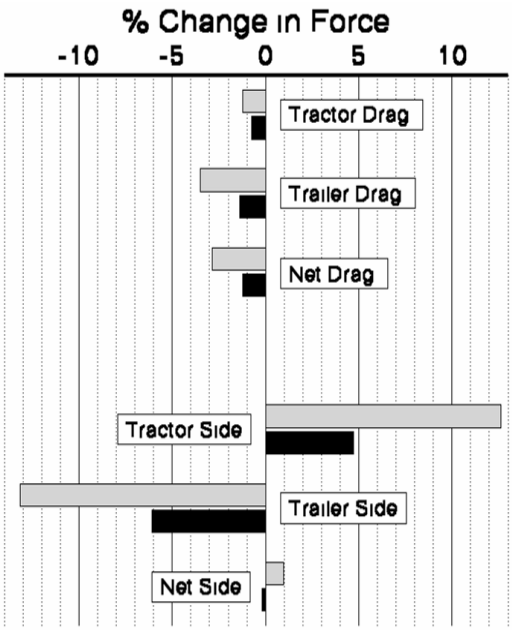


**Figure 11.** Full-scale MGTS body force modification at 0.38 length gap, Re = 7,000,000: Cab extenders — Gray, Splitter plate — Black

full-scale Reynolds numbers. However, drag reduction is comparable to tractor cab extenders, and improves with increasing gap length. Unlike tractor cab extenders, the trailer splitter plate does not appear to suffer from large increases in vehicle side force at yaw, perhaps even lessening side force while simultaneously reducing drag. Results indicate that for typical crosswinds, vehicle side force may be 50% larger than drag. Any device that serves to reduce drag without significant side force compensation may prove to be beneficial for both tire wear and vehicle stability. In addition, a vehicle equipped with a trailer splitter plate does not suffer from the reduced turning radii associated with cab extenders.

## Summary

The following are the main accomplishments for the FY05 effort in heavy vehicle aerodynamic drag reduction:

1. Assessed the performance of add-on drag reduction devices using CFD.
2. At lab-scale Reynolds numbers, both the tractor cab extenders and the trailer splitter plate produce a 5% drag reduction at large gap lengths.

3. At full-scale Reynolds numbers, the addition of a trailer splitter plate decreases vehicle drag by 1% while maintaining vehicle side force.
4. At full-scale Reynolds numbers, base flaps decrease the drag coefficient by 8–14%.
5. At full-scale Reynolds numbers, the wedge-shaped skirt decreases the drag coefficient by 2%.
6. Observed that at full-scale Reynolds numbers, the increased vertical flow in the gap between the tractor and trailer alters the gap flow structures.
7. Determined that base flaps function by increasing the pressure on the trailer base through the elimination of a recirculation zone on the trailer base.
8. Investigated the sensitivity of the drag coefficient reduction of the wedge-shaped skirt and base flaps to both grid refinement and steady versus unsteady simulations.

## References

Browand, F., Radovich, C., & Boivin, M., "Fuel Saving by Means of Flaps Attached to the Base of a Trailer: Field Test Results," browand@spock.usc.edu, University of Southern California, 2004.

Browand, F., Hammache, M., Arcas, D., "Flow in the Gap Between Two Bluff Bodies with Application to Heavy Trucks," To be published, 2005.

Cooper, K.R., "Truck Aerodynamics Reborn—Lessons from the Past," SAE Paper No. 2003-01-3376, 2003.

Hariharan, N., Wang, Z.J., Buning, P., "Application of Conservative Chimera Methodology in Finite Difference Settings," AIAA-97-627, 1997.

Menter, F.R., "Two-equation Eddy-Viscosity Turbulence Models for Engineering Applications", *AIAA Journal*, 32.8 (1994): 1598-1605.

Ortega, J.M. & Salari, K., "An Experimental Study of Drag Reduction Devices for a Trailer Base and Underbody," AIAA Paper No. 2004-2253, 2004.

Salari, K., Ortega, J.M., Castellucci, P.J., "Computational Prediction of Aerodynamic Forces for a Simplified Integrated Tractor-Trailer Geometry," AIAA-2004-2253, 2004.

Storms, B.L., Satran, D.R., Heineck, J.T., & Walker, S.M., "A Study of Reynolds Number Effects and Drag-Reduction Concepts on a Generic Tractor-Trailer," AIAA Paper No. 2004-2251, 2004.

# I.C. Computational Modeling of Spray Dispersion in Heavy Vehicle and Tire Assembly Wakes

*Kambiz Salari, Rose McCallen, Jason Ortega, Craig Eastwood, John S. Paschkewitz, Paul Castelucci*
*Lawrence Livermore National Laboratory*
*7000 East Ave, L-098, Livermore, CA 94551*
*(925) 423-0958, fax: (925) 422-3389, e-mail: mccallen1@llnl.gov*

*Technology Development Managers: Sid Diamond and Lee Slezak*
*(202) 586-2335, e-mail: Lee.Slezak@hq.doe.gov*

*Technical Program Manager: Jules Routbort*
*(630) 252-5065, e-mail: routbort@anl.gov*

---

*Contractor: Lawrence Livermore National Laboratory*
*Contract No.: W-7405-ENG-48*

---

## Objectives

- Analyze the formation and spread of spray clouds generated around and behind heavy vehicles using computational models.
- Build and leverage understanding of tire aerodynamics required for detailed drag calculations to investigate spray dispersion.
- Develop a set of predictive computational tools available to truck and tire manufacturers to estimate the effectiveness of splash and spray add-on devices while simultaneously determining the effects of aerodynamic drag.

## Approach

- Investigate water spray transport around truck and tire geometries using the commercial computational fluid dynamics (CFD) solver. Use StarCD in combination with the mesh generation tool Harpoon.
- Model spray generation processes resulting from both aerodynamic breakup as well as fine spray generation resulting from droplets hitting the truck or tire geometry. Inject droplets into the flow distributions from multiple points on the truck or tire using rough estimates for initial velocity and size; use empirical droplet breakup and collision models in StarCD.
- Obtain quantitative estimates of the resulting spray dispersion, droplet size distributions, and visibility impairment for the truck cases.
- Determine the differences between using the large eddy simulation (LES) and unsteady Reynolds-averaged Navier Stokes (RANS) turbulence modeling approaches on the predictions of spray transport.

## Accomplishments

- Completed the only known simulations of the detailed, unsteady flow fields around realistic rotating tandem dual tires.
- Completed the first CFD calculations of spray cloud generation and transport around truck and truck tire geometries.

- Demonstrated that aerodynamic drag-reducing add-on devices such as base flaps may actually impair motorist visibility by focusing drops into "passing zone" behind and to the left of truck.
- Determined that truck spray is a fine mist with droplets having diameters less than 0.1 mm; larger droplets travel along ballistic trajectories and do not interact strongly with the flow field.
- Determined that aerodynamic breakup is minimal and that the primary source of small droplets is collisions with other parts of the truck or tire.
- Discovered that the addition of fenders, fairings, or mudflaps make little difference in the transport of the small droplets in the spray cloud; we speculate that collision of larger droplets with these additional surfaces may actually serve to generate more spray without some type of surface treatment.
- Investigated simpler LES models in StarCD; compared the resulting spray transport in flows around a modified GTS geometry and demonstrated that Unsteady Reynolds-averaged Navier Stokes modeling (URANS) predicts substantially less dispersion than does LES.

### Future Directions

- Integrate understanding of spray transport dynamics into models of aerodynamic drag reducing devices.
- Incorporate experimental data on spray formation from effort at University of Southern California (USC) into calculations.
- Develop capability to model splash and integrate into existing models for spray transport.
- Investigate more sophisticated models for droplet collision and breakup on absorbent surfaces.

---

## Introduction

The spray clouds generated around trucks in wet weather conditions reduce motorist visibility and are often cited by motorists as a major safety hazard. There have been numerous experimental studies over the last 30 years that have failed to conclusively demonstrate that any aftermarket add-on devices reduce truck spray. As discussed in the AAA Foundation for Traffic Safety report by Manser (2003), much of the work done during the 1980s focused on what is still the best understanding of how spray is generated: water droplets are thrown from the tire treads and impact hard surfaces on the truck, breaking into small drops that get sucked into the vehicle wake. The more pronounced the vehicle wake, the greater the amount of droplet dispersion. Using a 1985 and 1997 Freightliner tractor, Manser demonstrated that the latter, more-aerodynamic tractor generated less spray. These improvements can be attributed to streamlining of the tractor and the reduction of the size of the wake around the front of the vehicle. Manser reported that lower-drag tractor designs, in combination with *absorbent* mudflaps that extend fully to the ground (to minimize any breakup leading to mist formation) "definitely helped reduce spray cloud density."

It is less clear that the addition of drag-reducing add-on devices, especially on trailers, will have a similar effect. Droplets can exhibit what is known as "particle focusing" in which small particles can get trapped in low-pressure vortex cores. It is possible that devices that manipulate trailer aerodynamics could reduce motorist visibility by "pushing" spray into the path of a passing car.

As experiments in this area are both difficult and expensive to perform, a predictive computational capability would be of great value to understanding and designing spray reduction methods. Our objective over the past year has been to demonstrate the capability of computational fluid dynamics (CFD) tools to investigate this problem and to make the first steps towards developing a predictive capability.

## Computational Methodology

The commercial CFD solver StarCD was used for all of the simulations presented here. The free-stream flow rate was set to a representative highway speed (29 m/s ~60 miles per hour [mph] for the generic conventional model [GCM] cases; 20 milliseconds [m/s] ~40 mph for the tire and ground transportation system [GTS] cases) and the resulting turbulent flow

field around the geometry was calculated using the Sheer Stress Transport (SST) turbulence model with a wall function, except in the case of the Large Eddy Spray (LES) simulations of the GTS, where the constant coefficient Smagorinsky LES model was used. In all cases, the simulations were completed in a time-dependent manner as droplet dispersion and breakup calculations are strongly dependent on the *dynamic* behavior of the flow to which they are exposed. Meshes varied in size from approximately 1.5 million cells (GCM) to over 7 million cells (dual tire). For tire simulations, a local kinematic boundary condition was employed to account for the rotation of the tire and a moving ground plane was used. For truck simulations, the ground plane was specified to be moving at the same velocity as the free stream.

The primary thrust of this work was the integration of StarCD's droplet atomization and transport models into the CFD simulations. The droplets were modeled as point particles having finite mass, drag and velocity. Several empirical aerodynamic breakup models are available; the model of Pilch and Erdman was used since it accounts for the widest range of breakup modes. Particle-particle collisions were also accounted for but are generally rare events in the computations. Each computational particle (or parcel) represents a collection of particles with a fixed mass; if breakup occurs during flight, the droplet size and number of particles represented by the parcel will change, but a new parcel will not be created. Collisions with surfaces, which are necessary to accurately model of the spray problem, were modeled using an empirical model derived for gasoline impingement on engine cylinders. While we anticipate that this model will not be quantitatively predictive for the problem at hand, it should illustrate qualitatively correct behavior. Note that new parcels *are* created as a result of droplet impacts using this model.

The initial conditions for the particles were difficult to specify without an experimental database with which to compare. As such, a distribution of particle sizes ranging from 5 microns to 1 millimeter (mm) was used and injection velocities were based on rough estimates: for example, droplets were injected near the base of the tires at a velocity equal to the tire rotational speed and an angle tangent to the tire tread.

## Results and Discussion

*Effect of Drag-Reducing Devices on Motorist Visibility*

A representative snapshot of the spray dispersion patterns in the wake of the baseline GCM is shown in Figure 1. We have observed the spray cloud is quantitatively more concentrated in the drag-reduced case (not shown). This effect is due to the focusing of droplets in the low pressure region in a vortex core that is pronounced in the base flap case. We have also observed that remarkably little droplet breakup occurs due to aerodynamic forces by watching individual droplet traces; almost all the droplet breakup occurs when large drops hit truck or tire surfaces.

We can quantitatively define a measure of motorist visibility by examining the particle concentration in a representative passing zone shown as a box in Figure 1 at a given simulation time. For the baseline GCM, the concentration is 2.15 particles/cubic meter while for the base flap case the concentration is 3.38 particles/cubic meter. This result suggests that the use of a drag-reducing device such as *base flaps may actually decrease motorist visibility on rainy days*.

*Detailed Tire Simulations and Effect of Fenders*

All of the truck-like geometries considered in our CFD studies to date have used simple representations of the wheels. Here, we consider the aerodynamics of more realistic tire assemblies with spray models in StarCD (tires alone) or with massed particle traces in our post-processing software,

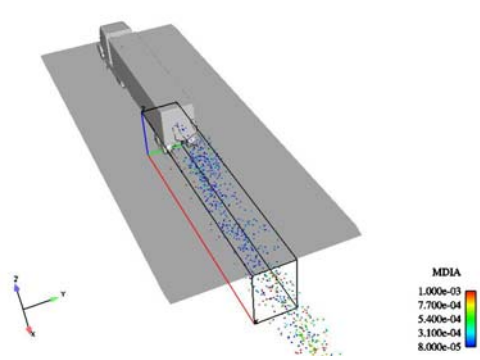


**Figure 1.** Sampling box for calculation of visibility reduction

which does not account for small droplets resulting from collisions but does illustrate the effectiveness of add-on devices for spray suppression. We have considered a simplified tandem dual slick tire arrangement representative of a trailer tire assembly both with and without fender add-ons.

As shown in Figure 2, we have been able to simulate a qualitatively realistic spray field using multiple droplet injectors. The flow field is quite complex and highly unsteady; the simulation presented here represents two iterations in mesh refinement to adequately resolve the fine scale structures on the front corners of the front tire, the gap between the tires and the wake region. As in the aforementioned GCM studies, the droplets that are most strongly transported by the flow field are on the order of 10 microns and are seen as dark drops along the top of the tire in the figure. Little aerodynamic breakup occurs but small droplets are created by collisions of large droplets from the front tire with the back tire.

In Figure 3, we present the results of massed particle traces for the case of a tandem dual tire with a fender. The lines represent the paths followed by

**Figure 2.** Droplet dispersion about tandem dual tire

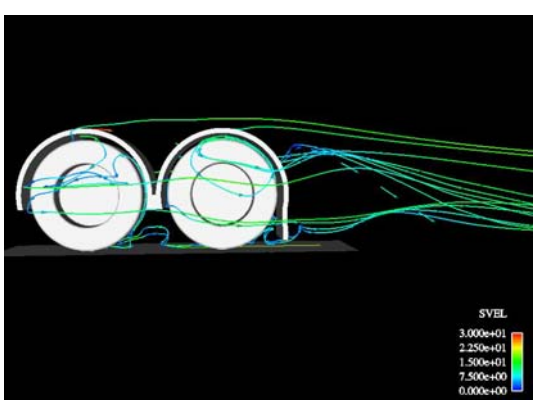


**Figure 3.** Massed particle traces in flow around tandem dual tire with fender

water droplets having a diameter of 10 microns. It is clear that the fender has little effect on the transport of this fine mist. Larger particles (not shown) typically impact the fender and if a full spray simulation were completed, would lead to the generation of smaller droplets easily transported by the flow. We have also considered the case of a Reddaway-type fender (not shown), which has a small fairing across the top of the fender; in this case, the lateral spray transport is decreased but the spray is "pushed" to the inboard side of the wheels. We speculate that spray would likely be concentrated into the region directly behind the truck. While the visibility for a passing motorist may be improved, the visibility for a motorist following the vehicle might actually be degraded. These simulations corroborate existing experimental data that demonstrate spray reducing add-on devices are ineffective but suggest that absorbent or breakup-suppressing surface treatments near the wheels may help mitigate the problem.

*Large Eddy Simulation Turbulence Modeling and Effect on Spray Dispersion*

All of the simulations presented thus far have utilized the URANS methodology for turbulence modeling. While this approach is robust and captures the time-dependent nature of the flow, it has been well established in the scientific literature that URANS models poorly predict the unsteady wakes behind bluff bodies such as tires and trucks. URANS fails to capture small-scale features through the Reynolds averaging process and can lead to erroneous predictions of transport of small particles or droplets that interact with them. To assess the possible error in our URANS simulations, we have completed some preliminary calculations of spray transport using an LES model and compared the results to those from a URANS simulation. In Figure 4a, we present an instantaneous snapshot of the velocity contours and spray cloud in the LES case, while in Figure 4b we present the URANS case. It is obvious that the wake has a far different structure and the droplets are more strongly dispersed in the vertical direction in the LES case. We can quantify this by considering the root-mean-square (RMS) distance of the particles from the ground (vertical dispersion) or the centerline (horizontal dispersion). The results are shown in Figure 5 for horizontal dispersion; we see similar

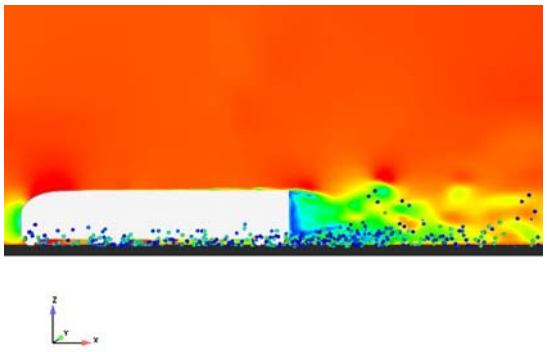

**Figure 4a.** Spray cloud behind simplified heavy vehicle geometry (MGTS) predicted using Large Eddy Simulation (LES)

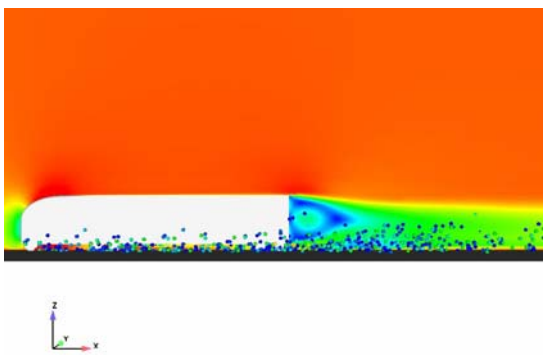

**Figure 4b.** Spray cloud behind MGTS predicted using Unsteady Reynolds Averaged Navier-Stoker (URANS) methodology

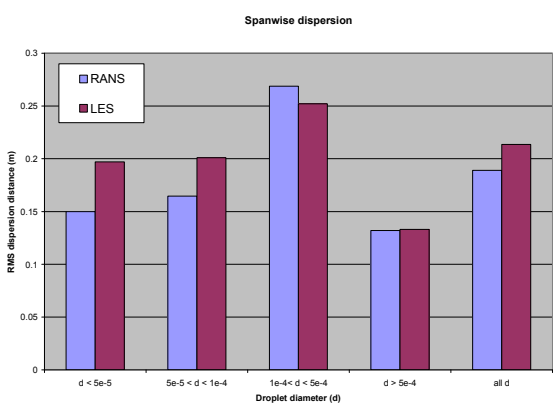


**Figure 5.** Horizontal spray dispersion in MGTS wake predicted using LES modeling and the URANS methodology

results for vertical dispersion. Our preliminary finding is that the URANS models appear to underestimate the amount of spray dispersion; using LES would likely improve the accuracy of any predictions but comes at a considerable computational cost.

## Summary

These are the highlights of what we achieved during FY 2005 in the area of simulation of heavy vehicle spray dispersion:

1. Demonstrated that drag-reducing add-on devices may make the spray problem worse using CFD.
2. Completed investigation of detailed tandem dual tire aerodynamics with spray propagation.
3. Illustrated that fenders and fairings are ineffective at mitigating spray problem.
4. Explored advanced turbulence models for spray dispersion modeling and showed that extra cost may lead to improved predictions.

## Conclusions

We have completed a preliminary computational investigation of spray propagation around truck and tire geometries. These simulations have demonstrated that motorist visibility may be adversely impacted by drag-reducing devices, and fenders or fairings have minimal impact on spray transport. However, these results are dependent on the details of how the spray is injected and how droplet-wall collisions are modeled. The former will benefit strongly from experimental data from the work performed by Prof. Fred Browand at USC and the latter will require the development of more sophisticated computational tools. These same tools are also required to model the process of splash — the process by which water in a puddle is displaced by the tire and breaks up into droplets — which is quite challenging computationally and is currently the focus of several research efforts in the combustion atomization and spray community. With these tools in place, it will be possible to develop a predictive tool of use to truck and tire designers.

## Reference

Manser, M., Koppa, R., & Mousley, P. "Evaluation of splash and spray suppression devices on large trucks during wet weather," AAA Foundation for Traffic Safety, www.aaafoundation.org/pdf/SplashSpray.pdf, 2003.

# I.D. Experimental Measurement of the Flow-field of Heavy Trucks

*Principal Investigator: Fred Browand*
*Aerospace & Mechanical Engineering, University of Southern California*
*RRB 203, Los Angeles CA 90089-1191*
*(213) 740-5359, fax: (213) 740-7774, e-mail: browand@spock.usc.edu*

*Technology Development Managers: Sid Diamond and Lee Slezak*
*(202) 586-2335, e-mail: Lee.Slezak@hq.doe.gov*
*Technical Program Manager: Jules Routbort*
*(630) 252-5065, e-mail: routbort@anl.gov*

---

*Contractor: Lawrence Livermore National Laboratory*
*Subcontract No.: B545349*

---

## Objective

- Improve the performance of heavy trucks by reducing aerodynamic drag, and by increasing safety.

## Approach

- Improved use of aerodynamic design decreases truck drag and consequently improves fuel economy. However, decreasing truck drag places more stress on truck brakes. We show that manipulation of the cab extender angle can be used either to minimize drag or to increase drag when additional braking power is required.
- Water spray from heavy truck tires is an important safety issue. The spray decreases the rearward visibility of the truck drivers. For automobiles in the immediate vicinity, spray obscures the roadway on either side of the truck.

## Accomplishments

- Manipulation of cab-extender angle
  - Wind tunnel drag measurements were made to study the effect of thin plates placed along the trailing edge of the tractor (cab). The plates can be inclined inward or outward from the alignment parallel to the side of the cab. The lowest drag position is with extenders aligned with the direction of the cab. Deflecting extenders outward increases drag, as might be expected. But surprisingly, deflecting the cab extenders inward results in a larger increase in drag. The cab extender angle can be adjusted to provide minimum drag in cruise, and an additional higher drag for braking situations.
- Design and construction of a new apparatus for the study of spray formation from rolling tires
  - In the new apparatus, two tires are rolled in contact with one another, and water is injected from a specially designed injector placed just upstream of the contact patch. The speed of the injected water jet is the peripheral speed of the tires.

## Future Directions

- In an effort to get devices on the road, continue investigation of aerodynamic devices that do not present operational and maintenance issues
- Initiate a program of study of tire spray using the newly constructed apparatus.

---

## Manipulation of Cab-Extender Angle

The variation of drag with varying cab-extender angle has been described in SAE Paper No. 2005-01-3527 entitled: "Wind Tunnel Test of Cab Extender Incidence on Heavy Truck Aerodynamics" by Charles Radovich.

A wind tunnel experiment has been conducted to determine the changes in drag and side force due to the presence and position of cab extenders on a model of a commercial tractor-trailer truck. The geometric variables investigated are(1) the cab extender angle of incidence, (2) the tractor-trailer spacing, and (3) the yaw angle of the vehicle. Three cab extender angles were tested — 0°, 15° (out) and −15° (in) with respect to the side of the tractor. The wind tunnel models of both cab and trailer had the same width and height.

Cab extenders having a length of 25.4 millimeters (mm) were constructed. Expressed as a fraction of the trailer width, w = 154 mm, the cab extender non-dimensional length was 0.165. There was an extender on each side of the cab and one on the top. Two views of the tractor with extenders in place are shown in Figures 1a and 1b.

Cab extender angle settings of 0°, 15° (out) and −15° (in) were tested, as sketched in Figure 2. All data were obtained at a freestream velocity ($U_\infty$) of 26 milliseconds (m/s). During the test, all three cab extenders were set with the same angle of incidence. As shown in Figures 1a and 1b, the two side edges of the top cab extender and the top edge of both side cab extenders were tapered to allow the devices to fold inward for the −15° case without touching. This resulted in a small gap between the extender edges at the 0° and 15° settings.

The minimum drag coefficient was found for the tractor and trailer combination when the cab extenders were set to 0° angle of incidence with respect to the headwind. This result holds for all yaw angles with moderate gap spacing between the tractor and trailer, as shown in Figures 3, 4, and 5.

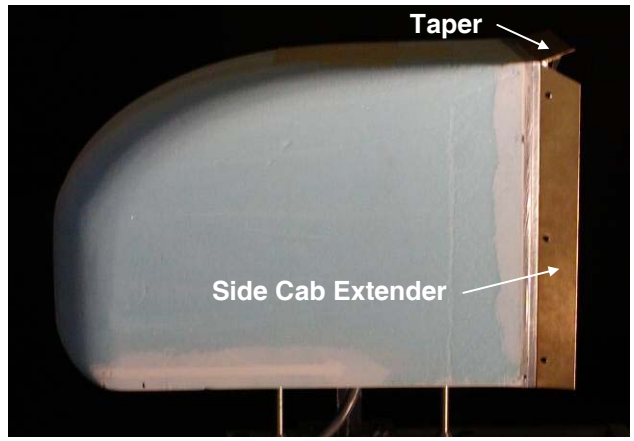


**Figure 1a.** Profile of tractor fitted with cab extenders

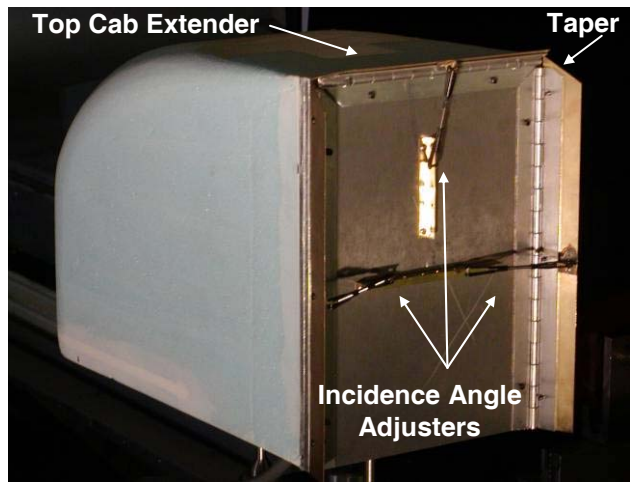


**Figure 1b.** Detail of cab extender attachment

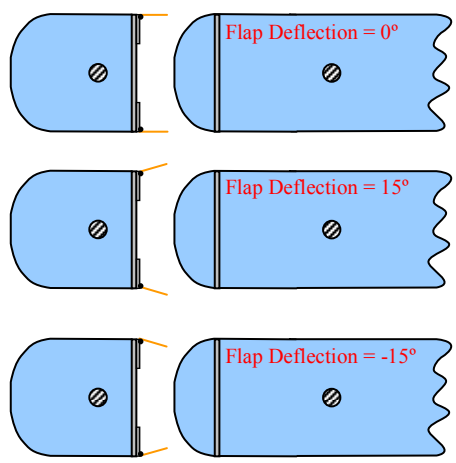


**Figure 2.** Cab extender flap angle settings

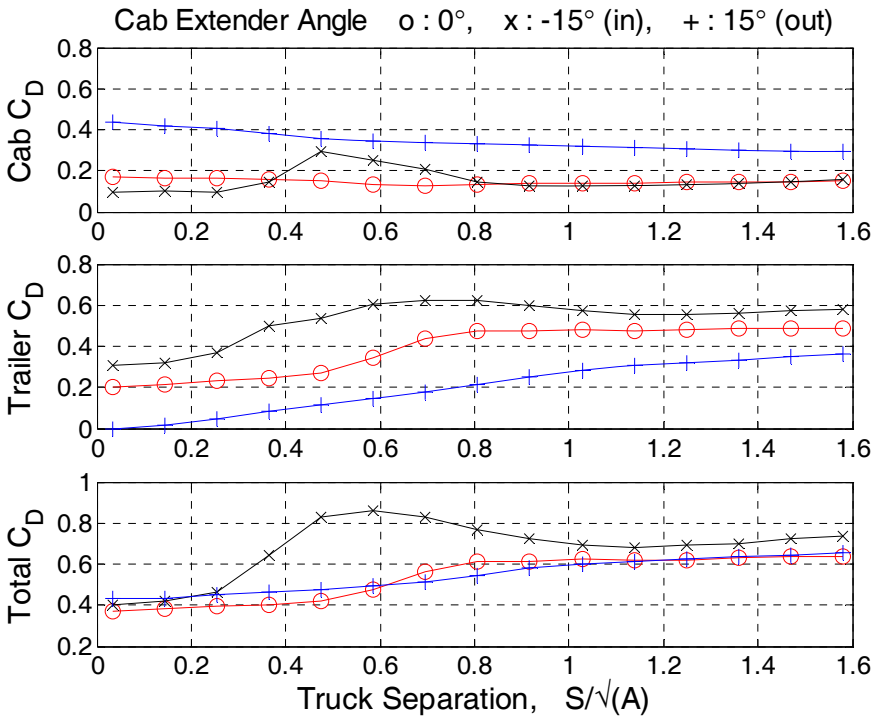


**Figure 3.** Yaw = 0°: Drag Coefficients for three cab extender angles

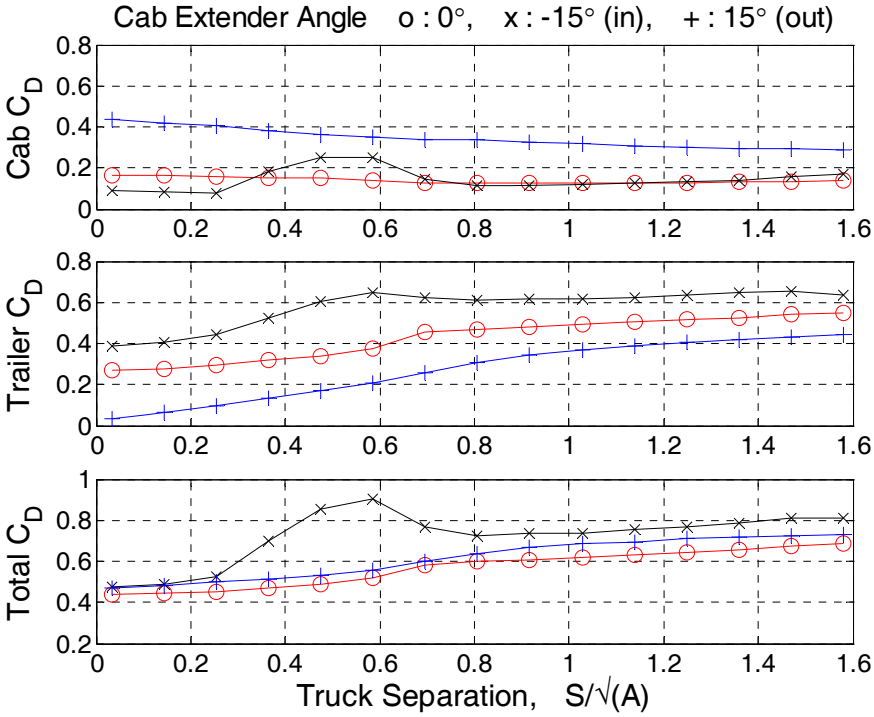


**Figure 4.** Yaw = 6°: Drag Coefficients for three cab extender angles

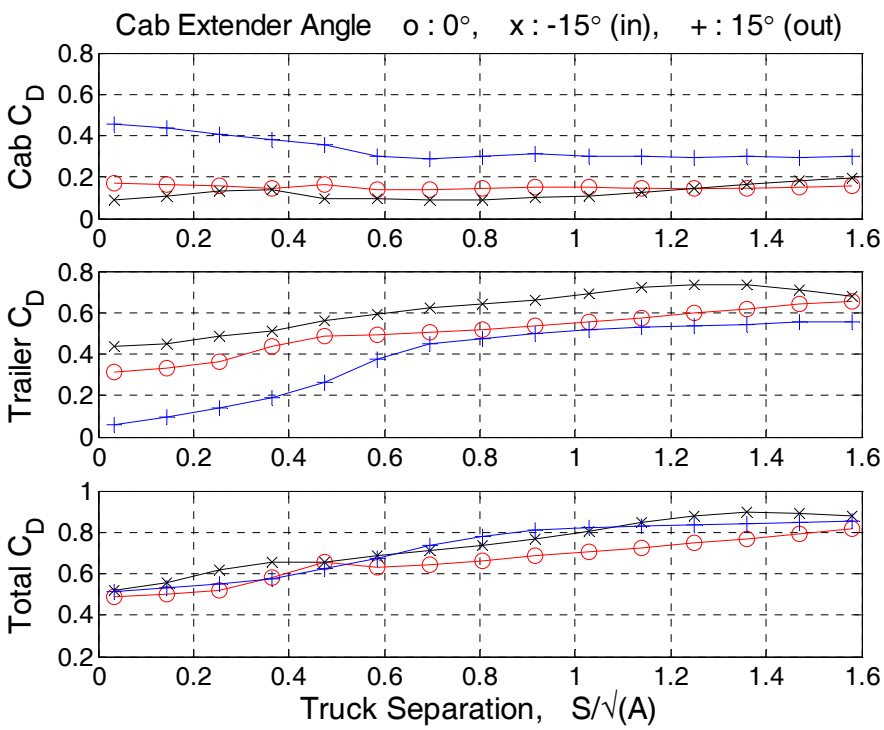


**Figure 5.** Yaw = 12°: Drag Coefficients for three cab extender angles

When no trailer is present, the tractor has less drag with the cab extenders inclined inward at −15°, as in Figure 6.

This study suggests that commercial tractor-trailer trucks can benefit from adjustable cab extender settings; 0° when using a trailer and minus 15° (−15°) when no trailer is used. When no trailer is present, at 0° yaw, a −15° setting has approximately 5% less drag compared to having extenders at 0°, and 18% less drag when compared to a similar truck with no cab extenders installed.

Increasing the drag coefficient is also possible by deflecting the cab extenders in either direction. Similar to engine braking, this effect might be desired to reduce the vehicle speed without the application of brakes. At moderate tractor-trailer spacing, the 15° (out) and −15° (in) settings can increase $C_D$ by about 10 – 20%, depending on yaw angle. At larger separations, the −15° setting can increase the drag coefficient ($C_D$) by as much as 90%.

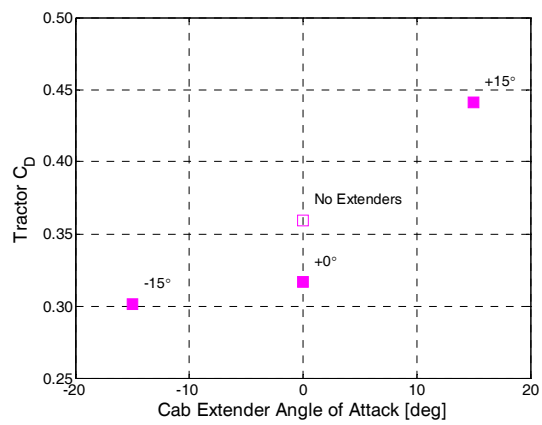


**Figure 6.** Tractor $C_D$ — no trailer present.

## Design and Construction of Apparatus for the Study of Spray Formation from Rolling Tires

A key factor in driving safety is driver visibility. Tires being driven through standing water create splash and spray which can decrease visibility for other drivers. Studying the formation of splash and spray will help in the understanding of how to maintain visibility.

Splash is water that is pushed out from the tire patch towards the sidewall of the tire. Spray is defined as the water forced into the tread pattern within the tire patch (contact patch) between the tire and the road. It is spray that we will be interested in here.

When tires produce spray, the water droplets form as a result of the break-up of jets and sheets of fluid.

## The Tire Geometry in the Laboratory

In order to correctly model a tire rolling over a wet road, the physics of the tire patch must be understood. There are two reference frames applicable, as shown in Figure 7.

In the first reference frame, an observer watches a tire rolling along wet pavement. In this scenario, the tire moves at velocity $U_{\text{car}}$ through stationary water. In the second reference frame, the observer rides with the car and sees water coming at the tire with velocity $U_{car}$. Now, using the principle of symmetry, the tire can be flipped so that a second tire represents the road, as shown in Figure 8. This principle of symmetry, and a reference frame riding with the car, is used to model the tire/water interaction in the laboratory.

## The Tire Spray Simulator

The experimental setup for capturing the formation of spray focuses on four main areas: the tire patch, the water jet, the imaging, and the lighting. The Tire Spray Simulator (TSS) machine met requirements for each of these four areas, as shown in Figure 9.

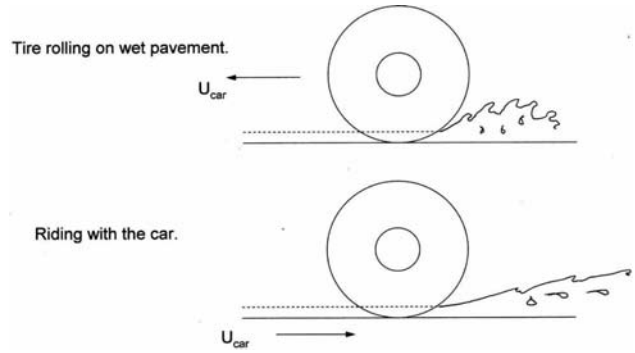


**Figure 7.** Two reference frames for tire rolling over a wet ground

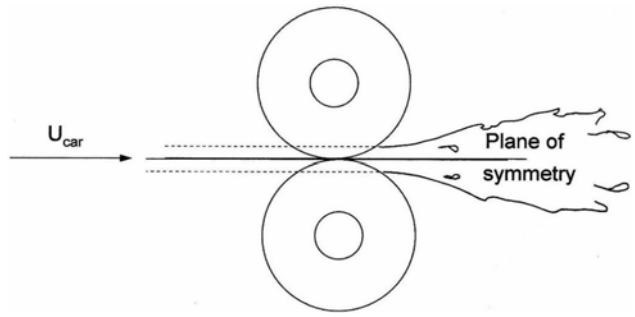


**Figure 8.** Using the principle of symmetry, a second tire represents the road.

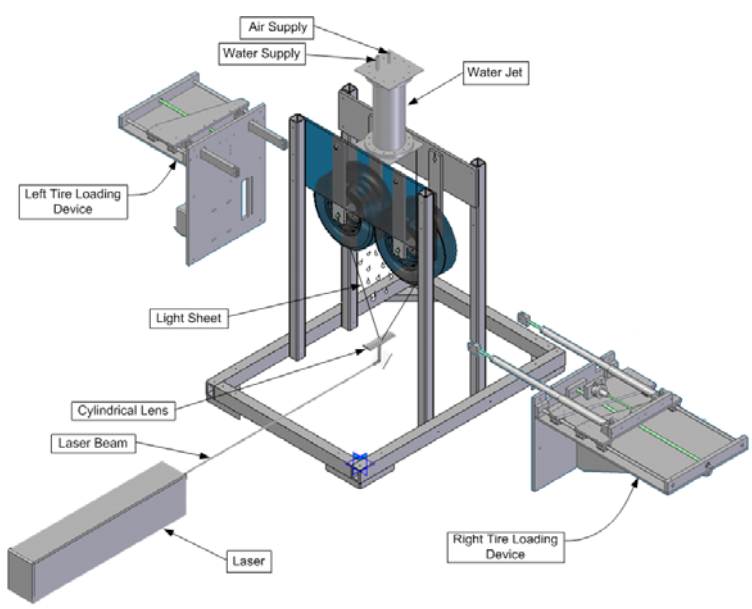


**Figure 9.** The Tire Spray Simulator

The moving tire patch is created using one tire having a smooth surface to represent the road, and another tire with a circumferential groove to simulate the tread of a car tire. The tire patch is formed when the two tires are pressed and held together using the left/right tire loading devices. Two shock/spring dampeners, controlled by two stepper motors, regulate the force on the tire patch (contact patch). A 0–250 pound (lb) Sensotech load cell loaded in-line with the dampeners measures this force. A 3-horsepower (hp) Leeson DC electric motor controls the rotation velocity of the tire to the left — the smooth tire in the present case. The second tire is driven by contact at the tire patch. A gear ratio of 30:21 is selected to properly step down the rotation of the tire. A 50 gage chain and chain-tensioner transfers rotational motion from the motor to the tires. Tires of varying grooves or tread patterns can be used to simulate different conditions.

In order to properly model the water coming into the tire patch, a jet of water traveling at the peripheral speed of the tire must be established. This is, by far the most difficult task. The water is stored in a pressurized stainless steel canister. Water and the air for pressurization enter at the top of the canister. A high-speed stepper motor drives a lead screw attached to a sliding gate at the bottom of the canister, as in Figure 10. A Teflon® sheet wraps around the gate, and actually provides a rolling contact with the seal at the exit nozzle. In operation, the stepper motor moves the sliding gate and the Teflon sheet rolls away from the exit nozzle. This process takes between 20 and 30 milliseconds. The gate remains open and water flows from the canister for a specified time, and the gate is closed. Nozzles of different sizes and shapes can easily be interchanged to allow tire treads of different sizes and geometries to be explored.

## Imaging

Image capture of the tire spray utilizes a high-speed digital video camera from Integrated Design Tools, Inc. (IDT). The camera has a resolution of 1260×1024 pixels. The camera has on-board memory of one gigabyte, or about 1,000 images. On-board memory is expandable to 8 gigabytes. Framing rate and exposure time can be controlled independently. The smallest exposure time is approximately 1 micro-second (μs). The maximum framing rate is dependent upon the size of the image. The camera limit represents a maximum transfer rate of about 7 gigabits/second for 10-bit pixel information.

Both backlighting and a laser sheet are used to light the region of interest because they provided different views of the flow. Backlighting integrates all the water droplets between the frosted glass and the camera, although some of these features may be intentionally out of focus. In contrast, the laser sheet illuminates the features in a thin sheet of light — usually 2–3 mm in thickness. In the cases shown here, the sheet is perpendicular to the plane of tire rotation, and passes through the central symmetry plane of the tire. In principle, the light sheet can be moved laterally across the face of the tires (from sidewall to sidewall), and it can be broadened beyond the usual 2–3 mm.

We are presently using a Quantel Scientific, twin-tube Yag laser capable of 150 mJoules per pulse. The lasing time is approximately 5–10 nanoseconds,

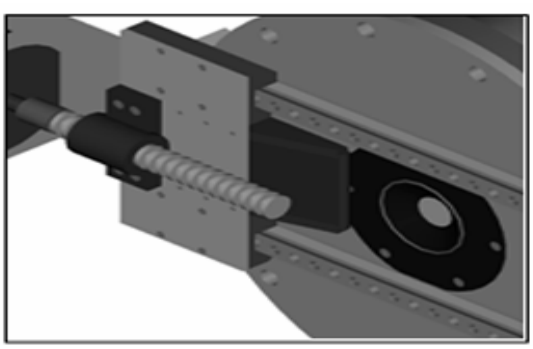

Bottom view of water jet, showing sliding wedge-shaped gate with leadscrew. A teflon sheet wraps around the wedge, sliding over the rounded nose as the gate is opened. The circular cutout receives nozzle inserts, allowing the nozzle shape to be easily changed.

**Figure 10.** Stepper-motor-controlled slider for precise water delivery

and the repetition rate is 10 Hertz (Hz) (pulses per second). The laser can be operated with one of the two tubes firing at 10 Hz, or with both tubes firing (10 Hz) with a prescribed time delay.

## Results

Figure 11 shows the experimental tire orientation a second time, and defines three cross-planes (A, B, and C) at various distances downstream from the tire patch.

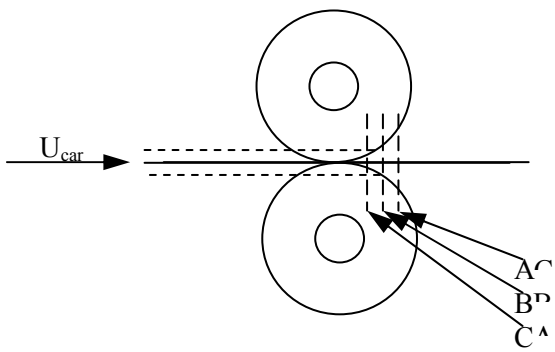


**Figure 11.** Tire orientation with three cross-planes A, B, and C

For the sake of the present argument, let both tires have the circumferential groove. Figure 12 shows what might be expected of the fluid at each cross-plane as it exits the tire groove (downstream from the tire patch). At Section A, just beyond the tire patch, water completely fills the tire groove. Farther downstream at Section B, the tires separate and are subjected to high accelerations. In a sense, the water is left behind as the tires move away from one another. Some of the water remains near the plane of symmetry as a jet, and some water remains in the grooves. At Section C, the tires have moved farther apart, the central jet is more clearly defined, and the water remaining in the groove is connected to this central jet by a thin web. With increasing tire separation, the web continually thins until breaks form and droplets are produced. Disturbances also act on the surface of the jet, and eventually break the jet into droplets.

If only one tire contains a groove, the situation is not materially different. Figure 13 gives a wide-angle view of the spray. Both tires are observed. The lower tire is the driving, smooth tire, and the upper tire is the driven, grooved tire. Lack of symmetry about a central horizontal line is evident. In the case shown, the incoming water velocity has been matched to the peripheral speed of the tires. This makes the initial Weber number of the jet larger, and the flow appears more disturbed or fractured.

The central jet is seen as a nearly periodic row of (darkened) water blobs connected to the tires by ligaments. The ligaments are relatively thick regions, and may indeed be a developing wave structure. Breaks in the web appear on both sides of the central jet, but more appear on the lower side next to the smooth tire. The web probably thins most near the surface of the smooth tire, because replenishment from the groove is not possible.

Figure 14 displays an image taken using a laser sheet. Similar to the backlight images, the web, central jet and connecting ligaments can be resolved. In addition there is a fine mist of extremely small droplets along the central plane in the picture. We believe these smallest droplets are a result of water forced between the tires themselves and into the contact patch. Digital particle imaging velocimetry (DPIV) is possible using images from this laser sheet technique.

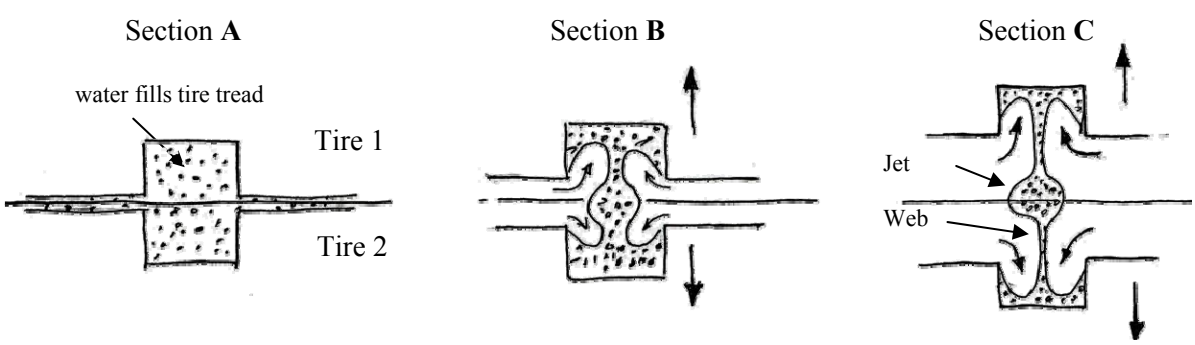


**Figure 12.** Expected behavior of water as it leaves the tire groove downstream from the tire patch

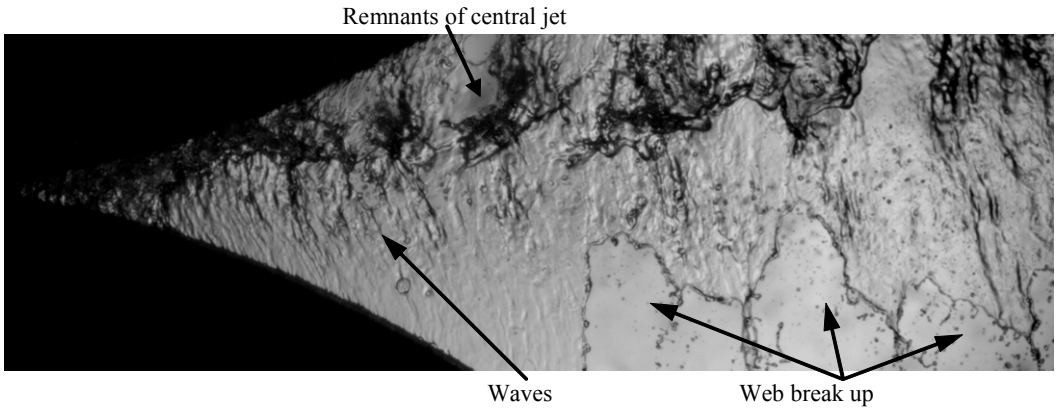


**Figure 13.** Spray from wider-angle perspective

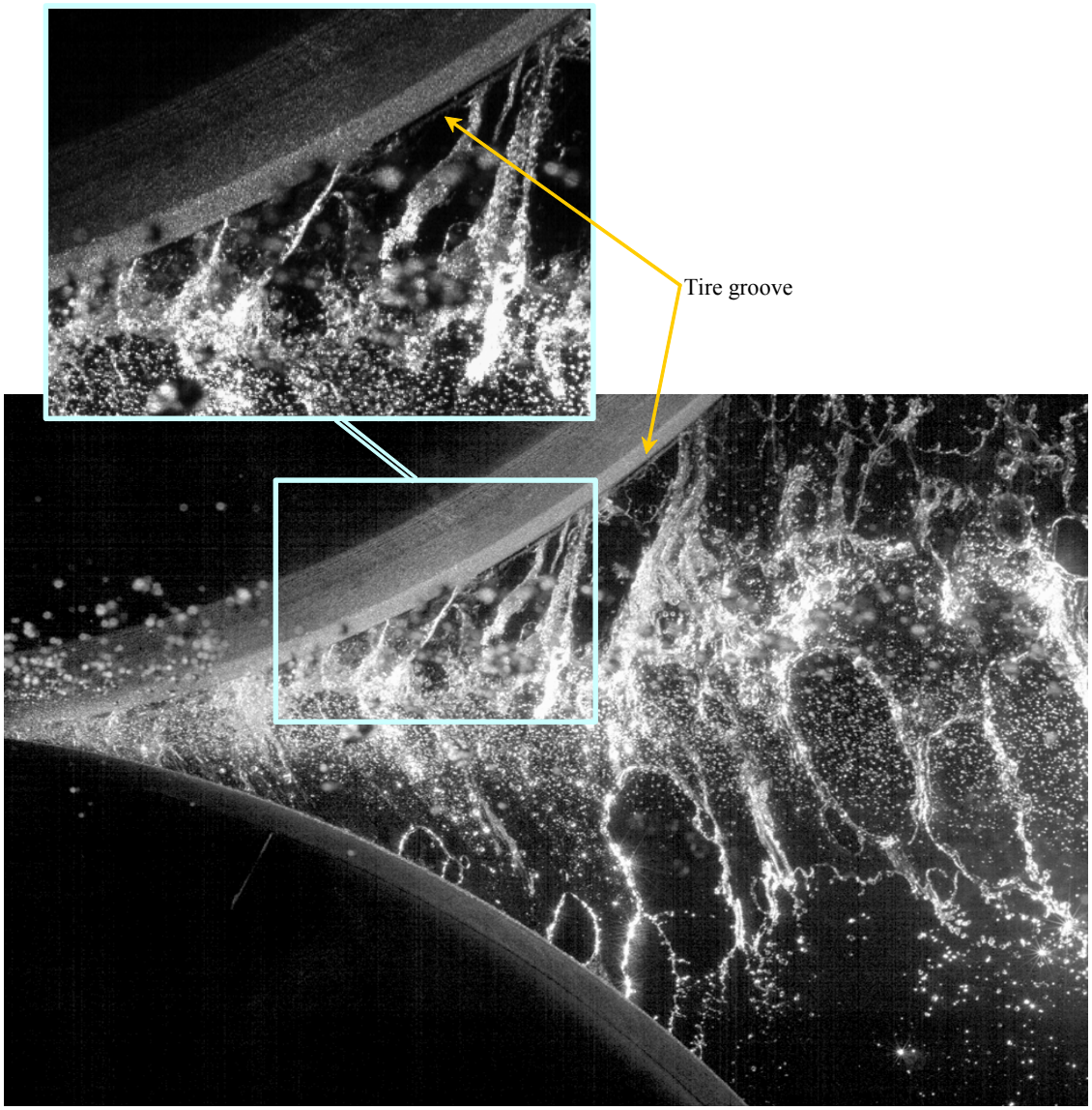


**Figure 14.** Spray image using a laser sheet (10-nanosecond pulse time)

## Conclusion

The Tire Spray Simulator (TSS) has demon-strated its usefulness in creating realistic spray. Qualitative results have been obtained with both the backlight and laser sheet procedures, and lead to an understanding of some the mechanisms behind the formation of jets and sheets, and of the eventual formation of droplets. The next step in analysis will be to measure droplet size and droplet velocity as a function of position within the spray field. Droplet sizes within the spray field are of first importance in themselves, but size information is also needed in order to resolve the velocity field according to size. We imagine evaluating droplet size in each image pair and filtering each image before the digital particle image velocimetry (DPIV) algorithms are applied.

# I.E. Detailed Experimental Results of Drag-Reduction Concepts on a Generic Tractor-Trailer

*Principal Investigator: Bruce L. Storms*
*AerospaceComputing, Inc.*
*M/S/260-1*
*NASA Ames Research Center*
*Moffett Field, CA 94035*
*(650) 604-1356, fax: (650) 604-4511, e-mail: bstorms@mail.arc.nasa.gov*

*Field Project Manager: James C. Ross*
*NASA Ames Research Center*
*M/S/260-1*
*Moffett Field, CA 94035*
*(650) 604-1356, fax: (650) 604-4511, e-mail: james.c.ross@nasa.gov*

*Technology Development Managers: Sid Diamond and Lee Slezak*
*(202) 586-2335, e-mail: Lee.Slezak@hq.doe.gov*

*Technical Program Manager: Jules Routbort*
*(630) 252-5065, e-mail: routbort@anl.gov*

*Participants*
*Dale R. Satran, James T. Heineck, Stephen M. Walker*
*NASA Ames Research Center*

---

*Contractor: NASA Ames Research Center*
*Contract No.: DE-AI01-99EE50559*

---

## Objectives

- Investigate Reynolds-number effects on the flow field and resulting aerodynamic forces generated by a 1:8-scale model of a Class 8 tractor-trailer configuration.
- Provide quality experimental data on a simplified tractor-trailer geometry for computational fluid dynamics (CFD) validation.

## Approach

- Vary the total pressure of the wind tunnel, thereby varying the Reynolds number from 500,000 to full-scale values over 6 million based on trailer width.
- Measure the forces and moments, surface pressure distribution, and off-body flow. Measurements were made at various yaw angles to study the influence of crosswind and to calculate wind-averaged drag coefficients. Several drag-reduction concepts were studied in order to document their potential benefit as well as their Reynolds-number sensitivity.

## Accomplishments

- CFD validation data are now available for use by interested industry and government researchers
- Detailed experimental results were presented for several configurations of interest with the most promising tractor and trailer add-on devices.

- The results of the study were presented at the Society of Automotive Engineers (SAE) 2005 Commercial Vehicle Engineering Conference in Chicago, IL, on November 3, 2005 (paper number SAE-2005-01-3525)

### Future Direction

- Additional drag-reduction devices will be examined for under-body flow control/drag reduction
- National Aeronautics and Space Administration (NASA) Technical Memo will be published summarizing the results from both the 12-foot and 7×10 facilities

---

## Introduction

For a typical heavy vehicle at a highway speed of 110 kilometers per hour (km/hr), the energy required to overcome aerodynamic drag is about 65% of the total expenditure (which includes rolling friction, transmission losses, and accessories). By altering the vehicle shape, it has been estimated that modern truck drag coefficients may be reduced by up to 50% resulting in an annual national fuel savings of eleven billion liters (McCallen et al. 2000). This large potential savings coupled with increasing fuel costs have spurred renewed interest in heavy-vehicle aerodynamics.

A significant number of experimental studies of heavy-truck geometries were conducted in the 1970s and 1980s (Cooper 2003). The resulting first-generation drag-reduction technology currently in use includes cab shaping, cab-mounted deflectors, trailer front-end fairings, cab side extenders, and body front-edge rounding. The cab deflectors and side extenders accounted for the majority of the wind-averaged drag reduction reducing the pre-1980 drag level by about 25%. Other drag-reduction technologies that are not widely used include tractor-trailer gap seals, trailer side skirts, and rear boat-tailing. Each of these technologies produce a reduction of the wind-averaged drag coefficient between 0.03 and 0.10, which is about one-half the benefit of the first-generation technologies. However, the benefits of these devices are additive and the resulting net reduction is relatively large.

The aerodynamic drag reduction and fuel savings of various tractor and trailer modifications was previously summarized in Cooper 1982. Since fuel consumption is the quantity of interest for commercial operators, a derivation of fuel consumption as a function of drag coefficient and road speed was provided. For trailer base flaps and skirts, the ranges of wind-averaged drag reduction were listed as 0.03–0.09 and 0.04–0.07, respectively.

More recently, a series of experimental and computational studies was funded by the U.S. Department of Energy (DOE), Heavy Vehicle Technology Program. With the goal of CFD validation, the experimental efforts have focused on simplified geometries at 1:8-scale and below. Early experiments (Croll et al. 1996; Storms et al. 2001; and Hammache et al. 2002) focused on the simplified geometry of the Ground Transportation System (GTS) model representative of a class 8 tractor-trailer with a cab-over-engine design. A 1:8-scale GTS model with no tractor-trailer gap and no wheels was first studied with the addition of several ogival boattails and slants to the base of the trailer (Croll et al. 1996). The largest overall drag reduction of 10% was obtained by a 2.4-meter (m) ogive configuration (full scale). The addition of boattail plates to the same model resulted in a 19% drag reduction and particle image velocimetry (PIV) measurements behind the trailer document a significant reduction in the wake size due to the flow turning provided by the plates (Storms et al. 2001). Variation of the tractor-trailer gap on a 1:15-scale model at zero yaw revealed relatively constant drag on the tractor while the trailer drag increased by a factor of three as the gap was increased from zero to 1.55*A**0.5 (Hammache et al. 2002).

Also part of the DOE effort, the Generic Conventional Model (GCM) of the current study was tested in two different facilities at NASA's Ames Research Center. This geometry included a tractor-trailer gap and a simplified conventional tractor geometry (detailed below). In the 7- by 10-foot (ft) wind tunnel, measurements were made at a Reynolds number of 1.1 million. Of particular interest are the detailed PIV data in the tractor-trailer gap with and without side extenders and in the

trailer wake with and without boattail plates (Heineck et al. 2002). A large subset of the configurations tested in the 7- by 10-ft tunnel were duplicated in the 12-ft pressure tunnel to determine the effects of Reynolds number variation (Storms et al. 2004). For all configurations, Reynolds number effects were evident at high yaw angles (greater than 8°) where there was a significant reduction in drag at lower Reynolds numbers. However, this difference did not significantly affect the computation of the wind-averaged drag coefficients (at highway speeds) which employs data at lower yaw angles.

The goal of the present study is to provide detailed experimental results for the most promising and practical drag-reduction concepts tested on the GCM. In addition to the force, moment, and pressure measurements, off-body details were obtained using three-dimensional (3-D) PIV. The uncertainty in the PIV measurements was ±2% in the in-plane velocities and ±4% in the out-of-plane velocity. Measurements were made at various yaw angles to study the influence of crosswind and to calculate wind-averaged drag coefficients.

## Experimental Setup

Measurements of the same model were conducted in both the 12-ft pressure wind tunnel and the 7- by 10-ft wind tunnel at NASA Ames Research Center. Apart from the PIV data, the majority of the results presented in this report are from the 12-ft pressure tunnel. The differences between the tunnels and the model installations are detailed below.

The 12-ft pressure wind tunnel can be pressurized from 0.25 to 6 atmospheres at Mach numbers from 0.1 to 0.5. The test section has a circular cross section 3.66 meters (m) in diameter with four 1.22-m wide flat surfaces centered about the horizontal and vertical centerlines. The root mean square (RMS) turbulence intensity in the test section was 0.27% and 0.52% at Reynolds numbers of 1 and 6 million, respectively. A ground plane was installed 53 centimeters (cm) above the tunnel floor providing a flat surface 3.05 m wide and 5.49 m long. Pressure taps were located on both the ground plane (2 rows of 64 taps) and the test-section walls (8 rows of 30 taps). A fairing was installed to isolate the model-support hardware from the air stream, and speed-correction probes were used to correct the facility speed due to the blockage of the ground plane and fairing. There was also an additional pitot-static probe installed on the upper left ceiling to measure the free-stream conditions in the test section. All of the data presented are referenced to the Mach number based on a wall tap located 1.88 m forward of the center of rotation at an azimuth of 60° from vertical (two o'clock looking downstream). Except where noted, all data were acquired at a Mach number of 0.15 which allowed for Reynolds number studies with no Mach-number effects. With the tunnel pressurized to six atmospheres, the Reynolds number was over 6 million based on the trailer width, which is comparable to a full-scale truck driving at 120 km/hr.

The 7- by 10-ft wind tunnel is a closed-circuit atmospheric facility incorporating a 4.57-m long test section with a constant height of 2.13 m and a nominal width of 3.05 m with a 1% wall divergence. The boundary layer thickness at the test section entrance is 5.3 cm which corresponds to a displacement thickness of 1.5 cm. The multiple turbulence-reducing screens in the circuit yield empty test-section turbulence intensities in the longitudinal, lateral, and vertical directions of 0.1%, 0.3%, and 0.3%, respectively, for a test condition of M = 0.22. These turbulence levels correspond to a RMS turbulence intensity of 0.25% and a turbulence factor of 1.2. For ease of comparison with CFD, the test section static pressure was obtained from a single wall pressure tap located at x/w = 4.5, y/w = 2.6, and z/w = -4.7. The 7- by 10-ft data presented in this report are for Mach and Reynolds numbers of 0.15 and 1.1 million, respectively.

A photograph of the GCM baseline configuration installed in the 12-ft wind tunnel test section is shown in Figure 1. This 1:8-scale model is representative of a generic class 8 tractor-trailer with the engine in front of the cab. Designed for CFD validation, the model includes a number of geometry simplifications in order to facilitate grid generation and avoid the associated flow complexities. In particular, no effort was made to duplicate the complex geometry of the undercarriage of either the tractor or trailer (both were approximated by flat surfaces). Similarly, the wheel wells of the tractor were not modeled and only the portion of the wheels below the tractor lower surface were included

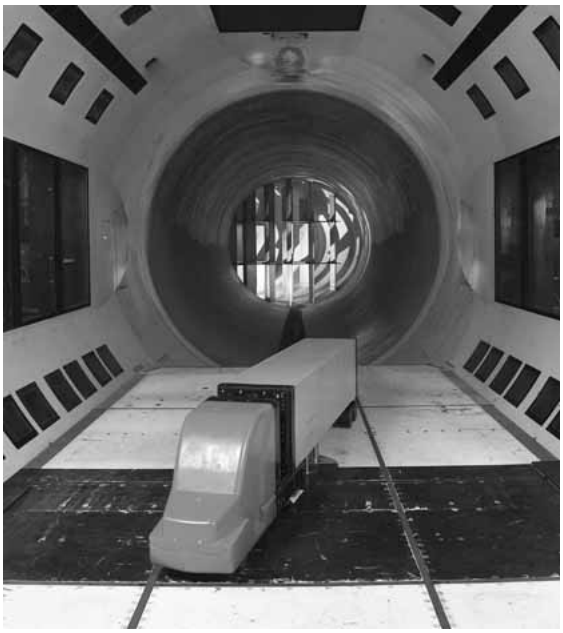

**Figure 1.** The Generic Conventional Model (GCM) installed in the 12-ft pressure wind tunnel

(Figure 2). Also, the tractor geometry (designed by the Calmar Research Corp.) is a streamlined shape representative of a modern tractor design while omitting most small-scale surface details and flow-through components. The trailer measures 13.7 m in length (full scale) with rounded front vertical edges (20-cm full-scale radius). The tractor-trailer gap for this study was held constant at the full-scale equivalent of 1 m. The moment center on the model was specified as the point between the rear tractor wheels along the model centerline at the bottom of the trailer.

In the 12-ft wind tunnel, the GCM was attached to the model-support hardware with four vertical posts that were 4.45 cm in diameter. The four posts were non-metric (i.e., their aero loads were not measured by the balance) with 0.75 millimeter (mm) of clearance as they passed through the trailer floor. The model was mounted with its wheels 3.8 mm above the ground plane and centered laterally in the tunnel. The center of rotation of the model was located 1.38 m aft of the tractor front bumper. The model frontal area of 0.154 $m^2$ gives a solid blockage of 1.5%. The overall model loads were measured with a six-component balance (10-cm Task balance Mark 2B) that was mounted inside the trailer. The manufacturer-specified accuracy of the internal balance in the axial (drag) direction was ±4.45 N, but the experimental data indicated repeatability on the order of ±2.2 N.

In the 7- by 10-ft wind tunnel, the model was located at a position 13.33 cm downstream of the beginning of the test section. Mounted level in the test section, the bottoms of the wheels were located 1.3 cm above the wind tunnel floor to account for the boundary-layer displacement thickness. Four cylindrical struts connected the model to the scale system and 3.8-cm-diameter cylindrical fairings (non-metric) extended from the floor to within 0.63 cm of the bottom of the model. The model was mounted on the facility scale system that included a turntable for remote model positioning. Since the facility scales measure wind-axis forces (parallel and

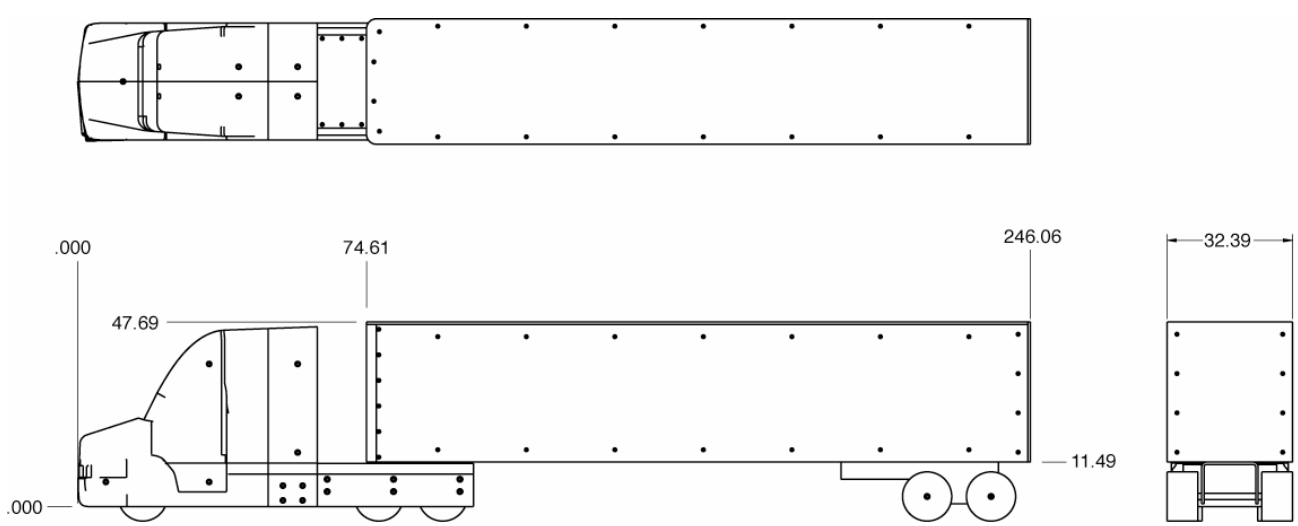


**Figure 2.** Three-view drawing of GCM (measurements in cm)

perpendicular to the axis of the wind tunnel), a coordinate transformation was employed to determine the body-axis drag (the force along the longitudinal axis of the model).

In both tunnels, the tractor was suspended from the trailer through a set of flexures and two load cells that measure the drag and yawing moment of the tractor alone. The specified accuracy of the load cells was ±2 N. The model was instrumented with 200 pressure taps on the tractor and 276 taps on the trailer. The surface pressures were measured with an electronically scanned pressure system and time averaging yielded an uncertainty in the calculated pressure coefficients of ±0.002 at Re = 6 million. There were also 12 unsteady pressure transducers mounted on the tractor rear surface, trailer front surface, and the trailer rear surface. A three-component PIV system was used to obtain horizontal-plane velocity measurements in the tractor-trailer gap and the trailer wake at 1/4, 1/2, and 3/4 of the trailer height (7×10 only). Details of the PIV system installation are presented in Heineck et al. 2003. The model was yawed through a range of angles between ±14°.

## Results and Discussion

Various add-on drag-reduction devices were tested on the bases of both tractor and trailer as well as on the trailer under-carriage. In this report, results will be presented for tractor side and roof extenders, trailer base flaps, and trailer skirts. Details of each device will accompany the discussion of the associated results.

The results presented below detail the body-axis forces and moments for the tractor-trailer combination and its components. This drag coefficient represents the force along the axis of the vehicle in the direction of travel. With the objective of CFD validation, no wall corrections were applied to the data and all coefficients were calculated based on the static pressure at a known point in the test section (as detailed above). Without wall corrections, the computed drag coefficients will differ from those of the equivalent model in free air. However, the measured differences between configurations should be representative of the effects of the associated geometric modifications.

Using the variation of drag with yaw angle, wind-averaged drag coefficients ($C_D$) were computed using the SAE Recommended Practice (SAE 1981). This practice assumes that the mean wind speed in the United States of 11.2 km/hr has an equal probability of approaching the vehicle from any direction. This mean wind speed and the vehicle velocity were used to calculate a weighted average based on the variation in drag coefficient over a range of yaw angles. The wind-averaged drag coefficients reported in this paper were computed for a highway speed of 88 km/hr. Note that the uncertainty in the wind-averaged drag coefficient was less than the values listed in Table 1 due to the effects of averaging. In particular, the repeatability of the wind-averaged drag for the baseline configuration was ±0.0004.

Except where noted, the data presented below are from the measurements conducted in the 12-ft pressure wind tunnel at a Reynolds number of 6 million. All data were acquired for increasing yaw angle. Details of the observed hysteresis were presented previously in Storms et al. 2004.

**Table 1.** Force and moment coefficient uncertainty (±). Values have been omitted for coefficiencts not reported.

| Tunnel Rex$10^6$ | $C_L$ | $C_D$ | $C_S$ | $C_{PM}$ | $C_{YM}$ | $C_{RM}$ |
|---|---|---|---|---|---|---|
| 12-ft (6.2) | 0.043 | 0.002 | 0.021 | 0.003 | 0.002 | 0.006 |
| 12-ft (1.1) | – | 0.009 | – | – | – | – |
| 7×10 (1.1) | – | 0.009 | – | – | 0.034 | – |

### *Tractor Extenders*

Similar to the components of a modern tractor aero package, side and roof extenders were attached to the rear of the tractor as shown in Figure 3. The extenders were 1/8-inch (in) thick (model scale) with four different lengths ranging from 30% to 60% of the tractor-trailer gap. As detailed previously (Storms et al. 2004), the results indicated a consistent trend of increasing drag reduction with increasing extender length. The most effective side and roof extender length of 60% gap was chosen as the baseline for all subsequent comparisons in the current analysis. The wind-averaged drag (defined above) of this configuration was 0.422.

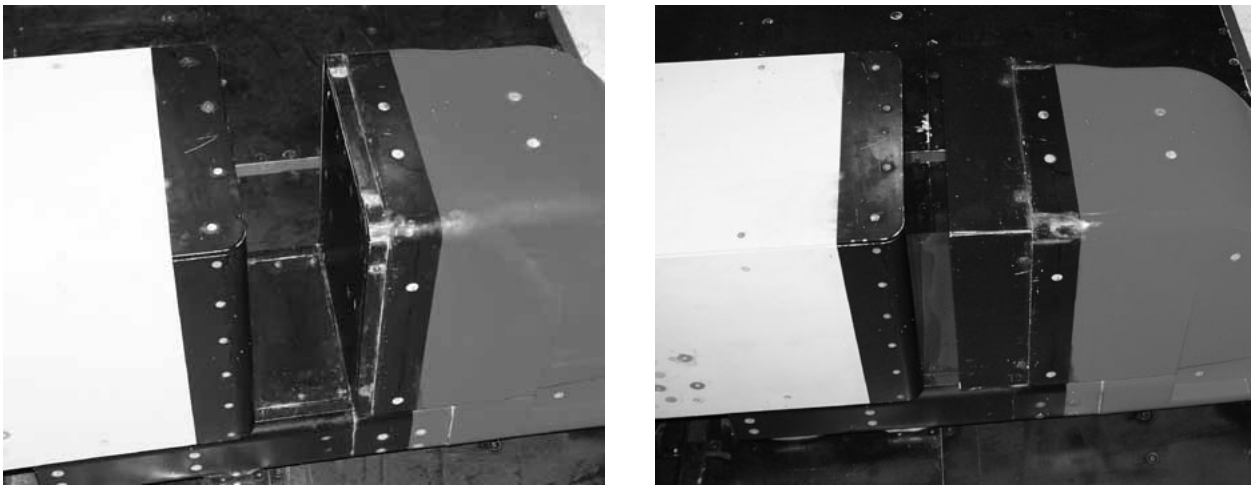

**Figure 3.** Close-up of tractor-trailer gap with and without side and roof extenders (60% gap)

Since tractor aero packages frequently only include side extenders, the effect of the roof extender was investigated by testing the 60%-gap side extenders alone in the 7- by 10-ft wind tunnel. The drag curves (Figure 4) indicate that the addition of a roof extender provides a significant drag reduction at all yaw angles. The change in wind-averaged drag relative to the baseline for side extenders only was 0.009. The change in drag coefficient by component is illustrated in Figure 5. As expected from the drag curves, the drag on the tractor without the roof extender is increased relative to the baseline (side and roof extenders). The drag of the trailer, however, is reduced by removing the roof extender, likely as a result of the modified gap flow. The effect of the roof extender on the yawing moment (Figure 6) is

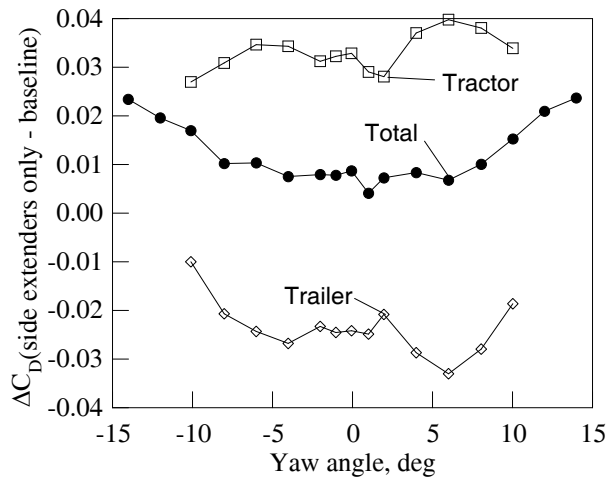


**Figure 5.** Effect of roof extender on component drag differences (0.6g extenders, Re = 1.1 million, 7×10)

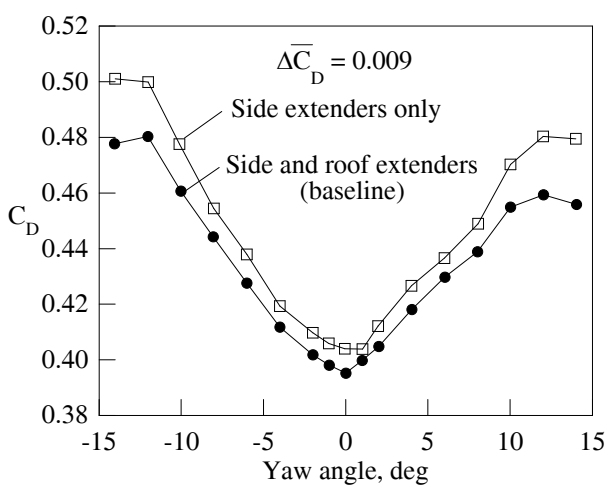


**Figure 4.** Effect of roof extender on drag coefficient (0.6g extenders, Re = 1.1 million, 7×10 wind tunnel)

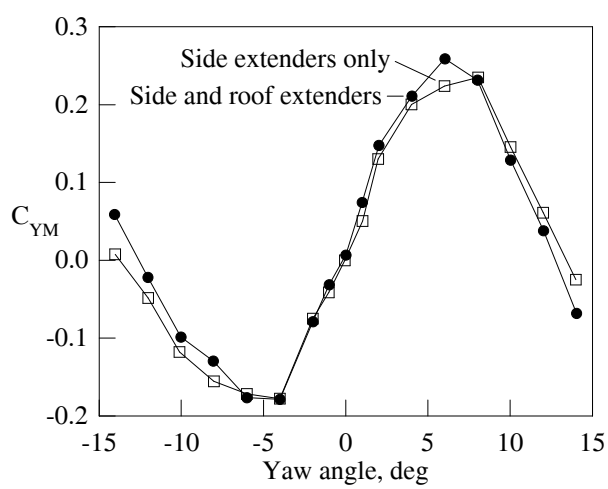


**Figure 6.** Effect of roof extender on yawing moment (0.6g extenders, Re = 1.1 million, 7×10 wind tunnel)

minimal with minor differences evident at the higher yaw angles. All other forces and moments (not shown) were relatively unchanged.

The effect of the extender length, as mentioned previously, indicated a general trend of increasing drag reduction with increasing extender length. This effect is illustrated at two Reynolds numbers for the 30% and 60% gap lengths in Figure 7. Relative to the 60%-gap baseline, the shorter extenders yielded an increase in wind-averaged drag of 0.003 and 0.011 for Reynolds numbers of 1.1 and 6.2 million, respectively. This difference suggests a sensitivity of the extender effectiveness to Reynolds number. Similar to the effect of the roof extender, the shorter extenders serve to increase the drag on the tractor while slightly reducing the drag on the trailer (Figure 8). The shorter extenders also yield a significant decrease in the yawing moment that increases with yaw angle (Figure 9). All other forces and moments (not shown) were relatively unchanged.

The GCM was instrumented with 476 surface pressure taps, many of which are located on the back of the tractor (39) and the front and back of the trailer (24 and 39, respectively). Figures 10–12 present pressure coefficient contours on these surfaces for the baseline configuration at yaw angles of zero and 10°. Note that all but three pressure taps were located on the left side of the model with clustering near the edges. For zero yaw, symmetry is assumed and the data are duplicated on

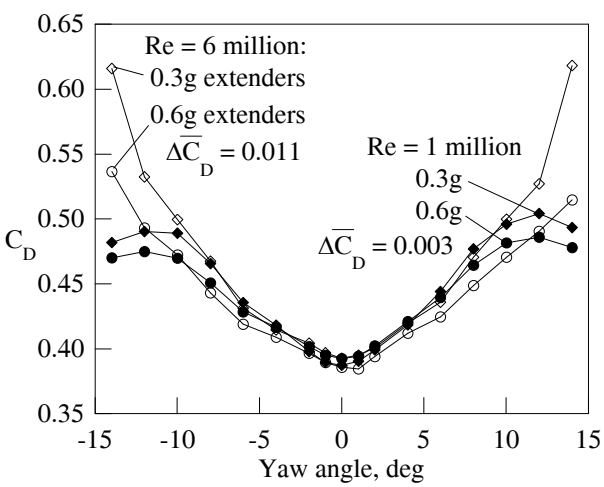


**Figure 7.** Effect of extender length on drag coefficient (baseline, 12-ft wind tunnel)

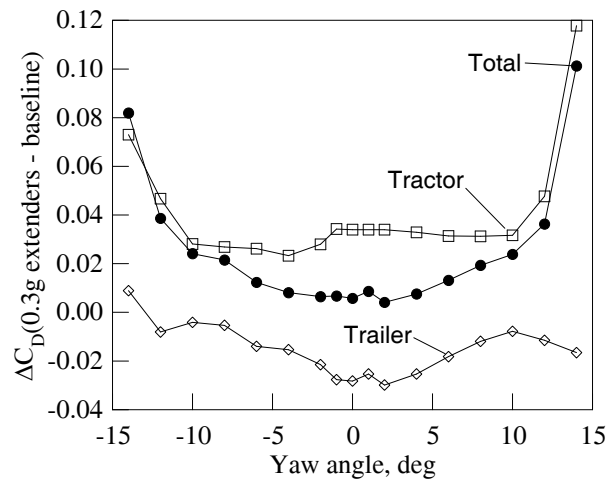


**Figure 8.** Effect of extender length on component drag differences (baseline, Re = 6 million)

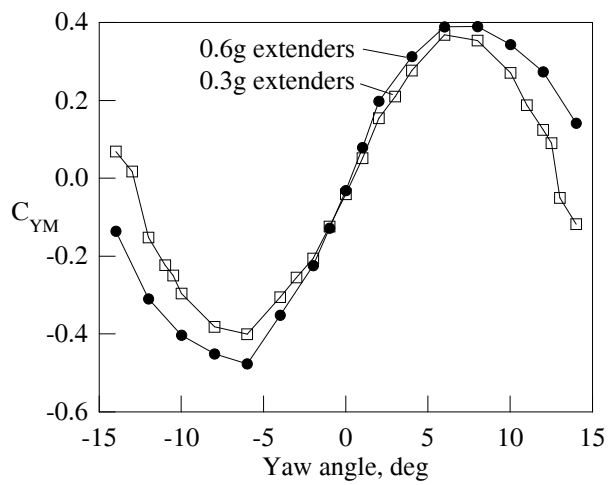


**Figure 9.** Effect of extender length on yawing moment (baseline, Re = 6 million)

the right side of the figure. For 10°, the right half of the figure includes data for the –10° yaw angle.

In both test facilities PIV measurements were obtained in the gap between the tractor and trailer at yaw angles of zero and 10°. The 12-ft wind tunnel results were previously reported for a configuration without side extenders (Storms et al. 2004). In the 7- by 10-ft wind tunnel, measurements were conducted with and without 50%-gap side extenders and the resulting stream traces (Figure 13) indicate their effect on the gap flow. At zero degrees, the flow fields with and without extenders are similar with two counter-rotating recirculation regions. Closer examination reveals that the presence of the

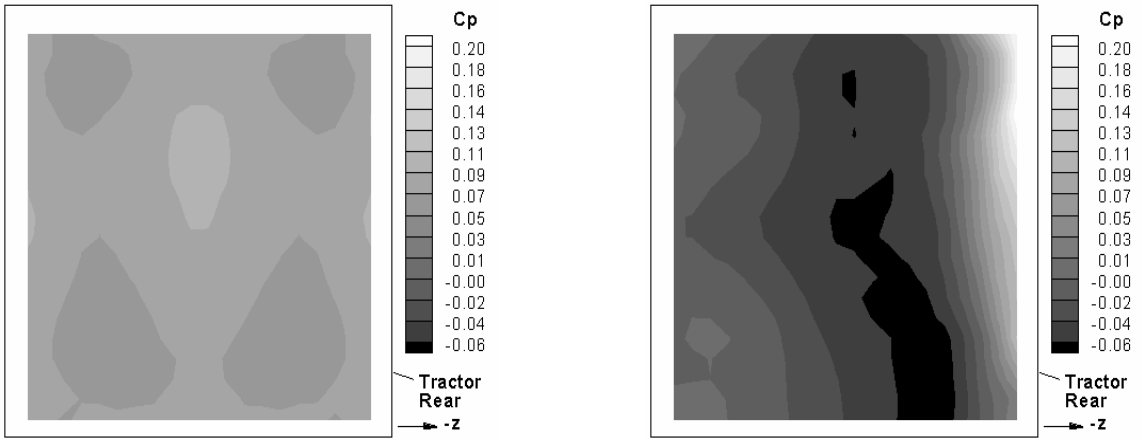


a) Ψ = 0 deg b) Ψ = 10 deg

**Figure 10.** Pressure coefficient contours on the back of the tractor with 0.6g side and roof extenders, Re = 6 million. Symmetry assumed for zero yaw. For Ψ = 10°, right half of image represents data at Ψ = –10°.

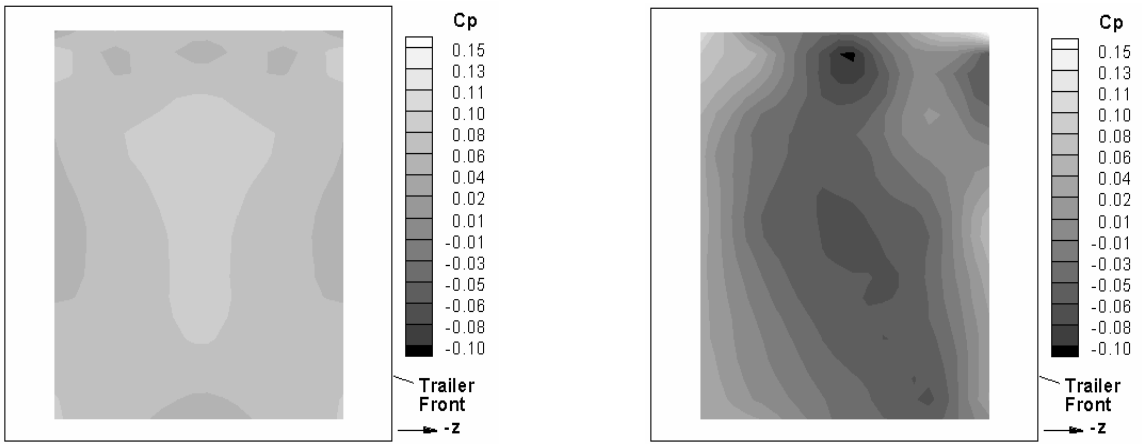


a) Ψ = 0 deg b) Ψ = 10 deg

**Figure 11.** Pressure coefficient contours on the front of the trailer with side and roof extenders, Re = 6 million

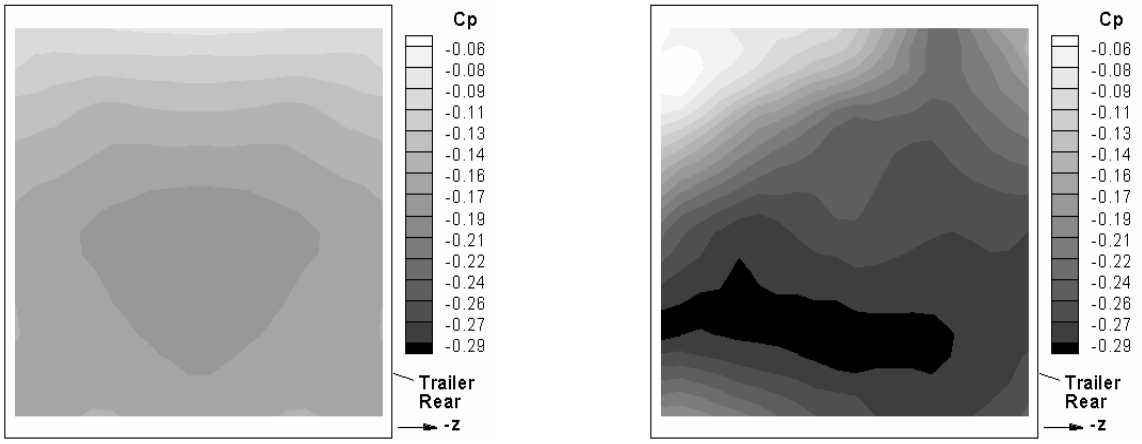


a) Ψ = 0 deg b) Ψ = 10 deg

**Figure 12.** Pressure coefficient contours on the back of trailer with side and roof extenders, Re = 6 million

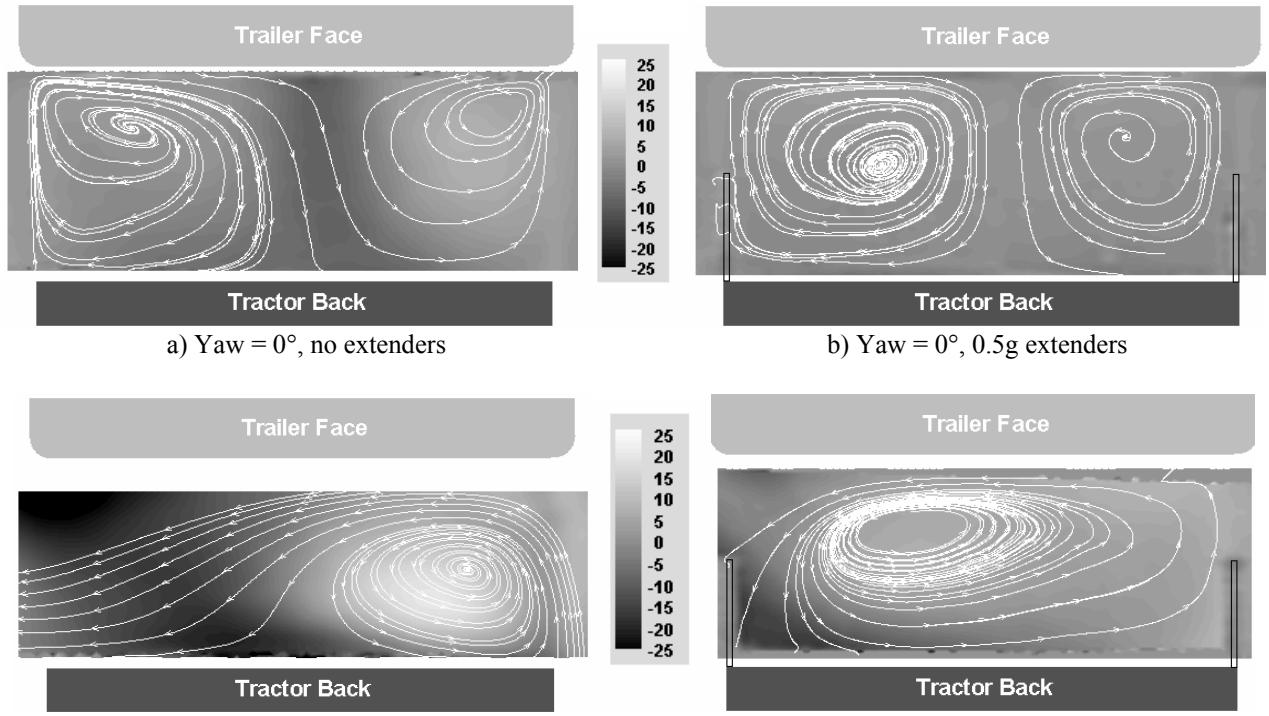


a) Yaw = 0°, no extenders

b) Yaw = 0°, 0.5g extenders

c) Yaw = 10°, no extenders

d) Yaw = 10°, 0.5g extenders

**Figure 13.** Partical image velocimetry (PIV) data in the tractor-trailer gap with and without 0.5-gram (g) side extenders. Images are shaded by out-of-plane velocity and flow is from bottom to top of the page (7×10 wind tunnel, Re = 1 million).

extenders tend to move centers of these regions closer to the cab, minimize crossflow, and reduce the vertical velocity (Vmean) in the gap. At 10°, the stream traces without extenders indicate one recirculation region to the right with dramatic crossflow and downflow. The effect of the extenders is to reduce both crossflow and downflow (thereby increasing pressure), which results in a low-vorticity recirculation near the middle of the gap. A more detailed discussion of the PIV measurements is found in Heineck et al. 2003.

## *Trailer Base Flaps*

As previously documented (Cooper 1985), an effective method of aerodynamic boat-tailing is what will be referred to as base flaps. In this embodiment, the panels are attached to all edges of the trailer base and angled inward. In the current study, measurements were made for a base-flap length of 63.5 cm full scale (non-dimensional length = l/A**0.5 = 0.20) at angles ranging from zero to 28°. The installation photo (Figure 14) shows the base flaps with a 20° deflection mounted on the rear of the trailer. Note that the linkages

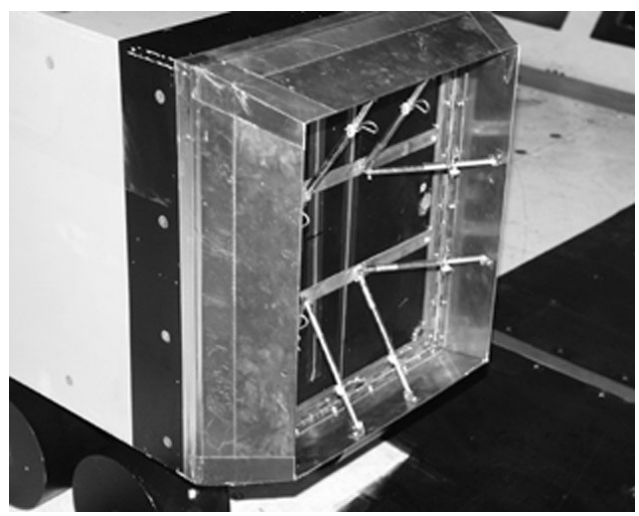

**Figure 14.** Base flaps installed on trailer base (flap angle = 20°)

connecting the flaps to the base were designed for easy angle change and are not representative of the full-scale hardware.

An analysis of base-flap effectiveness as a function of flap angle on the GCM (Storms et al. 2004)

indicated an optimum angle near 20°. However, other small-scale wind tunnel tests and road tests show the optimum angle to be closer to 15° (Cooper 1985; Broward and Radovich 2004). This difference is likely due to the absence of the lower base flap in the studies referenced above. In the current study, data will be presented for a base-flap angle of 16° due to the limited data available for the 20° deflection.

Relative to the baseline with side and roof extenders, the effect of the base flaps on the forces and moments is presented in Figures 15–20. As indicated in Figure 17, the base flaps provided a relatively constant drag reduction that increases slightly with angle of attack. The baseline drag curve for Re = 1 million is notably higher than that for Re = 6 million. The change in the associated wind-averaged drag was –0.087 and –0.079 for Reynolds numbers of 1 million and 6 million, respectively, suggesting some Reynolds-number sensitivity. These values are at the upper end of the range reported in previous studies (Cooper 1982) that differ from the current configuration by the absence of the lower base flap. The base flaps also provided an increase in lift (Figure 15) due to the downwash created by the flow turning of the top flap. The lift increase on the trailer is reflected by a corresponding pitching moment decrease (Figure 18). Also, the addition of the base flaps resulted in larger yawing moments (more positive and more negative for positive and negative yaw angles, respectively, as shown in Figure 19). The side force and rolling moment were relatively unaffected (Figures 16 and 20). As expected, the change in the drag and yawing-moment coefficients by component (Figure 21) indicate that the trailer is the source of the observed differences.

The trailer was instrumented with a line of pressure taps running axially along the centerline of the top and left side. The pressure distributions with and without base flaps are presented in Figures 22–23 for yaw angles of zero and 10°. On both the top and side, the base flaps serve to reduce the pressure towards the rear of the trailer. The effect of the base flaps on the forward two-thirds of the pressure distribution was minimal. The pressures on the tractor (not shown) were unaffected. Hence, the base flaps have a relatively local effect on the truck pressure distributions. The pressure distributions at –10° (not shown) exhibit similar trends.

The differences in the pressure distributions on the back of the trailer with base flaps (Figure 24) indicate significantly increased pressures relative to the baseline. At zero yaw, the increase in pressure is relatively constant with an average change in pressure coefficient of 0.14. At 10°, however, the increase in pressure is far from uniform, with the greatest increase on the bottom half of the trailer base. The extremes of the pressure difference occur on the windward side of the trailer base. The pressures on the back of the tractor and front of the trailer (not shown) were relatively unchanged by the presence of the base flaps.

No PIV measurements were obtained in the wake of the base flaps due to technical difficulties encountered in the high-pressure environment of the 12-ft wind tunnel. However, PIV data were obtained in the truck wake with and without boattail plates in the 7- by 10-ft wind tunnel. Mounted perpendicular to the trailer base and slightly inset from the edge (see Storms et al. 2004 for details), the boattail plates function similarly to the base flaps by turning the flow and reducing the associated wake size. The PIV images with and without boattail plates (Figure 25) illustrate the how aerodynamic boat-tailing serves to reduce the wake size by deflecting the flow inward.

### *Trailer Skirts*

Trailer skirts have been previously investigated (Cooper 1982) as an effective add-on to minimize the crossflow under the trailer and shield the rear wheels. As shown in Figure 26, the skirts extended from a short distance behind the tractor to just in front of the rear wheels. The skirts measured 0.355 truck widths in height allowing a full-scale ground clearance of 0.3 m.

The effect of the trailer skirts on the overall forces and moments is presented in Figures 27–32. The skirts significantly reduce the drag across the yaw range with the greatest reduction at the higher angles (Figure 29). The associated change in wind-averaged drag relative to the baseline was –0.036. This value is at the lower end of the range reported

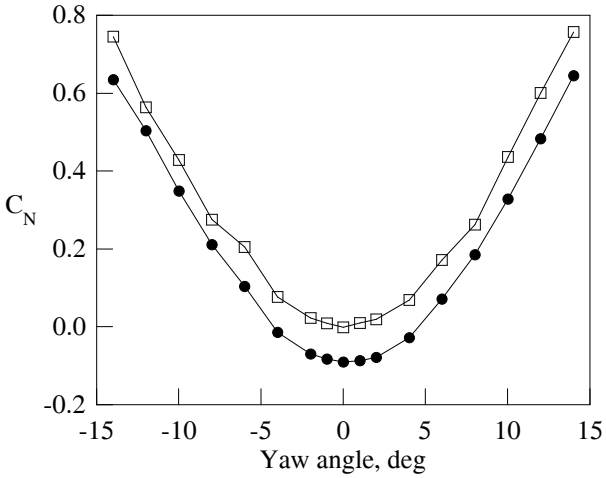


**Figure 15.** Normal force coefficient comparison (solid: baseline, open: base flaps, Re = 6 million)

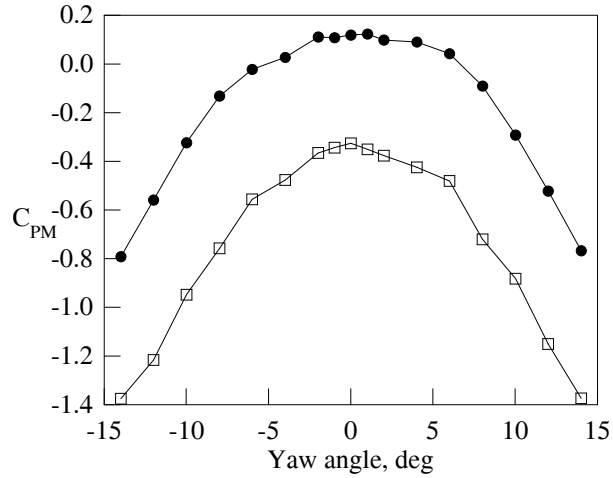


**Figure 18.** Pitching moment coefficient comparison (solid: baseline, open: base flaps, Re = 6 million)

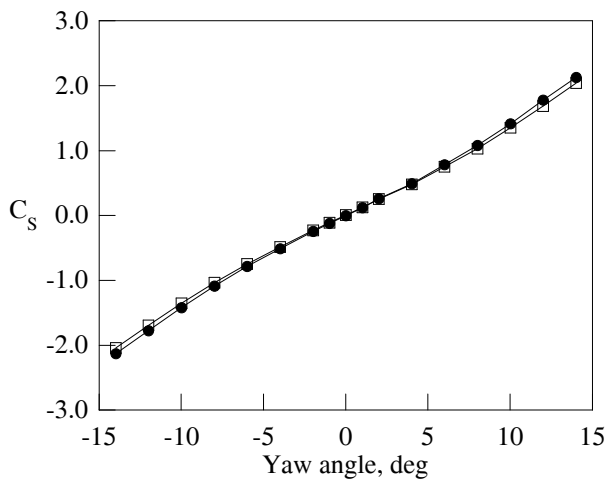


**Figure 16.** Side force coefficient comparison (solid: baseline, open: 16-deg base flaps, Re = 6 million)

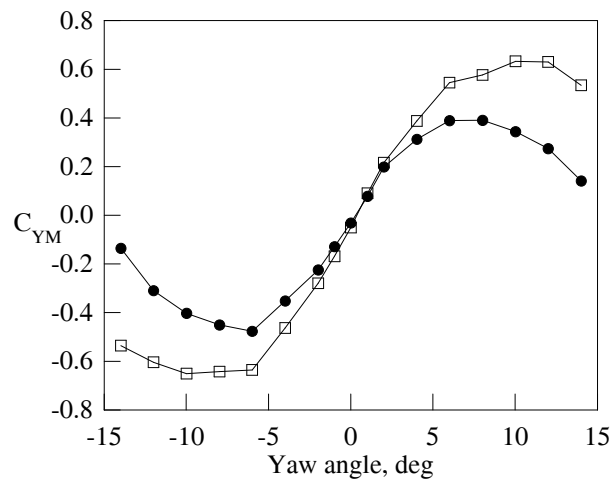


**Figure 19.** Yawing moment coefficient comparison (solid: baseline, open: base flaps, Re = 6 million)

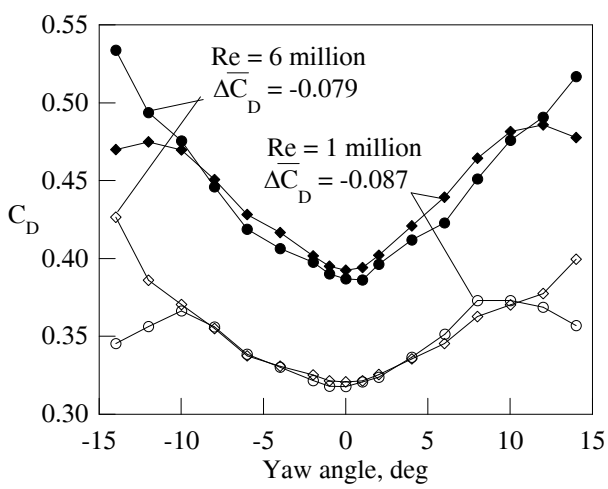


**Figure 17.** Drag coefficient comparison (solid: baseline, open: 16-deg base flaps)

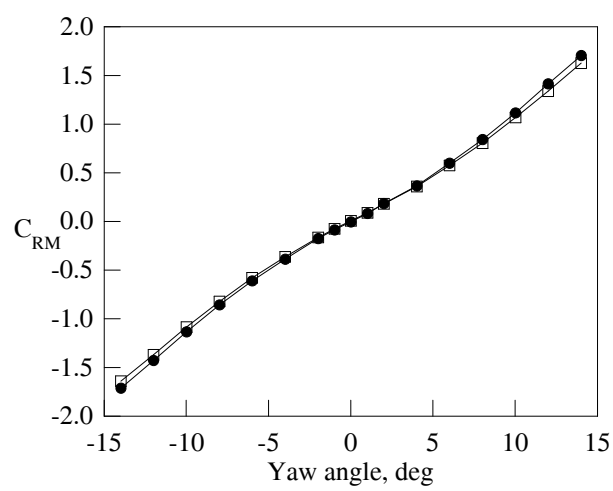


**Figure 20.** Rolling moment coefficient comparison (solid: baseline, open: 16-deg base flaps, Re = 6 million)

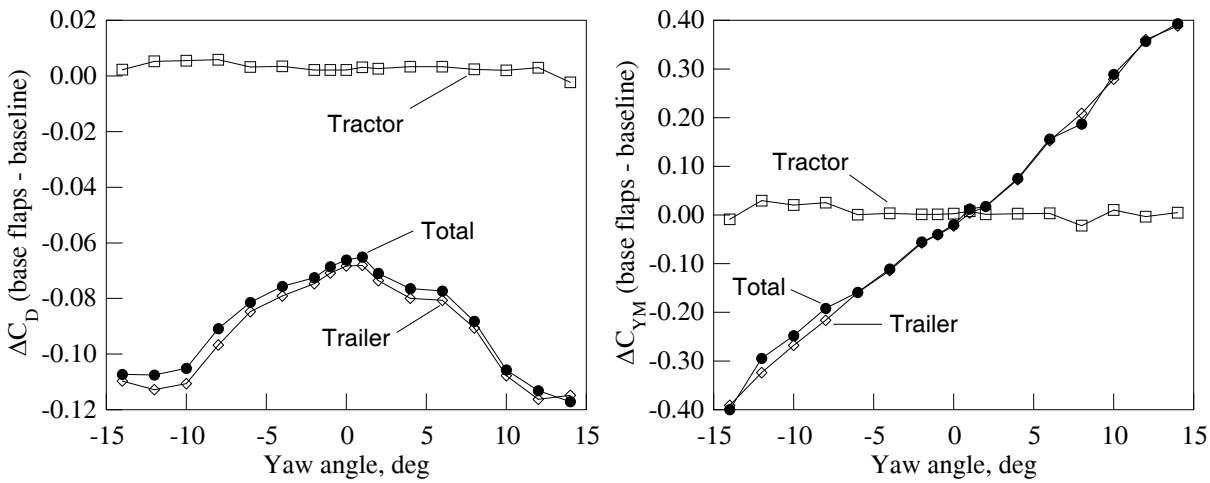


**Figure 21.** Effect of 16° base flaps on component drag and yawing-moment differences at Re = 6 million

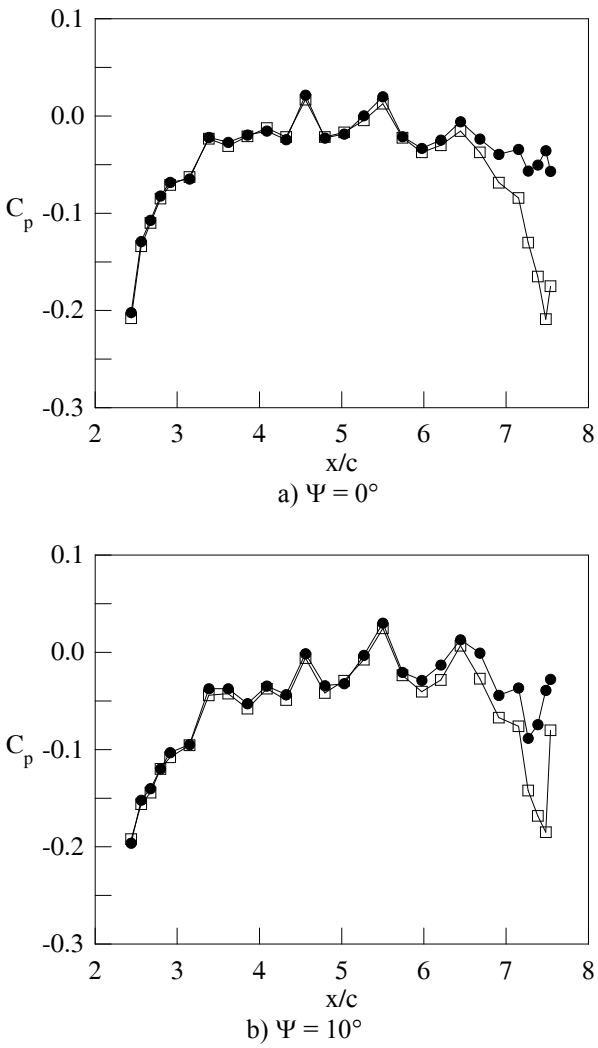


**Figure 22.** Effect of 16° base flaps on trailer top centerline pressure coefficients, z/w = 0.0 (solid: baseline, open: base flaps, Re = 6 million)

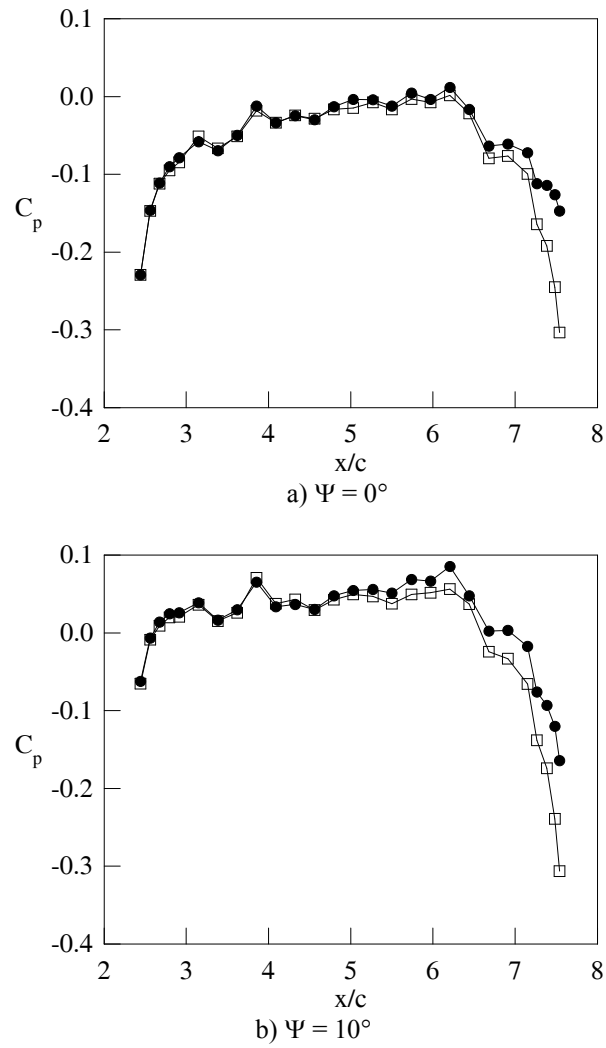


**Figure 23.** Effect of 16° base flaps on trailer side centerline pressure coefficients, y/w = 0.9 (solid: baseline, open: base flaps, Re = 6 million)

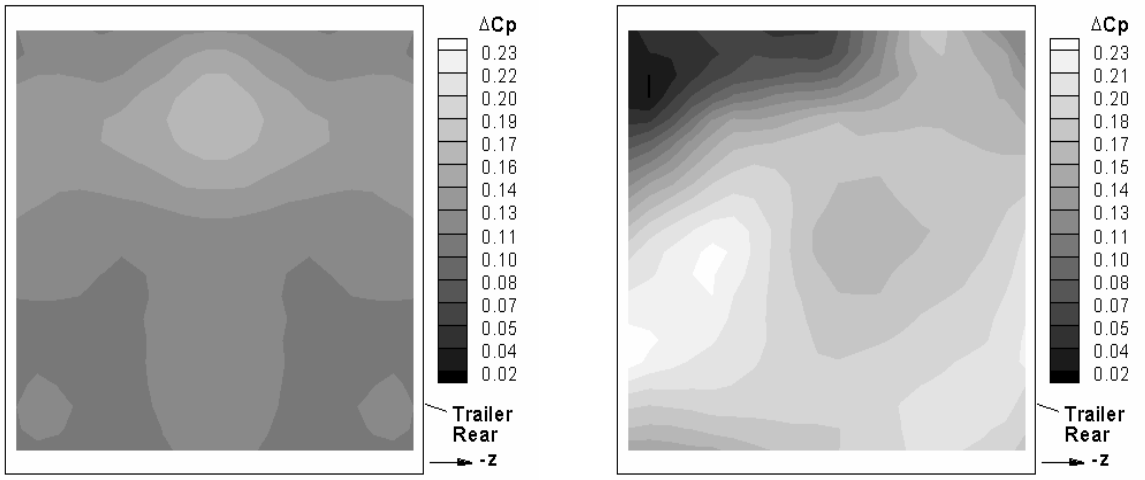


a) Ψ = 0 deg b) Ψ = 10 deg

**Figure 24.** Effect of 16° base flaps on the pressure distribution on the back of the trailer (relative to extender baseline), Re = 6 million. Symmetry assumed for zero yaw. For Ψ = 10°, right half of image represents data at Ψ = –10°.

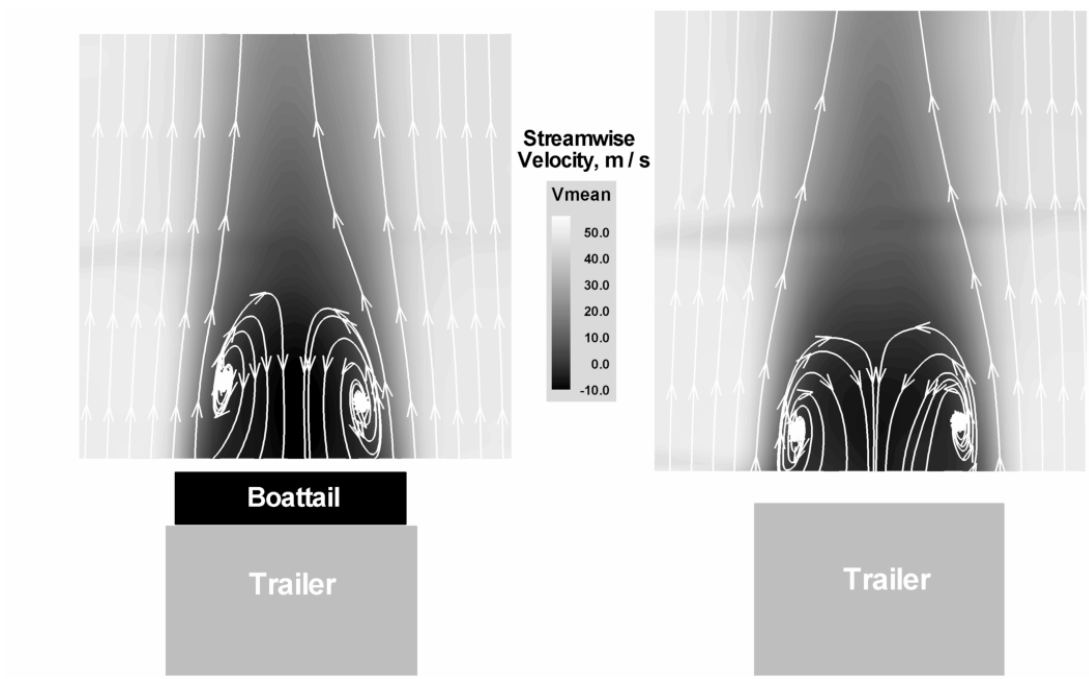


**Figure 25.** PIV data in the trailer wake with and without boattail plates. Images are colored by out-of-plane velocity and flow is from bottom to top (7×10 wind tunnel, Re = 1 million).

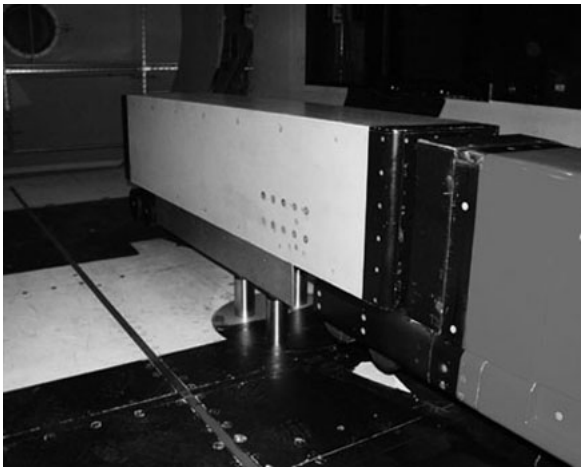

a) Front side of trailer with skirt (grey plate)

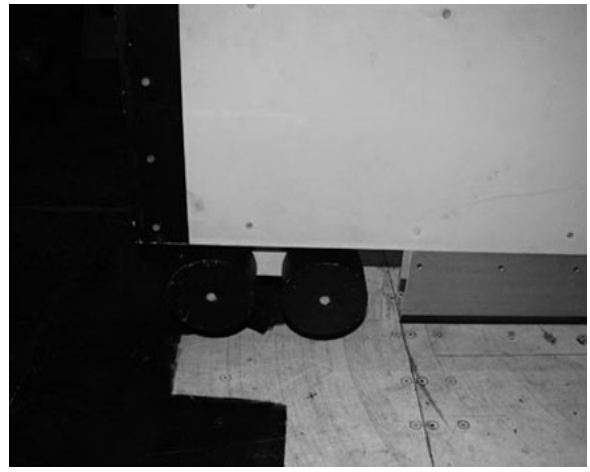

b) Rear side of trailer with skirt (at lower right)

**Figure 26.** Trailer skirt installation photos

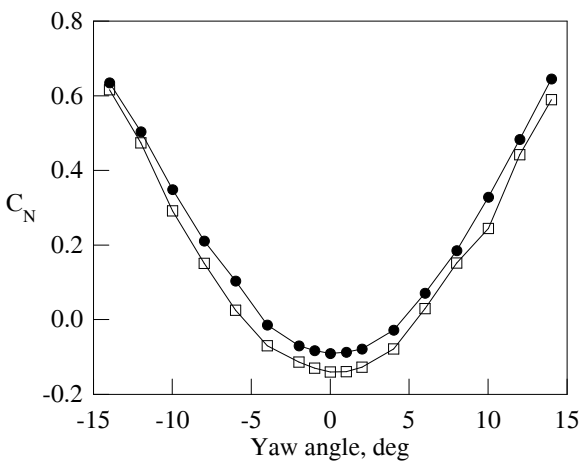


**Figure 27.** Normal force coefficient comparison (solid: baseline, open: skirts, Re = 6 million)

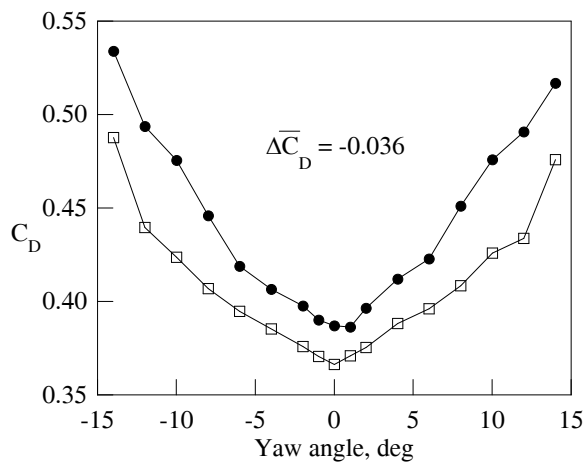


**Figure 29.** Drag coefficient comparison (solid: baseline, open: skirts, Re = 6 million)

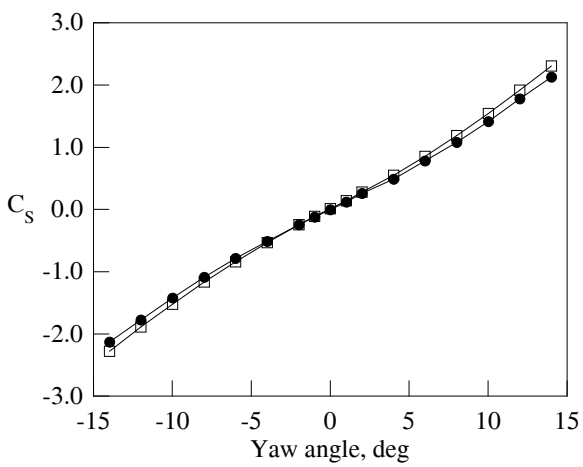


**Figure 28.** Side force coefficient comparison (solid: baseline, open: skirts, Re = 6 million)

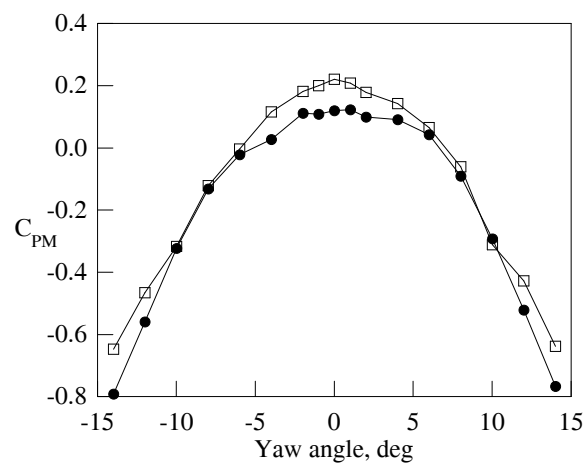


**Figure 30.** Pitching moment comparison (solid: baseline, open: skirts, Re = 6 million)

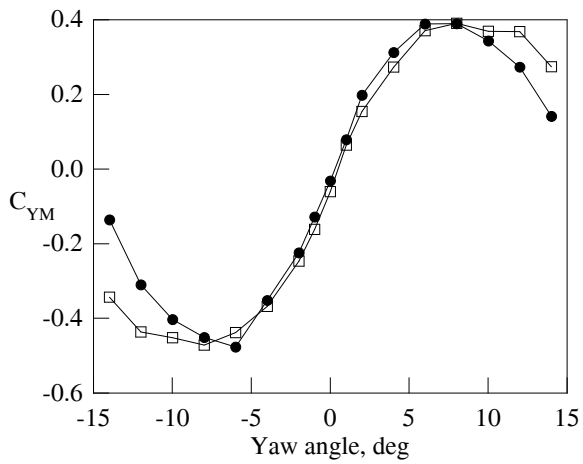


**Figure 31.** Yawing moment comparison (solid: baseline, open: skirts, Re = 6 million)

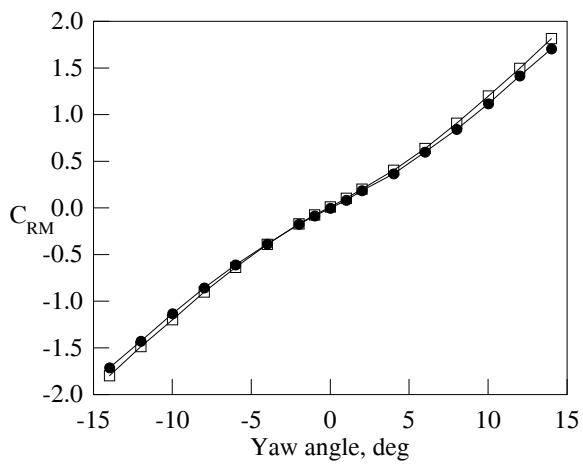


**Figure 32.** Rolling moment comparison (solid: baseline, open: skirts, Re = 6 million)

in previous studies (Cooper 1982) which is likely due to the simplified geometry of the GCM undercarriage. Due to time constraints, an analysis of Reynolds-number effects was not possible for this configuration. The skirts also provided a reduction in the normal force (Figure 27) with a small corresponding increase in the pitching moment (Figure 30) at most yaw angles. This is likely due to reduced pressure on the undercarriage due to vortical flow generated by the skirts under crossflow conditions. The skirts also yield small differences in the yawing moment (Figure 31) with significantly greater variation at higher angles (unimportant at typical highway speeds). The side force and rolling moment were relatively unaffected (Figures 28 and 32).

The effects of the skirts on the component drag and yawing-moment differences are presented in Figure 33. Similar to that of the base flaps, the change in drag coefficient by component indicates that the measured drag reduction is due to the effect of the skirts on the trailer. However, the skirts also generate a smaller, but measurable drag increase on the tractor. The total difference in yawing moment for the skirts is approximately half of that generated by the base flaps. Unlike the base flaps, both the tractor and trailer contributed to the observed yawing-moment differences.

The axial pressure distributions on the side and bottom of the trailer (Figures 34–35) illustrate that the general effect of the skirts is to reduce the

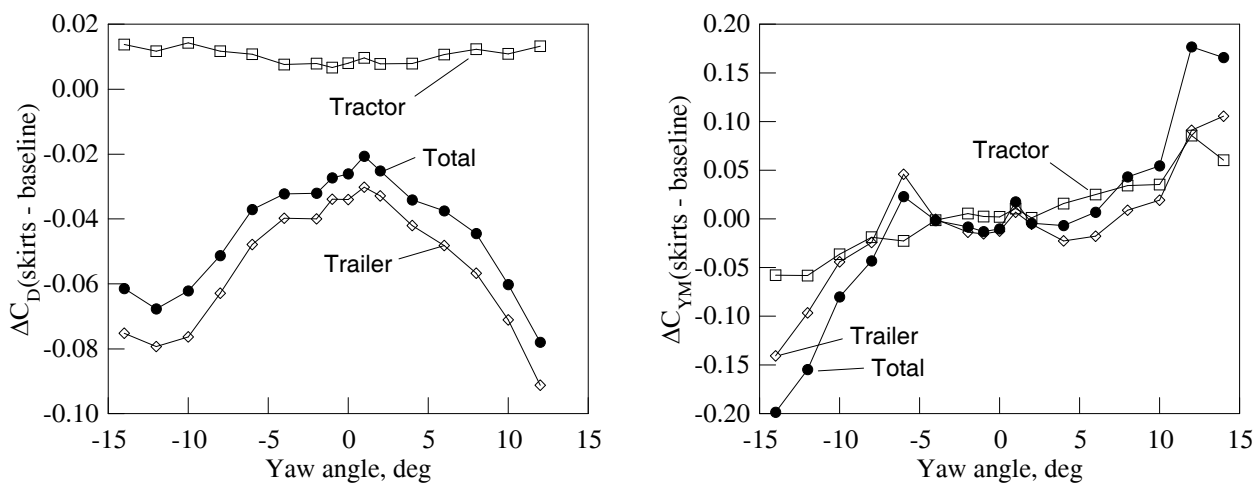


**Figure 33.** Effect of trailer skirts on component drag and yawing-moment differences at Re = 6 million

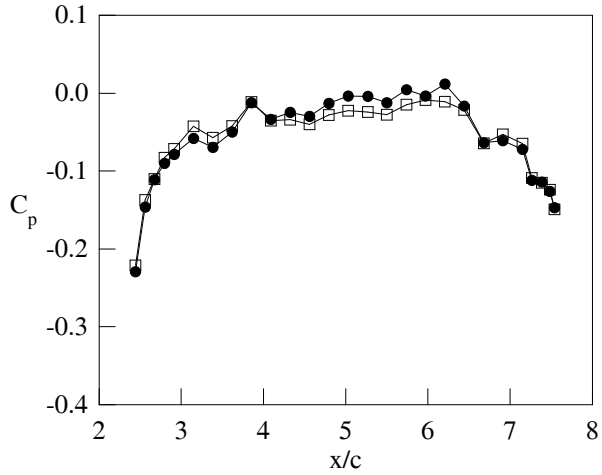


a) Ψ = 0°

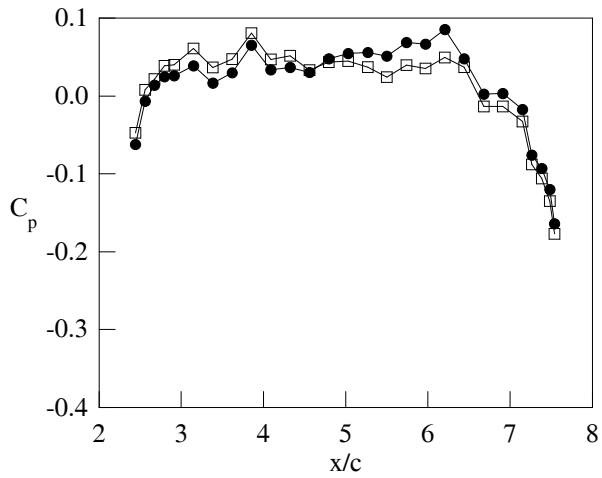


b) Ψ = 10°

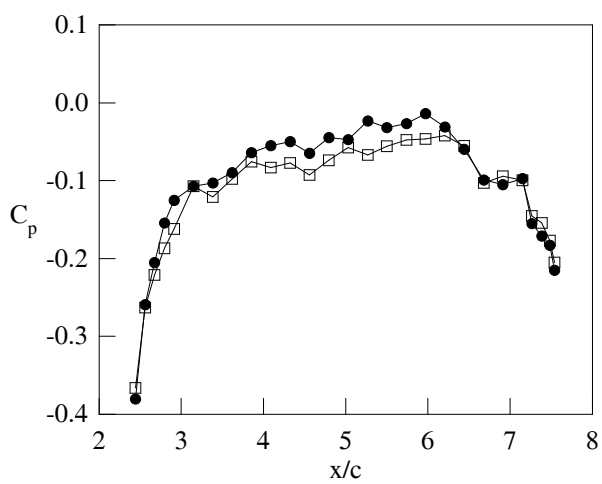


c) Ψ = -10°

**Figure 34.** Effect of trailer skirts on trailer side centerline pressure coefficients, y/w = 0.9 (solid: baseline, open: skirts, Re = 6 million)

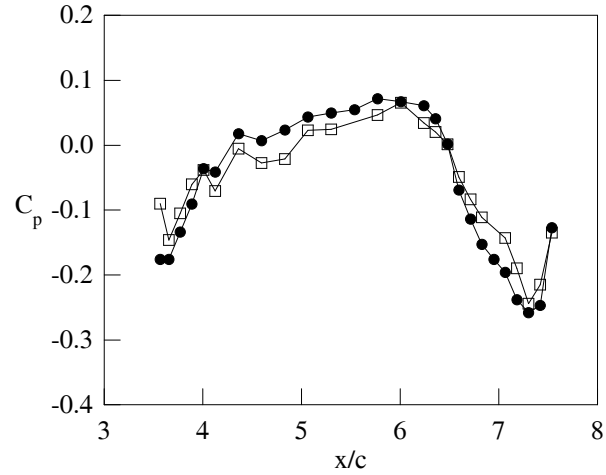


a) Ψ = 0°

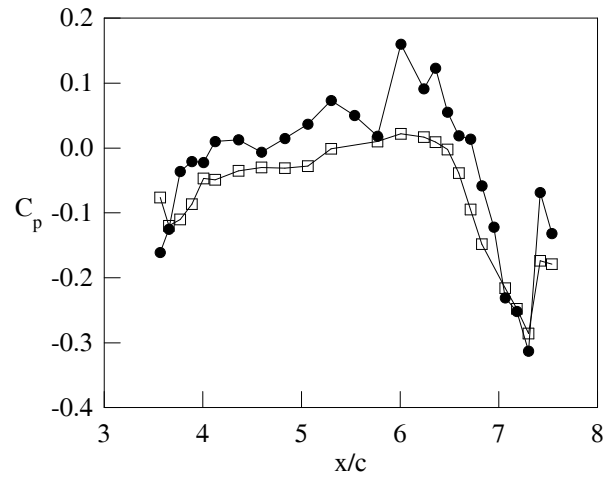


b) Ψ = 10°

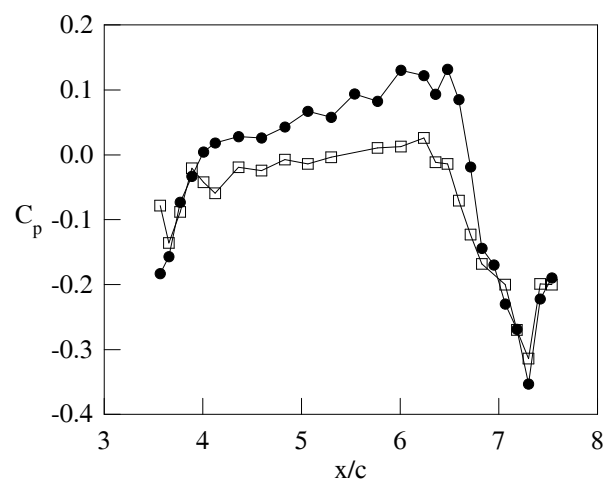


c) Ψ = -10°

**Figure 35.** Effect of trailer skirts on trailer bottom centerline pressure coefficients, z/w = 0.0 (solid: baseline, open: skirts, Re = 6 million)

pressures, especially on the bottom at ±10°. As suggested previously, the reduced pressures on the bottom of the trailer account for the reduced normal force generated by the skirts. Especially at high yaw angles, the windward skirt likely generates significant vorticity from the accelerated flow separating off the lower edge. The axial pressures on the side indicate slightly higher pressures on the forward third of the trailer except at –10° where the taps are on the leeward side. At mid-length on the side of the trailer, the skirts provide a noticeable decrease in pressure. The pressure distribution on the top of the truck (not shown) was relatively unchanged.

The contour plots of Figures 36–38 show the effect of the trailer skirts on the pressure distributions on the back of the tractor and the front and back of the trailer. At zero yaw, there appears to be little difference on all three surfaces except for a slight increase in pressure on the back of the trailer. At 10°, a significantly larger increase in pressure is evident on the back of the trailer, especially on the right (leeward) side. A lesser increase in pressure is also observed on the front of the trailer, mainly on the upper half. A small decrease in pressure is also discernable on the back of the tractor, which accounts for the observed increase in tractor drag.

Although not tested directly in the current study, a previous study suggests that the combination of the trailer base flaps and skirts would yield a drag reduction equal to the sum of their individual effects (Cooper 1982). If this is the case, a total drag reduction of 0.115 could be expected from the combination. The corresponding change in fuel consumption (also from the reference above) would be 3.68 liters/100 km.

## Conclusions

Experimental measurements were obtained of a 1:8-scale generic Class 8 tractor-trailer model in the NASA-Ames 12-ft and 7- by 10-ft wind tunnels. Data were acquired at a Reynolds number of 1 million in both facilities and at 6 million (equivalent to full scale at 75 mph) in the 12-ft pressure wind tunnel. Forces and moments, surface pressures, and 3-D PIV were employed to detail a baseline configuration representative of a modern aero package with and without trailer base flaps and trailer skirts.

The tractor side extenders were tested with and without a roof extender. The addition of the roof extender provided a significant drag reduction (0.009) by reducing the drag on the tractor while slightly increasing the drag on the trailer. The drag reduction of side and roof extenders was also found to increase with extender length. Apart from decreasing drag, the longer extenders also generated higher yawing moments. PIV measurements with and without extenders provided insight into the flow field and are also useful for CFD validation.

Relative to the baseline with 60%-gap side and roof extenders, the base flaps provided a sizable drag reduction (0.079) while increasing both normal force and yawing moment on the tractor. The effectiveness of both the side extenders and base flaps were found to be sensitive to Reynolds number for the reported range of one to six million.

Trailer skirts also reduced the wind-averaged drag (0.036) while marginally reducing the normal force due to lower pressure on the undercarriage. Pressure distributions indicated significantly increased trailer base pressures with little effect on the tractor.

Assuming that the benefits are additive, the combined effect of the base flaps and skirts would correspond to a fuel savings of 3.68 liters/100 km. For more details and a list of references, please see the associated technical paper: SAE-2005-01-3525.

## References

Browand, F., and Radovich, C., "Fuel Savings by Means of Flaps Attached to the Base of a Trailer: Field Test Results," USC Research Report, May 2004.

Cooper, K., "The Wind Tunnel Testing of Heavy Trucks to Reduce Fuel Consumption," SAE Paper 821285, November 1982.

Cooper, K., "The Effect of Front-Edge Rounding and Rear-Edge Shaping on the Aerodynamic Drag of Bluff Vehicles in Ground Proximity," SAE Paper 850288, March 1985.

Cooper, K.R., "Truck Aerodynamics Reborn – Lessons from the Past," SAE Paper 2003-01-3376, November 2003.

Croll, R.H., Gutierrez, W.T., Hassan, B., Suazo, J.E., and Riggins, A.J., "Experimental Investigation of the Ground Transportation Systems (GTS) Project for Heavy Vehicle Drag Reduction," SAE Paper 960907, February 1996.

Hammache, M., Michaelian, M., and Browand, F. "Aerodynamic Forces on Truck Models, Including Two Trucks in Tandem," SAE Paper 2002-01-0530, March 2002.

Heineck, J.T., Walker, S.M., and Satran, D., "The Measurement of Wake and Gap Flows of the Generic Conventional Truck Model (GCM) using Three-Component PIV," The Aerodynamics of Heavy Vehicles: Trucks, Buses and Trains, Monterey-Pacific Grove, CA, Dec. 2002.

Heineck, J.T., Walker, S.M., and Yaste, D.M., "The Development of a 3C-PIV System for the 12-Foot Pressure Tunnel at NASA Ames Research Center," *International Congress on Instrumentation of Aerospace Simulation Facilities*, Goettingen, Germany , August, 2003.

McCallen R., Flowers, D., Dunn, T., Owens, J., Leonard, A., Brady, M., Brownad, F., Hammache, M., Salari, K., Rutledge, W., Ross, J., Storms, B., Heineck, J.T., Driver, D., Bell, J., Zilliac, G., Walker, S., "Aerodynamic Drag of Heavy Vehicles (Class 7-8): Simulation and Benchmarking," 2000-01-2209, SAE Gov/Industry Meeting, Washington, D.C., June 19–21, 2000.

"SAE Wind Tunnel Test Procedure for Trucks and Buses," SAE J1252 JUL81, SAE Recommended Practice, July 1981.

Storms, B.L., Ross, J.C., Heineck, J.T., Walker, S.M., Driver, D.M. and Zilliac, G.G., "An Experimental Study of the Ground Transportation System (GTS) Model in the NASA Ames 7- by 10-Foot Wind Tunnel," NASA/TM-2001-209621, February 2001.

Storms, B.L., Satran, D.R., Heineck, J.T., and Walker, S.M., "A Study of Reynolds Number Effects and Drag-Reduction Concepts on a Generic Tractor-Trailer," AIAA Paper 2004-2251, June 2004.

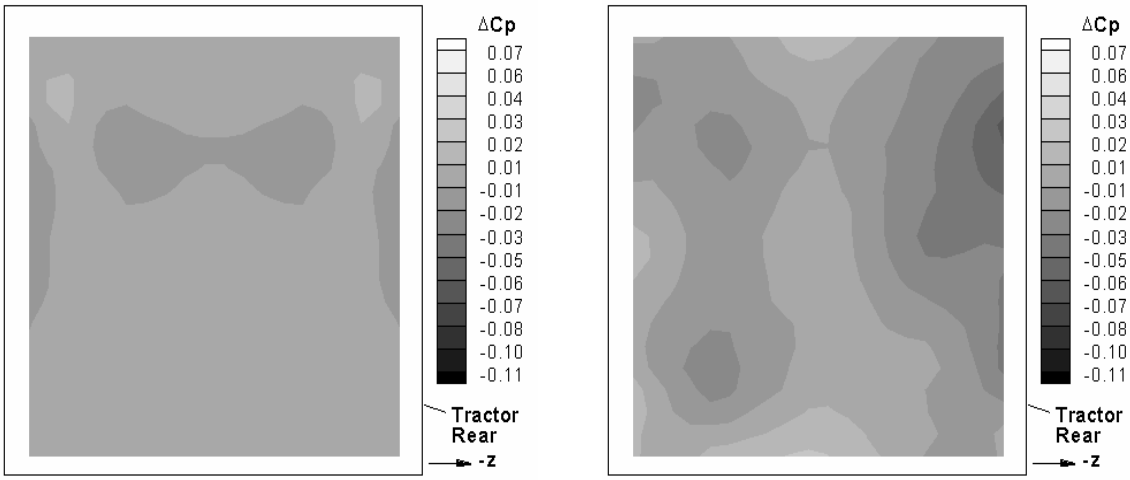


a) Ψ = 0 deg b) Ψ = 10 deg

**Figure 36.** Effect of trailer skirts on the pressure distribution on the back of the tractor (relative to extender baseline), Re = 6 million. Symmetry assumed for zero yaw. For Ψ = 10°, right half of image represents data at Ψ = –10°.

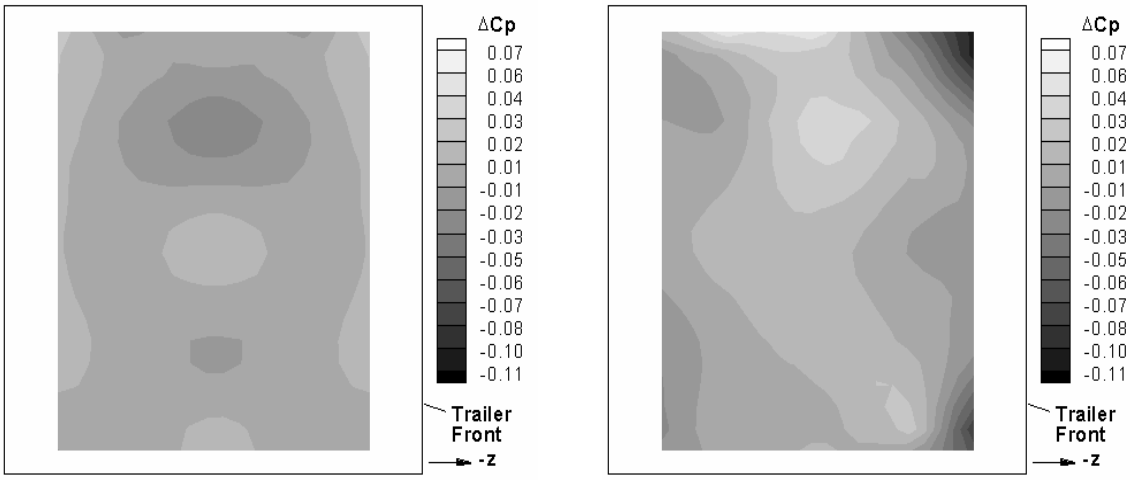


a) Ψ = 0 deg b) Ψ = 10 deg

**Figure 37.** Effect of trailer skirts on the pressure distribution on the front of the trailer (relative to extender baseline)

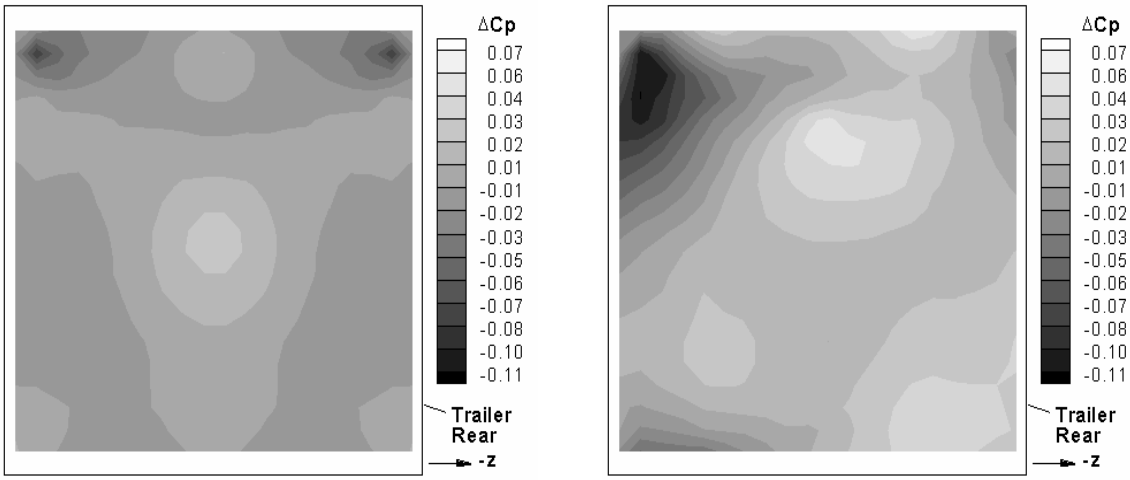


a) Ψ = 0 deg b) Ψ = 10 deg

**Figure 38.** Effect of trailer skirts on the pressure distribution on the back of the trailer (relative to extender baseline)

# I.F. Commercial CFD Code Validation for External Aerodynamics Simulations of Realistic Heavy-Vehicle Configurations

*Principal Investigator: W. David Pointer*
*Argonne National Laboratory*
*9700 S Cass Avenue, NE-208, Argonne, IL 60439*
*(630) 252-1052, fax: (630) 252-4500, email: dpointer@anl.gov*

*Technology Development Managers: Sid Diamond and Lee Slezak*
*(202) 586-2335, e-mail: Lee.Slezak@hq.doe.gov*

*Technical Program Manager: Jules Routbort*
*(630) 252-5065, e-mail: routbort@anl.gov*

*Participants*
*Suneet Singh, University of Illinois Urbana-Champaign*
*Tanju Sofu, Argonne National Laboratory*
*David Weber, Argonne National Laboratory*

---

*Contractor: Argonne National Laboratory*
*Contract No.: W-31-109-ENG-38*

---

## Objectives

- Evaluate capabilities in standard commercial computational fluid dynamics (CFD) software for the prediction of aerodynamic characteristics of a conventional United States (U.S.) Class 8 tractor-trailer truck.
- Develop "best practice" guidelines for the application of commercial CFD software in the design process of Class 8 vehicles.

## Approach

- Develop computational models of the experiments completed in the National Aeronautics and Space Administration (NASA) Ames Laboratory's 7- by 10-ft wind tunnel using the Generic Conventional Model (GCM).
- Compare the predictions of the computational models with experimental measurements of vehicle aerodynamic drag force and pressure field distributions.

## Accomplishments

- Experimental measurements and computational predictions of the vehicle drag coefficient agree within less than 1% in the best case simulations at zero yaw. Experimental measurements and computational predictions of the pressure distribution along the surface of the vehicle agree well everywhere except the rear faces of the cab and the trailer.
- Evaluations of computational predictions of the vehicle at yaw angles greater than zero indicate that vehicle drag coefficients can be predicted with 5 to 10% of measured values.

## Future Directions

- Confirm applicability of guidelines to real tractor trailer geometries as part of a Cooperative Research and Development Agreement (CRADA) with PACCAR.

- Consider alternate GCM configurations using various add-on devices to examine capabilities for the prediction of changes in drag coefficient.
- Evaluate effects of changes in radiator size and effects of underhood flow on drag predictions as part of CRADA with Caterpillar, Inc.
- Suggest potential drag reduction design options based on knowledge gained from computational effort.

---

## Introduction

With rising oil prices, the issue of energy economy in transportation is getting much attention. At the same time, new emissions standards for tractor-trailer vehicles introduce additional challenges for the manufacturers to achieve improvements in vehicle fuel economy. As part of the U.S. Department of Energy's FreedomCAR and Vehicle Technologies Program's Heavy Vehicle Aerodynamic Drag Consortium, Argonne National Laboratory is currently developing guidelines for the use of commercial CFD software to facilitate energy efficiency improvements through improved aerodynamic design of tractor-trailer vehicles. The development of these guidelines requires the consideration of the sensitivity of the accuracy of the analysis to the various modeling choices available to the end user. Early investigations focused on the sensitivity of the predictions of drag coefficients and surface pressure distributions for the standard configuration of the GCM at zero yaw to the size and structure of the computational mesh and the selection of turbulence model. Current assessments are focusing on the impact of these parameters on simulations of the standard GCM at yaw angles greater than zero and on the ability to predict the change in the drag coefficient when drag reduction devices are employed.

## Modeling Strategy

This program will provide guidance for the use of commercial CFD software in heavy vehicle design, including the expected impact of grid resolution and structure on prediction accuracy, the impact of the Reynolds-averaged Navier Stokes (RANS) turbulence model formulation selected, the impact of considering only half of a vehicle to speed up initial simulations. The guidelines developed by this program are intended to be generic advice for the application of a commercial CFD software package to the prediction of heavy vehicle aerodynamic drag coefficients. Since this market is currently dominated by finite volume formulations, the guidelines will focus upon software using this methodology.

## Selection of Commercial CFD Software

Preliminary guideline development will be completed using the commercial CFD code Star-CD. The Star-CD software was selected for this purpose largely because the code offers a great deal of the flexibility in computational mesh development with the ability to utilize polyhedral "cut" cells and recognize both integral and arbitrary interfaces between regions of the computational domain. Furthermore, user subroutines allow the user to implement significant modifications to most features of the code if such modifications are needed. It is anticipated that the applicability of the general guidelines to other commercial CFD codes, will be examined and that the extension of the guidelines to alternate commercial CFD software methodologies, such as Lattice-Boltzmann, will be pursued following the initial development stage.

## Selection of Tractor Trailer Geometry

The GCM, developed by NASA Ames Research Center for scaled wind tunnel testing, is a generalized representation of a conventional U.S. tractor-trailer truck, as shown in Figure 1. The 1/8th scale model is approximately 2.5 meters (m) long by 0.3 m wide by 0.5 m high. The studies contained herein consider experiments that were completed in the NASA Ames 7- by 10-foot (ft) wind tunnel. Instrumentation included a force balance, 476 steady pressure transducers, 14 dynamic pressure transducers, and three-dimensional Particle Image Velocimetry (PIV). Data

**Figure 1.** Generic Conventional Model (GCM)

were collected at various Reynolds number values and yaw angles. The initial studies presented herein consider only the case using the standard configuration of the GCM with a vehicle-width based Reynolds number of Re = 1.15 million. Measurements using alternate configurations with add-on devices will be used to evaluate whether computational modeling guidelines developed based upon these studies are sufficiently general to be applied in the evaluation of the aerodynamic characteristics of other vehicles under different operating conditions.

## Computational Model

The computational model employed in these studies was developed using the ES-Aero tool for aerodynamic drag simulation that is available as part of the Star-CD software package. The surface of the standard configuration GCM is defined using approximately 500,000 triangular surface elements based upon Computer-Aided Design (CAD) data representations taken from optical scans of the actual model. A computational domain, which as external dimensions that are based on the cross-sectional dimensions of the wind tunnel, is developed based upon this surface definition using a semi-automated process that begins by creating a hexahedral mesh that is successively refined in smaller zones around vehicle, with integral cell coupling employed at the interfaces between zones. The dimensions of hexahedral elements that make up the zone immediately surrounding the vehicle are specified by user as the near vehicle cell size. The mesh elements near the vehicle surface are then further refined based upon local surface features identified by the user or selected automatically based on curvature or gap width. The user specifies a minimum allowable cell size that limits the refinement of the mesh in this step.

Using this locally refined hexahedral mesh, the original surface is "wrapped" by projecting the hexahedral mesh onto the original surface. The "wrapped" surface definition is then volumetrically expanded to create a subsurface which is used to cut away the portions of the locally-refined hexahedral mesh that fall inside the vehicle. A brick and prism cell extrusion layer is then created to fill the gap between the sub-surface and the "wrapped" surface. In this way, the polyhedral cut cells are removed some distance from the surface, and a consistent $y^+$ value between approximately 20 and 200, can be maintained regardless of grid resolution, insuring that the computational meshes are suitable for the turbulence models used in these studies. A final step further refines the wake region and the underbody region in order to better capture important flow features. An example of the mesh construction of the computational domain used in the GCM simulations is shown in Figure 2.

Using locally refined, face-coupled computational domains with substantial numbers of non-hexahedral cells makes the standard practice of evaluating grid convergence by uniformly refining the entire mesh in all directions intractable. In the computational meshes used in these studies, two separate parameters determine the size of the mesh. Mesh sensitivity analyses included in these studies examine the effects of changes in the near-vehicle cell size and minimum cell size parameters on the prediction of the drag coefficient. However, this is not equivalent to the traditional grid convergence study because the grid is not uniformly refined in all directions throughout the domain and the vehicle surface definition cannot be exactly maintained for all models since the final surface definition is dependent upon the local refinement of the computational mesh.

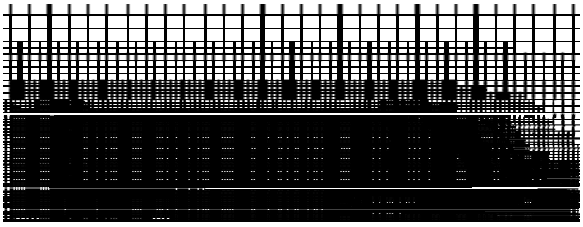

**Figure 2.** Example of computational mesh structure used in the simulation of the aerodynamic characteristics of the GCM

## Computational Requirements

Models are constructed using a 64-bit Itanium2 Linux workstation with 24 gigabytes (GB) of random access memory (RAM). The construction of the most coarsely-meshed models included in this study, from International Global Positioning System (IGS) data to final model, requires approximately three hours and peak memory usage is approximately 1 GB. The most finely meshed models requires approximately 12 hours and the

peak memory usage is approximately 5 GB. Since the automated mesh wizard included with the software package is used, little intervention is required by the user during this process. As with any software, initial models created by a novice user will likely require a larger initial time investment. All models employed in these studies are used as supplied from the automated tool with no manual repair or modification.

Argonne National Laboratory's Nuclear Engineering Division maintains a Beowulf cluster for performing engineering mechanics, fluid dynamics, and reactor engineering analyses. The cluster consists of three front-end (i.e., control) nodes and seventy-five compute nodes. One of the front-end nodes is a 32-bit servers contains dual Athlon MP 2.2GHz processors and 4 GB of memory. The two remaining front ends are 64-bit front-end servers: one with dual Itanium2 processors and 24 Gigabytes of memory, the other with dual Xeon processors and 8 GB of memory. The cluster's file server provides nearly 1 terabyte of home file system space. Each of the 75 compute nodes has a 3.2 gigaHertz (GHz) Pentium IV processor with 2 GB of memory. All of the machines in the cluster are interconnected via Gigabit Ethernet. All of the systems run RedHat Enterprise Linux.

## Brief Summary Of Prior Results at Zero Yaw

Initial studies focus on the prediction of the aerodynamic characteristics of the GCM at a yaw angle of zero. For this case, a preliminary mesh sensitivity study considering the effect of near vehicle cell size and minimum cell size on the accuracy of aerodynamic characteristics has been completed. Additional studies have considered the impact of turbulence model selection and the use of half vehicle versus full vehicle models.

## Bulk Resolution Sensitivity

In previous efforts, five computational domains were generated based on the standard GCM configuration in order to evaluate the effects of the near vehicle cell size parameter on the prediction of the drag coefficient. Near-vehicle cell sizes of 16.0, 12.0, 10.0, 8.0 and 6.0 millimeters (mm) were considered. In each case, the minimum cell size resulting from local feature-based refinements is 12.5% of the near vehicle cell size. An additional restriction requires that a minimum of 16 elements are used to define any circle. In order to ensure that the quality of the vehicle surface is maintained, the cell layer immediately adjacent to the surface is refined to 25% of the original size prior to trimming. The computational domain characteristics are shown in Table 1.

In simulations using these models, a uniform inlet velocity condition and a zero gradient outlet condition were specified, and the standard high Reynolds number k-ε model was utilized. Convergence criteria were set so that 3,000 iterations were completed, and all residuals fall below $10^{-4}$ by the 3,000th iteration. Total computational time and clock time when using 16 processors for each simulation are shown in Table 2. Predicted drag coefficients from each of the five cases are compared with experimental data from wind tunnel tests in Table 3. Pressure coefficient data was also extracted along the centerline of the vehicle for each case and compared with experimental data as shown in Figure 3. These comparisons show that the difference in the accuracy of the drag coefficient prediction as a function of the near vehicle cell size is a result of small differences in the pressure distribution over the entire surface rather than large localized differences.

**Table 1.** Summary of Computational Domain Characteristics for Evaluation of Bulk Cell Size Effects

| Near-Vehicle Cell Size (mm) | Minimum Cell Size (mm) | Total Number of Volume Elements | Number of Volume Elements on Surface |
|---|---|---|---|
| 16.0 | 2.0 | 1012338 | 73574 |
| 12.0 | 1.5 | 1737085 | 126119 |
| 10.0 | 1.25 | 2345640 | 175105 |
| 8.0 | 1.0 | 3282426 | 266666 |
| 6.0 | 0.75 | 5695622 | 400382 |

**Table 2.** Summary of Computational Cost for Each Case Considered in the Evaluation of Bulk Cell Size Effects

| Near-Vehicle Cell Size (mm) | Total CPU Time (seconds) | Total Clock Time (seconds) |
|---|---|---|
| 16 | 206072 | 16454 |
| 12 | 390113 | 29392 |
| 10 | 417686 | 32182 |
| 8 | 610958 | 44967 |
| 6 | 2720956 | 188577 |

**Table 3.** Effects of Near-Vehicle Cell Size Parameter on Accuracy of Drag Coefficient Prediction

| Near-Vehicle Cell Size (mm) | Predicted Drag Coefficient | Error in Drag Coefficient |
|---|---|---|
| Experiment | 0.398 | |
| 16 | 0.449 | 12.0 |
| 12 | 0441 | 10.3 |
| 10 | 0.418 | 4.9 |
| 8 | 0.415 | 4.2 |
| 6 | 0.405 | 1.7 |

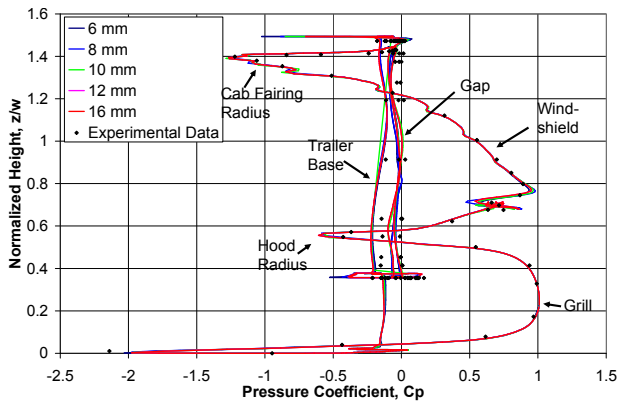


**Figure 3.** Comparison of predicted pressure coefficient distributions on the vehicle surface for various values of the near-vehicle cell size parameter with experimental data for the GCM geometry

## Near-Wall Resolution Sensitivity

Following the assessment of the effects of the near-vehicle cell size parameter on the accuracy of the drag coefficient prediction, the effect of the near-wall cell size parameter was also considered. The near-vehicle cell size was set to 8 mm and the minimum cell size for local refinement was reduced from 1 mm to 0.5 mm. The change in the near-wall resolution increases the number of computational elements from 3,282,426 to 4,264,232. The change in the computational mesh resolution results in a increase in the total central processing unit (CPU) time from 610,958 seconds to 703,027 seconds. The change in the near-wall refinement parameter results in a reduction in the error of the drag coefficient prediction from 4.2% to 1.0%.

## Turbulence Model Selection Sensitivity

In all simulations completed for the computational mesh sensitivity studies, the high Reynolds number k-ε turbulence model was used in conjunction with a standard logarithmic wall function for the prediction of turbulent kinetic energy and eddy diffusivity. While the high Reynolds number k-ε turbulence model is a robust general-purpose turbulence model, the strong adverse pressure gradients and large flow recirculation regions associated with the GCM geometry may limit the applicability of steady-state RANS modeling strategies. Using the computational mesh with a near-vehicle cell size of 8 mm and a near-wall cell size limit of 0.5 mm, simulations of the aerodynamic characteristics of the GCM model were repeated using five steady RANS turbulence models and their associated wall functions: (1) the standard high-Reynolds number k-ε model with logarithmic wall function, (2) the Menter k-ω SST model, (3) the renormalization group (RNG) formulation of the k-ε model, (4) the Chen formulation of the k-ε model, and (5) the quadratic formulation of the k-ε model. Drag coefficients predicted using each of the selected steady-RANS turbulence models are shown in Table 4. Comparisons of the predicted pressure coefficient distributions when using the selected turbulence models are shown in Figure 4. The differences in the predicted drag coefficient are largely a result of localized discrepancies in the surface pressure coefficient predictions in the regions of separated flow, with the largest discrepancies appearing in the underbody region just behind the tractor.

**Table 4.** Results of the Evaluation of Two-Equation Turbulence Models for Prediction of Drag Coefficients for the GCM Geometry

| Turbulence Model | Predicted Drag Coefficient | Percent Error in Prediction |
|---|---|---|
| Experiment | 0.398 | – |
| High-Reynolds Number k-epsilon Model | 0.402 | 1.0 |
| Mentor k-ω SST model | 0.401 | 0.8 |
| RNG model | 0.389 | 2.3 |
| Chen's model | 0.3919 | 1.61 |
| Quadratic model | 0.3815 | 4.32 |

## Half-Vehicle Versus Full-Vehicle Models

In order to evaluate the effects of considering only half of the vehicle rather than the full vehicle, two models were created using the full vehicle geometry. These models use the same mesh parameter settings as the two coarsest models considered in the mesh sensitivity study. The full vehicle models are based

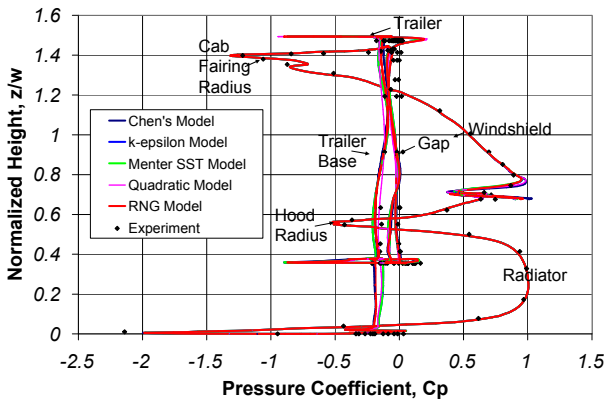


**Figure 4.** Comparison of predicted pressure coefficient distributions on the vehicle surface with experimental data for selected turbulence models

upon near-vehicle cell sizes of 12 mm and 16 mm, with minimum near-wall cell sizes of 1.5 mm and 2.0 mm, respectively. As in all previous studies, 3,000 iterations were completed for each steady-state simulation and the convergence of the drag coefficient was monitored. As shown in Table 5, drag coefficient predictions show a slight improvement in agreement with experimental measurements when the full-vehicle model is used. The GCM geometry is in reality slightly asymmetric and the consideration of this geometric asymmetry is likely the primary difference in the models that contributes to these discrepancies.

**Table 5.** Drag Coefficient Predictions for Full Vehicles

| Near-Vehicle Cell Size (mm) | Predicted Drag Coefficient | Percent Error in Prediction |
|---|---|---|
| 16 | 0.441 | 10.3 |
| 12 | 0.426 | 6.7 |

## Results at Non-Zero Yaw Angles

As an initial test of the general applicability of the lessons learned from the zero yaw angle sensitivity studies, the aerodynamic characteristics of the GCM were evaluated at yaw angles ranging from 1 to 14°. In the wind tunnel experiments, three separate drag states are observed over this range. In the near-zero yaw range, drag, lift and side force coefficient values are all at their lowest values. Between 2 and 3°, drag force coefficients rise rapidly to a higher drag state, presumably as a consequence of large separation zones forming on the leeward side of the vehicle. Between 10 and 15°, drag force coefficients fall to a lower drag state, presumably because side forces grow to become the dominant forces in this range. Considerable hysteresis was noted in the experiments between yaw angle sweeps moving from positive to negative angles versus negative to positive angles.

## Yaw Angle Sensitivity of Nominal Model

For each yaw angle, computational models were constructed using a near vehicle cell size of 8 mm and a near-wall cell size of 1 mm. Since the yawing of the GCM at angles greater than zero removes the option of considering only a half-vehicle because there is no longer a symmetric plane, only full vehicle models were considered. All simulations use the standard high Reynolds number k-ε model with a logarithmic wall function. As in all previous studies, 3,000 iterations were completed for each steady-state simulation and the convergence of the drag coefficient was monitored.

Predicted drag force coefficients are compared with experimental data from wind tunnel studies in Figure 5. Predicted drag coefficients appear to capture the jump from the low drag state to high drag state between 2° and 3°. However, the low drag state predictions are much more accurate when compared to experimental data. Low drag state predictions exhibit less than 4% error while high drag state predictions exhibit errors of slightly more

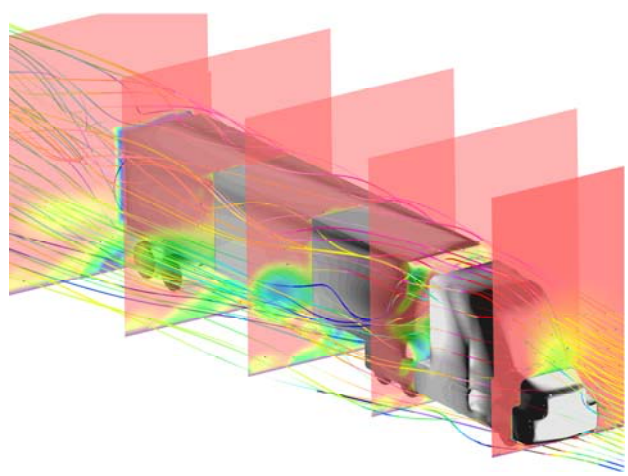

**Figure 5.** Streamlines showing predicted air flow across the surface of the GCM at a yaw angle of 10°. Streamline color and translucent cutting planes indicate local velocity magnitude. Vehicle surface shading indicates pressure distribution.

than 10%. Drag coefficient predictions do not appear to capture the observed drop to a lower drag state at higher yaw angles.

Predicted lift and side force coefficients are compared with experimental data in Figures 6 and 7, respectively. Both lift and side force predictions appear to capture the trends observed in the wind tunnel experiments well. Lift force coefficient predictions exhibit a maximum error of approximately 35% at zero yaw. Side force coefficient predictions exhibit a maximum error of approximately 15% at 4° yaw.

At yaw angles greater than 2°, large flow separation zones begin to form along the leeward side of both the tractor and trailer, introducing significant turbulent instability into the flow field.

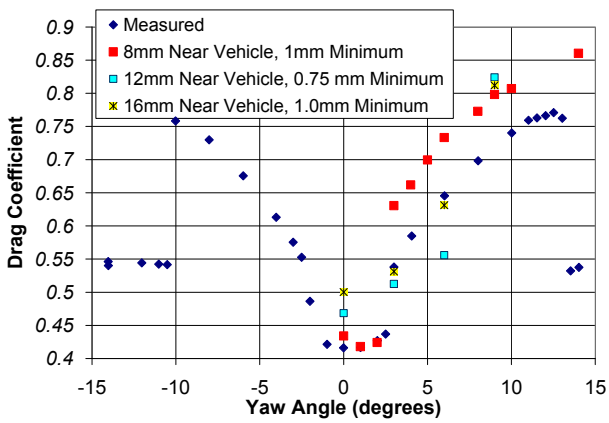


**Figure 6.** Comparison of drag coefficient predictions as a function of yaw angle and near-vehicle cell size

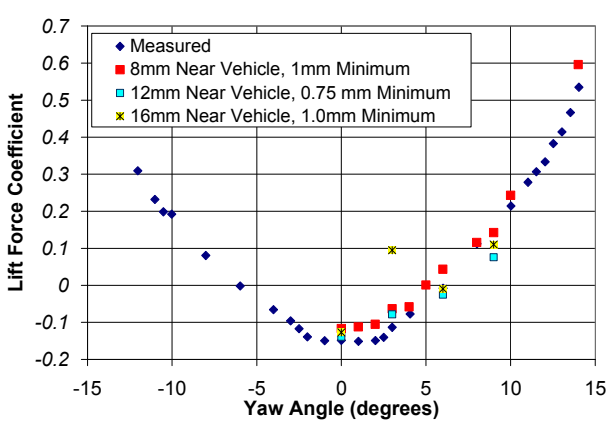


**Figure 7.** Comparison of lift force coefficient predictions as a function of yaw angle and near-vehicle cell size

The instability is further exacerbated by the formation of a highly turbulent jet through the gap between the tractor and trailer which washes over the logical separation points on the leeward side of the trailer, extending the separation zone. While two-dimensional (2-D) representations may illustrate the primary challenges in modeling the flow field surrounding the GCM at yaw angles greater than zero, the true complexity of the flow can only be visualized when considered in the three-dimensional (3-D) as in Figure 8. It is anticipated that selective refinement of the separation regions or the application of a more rigorous turbulence modeling strategy may lead to improvements in predictive capability.

## Bulk Resoultion Sensitivity of Predictions at Non-Zero Yaw Angles

To evaluate the sensitivity of aerodynamic coefficient predictions to changes in the near vehicle cell size, a parametric evaluation was completed using near vehicle cell sizes of 8 mm, 12 mm, and 16 mm as a basis for models of the GCM geometry at angles of 3, 6, and 9°. Predicted drag coefficients are compared with experimental data in Figure 6. While the cases using the 8mm near vehicle cell size clearly capture the shape of the drag curve within a fairly consistent error, the coarser cases do not clearly show the same trend and the error band is not as regular. While this may indicate that the use of a smaller near-vehicle cell size could improve the quality of the prediction, the resultant mesh would be too cumbersome to be of practical

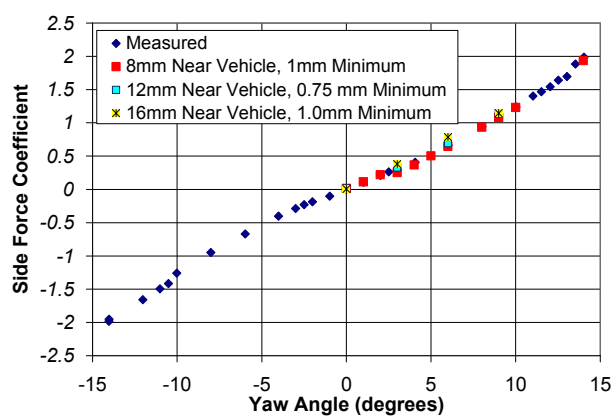


**Figure 8.** Comparison of side force coefficient predictions as a function of yaw angle and near-vehicle cell size

use in a design effort, and this possibility has not been considered in this study.

Predicted lift and side force coefficients are shown in Figures 7 and 8. As with the drag coefficient, the 8 mm case appears to capture the shape of the lift force coefficient curve while the coarser models fail to predict the curve shape. For the lift force coefficient, the error band is fairly regular for the 8 mm near vehicle cell size while the error in the prediction with the coarser models is more irregular. The error in the prediction of the side force appears to be relatively insensitive to the near vehicle cell size.

## Near-Wall Resolution Sensitivity of Predictions at Non-Zero Yaw Angles

To evaluate the sensitivity of aerodynamic coefficient prediction to changes in the near wall cell size, a parametric evaluation was completed using a near-vehicle cell size with near-wall cell sizes of 1.0 mm, 0.5 mm, and 0.25 mm as the basis for models of the GCM at yaw angles of 3, 6, and 9°. Predicted drag coefficients are compared with experimental data in Figure 9. The additional near-wall refinement of the 0.5 mm case clearly provides an improvement over the nominal 1.0 mm case. However, the improvement that results from further refinement to 0.25 mm is minimal.

The predicted lift and side force coefficients are compared with experimental data in Figures 10 and 11, respectively. The lift force coefficient does not show the same consistent improvement as is seen

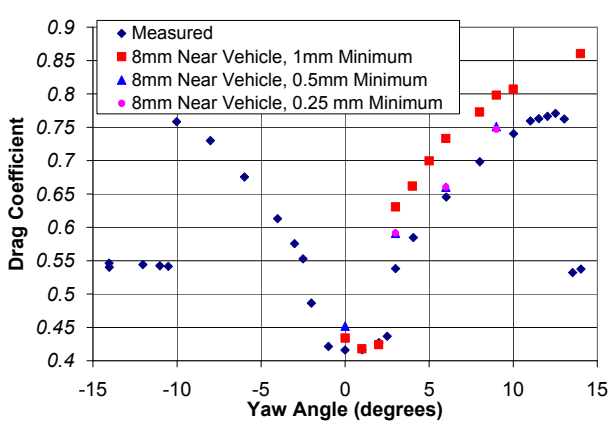


**Figure 9.** Comparison of drag coefficient predictions as a function of yaw angle and near-wall cell size

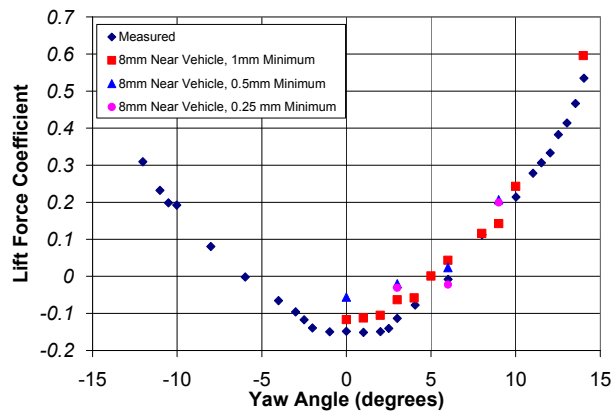


**Figure 10.** Comparison of lift force coefficient predictions as a function of yaw angle and near-wall cell size

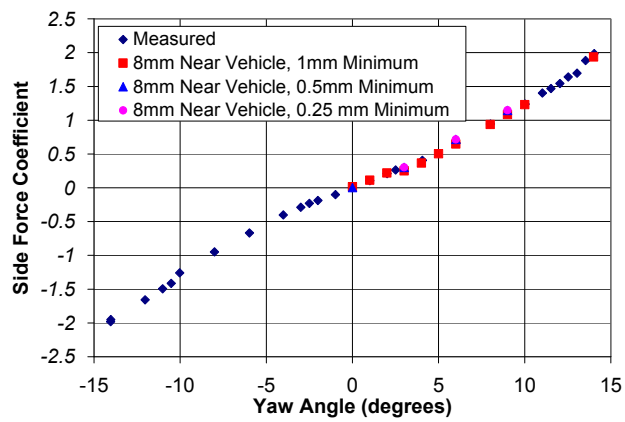


**Figure 11.** Comparison of side force coefficient predictions as a function of yaw angle and near-wall cell size

with the drag coefficient, with larger errors seen for the 6° case. As in previous sections, the error in the side force coefficient prediction is small in comparison to the errors in the other coefficients.

## Turbulence Model Selection Sensitivity of Predictions at Non-Zero Yaw Angles

To evaluate the effects of turbulence model selection on the accuracy of drag coefficient predictions at non-zero yaw angles, a parametric study was completed using the computational model with an near vehicle cell size of 8mm and near wall cell size of 0.5 mm. Three different turbulence models were considered: (1) the standard high-Reynolds number k-ε model, (2) the Menter k-ω SST model, and (3) the renormalization group (RNG) formulation of the k-ε model. All of these models were employed in

conjunction with model-specific logarithmic wall functions.

Predicted drag coefficients are compared with experimental data in Figure 12. Lift and side force coefficients are compared with experimental data in Figures 13 and 14, respectively. In the prediction of drag coefficient, the high-Reynolds number k-ε model shows some advantage over the other models considered at higher yaw angles. The predicted drag coefficient typically exhibits an oscillatory behavior as a function of iteration number, and the difference between the Menter k-ω SST model and the renormalization group (RNG) formulation of the k-ε model is within the band of oscillation of the drag coefficient over the final 200 iterations. The accuracy of the lift force coefficient prediction appears to increase with yaw angle, with the largest errors seen at 0° for this case. For both the

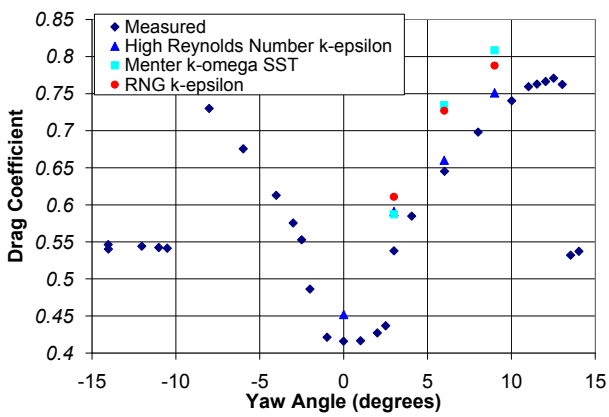


**Figure 12.** Comparison of drag coefficient predictions as a function of yaw angle and turbulence model

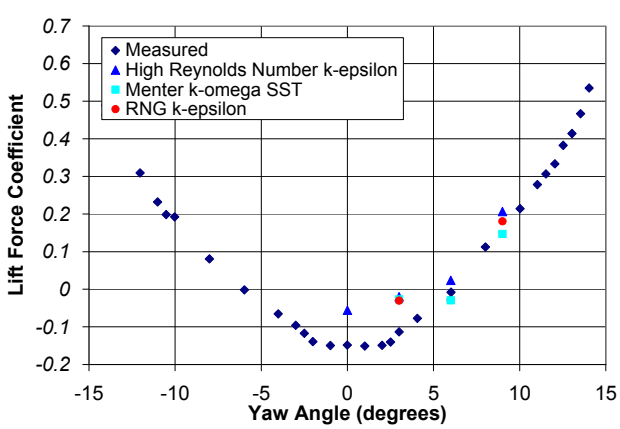


**Figure 13.** Comparison of lift force coefficient predictions as a function of yaw angle and turbulence model

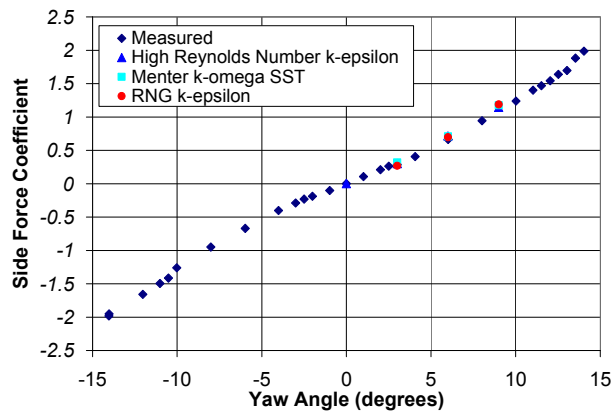


**Figure 14.** Comparison of side force coefficient predictions as a function of yaw angle and turbulence model

lift force coefficient and the side force coefficient predictions, all three turbulence models appear to provide comparable performance.

## Consideration of Add-on Devices

As an initial test of the capability of the approach used in these studies to predict changes in drag coefficient when after-market drag reduction devices are employed, a modified version of the GCM was developed which incorporates an ogive boat tail based upon the inflatable boat tail design of Aerovolution, Inc. Aerovolution provided CAD data describing the surface of the boat tail, which was scaled to the match the rear face of the GCM trailer. Surfaces were created based on this description and merged with the GCM model to create the geometry shown in Figure 15. Using the methodology outlined above, three models were generated to assess the mesh sensitivity of the results and try to provide some feel for the accuracy of the solutions. The models use near vehicle cell sizes of 8 mm and 12 mm and near-wall cell sizes of 1.0 mm and 0.5 mm. The standard high-Reynolds number k-ε model was used in all cases. The predicted drag coefficients are shown in Table 6. For the case with a near-vehicle cell size of 8 mm and a near-wall cell size of 0.5 mm, these results indicate a reduction in the drag coefficient of approximately 7%. At highway speeds, this would correspond to a fuel savings of approximately 3.5%.

Road test data have been requested from Aerovolution for comparison with the prediction results to confirm the accuracy of the solution.

**Figure 15.** Modified GCM Geometry with Aerovolution's Inflatable Boat Tail Device

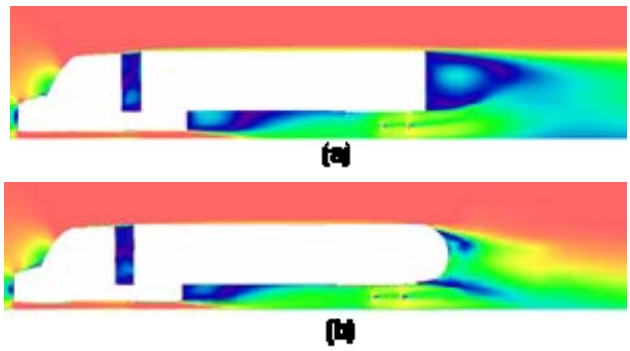

**Figure 16.** Comparison of Velocity Magnitude Predictions without (a) and with (b) the boat tail device installed.

**Table 6.** Drag Coefficient Predictions for Vehicle with Boat Tail Device as a Function of Mesh Parameters

| Near-Vehicle Cell Size (mm) | Near-Wall Cell Size (mm) | Drag Coefficient |
|---|---|---|
| 12 | 2 | 0.4179 |
| 8 | 1 | 0.4116 |
| 8 | 0.5 | 0.3975 |

## Conclusion

These studies are the initial components of an ongoing assessment of the capabilities for the prediction of heavy vehicle aerodynamic characteristics using current generation commercial computational fluid dynamics software. Based on the outcomes of these studies, guidelines are being developed for the immediate application of these current generation tools by the heavy vehicle manufacturing community. Initial assessments have shown that drag coefficients can be predicted within less than 1% of the measured value and the surface pressure distributions can be predicted with reasonable accuracy for vehicles at zero yaw angle, even when the standard k-ε type models and logarithmic wall functions are utilized. Near wall resolution appears to have more impact than bulk resolution on the accuracy of the results, indicating that resources should be focused in the near wall region. For the bare 1/8$^{th}$ scale GCM geometry, a near wall cell size of 1.0 mm overall and 0.5 mm in regions of geometric complexity, such as the hood vent, combined with a near vehicle cell size of 8 mm provides predictive accuracy for the drag coefficient on the order of 1%. As yaw angle increases to values greater than zero, predictive accuracy is somewhat eroded, but the prediction of general trends is still observed. It is anticipated that ongoing sensitivity studies may lead to additional guidance for the consideration of tractor-trailer vehicles at yaw angles greater than zero. Additional studies will evaluate the applicability of these trends to more realistic geometries.

## Reference

Satran, D., "An Experimental Study of the Generic Conventional Model (GCM) in the NASA Ames 7-by-10-Foot Wind Tunnel," United Engineering Foundation Conference on the Aerodynamics of Heavy Vehicles: Trucks, Buses, and Trains, United Engineering Foundation, New York, 2002.

# I.G. Test, Evaluation, and Demonstration of Practical Devices/Systems to Reduce Aerodynamic Drag of Tractor/Semitrailer Combination-Unit Trucks

*Principal Investigator: Robert M. Clarke*
*Truck Manufacturers Association*
*1225 New York Avenue, NW, Suite 300*
*Washington, DC 20005*
*(202) 638-7825, fax: (202) 737-3742, e-mail: robertmclarke@truckmfgs.org*

*DOE Project Officer: Steven Cooke*
*National Energy Technology Laboratory*
*Morgantown, WV 26505*
*(304) 285-5437, e-mail: Steven.Cooke@netl.doe.gov*

*Technology Development Managers: Sid Diamond and Lee A. Slezak*
*FreedomCAR and Vehicle Technologies Program*
*U.S. Department of Energy*
*1000 Independence Ave., S.W.*
*Washington, D.C.*
*(202) 586-2335, fax: (202) 586-2476, e-mail: Lee.Slezak@hq.doe.gov*

*Field Technical Manager: Jules L. Routbort*
*(630) 252-5065, fax: (630) 252-4289, e-mail: jules.routbort@anl.gov*

*Participants*
*Scott Smith, Karla Younessi, Freightliner LLC*
*Ronald Schoon, International Truck and Engine Corporation*
*Justin Clark, Conal Deedy, Volvo Technology of America (Volvo Trucks, Mack Trucks)*

---

*Contractor: Truck Manufacturers Association, 1225 New York Avenue, NW, Suite 300, Washington, DC 20005*
*Contract No.: DE-FC26-04NT42117*

---

## Objective

- To reduce aerodynamic drag of tractor/semi trailer combination trucks through development, test, and demonstration of aerodynamic aids and systems of aerodynamic aids from the viewpoint of manufacturability and practicality for over-the-road use.

## Approach

- Pursue complementary research paths for aerodynamic devices and systems that fit individual manufacturer needs and technical strengths.
    - Research areas include the effect of mirror design on truck aerodynamics; the effect of aerodynamic treatments of tractor trailer gap, trailer side, and trailer wake on truck aerodynamics; the effect of trailer aerodynamics, trailer gap enclosure, and trailer gap flow control on truck aerodynamics; and the effect of vehicle underside design and management of tractor-trailer air flows on truck aerodynamics.

- Phase I: Conduct preliminary testing and analysis on a wide range of candidate devices and systems to determine effectiveness of such devices and establish promising sets of devices for further research. This testing will involve both full-size vehicles and scale models in wind tunnels and real-world driving tests. Computational fluid dynamics (CFD) will also be used to establish effects of aerodynamic devices on truck aerodynamics.
- Phase II: Construct prototype devices for installation on full-size Class 8 trucks for testing in wind tunnels or in real-world environments (potentially in fleet applications). This testing will quantify the optimal fuel economy benefits achievable through the use of these devices and systems in terms of a percentage improvement relative to a similar baseline truck and trailer.

## Accomplishments

- Completed wind tunnel tests of a current state-of-the-art standard head/mounting mirror system on a full-scale Class 8 tractor establishing the effect of the mirror system on aerodynamic drag and flow behavior. These data are being used to correlate with CFD modeling. Evaluated aerodynamic characteris-tics of the truck with mirrors to baseline truck without mirrors. The CFD models have been constructed and are currently running through the computer system. (Freightliner)
- Completed evaluation of modifications to trailer sides, trailer wake, and tractor-trailer gap through two rounds of one-eighth scale model wind tunnel testing. The first round of scale model testing quantified the effects of a number of vehicle modifications in order to select a subset of these for a second round of scale model testing. Testing of several additional vehicle modifications was also conducted in the second round: these additional modifications were the result of customer input on practical devices. Aerodynamic drag reductions of up to 23% were demonstrated in wind tunnel testing using the 1/8 scale models. (International)
- In process of completion of CFD analysis of the effect of trailer aerodynamics, trailer gap enclosure, and trailer gap flow control on truck aerodynamics through use of StarCD CFD software. Several aerodynamic aids (vortex generators, trailer boat-tails, etc.) are being analyzed through CFD work for selecting promising technologies for further full-size vehicle testing. A trailer equipped with a boat tail and side skirts has been acquired for use in fuel economy tuning tests. (Mack)
- In process of completion of CFD analysis of the effect of vehicle underside design and airflow management on truck aerodynamics. Estimated that vehicle underside design is associated with approximately 35% of total vehicle drag, and that improvements to underside design, trailer gap manipulation, and trailer bogie improvements could reduce overall drag by approximately 11%. In process of establishing device designs to be considered for full-scale on-road testing, using results obtained to date from CFD analysis. (Volvo)

## Future Directions

- Pending Phase II approvals, continue wind tunnel tests on the same tractor used for Phase I utilizing two different types of mirrors commonly used in the marketplace. The West Coast-style mirror will be tested because it is a commonly utilized mirror that is considered to be less aerodynamic than most mirrors due to the multiple support tubes. A mirror design will also be selected that appears to have more aerodynamic qualities such as fewer support structures and sleeker styling of the mirror head. Wind tunnel findings will be correlated with CFD modeling. Efficiency improvements and energy savings potential will be documented. The percentage of drag difference between the baseline with no mirror and the different tested mirrors will be presented. (Freightliner)
- Pending Phase II approvals, fabricate prototype devices for modifying trailer side, trailer wake, and tractor-trailer gap characteristics established as having good potential in Phase I scale-model work for testing in full-scale vehicles to establish in-service fuel economy benefits using SAE Type II fuel economy test protocols. Develop potential partnerships with customers and trailer manufacturers to develop and test these full-scale devices. (International)
- Pending Phase II approvals, perform initial tuning tests on truck and trailer for SAE Type II testing. Install devices and systems to modify trailer aerodynamics, trailer gap enclosure characteristics, and trailer gap flow characteristics that were determined to be most promising in Phase I on trucks for back-to-back SAE Type II

fuel economy testing over a fixed test route. A truck with the aerodynamic aids will be tested at the same time as a similar baseline vehicle without aerodynamic aids. (Mack)

- Pending Phase II approvals, fabricate and install vehicle underside airflow management devices that were determined to be most promising in Phase I on trucks for back-to-back SAE Type II fuel economy testing over a fixed test route. Perform tuning tests for truck and trailer in preparation for SAE Type II fuel economy testing. A truck with the aerodynamic aids will be tested at the same time as a similar baseline vehicle without aerodynamic aids. (Volvo)

---

## Introduction

Class 8 heavy-duty trucks represent over three-quarters of the total diesel fuel used for trucks in the United States each year, transporting vital goods to destinations across the country. At highway speeds for these trucks, aerodynamic drag is a major part of total horsepower needs for driving the truck down the highway, and reductions in aerodynamic drag can yield measurable benefits in fuel economy with relatively inexpensive and simple devices. The goal of this project is to examine a number of aerodynamic drag devices and systems and determine their effectiveness in reducing aerodynamic drag of Class 8 tractor/semitrailer vehicles, thus contributing to the Department of Energy's (DOE's) goal of reducing petroleum use for transportation.

## Project Team

The project team represents virtually all of the key heavy truck manufacturers in the United States, along with the management and industry expertise of the Truck Manufacturers Association (TMA) as the lead investigative organization. The TMA is the national trade association representing the major North American manufacturers of Class 6–8 trucks (gross vehicle weight ratings [GVWRs] over 19,500 pounds [lbs]). Four major truck manufacturers are participating in this project with TMA: Freightliner, LLC; International Truck and Engine Corporation; Mack Trucks Inc.; and Volvo Trucks North America, Inc. Together, these manufacturers represent over three-quarters of total Class 8 truck sales in the United States. These four manufacturers are pursuing complementary research efforts that fit their individual corporate focus areas and strengths.

## Project Structure and Roles

The project work has been separated into two phases to be conducted over a period of two years. In Phase I, initial screening of aerodynamic devices and systems will be conducted to focus research and development attention on devices that offer the most potential. This screening will be done through full-size vehicle testing, scale model testing, and CFD analysis. In Phase II, the most promising devices will be installed on full-size trucks and their effect on fuel economy will be determined, either through on-road testing or full-size wind tunnel testing.

As noted above, the participating manufacturers are conducting complementary research and development of aerodynamic aids. In particular, Freightliner is working on outside mirrors; International is looking at tractor trailer gap, trailer side, and trailer wake effects on truck aerodynamics; Mack is examining trailer aerodynamics, trailer gap enclosure, and trailer gap flow control; and Volvo is working on vehicle underside design and management of tractor-trailer air flows. All of the manufacturers are working with devices and systems that offer practical solutions to reduce aerodynamic drag, accounting for functionality, durability, cost effectiveness, reliability, and maintainability.

A layout of the project team members and their roles and responsibilities is illustrated in Figure 1.

## Project Activities

Phase I activities of the four truck manufacturers are described in more detail below, organized by truck manufacturer.

*Freightliner:* Freightliner completed testing of a typical standard mirror system (aerodynamic-style mirrors) on a full-scale truck, establishing the effect of mirror systems on aerodynamic drag. These tests were performed on a full-size Freightliner Century Class S/T conventional Class 8 sleeper cab truck with a raised sleeper roof, one of Freightliner's most advanced current production truck designs. All tests

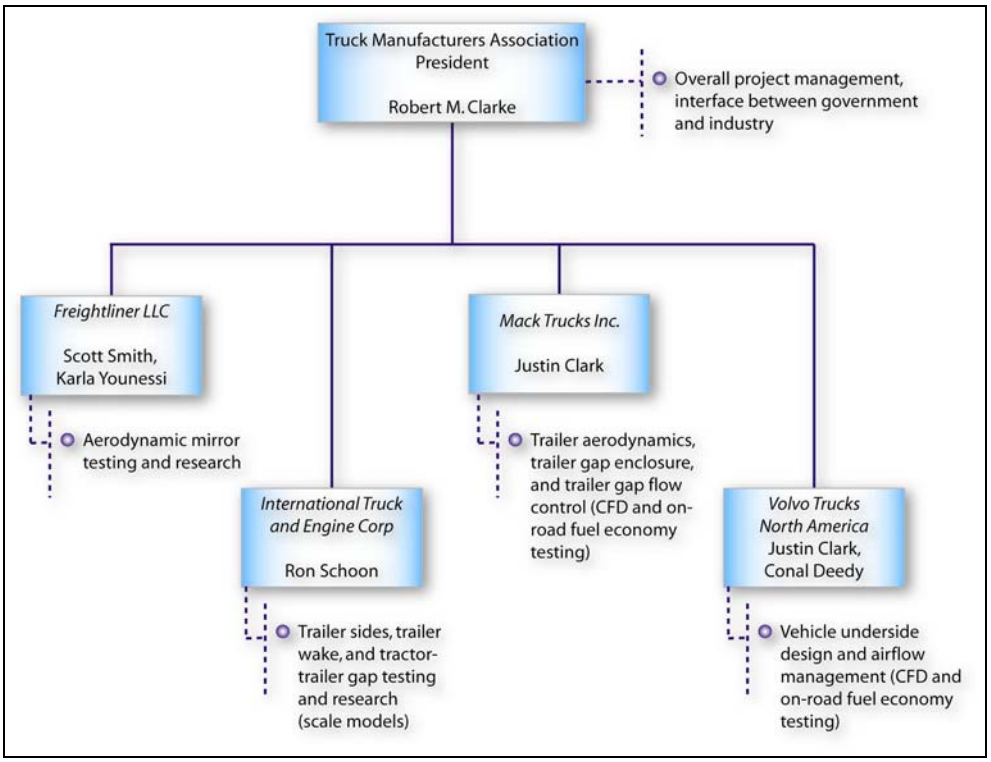


**Figure 1.** Project roles and responsibilities

were done in Freightliner's company wind tunnel located in Portland, Oregon. This tunnel has the capability of accommodating a full-size Class 8 truck in its 12,000 square foot facility. The Freightliner Wind Tunnel features a unique and efficient design that differs from those of traditional automotive and aviation wind tunnels. Standard building materials were used in innovative ways to build the structure. The power section is revolutionary as well, using ten industrial blower fans, all synchronized by computer, in place of what would typically be one large custom-designed and built fan. The fans have a combined 2,500 horsepower capability and process over 2.5 million cubic feet per minute (CFM) of air. This allows for test section wind speeds of over 65 miles per hour (mph). Figure 2 illustrates the test truck in the Freightliner wind tunnel, and Figure 3 shows some typical mirror configurations for Class 8 trucks.

Tests were also conducted on the Century S/T vehicle without any mirrors installed to determine a baseline aerodynamic drag of the truck itself. As a late addition to the project activities, Freightliner conducted testing to qualify the effect of mirror design on surface water management for mirror

**Figure 2.** Freightliner Class 8 truck being tested in Freightliner wind tunnel

surfaces to show how truck airflow affects mirror soiling.

The wind tunnel testing on the full-size vehicle is being correlated with CFD modeling using PowerFLOW® software with assistance from Exa Corporation (maker of the software). Results from typical CFD analysis runs of this type can be seen in Figure 4: this graphic is from previous Freightliner

**Figure 3.** West Coast-style mirror (left) and one type of aerodynamic mirror (right) on Freightliner trucks

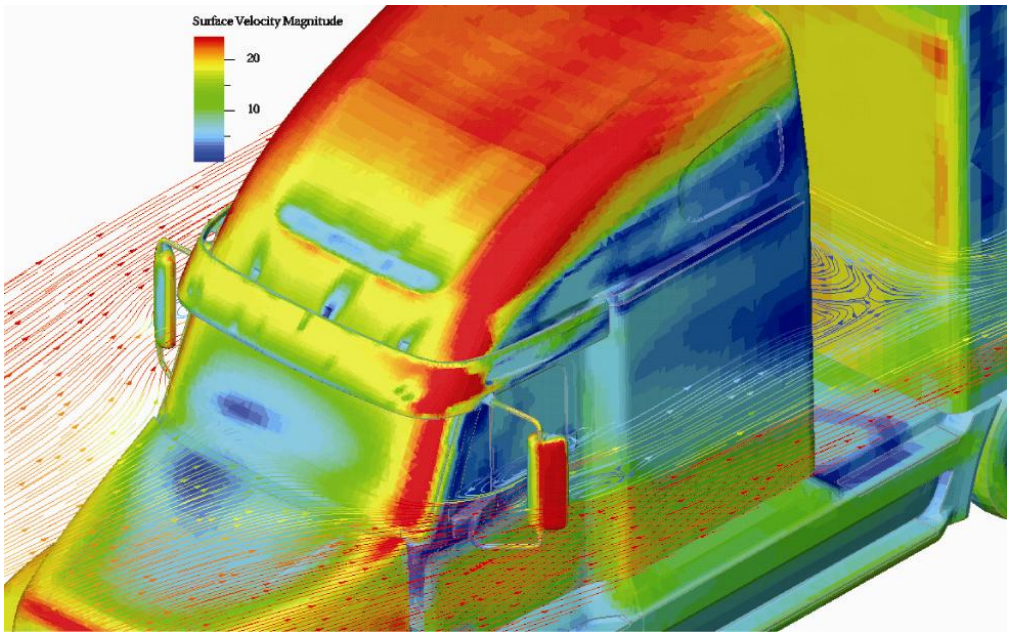


**Figure 4.** Previous Freightliner mirror simulations reviewed for current study

CFD work on a truck design similar to the Century Class truck. The correlation work consists of two components:

1. First, qualitative comparison of wind tunnel test results vs. CFD simulation for streamline patterns, surface pressures, and general flow behavior. CFD plots will be created with views of appropriate results data that can be compared to corresponding images captured during the wind tunnel tests.
2. Second, relative drag comparison for CFD vs. wind tunnel tests. The relative increase in overall drag for no mirror vs. with mirror will be compared for zero and +/−6° yaw cases.

Initial CFD simulations that have just been completed are for the two zero yaw cases; one with mirrors and one without mirrors. The remaining non-zero yaw cases are expected to be executed by December 2, 2005. Initial processed results and plots for the zero yaw cases are expected to be available by November 29, 2005.

*International:* International testing involves evaluation of modifications to trailer sides, trailer wake, and tractor-trailer gap through two rounds of one-eighth scale model wind tunnel testing. Wind tunnel testing for this portion of the project was conducted at Texas A&M University's wind tunnel facilities. The first round of scale model testing

quantified the effects of a number of vehicle modifications in order to select a subset of these for a second round of scale model testing. Testing of several additional vehicle modifications was also conducted in the second round: these additional modifications were the result of customer input on practical devices. All of International's Phase I work was conducted at the 1/8-scale model level in the wind tunnel, using a model of a commercially available International truck design.

In the Phase I testing, International has demonstrated aerodynamic drag reduction of up to 23% in wind tunnel testing using the 1/8 scale models. As Table 1 shows, an aerodynamic drag reduction of 20% or more has been demonstrated on multiple configurations, which provides options/choices for significant drag reduction with "practical" execution. In addition to overall drag reduction of combinations of technologies, International has also categorized a range of aerodynamic drag reduction opportunities for individual concepts in each area of focus (see Table 2). For demonstration of these aerodynamic concepts in real-world testing, International has signed non-disclosure agreements with one customer and two trailer manufacturers, and is negotiating partnerships for the Phase II efforts, which International expects to result in Phase II partners by January 2006.

International has obtained internal funding approval for Phase II efforts, and work is beginning on potential Phase II designs, focusing on innovative, practical executions of the best designs determined through Phase I efforts. International plans full-scale road testing, likely using SAE Type II fuel economy protocols; this could begin as soon as April 2006 depending on funding.

**Table 1.** Phase I Significant Results (International Truck) – Select Combination Performance

| | **Combinations** | | | | | |
|---|---|---|---|---|---|---|
| | **Tractor Trailer Gap** | | | **Trailer Side** | | **Trailer Wake** |
| **% $C_D$ Improvement (+)** | **Side Ext. Length** | **Nose Cone** | **Plates** | **Skirts** | **Belly Box** | **Plates** |
| +23 | ● | | | ● | | ● |
| +21 | | ● | | ● | | ● |
| +17 | | | | ● | | ● |
| +21 | | | | ● | ● | ● |

**Table 2.** Phase I Significant Results (International Truck) – Individual Concept Performance

| **% $C_D$ Improvement (+)** | | |
|---|---|---|
| **Low** | **High** | **Tractor Trailer Gap** |
| 0 | 3.5 | Side Extender Length |
| -0.5 | 3 | Trailer Nose Cone |
| 0 | 1 | Vertical Plates |
| **% $C_D$ Improvement (+)** | | |
| **Low** | **High** | **Trailer Side** |
| 3 | 7.5 | Skirt Shape |
| 5* | 9.5* | Skirt Height* |
| -- | 5.5 | Belly Box |
| **% $C_D$ Improvement (+)** | | |
| **Low** | **High** | **Trailer Wake** |
| 1 | 9 | Flat Plate: Angle & Length |
| 6.5 | 8 | Curved Plate |

* Range is shape-dependent

*Mack:* Mack is conducting its Phase I tests through a combination of CFD analysis for aerodynamic aids and on-road baseline fuel economy testing of a conventional truck to establish current levels of performance. The truck chosen by Mack for testing is the commercially available Vision CX Class 8 tractor with a "mid-rise" (mid-height) sleeper cab (see Figure 5). In Phase I, Mack employed CFD analysis of the effect of trailer aerodynamics, trailer gap enclosure, and trailer gap flow control on truck aerodynamics through use of StarCD CFD software. Mack used the expertise of the StarCD software team to perform these analyses using configuration data files provided by Mack. Several aerodynamic aids (vortex generators, trailer boat-tails, etc.) were analyzed through CFD work for selecting promising technologies for further full-size vehicle testing. Results of these CFD analyses were to be completed in early December 2005. In addition, Mack planned to supplement this CFD work through consultation with several experts in the field of trailer aerodynamics during December 2005. Mack also acquired a trailer to use in initial full-size vehicle fuel economy tuning testing (using SAE Type II test protocols) of the truck and trailer combination (see Figure 6). The trailer (a standard box trailer) is equipped with a boat tail and side skirts, as illustrated in the figure. Fuel economy data will be collected over a fixed route near Mack/Volvo testing facilities in Greensboro, North Carolina.

**Figure 5.** Mack Vision CX tractor

*Volvo:* Volvo is also conducting its Phase I tests through a combination of computational fluid dynamics analysis for aerodynamic aids and on-road baseline fuel economy testing of a conventional truck to establish current levels of performance. They conducted computational fluid dynamics analysis of the effect of vehicle underside design and airflow management on truck aerodynamics. Preliminary results of this testing predicts that 16% of the complete vehicle drag is produced on the underside of the tractor and 19% is a result of the trailer underside. Therefore, roughly 35% of the total vehicle drag is associated with the complete vehicle underside, as illustrated in Figure 7.

Volvo also developed aerodynamic modifications to be considered for further testing and estimated their potential benefits. The analysis performed to date indicates that drag reductions of up to 11% may be possible with optimization of vehicle underside

**Figure 6.** Box trailer with aerodynamic enhancements to be used in Mack tests

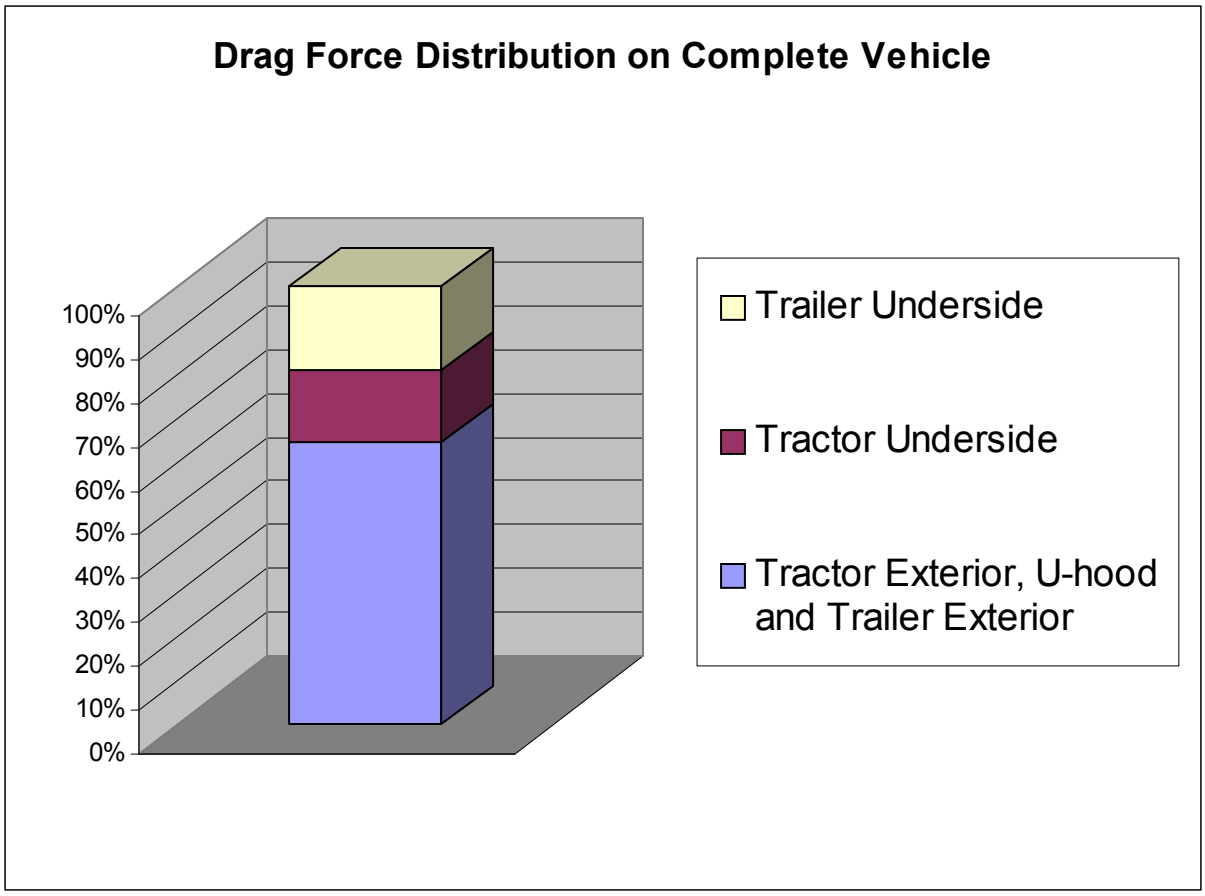


**Figure 7.** Preliminary analysis from Volvo on drag force distribution on complete vehicle

design combined with trailer gap manipulation and improvements to trailer bogie design. These results are summarized in Table 3 and Figure 8. Note that more analysis will be performed through CFD to confirm the results of drag reductions of the Concept 2 Gen 2 designs shown in the Table 3 and Figure 8. The Volvo team will also be performing SAE Type II fuel economy testing over a fixed loop near Mack/Volvo testing facilities in Greensboro, North Carolina.

**Summary**

Highlights of the progress during FY 2005 are as follows:

1. Phase I wind tunnel testing completed by September 9, 2005 as planned. (baseline wind tunnel run with standard mirror; wind tunnel run without mirror; and water management wind tunnel run to study the effects of water accumulation). (Freightliner)
2. CFD analysis is in process and due to be completed by December 1, 2005. (Freightliner)
3. Phase I scale model testing of individual aerodynamic aids and combination of aids completed. Up to 23% improvement in aerodynamic drag was demonstrated. (International)
4. Conducted CFD analysis on trailer aerodynamics and aerodynamic enhancements, and procured a trailer with aerodynamic enhancements for on-road testing. (Mack)
5. Established that approximately 35% of total vehicle drag is associated with complete vehicle underside. Performed CFD analysis on vehicle underside design changes, trailer gap manipulations, and trailer axle design to determine potential effects of these changes on overall drag: estimated drag reductions of up to 11% could potentially be achieved (to be confirmed through further analysis). (Volvo)

**Table 3.** Preliminary Results of Volvo Analysis of Potential Geometry Changes to Vehicle Underside and Trailer Gap

| Analyzed or Measured Vehicle Configuration | Change in Drag (%) vs. Baseline |
|---|---|
| Baseline | 0 |
| Baseline with underside geometry Concept 1 | +0.5% |
| Baseline with underside geometry – Concept 2 — Gen 1 | -2.0% |
| Baseline with underside geometry Concept 2 — Gen 1 and trailer gap manipulation | -4.8% |
| Baseline with optimized underside (Concept 2 — Gen 2) and trailer gap manipulation | -6.0% ** |
| Baseline with optimized underside (Concept 2 — Gen 2), trailer gap manipulation and trailer bogie improvements | -11.0% ** |
| Incremental effect of external trailer gap devices — adjustable roof extender and optimized side deflector extensions | -2.5% |

** Results to be confirmed through further analysis

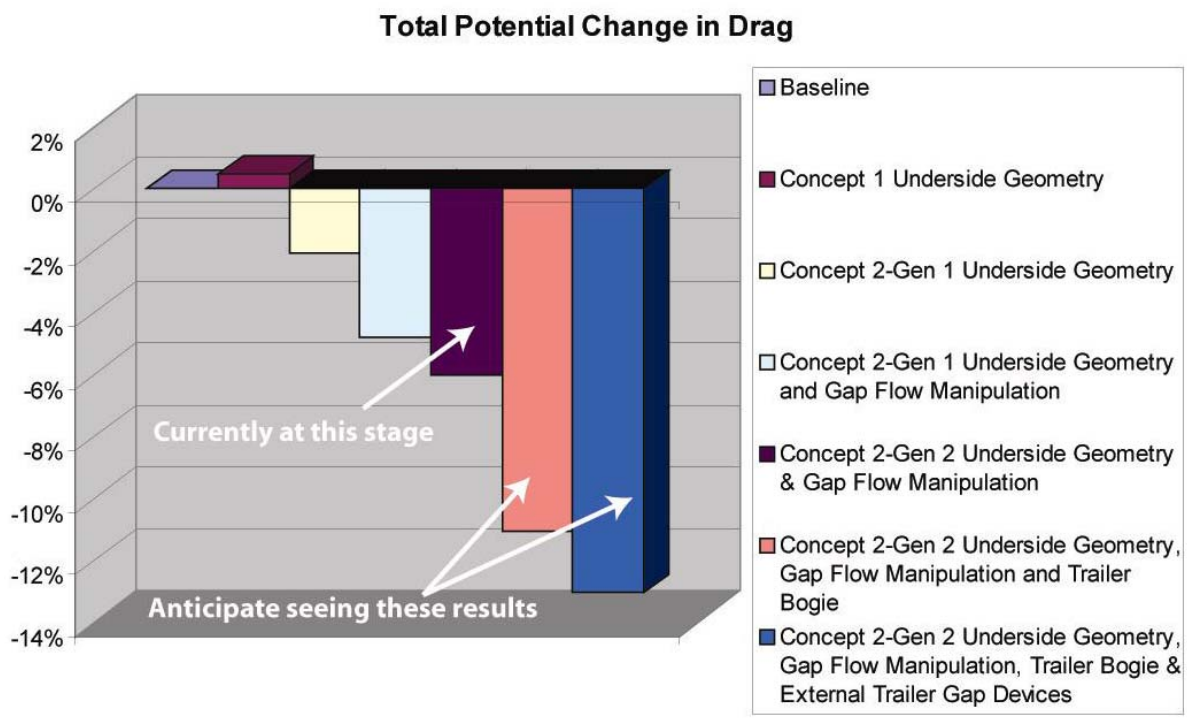


**Figure 8.** Preliminary and projected results from CFD analysis of Volvo truck with vehicle underside and gap flow modifications

## Conclusions

*Freightliner:* The following results are gathered from wind tunnel testing alone as the final CFD analysis is currently in process. (1) Freightliner's current "aerodynamic" mirror contributes approximately 4.5% to total tractor-trailer drag of a Century Class vehicle combination. (2) This increment can degrade fuel economy by as much as 2% for over-the-road applications. (3) Evaluation of streamlines indicates a sizeable wake structure behind the mirror. (4) Soiling studies reveal that water entrained in this wake structure is deposited on the mirror surface.

*International:* An aerodynamic drag reduction of 20% or more has been demonstrated on multiple configurations of trailer gap, trailer side, and trailer wake modifications, which provides options/choices for significant drag reduction with "practical" execution. A maximum drag reduction of 23% was seen in the initial scale model testing. Individual components for trailer gap, trailer side, and trailer wake modification can provide aerodynamic drag reductions of anywhere from zero to just over 9%.

*Mack:* CFD analysis on trailer modifications is nearly complete. A trailer has been procured for on-road vehicle testing, and is currently equipped with a boat tail and side skirts as aerodynamic enhancements.

*Volvo:* Preliminary CFD work has been performed on the distribution of drag between the trailer underside, the tractor underside, and the rest of the truck/trailer body: approximately 35% of total vehicle drag is associated with the vehicle underside (tractor and trailer). Based on this work, Volvo estimates that improvements to vehicle underside design and manipulation of trailer gap combined with trailer axle design optimization can offer drag reductions of up to 11% (to be confirmed through further analysis).

## Publications

At this stage, the project team has not published any technical papers on its work. A combined Phase I technical report will be provided to the Department of Energy detailing the work done in this phase. Plans are to potentially offer technical papers at the 2006 SAE Commercial Vehicle Engineering Congress and Exhibition in Chicago, Illinois, if Phase II work proceeds to completion by that time (November 2006).

# II. THERMAL MANAGEMENT

## II.A. Cooling Fan and System Performance and Efficiency Improvements

*Principal Investigator: R.L. Dupree*
*Caterpillar, Incorporated*
*Technical Center, Building E*
*P. O. Box 1875, Peoria, Illinois 61654*
*(309) 578-0145, fax: (309) 578-4277, e-mail:* dupree_ron_l@cat.com

*Investigator: Dr. John F. Foss, Professor*
*Michigan State University*
*A118 Research Complex-Engineering*
*East Lansing, Michigan 48824*
*(517) 355-3337, fax (517) 353-7179, e-mail: Foss@egr.msu.edu*

*Technology Development Managers: Sid Diamond and Lee Slezak*
*(202) 586-2335, e-mail: Lee.Slezak@hq.doe.gov*

*Participants*
*Mike Dusel, Michigan State University*
*Kyle Bade, Michigan State University*
*Brandon Dykstra, Caterpillar Inc.*

---

*Contractor: Caterpillar, Inc*
*Contract No.: DE-FC04-2002AL68081*

---

### Objective

- Develop cooling system fans and fan systems that will allow off-highway machines to meet Tier 3 emissions regulations, and reduce spectator sound levels with improved fuel efficiency and within the functional constraints of machine size.

### Approach

- Task 1 is to develop a large, high performance axial fan.
- Task 2 is to develop an active fan shroud for use with large axial fans.
- Task 3 is to develop fan modeling techniques to improve the ability to predict fan performance and component airflows in cooling systems with side by side heat exchangers.
- Task 4 is to demonstrate the performance of a lab-developed swept blade, mixed flow fan in an off-road machine.
- Task 5 is to develop a high-efficiency continuously variable speed fan drive for use in high-horsepower fan systems.
- Task 6 is to develop cooling system air filtration concepts that can allow more dense (higher performance) heat exchangers to be used in off-road machines.

## Accomplishments

- Task 1 — The initial plan was to use Genetic Algorithms to do an automated fan design, incorporating forward sweep for low noise. When first- and second-generation concepts could not meet either performance or sound goals, an experienced turbomachinery designer, using a specialized computational fluid dynamics (CFD) analysis program, took over the design. At the end of the contract, we have been able to demonstrate a 5% flow improvement (vs 10% goal) and 10% efficiency improvement (vs 10% goal) using blade twist only.
- Task 2 — Performance testing at Michigan State University showed the design is capable of meeting performance goals relative to flow, but over a very narrow operating range of fan performance. The shroud had an effect of reducing noise at constant flow by 0 to 2 decibels (dB).
- Task 3 — A CFD fan system modeling guide has been completed. Current, uncontrolled modeling practices produce flow estimates in some cases within 5% of measured values, and in some cases within 25% of measured values. The techniques in the modeling guide reduced variability to + 5% for the case under study.
- Task 4 — Task was completed in 2003. Fan was not able to meet performance goals due to significant performance loss when it was installed close to the front of the engine.
- Task 5 — Task was terminated in 2003 during a performance review. Dual ratio clutch is not able to meet efficiency goals, and alternative continuously variable transmission (CVT) concepts will not fit within the space allowed.
- Task 6 — Initial sensitivity testing demonstrated that fan speed has a significant impact on the fouling of radiator cores due to fine dusts, so machines equipped with continuously variable speed fan drives would be expected to have more radiator debris fouling problems than a machine with a constant speed fan. Filtration concepts looked at a wide range of filtration technologies, but the combination of pressure drop constraints and the small size of the debris to be filtered made this a futile exercise. The most successful technologies evaluated all incorporate some way to increase the Reynolds number inside the heat exchanger air flow path. A form of an "air knife" concept has emerged as the most promising technology to pursue.

## Future Direction

- This contract was completed on July 31, 2005. Final documentation is in progress.

---

## Introduction

The original development of the Aeroshroud was motivated by the relatively large tip clearance of cooling fans in light and medium duty trucks. The large tip clearance is necessary because of the large relative motions between the engine mounted cooling fan and the chassis mounted shroud and radiator (Morris 1997). Morris was the first to investigate the efficacy of the aerodynamic shroud on an automotive cooling fan with a diameter of 457 mm and a tip clearance of 25 mm. Integral flow measurements such as fan input power and volume flow rate were acquired in addition detailed velocity measurements in the wake of the fan. These data demonstrated that the aerodynamic shroud increased performance at higher flow rates but decreased performance at lower flow rates. Because of this result, it was concluded that system resistance, characterized by the fan grill, radiator, and air-conditioning condenser in an automobile, plays an important role in determining the efficiency of the aerodynamic shroud and fan combination. In particular, a large system resistance lessens the efficiency and a smaller system resistance allows the aerodynamic shroud to increase the efficiency of the fan. Furthermore, qualitative observations using a tuft in the wake of the fan showed that the high momentum annular jet changed the reverse flow in the tip clearance area to a positive axial flow providing an additional contribution to the net flow rate through the fan.

In the original investigation by Morris (1997), the cooling fan was partially immersed in the shroud. In

particular, the shroud covered only the upper portion of the fan blades and had a sharp edge outlet. The partially shrouded configuration allowed the fan to produce static pressures even throughout the stall range, which is characterized by strong radial flow. However, when the aerodynamic shroud was used, it forced the flow in an axial direction explaining the decrease in performance at the lower flow rates. In a later study (Morris and Foss 2001), the authors used a rounded outlet that accommodated this radial flow and found that the enhanced performance of the fan with the aerodynamic shroud was extended into even lower flow rates.

The object of this task was to incorporate the Aeroshroud principle into a rounded inlet/rounded outlet shroud with tight tip clearance to improve fan airflow. In addition, the effects of the Aeroshroud concept on fan noise would be documented as well.

## Experimental Procedure

Fan performance data was acquired at Michigan State University (MSU) as described in Morris et al. 1997. This involves mounting the fan and shroud in a fan performance test plenum, and evaluating the performance using ANSI/AMCA Standard 210-99, "Laboratory Methods Of Testing Fans for Aerodynamic Performance Rating," using Figure 11 'Outlet Chamber Setup-Nozzle on End of Chamber.' Fan sound data was acquired by constructing a mockup cooling system with variable restriction, then testing using the methods outlined in European Union Directive 2000/14/EC to measure the fan sound power. This work was fully documented in Dusel 2005.

## Results and Discussion

The shroud, on the left side of Figure 1, is a pressure vessel that contains air pressurized by an external source. The air escapes via a Jet Gap that extends 360 degrees around the shroud. The escaping air remains attached to the surface of the shroud due to the Coanda effect, to provide the performance benefits of the shroud. The shroud built for this evaluation used a rounded inlet/rounded outlet as shown in Figure 2.

There was a concern about the interaction of the fan and shroud, so a fan was chosen that would most

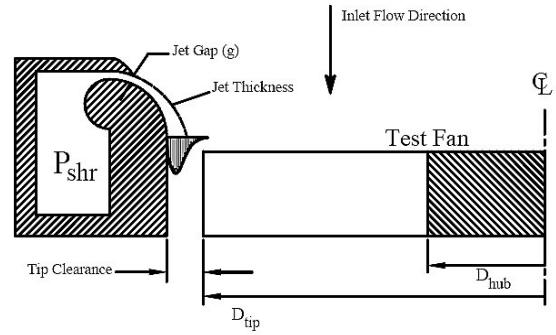


**Figure 1.** Aeroshroud as designed by Foss

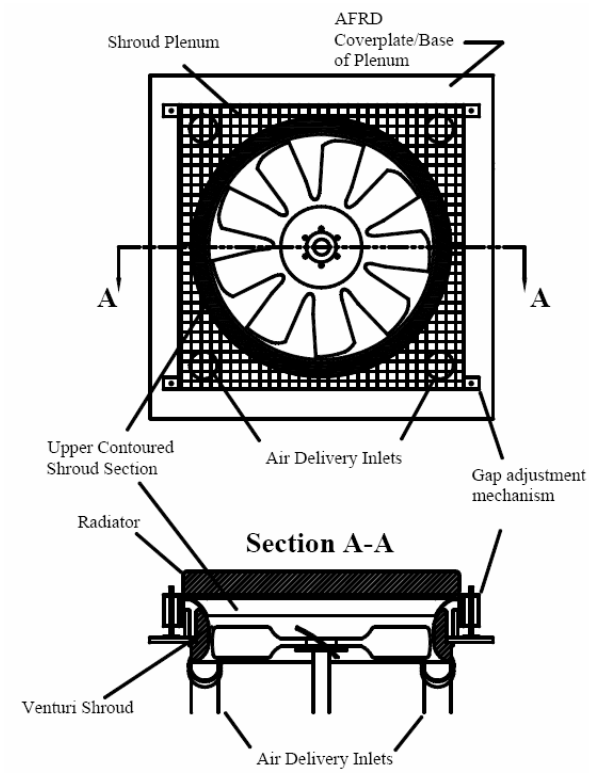


**Figure 2.** Aeroshroud as tested

nearly represent a potential high performance axial fan that might be designed as part of Task 1.

Figure 3 shows the change of the performance of the fan as a function of flow through the aeroshroud, where fl represents the flow through the shroud (as indicated by internal shroud pressure. Higher pressure means higher shroud air flow). Ds of 1.5 to 1.8 represents the range of system restriction of interest for this project.

These results show that the amount of shroud air flow can significantly change the stall point of the

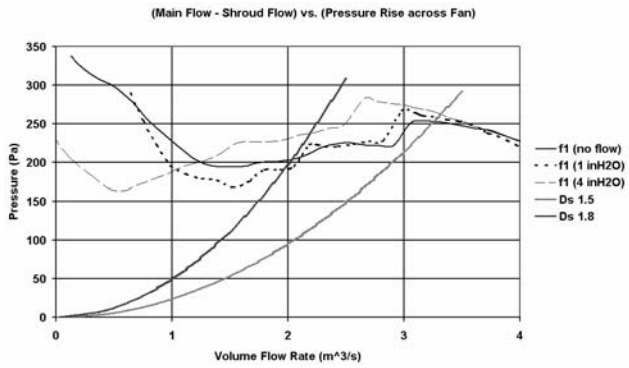


**Figure 3.** Effect of shroud flow on fan performance

fan, but has no effect on the performance of the fan in the axial region. To compare with earlier Michigan State University claims, we were able to demonstrate significant fan performance benefits in low flow conditions, but saw no performance benefits in high air flow conditions.

At this point, we had demonstrated that the aeroshroud could dramatically change the fan stall point and provide higher flows at operating points where the fan would traditionally be in stall, but we could not affect fan performance in the higher flow lower restriction region of fan performance, and the aeroshroud was providing no system efficiency benefits. Instead of proceeding to a field test of the system, the lab testing was continued with two different fans to study the fan/shroud interaction to determine if there was a better fan to use with the aeroshroud concept.

To ensure that the performance of the aeroshroud was not a fluke due to the chosen prototype fan, two sheet metal fans were provided for evaluation. Fan 2 was a low chord angle design, while Fan 3 was a high chord angle design, to explore the potential range of conventional fans that might be available for use with the aeroshroud. The effect of the aeroshroud on fan performance was similar to that seen in the initial testing.

Michigan State University does not have noise measurement capabilities at its facility, so the aeroshroud system was delivered to Caterpillar for noise evaluation. The aeroshroud was mounted on a cooling system mockup for evaluation. The mockup consisted of a radiator core, along with a varying number of perforated metal screens mounted in front of the fan. By varying the porosity, and number of screens we could change the restriction to place the fan in the axial, or radial flow region of the fan performance curve.

Figure 4 shows typical fan noise data, as measured with Fan 3 operating at 950 revolutions per minute (rpm):

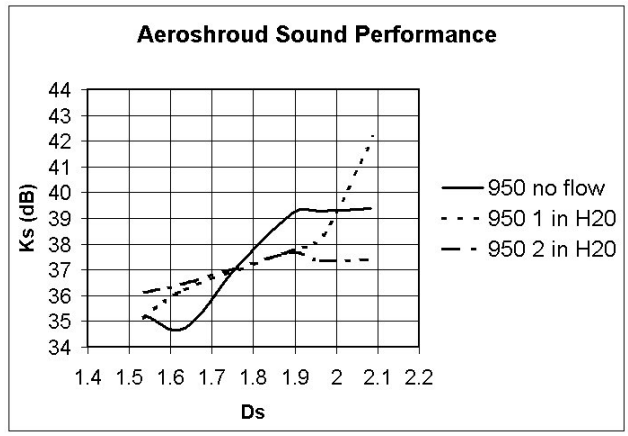


**Figure 4.** Effect of aeroshroud on fan noise

Specific noise is a relationship between the theoretical noise level of the fan based on its pressure and flow, compared with the actual noise level measured. The lower the specific noise, the quieter the fan. The blower system for the aeroshroud was located outside of the hemi anechoic test chamber to minimize its effect on fan noise. The aeroshroud has a similar effect on noise that it has on fan performance. In the fan stall region, the aeroshroud can provide significant fan noise level reductions, in addition to the flow gains, while in the axial flow region, the aeroshroud may actually increase fan noise levels over a similar shroud design without air injection. These comments on fan noise effects do not account for any potential noise contribution from the fan or other means of providing the secondary airflow.

## Summary

These are the highlights of the progress on this task during FY 2005:

1. An aeroshroud can significantly affect the stall point of a fan/shroud combination.

2. The magnitude of the effect of the aeroshroud on fan performance is a strong function of the secondary airflow provided to the shroud.
3. At the same time that airflow is increased in the stall region, noise (at constant airflow) is reduced by use of the aeroshroud.
4. The aeroshroud does not affect fan performance in the axial region.
5. The aeroshroud may increase fan noise levels (at constant flow) in the axial flow region.

## Conclusions

The conclusions from this work are that regardless of fan tested the aeroshroud had a significant effect on the performance in the stall region, but virtually no effect on the fan performance in the axial flow region. This narrow region of performance improvement, combined with the lack of effect on system efficiency in the axial flow range limit the usefulness of the aeroshroud for general off-road machine applications.

## References

Dusel, M.D., "An Experimental Investigation of the Aerodynamic Shroud with an Off-Highway Engine Cooling Fan," Masters thesis, Michigan State University, 2005.

Morris, S.C., "Experimental Investigation of an Aerodynamic Shroud for Cooling Fan Applications," Masters thesis, Department of Mechanical Engineering, Michigan State University, East Lansing, Michigan, 1997.

Morris, S.C., J.F. Foss, and J.E. Pakkala, "Automotive Cooling Fan Research and Development Facility," SAE Paper 971784, 1997.

Morris, S.C. and J.F. Foss, "An Aerodynamic Shroud for Automotive Cooling Fans," *ASME J. Fluids Eng.*, 123:287–292, 2001.

# II.B. Efficient Cooling in Engines with Nucleate Boiling

*Principal Investigator: J.R. Hull*
*Argonne National Laboratory*
*9700 South Cass Avenue, Building 335, Argonne, IL 60439*
*(630) 252-8580, fax: (630) 252-5568, e-mail: jhull@anl.gov*

*Technology Development Managers: Sid Diamond and Lee Slezak*
*(202) 586-2335, e-mail: Lee.Slezak@hq.doe.gov*
*Technical Program Manager: Jules Routbort*
*(630) 252-5065, e-mail: routbort@anl.gov*

---

*Contractor: Argonne National Laboratory*
*Contract No.: W-31-109-ENG-38*

---

## Objectives

- Investigate potential of two-phase flow in engine cooling applications.
- Determine limits on two-phase heat transfer (occurrence of critical heat flux or flow instability).

## Approach

- Experimentally determine heat transfer rates and critical heat fluxes in small channels with water and 50% ethylene glycol in water mixture.
- Perform experiments over a concentration range of ethylene glycol in water.
- Perform experiments with alternative fluids.

## Accomplishments

- Completed experimental tests and data analysis for the two-phase pressure gradients and boiling heat transfer coefficients of horizontal flows to water and ethylene glycol/water mixtures.
- Developed a pressure drop correlation modified from the Chisholm's correlation with a concentration factor to better predict pressure drops for ethylene glycol/water mixtures.
- Developed a general correlation of boiling heat transfer coefficients modified from the Argonne's boiling heat transfer correlation with a concentration factor for the prediction of boiling heat transfer rates of flow boiling in small channels including refrigerants, water, and ethylene glycol/water mixtures.
- Fabricated a new vertical experimental test section, calibrated the instruments attached to the test section, modified the test facility and test monitoring program for vertical flow boiling tests.

## Future Directions

- Perform systematical single-phase and two-phase heat transfer experiments of water and ethylene glycol/water mixtures with vertical flows to provide essential information for nucleate-boiling cooling system design.
- Study the impact of vertical vs horizontal flows on two-phase heat transfer.
- Perform systematic experiments with alternative fluids.

---

## Introduction

Analyses of trends in the motor vehicle development sector indicate that future engine cooling systems will have to cope with greater heat loads because of more powerful engines, more air conditioning, more stringent emissions requirements, and additional auxiliary equipment. Moreover, there is considerable interest in reducing the size of the cooling systems to obtain a better aerodynamic profile. To meet these conditions, it is necessary to design cooling systems that occupy less space, are lightweight, have reduced fluid inventory, and exhibit improved performance. Among various new cooling systems proposed by researchers, the nucleate-boiling cooling system has high potential to meet these challenges. Order-of-magnitude higher heat transfer rates can be achieved in nucleate-boiling cooling systems when compared with conventional, single-phase, forced-convective cooling systems. However, successful design and application of nucleate-boiling cooling systems for engine applications requires that the critical heat flux and flow instability not be reached. Therefore, a fundamental understanding of flow boiling mechanisms under engine application conditions is required to develop reliable and effective nucleate-boiling cooling systems.

Cooling engine areas such as the head region often contain small metal masses that lead to small coolant channels. This geometry, in turn, leads to low mass flow rates in order to minimize pressure drop. Although significant research has been performed on boiling heat transfer and the critical heat flux phenomenon, results on the conditions necessary for engine cooling systems are limited. It is the purpose of the present study to experimentally investigate the characteristics of coolant boiling, critical heat flux, and flow instability under conditions of small channel and low mass flux.

The test apparatus used in this investigation was designed and fabricated to study boiling heat transfer, critical heat flux, and flow instability of flowing water, ethylene glycol, and aqueous mixtures of ethylene glycol at high temperatures (up to 250°Celsius [C]) and low pressure (<345 Kilopascal [kPa]). Figure 1 shows a schematic of the apparatus. It is a closed-loop system that includes two serially arranged pumps with variable speed drives, a set of flowmeters, an accumulator, a preheater, a test section, and a condenser. The flowmeter set, including various types and sizes, was chosen to cover a large range of flow rates and was calibrated with a weighing-with-stop-watch technique. The estimated uncertainty in

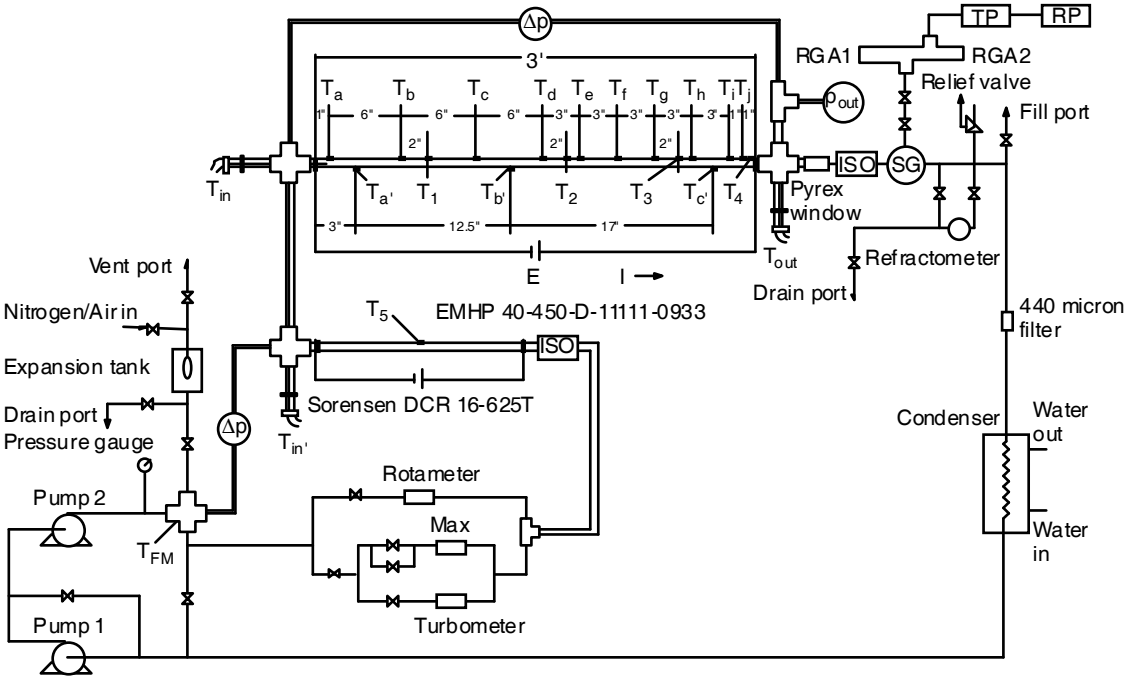


**Figure 1.** Schematic diagram of nucleate-boiling cooling test apparatus

the measurements of flow rates was ±3%. The bladder-type accumulator allows for stable control of the system pressure. The preheater provides a means to set the inlet temperature of the test section at various desired levels. Both the preheater and test section were resistance-heated with controllable direct current (DC) power supplies. Provisions were made to measure temperatures along the test section for calculating heat transfer coefficients. The pressures and temperatures at the inlet and outlet of the test section were also measured. Pressure transducers and thermocouples were calibrated against known standards. The estimated uncertainty in the measurements of pressures and temperatures were ±3% and ±0.2°C, respectively. As a safety precaution, both the preheater and test section were provided with high-temperature limit interlocks to prevent them from overheating. After leaving the test section, the two-phase flow was condensed into a single-phase flow, which returned to the pumps to close the system.

A data acquisition system consisting of a computer and a Hewlett-Packard multiplexer was assembled to record outputs from all sensors. A data acquisition program, which includes all calibration equations and conversions to desired engineering units, was written. The data acquisition system provides not only an on-screen display of analog signals from all sensors and graphs of representative in-stream and wall-temperature measurements but also a means of recording temperature measurements and pertinent information such as input power, mass flux, outlet pressure, pressure drop across the test section, and outlet quality for further data reduction.

## Results and Discussion

Both experimental tests and data analysis for two-phase boiling heat transfer of horizontal flows to water and ethylene glycol/water mixtures have been completed. The main results are reported below.

### Boiling Curve

Figure 2 shows the heat flux as a function of wall superheat for boiling of water and ethylene glycol/water mixtures in small channels. As can be seen from Figure 2, generally, the saturation boiling in small channels can be divided into three regions, namely convection-dominant-boiling region, nucleation-dominant-boiling region, and transition-boiling region. Both convective heat transfer and boiling heat transfer exist in all three regions, but their proportions are different in these three regions. In the convection-dominant-boiling region, the wall superheat is low, usually less than a few degrees centigrade. Although there is boiling heat transfer, the dominant mechanism is convective heat transfer. As a result, the mass quality and heat transfer rate are quite low comparing with those in the other two regions. In the nucleation-dominant-boiling region, the wall superheat is higher than that in the convection-dominant-boiling region but lower than certain upper limits that depend on mass flux. Opposite to the convection-dominant-boiling, the boiling heat transfer in the nucleation-dominant boiling is so developed that it becomes dominant and the heat transfer rate is much higher than that in convection-dominant boiling. As can be seen from Figure 2, the heat flux in this region is independent of mass flux and can be predicted with a power-law function of wall superheat. This characteristic was used in correlating the heat transfer data. In the transition-boiling region, the wall superheat is relatively high. The heat flux in this region is also high and close to the critical heat flux. The boiling in this region is unstable and a small change in the heat flux will result in a big change in wall superheat. If the heat flux increases further, it is possible for the system to reach the critical point producing an undesirably large jump in the wall superheat.

The above discussion shows that the nucleation-dominant boiling is desired in engineering applications for both high heat transfer rate and stable flow boiling without reaching the critical point.

### Two-Phase Pressure Drop

The concept of two-phase multipliers proposed by Lockhart and Martinelli and the correlation of those multipliers by Chisholm was used to compare with the present experimental data. As can be seen from Figure 3, the experimental data are in reasonable agreement with the Chisholm predictions both in

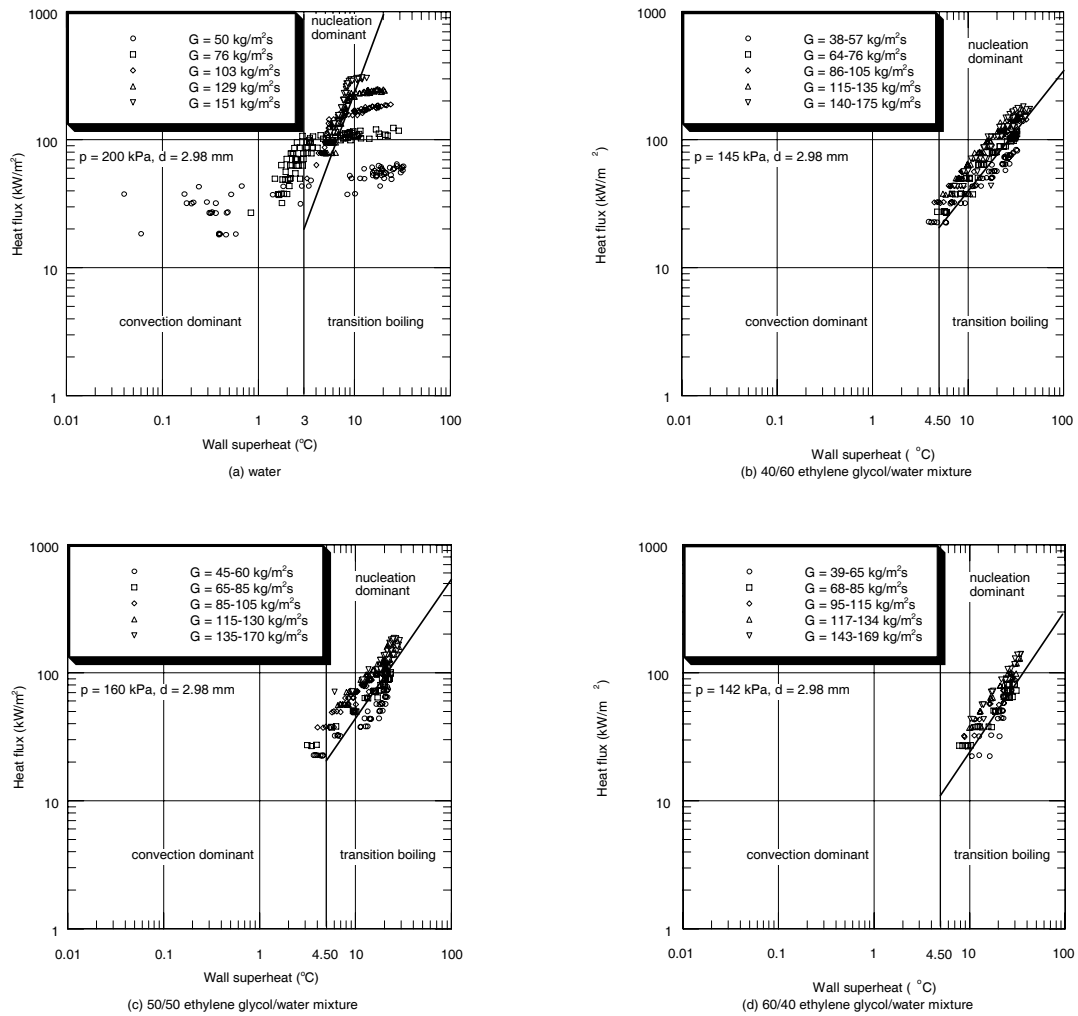


**Figure 2.** Heat flux as a function of wall superheat

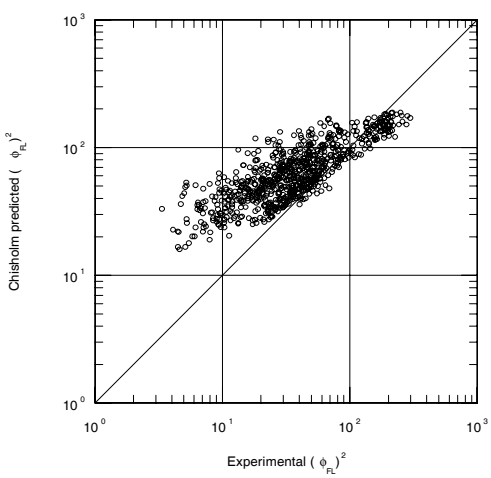


**Figure 3.** Two-phase frictional pressure gradient

values and trends, although the Chisholm correlation slightly overpredicts the experimental data.

To better predict the experimental data and to take the concentration factor into account, the constant parameter $C = 12$ in Chisholm's correlation was modified into a function of the volume concentration $v$ of ethylene glycol/water mixtures and Chisholm's correlation becomes

$$\phi_{FL}^2 = 1 + \frac{12[1 - 2.8v(1-v)]}{X} + \frac{1}{X^2}$$

This correlation has a feature that it reduces to Chisholm's correlation for both pure water ($v = 0$) and pure ethylene glycol ($v = 1$). In Figure 4, the

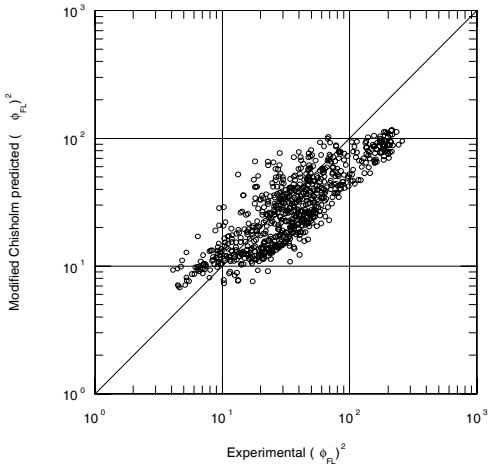


**Figure 4.** Two-phase frictional pressure gradient

experimental data is compared with the predictions of the modified Chisholm's correlation. This modification improves the predictions both in values and trends.

## Heat Transfer Coefficient

In the present study, the nucleation-dominant boiling data have the following characteristics.

(a) Although both convective heat transfer and nucleate boiling heat transfer exist, the dominant heat transfer mechanism is nucleate boiling. Since nucleate boiling heat transfer rate is much higher than convective heat transfer, the latter can be neglected.

(b) As shown in Figure 2, the boiling heat transfer is dependent on heat flux but almost independent of mass flux, which means that, for a certain fluid, the boiling heat transfer coefficient can be expressed as a function of heat flux.

(c) The heat transfer coefficients have different dependence on heat flux for different fluids. Therefore, to get a general correlation for boiling heat transfer coefficients, it is necessary to include fluid properties in the correlation.

(d) Argonne researchers employed the dimensionless parameter combination form of Boiling number, Weber number, and liquid-to-vapor density ratio in developing different predicted correlations for boiling heat transfer coefficients to different fluids, and the predicted results are quite good.

Based on the above facts, we extended the property term to including liquid-to-vapor viscosity ratio and were able to correlate boiling heat transfer data for water, 50/50 ethylene glycol/water mixture, refrigerant 12, and refrigerant 134a.

$$h = 135000(BoWe_l^{0.5})^{0.5}\left[(\rho_l/\rho_v)^{-0.5}(\mu_l/\mu_v)^{0.7}\right]^{-1.5}$$

In the above equation, the Boiling number $Bo$ and the Weber number $We_l$ are defined respectively by $Bo = q''/(Gi_{fg})$ and $We_l = G^2 D/(\rho_l \sigma)$, where $\rho$ is the density, $\mu$ is the viscosity, $G$ is the mass flux, $D$ is the diameter, and $\sigma$ is the surface tension. For this equation to be used for the predictions of experimental data of ethylene glycol/water mixtures with concentrations other than 50/50, we further modified the above correlation with a concentration correction factor, which reduces to 1 for concentrations $v = 0$ and $v = 0.5$. The new correlation can be expressed as

$$h/h^* = [1 + 6v(v - 0.5)](BoWe_l^{0.5})^{0.5}\left[(\rho_l/\rho_v)^{-0.5}(\mu_l/\mu_v)^{0.7}\right]^{-1.5}$$

where $h^*$ is a characteristic heat transfer coefficient of 135 kW/m$^2$K above all of the data.

Figure 5 shows the experimental data and the predicted values obtained with the correlation for all fluids. The predictions of the equation are in good agreement with the experimental data, and most of the predictions are within ±30% of the experimental data. It should be noted that the comparisons are only for the data within the nucleation-dominant-boiling region. The success of the correlation in predicting the heat transfer coefficients of all fluids boiling in small channels is directly related to the trend, as presented in Figure 2, that the heat transfer data are heat flux but not mass flux dependent. The fact that the equation is also heat-flux- but not mass-flux-dependent is in accordance with the experimental data.

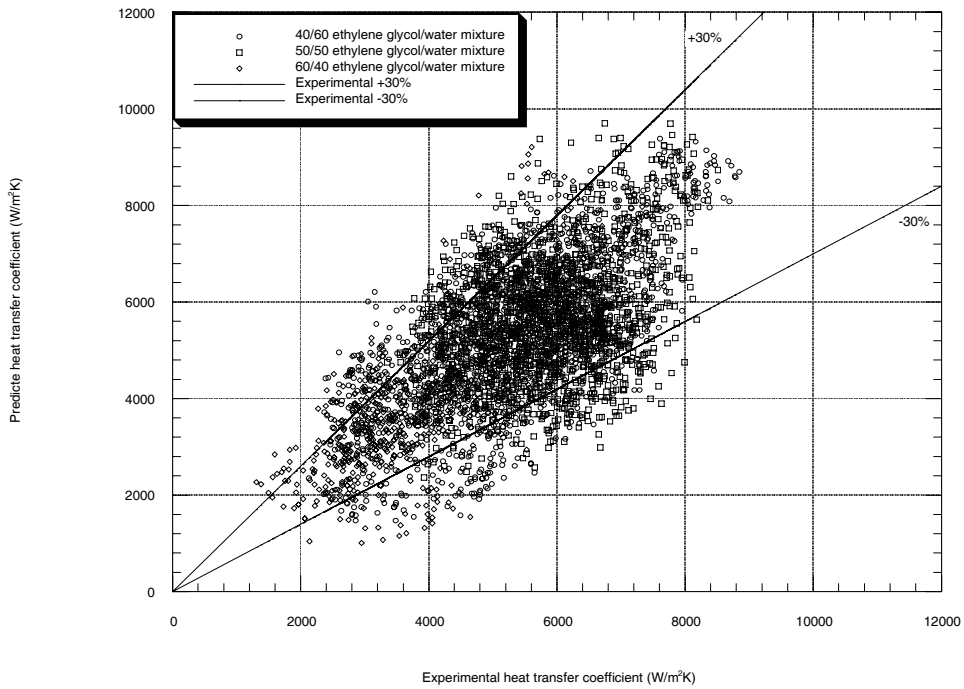


**Figure 5.** Heat transfer coefficient comparisons (nucleation-dominant-boiling region)

## Vertical Flow Boiling Heat Transfer

In the applications of engine cooling, both horizontal and vertical flows exist. Therefore, it is necessary to investigate the impact of vertical flows vs. horizontal flows on two-phase heat transfer. During FY 2005, we fabricated a new vertical experimental test section, the design of which is similar to the existing horizontal experimental test section. The instruments attached to the vertical test section including thermocouples and pressure transducers were calibrated against the National Institute for Standards and Technology (NIST) traceable thermocouple and standard device to ensure accurate measurements of temperatures and pressures. The test facility and test-monitoring program were also modified to adapt to both horizontal and vertical flow tests. Figure 6 shows a picture of the vertical test section before insulated. During FY 2006, systematic vertical flow tests will be performed. We are planning to use water and ethylene glycol/water mixtures for single-phase and two-phase boiling heat transfer experiments of vertical flows. The tests are expected to provide essential information for the design of nucleate-boiling cooling systems.

**Figure 6.** Vertical experimental test section

## Conclusions

Excellent progress has been made on both the experiments and analysis during FY 2005.

(a) Two-phase frictional pressure gradients of ethylene glycol/water mixtures follow similar trends as those of water. The results are in reasonable agreement with the predictions of Chisholm's correlation. A modification has been made to Chisholm's correlation, which reduces to Chisholm's correlation for concentrations $v = 0$ and $v = 1$. This modified Chisholm's correlation improves the predictions of pressure drop data of ethylene glycol/water mixtures.

(b) The experiments show a very high heat transfer rate with ethylene glycol/water mixtures, which is positive to engine cooling applications. A general correlation has been developed based on data of water, ethylene glycol/water mixtures (concentrations 40/60, 50/50, and 60/40), and refrigerants. This correlation predicts the experimental data quite well, and most of the predicted values are within ±30% of the experimental data.

(c) It was found that the boiling heat transfer of ethylene glycol/water mixtures is mainly limited by flow instability rather than critical heat fluxes that are usually the limits for water boiling heat transfer. Tests show that stable long-term two-phase boiling flow is possible for ethylene glycol/water mixtures as long as the mass quality is less than a certain critical value (approximately <0.2). The heat transfer rate at this mass quality is significantly higher than that of conventional, single-phase, forced-convective heat transfer.

(d) During FY 2006, systematic vertical flow tests will be performed. We are planning to use water and ethylene glycol/water mixtures for single-phase and two-phase boiling heat transfer experiments of vertical flows. The tests are expected to provide essential information for the design of nucleate-boiling cooling systems.

# II.C. Nanofluids for Thermal Control Applications

*Principal Investigator: S.U.S. Choi*
*Argonne National Laboratory*
*Argonne, IL 60439*
*(630) 252-6439, fax: (630) 252-5568, e-mail: choi@anl.gov*

*Technology Development Managers: Sid Diamond and Lee Slezak*
*(202) 586-2335, fax: (202) 586-2476, e-mail: Lee.Slezak@hq.doe.gov*

---

*Contractor: Argonne National Laboratory*
*Contract No.: W-31-109-Eng-38*

---

## Objectives

- Exploit the unique properties of nanoparticles to develop heat transfer fluids with ultra-high thermal conductivity.
- Characterize the thermal properties and heat transfer performance of nanofluids.
- Develop nanofluid technology for vehicle thermal control.
- Reduce the size and weight of heavy vehicle cooling systems by >10%.

## Approach

- Measure the thermal conductivity of nanofluids.
- Measure the heat transfer coefficient of nanofluids.
- Develop models of nanofluids for cooling system performance simulation.
- Conduct radiator and full vehicle cooling tests in collaboration with truck companies, radiator manufacturers, and coolant manufacturers.

## Accomplishments

- Developed new capabilities to measure the heat transfer coefficient of nanofluids.
- Developed new capabilities to measure the thermal conductivity of nanofluids from room temperature to 100° Celsius (C).
- Measured the thermal conductivity of $Al_2O_3$ nanofluids as a function of temperature and particle size and experimentally validated the theoretical conjecture (Jang and Choi 2004) that the Brownian motion of nanoparticles is a key mechanism of the thermal conductivity enhancement with increasing temperature and decreasing nanoparticle size.
- Developed and improved nanofluid models which account for the arrangement of nanoparticles.

## Future Directions

- Produce and characterize nanofluids containing nanoparticles less than 10 nanometers (nm).
- Conduct nanofluid flow and heat transfer experiments in laminar and turbulent flow.
- Modify the one-step nanofluid production system for a larger quantity of nanofluids.

- Refine models of nanostructure-enhanced and nanoparticle-mobility-enhanced thermal conductivity of nanofluids for cooling system performance simulation.
- Conduct radiator and full vehicle cooling tests in collaboration with truck companies, radiator manufacturers, and coolant manufacturers.

---

## Introduction

The ever-increasing heat rejection requirements due to trends toward more power output and stringent emission requirements for engines bring cooling to the forefront issue. The conventional method to increase heat rejection rates is to use extended surfaces such as fins. However, current designs have already stretched this technology to its limits. Furthermore, conventional heat transfer fluids used in today's thermal control of vehicles, such as lubricants and engine coolants, are inherently poor heat transfer fluids. Therefore, a strong need exists for new and innovative concepts to achieve ultra-high-performance cooling in thermal control systems for vehicles.

Scientists have tried adding particles to fluids to improve thermal conductivity for more than a century. However, studies of thermal conductivity of suspensions have been confined to millimeter (mm)- or micrometer (µm)-sized particles. The major problem with the use of such large particles is the rapid settling of these particles in fluids. Other problems are abrasion and clogging. To overcome these problems Argonne has pioneered nanofluids by uniformly and stably suspending nanometer-sized particles in fluids. Nanofluids are nanotechnology-based heat transfer fluids engineered by dispersing a very small quantity (preferably <1% by volume) of nanoparticles in conventional coolants (Choi 1995).

The potential benefits of using nanofluids include:

- Improve heat transfer of engine coolants and oils
- Reduce heat exchanger size and weight
- Reduce heat transfer fluid inventory
- Reduce vehicle emissions
- Improve wear resistance
- Reduce friction coefficient
- Reduce pumping energy in existing systems

The goal of the project is to reduce the size and weight of heavy vehicle cooling systems (radiator, oil cooler, pump, fan, etc.) by >10%, despite the higher cooling demands of higher-power engines and exhaust gas recirculation. Nanofluids are among the most promising coolants for the transportation industry. However, the ways in which the nanoparticles in these nanofluids generate enhanced properties are not completely understood. Therefore, to achieve this goal for the industry through 2009, both basic understanding of the mechanisms of enhanced thermal conductivity and stability of nanofluids and development of nanofluid technology are required. Consequently, the main objectives of the project are the following:
(1) explore and exploit the unique properties of nanoparticles to develop heat transfer fluids with high thermal conductivity, (2) characterize the thermal conductivity and heat transfer behavior of nanofluids, (3) determine the basic mechanisms of enhanced thermal conductivity and stability of nanofluids, (4) experimentally determine heat transfer rates and pressure drops in flowing nanofluids, (5) develop and validate new models for nanofluids, (6) develop nanofluid technology for increasing the thermal transport of engine coolants and lubricants, and (7) conduct radiator and full vehicle cooling tests.

## Approach

Our approach to overcoming the poor heat transfer rates of conventional heat transfer fluids is to significantly increase the thermal conductivity of the liquids. An attractive method in that regard is the use of a suspension of solid nanoparticles in a liquid. Solids with thermal conductivities orders of magnitudes higher than those of the liquids are chosen. For example, the thermal conductivity of copper at room temperature is about 3,000 times greater than that of engine oil. In fact, numerous theoretical and experimental studies of the effective thermal conductivity of dispersions that contain solid particles have been conducted since Maxwell's

theoretical work was published about 100 years ago (Maxwell 1881). However, studies on thermal conductivity of suspensions have been confined to millimeter- or micrometer-sized particles. The major problem with the use of such large particles is the rapid settling of these particles in fluids. Another is the abrasive nature of the suspension. In contrast, use of nanoparticles has the potential to produce the increased thermal conductivity sought in heat transfer fluids without the problems of settling and abrasion. Maxwell's concept of enhancing the thermal conductivity of fluids by dispersing solid particles in them is old, but what is new and innovative with the concept of nanofluids is the idea that size matters in nanofluids for suspension stability (gravity is negligible) and for dynamic thermal interactions.

The ANL nanofluid team has developed two techniques to make nanofluids: the single-step direct evaporation method, which simultaneously makes and disperses the nanoparticles directly into the base fluid, and the two-step method, which first makes nanoparticles and then disperses them into the base fluid. Although the two-step technique works well for oxide nanoparticles, it is not as effective for metal nanoparticles such as copper. For nanofluids containing high conductivity metals, the single-step direct evaporation technique is preferable to gas-condensation processing. Nanoparticles agglomerate before dispersion and agglomerates settle rapidly. However, our innovation was dispersing nanoparticles into fluids before agglomeration by a single-step method.

ANL has already produced oxide and carbon nanotube nanofluids by the two-step technique and metal nanofluids by the single-step technique. In particular, it was demonstrated that stable suspensions can be achieved by maintaining the particle size below a threshold level.

We have made and used the transient hot wire apparatus to measure the thermal conductivity of nanofluids at room temperature. However, recent studies show the importance of measuring the temperature-dependent thermal conductivity of nanofluids. Therefore, new capabilities to measure the thermal conductivity of nanofluids from room temperature to 100°C have been developed. The thermal conductivity of oxide nanofluids with low particle concentrations (<1 % by volume) was measured as a function of temperature and particle size using the transient hot wire method.

A major focus in nanofluids has been on their thermal conductivity. However, a new focus will be on the flow and heat transfer of nanofluids. We believe that it is critical to characterize the flow and heat transfer behavior of nanofluids in tubes in order to explain and exploit nanoparticle size-, shape-, and concentration-dependent pressure drop and heat transfer coefficient of nanofluids in tubes. For example, theories of flow in tubes or porous materials have been developed at the macroscopic level. However, we believe that it is vital to connect the structure and mobility of nanoparticles at the nano- or micro-scale to the properties of nanofluids measured at the macroscopic level. Therefore, we have developed new capabilities to measure the heat transfer coefficient of nanofluids.

We plan to conduct radiator and full vehicle cooling tests in collaboration with truck companies, radiator manufacturers, and coolant manufacturers in order to demonstrate nanofluid technology for vehicle thermal control applications.

## Results and Discussion

We have completed the design and construction of the Nanofluid Heat Transfer Test Facility, as shown in Figure 1, for measuring heat transfer rates to flowing nanofluids under a variety of flow conditions and using a variety of nanofluids. The new Nanofluid Heat Transfer Test Facility has been carefully scrutinized for instrument accuracy, data acquisition process, and test procedure. The Nanofluid Heat Transfer Test Facility has been filled with water for initial tests and shake-down purposes. Single-phase pressure-drop and heat transfer testing has begun at room temperature and at an elevated temperature of 100°C. During the first tests, it was found that it was necessary to make some modifications to the Test Facility. Transparent reservoirs were added to the pump suction and discharge to allow visual confirmation of proper fluid fill level in the system. An additional electrical isolation tube was added to the flow circuit to insure that there is no current leakage through the

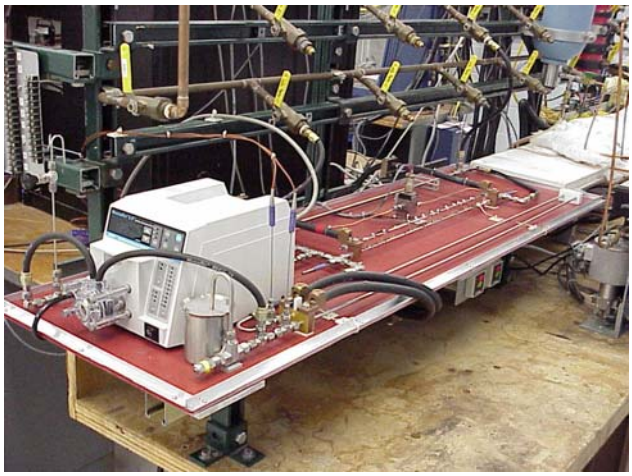

**Figure 1.** Picture of nanofluid heat transfer test facility

differential pressure transducer across the test section. The test facility pump was reconfigured and test procedures changed in a manner to increase its precision over a long time period. Finally, a high accuracy flow meter was put in parallel with the test facility flow meter for use only when water, and not nanofluid, is the test fluid. With these modifications in place, the test section pressure transducers were recalibrated (to NIST standards) and shake-down testing was resumed. Special attention is being given to the test facility pump and flow meter specially selected for nanofluid use. Upon completion of these shake-down tests, pressure-drop and heat transfer tests will commence with nanofluids.

In 2004, we developed a simplified nanofluid model and showed, for the first time, that Brownian motion of the nanoparticles is a key mechanism of the temperature- and size-dependent thermal conductivity (Jang and Choi 2004). This is a major milestone in the development of nanofluid technology for vehicle thermal control applications because the size-as-a-parameter approach to enhance the thermal conductivity of base fluids instead of the conventional adding-more-particles approach would be an important technological breakthrough.

This year we have measured temperature-dependent thermal conductivities of nanofluids with 11-nm-, 47-nm-, and 150-nm-sized $Al_2O_3$ nanoparticles at 1 and 4 vol.% concentration to delineate the effects of the nanoparticle size and nanofluid temperature (Chon et al. 2005). Figure 2 shows the measured thermal conductivity data normalized to the base fluid conductivity at each specified temperature (symbols) and the corresponding empirical correlations (curves) for different nanoparticle sizes and volume concentrations. It is clear that the nanofluid conductivity increases with increasing nanofluid temperature and with decreasing nanoparticle size. Thus, we have experimentally validated the theoretical conjecture (Jang and Choi 2004) that the Brownian motion of nanoparticles is a key mechanism of the thermal conductivity enhancement with increasing temperature and decreasing nanoparticle size.

The theoretical investigation of the effective thermal conductivities of nanofluids is important in both predicting and designing nanofluids with effective

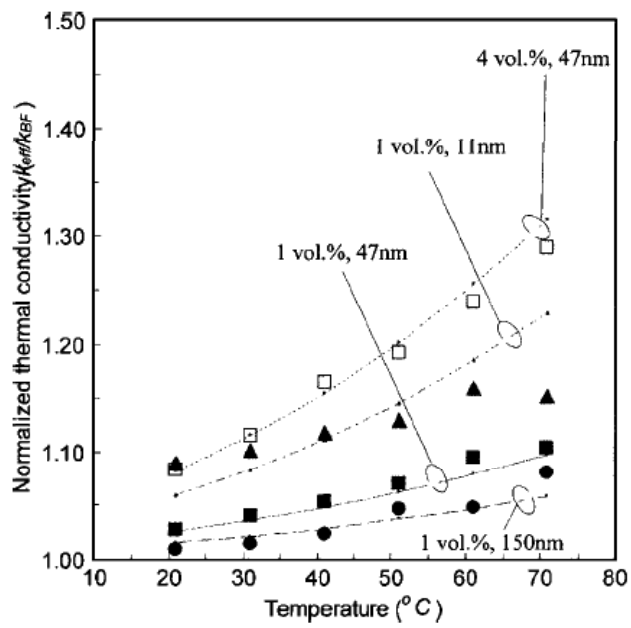


**Figure 2.** Temperature dependence of the thermal conductivity enhancement of three different nanofluids with 11-nm, 47-nm, and 150-nm sized $Al_2O_3$ nanoparticles at 1 and 4 vol.% concentration, normalized by the thermal conductivity of the base fluid at the specific temperature. Symbols represent experimental data, and the corresponding curves represent empirical correlation. At a fixed concentration, nanofluid conductivity increases with decreasing nanoparticle size and increases with increasing temperature. It should be noted that the gradually accelerating temperature dependence with increasing temperature is manifested as a slightly nonlinear function of temperature.

thermal conductivities. We have developed a new thermal-conductivity model for nanofluids that is based on the assumption that monosized spherical particles are uniformly dispersed in the liquid and are located at the vertexes of a simple cubic lattice, with each particle surrounded by a liquid layer having a thermal conductivity that differs from that of the bulk liquid (Yu and Choi 2005). Figure 3 shows the thermal conductivity ratio $k_e^*$ as a function of the volume concentration for four $k_p^*$ values, where where $k_p^*$ is the ratio of the thermal conductivity of the nanoparticle to that of the base fluid. It is obvious that the thermal conductivity ratio $k_e^*$ is a nonlinear function of the volume concentration with an increase pattern that curves convex-upwards. This increase pattern significantly affects the effective thermal conductivities of mixtures; it indicates that even at very low volume concentrations, the effective thermal conductivities of mixtures could be very enhanced when compared with those of base liquids. A comparison of predicted thermal conductivity values and experimental data shows that the predicted values are much higher than the experimental data, a finding that indicates that there is a potential to further improve the effective thermal conductivities

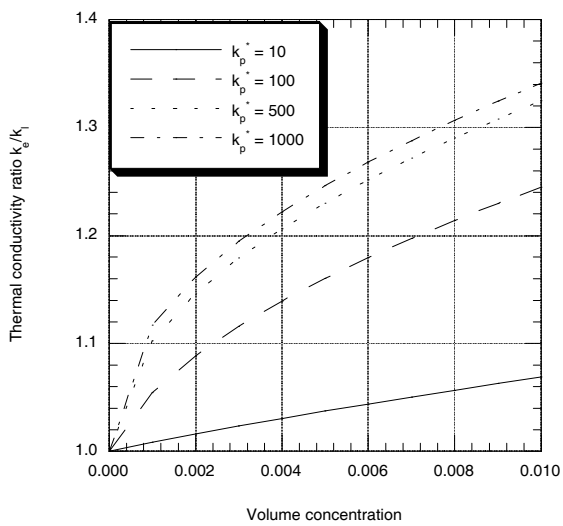


**Figure 3.** The thermal conductivity ratio as a function of the volume concentration for four $k_p^*$ values where $k_p^*$ is the ratio of the thermal conductivity of the nanoparticle to that of the base fluid

of nanofluids with more uniformly dispersed particles. Furthermore, this model nanofluid with a cubical arrangement of nanoparticles gives a more practical upper limit of thermal conduction than a model nanofluid with a parallel arrangement of nanoparticles.

Our recent theoretical study has led to the discovery that nanoscale convection induced by Brownian motion of nanoparticles is a dominant mechanism governing their thermal behavior (Jang and Choi 2004). In related work, we have thus designed and fabricated nanofluid conductivity control and measurement apparatus. The objective is to assess the feasibility of externally controlling the motion of nanoparticles and in turn the thermal conductivity of nanofluids. This new project would directly benefit nanofluid technology development for vehicle thermal control applications.

## FY 2005 Publications

Yu, W., and S.U.S. Choi, "The Role of Interfacial Layers in the Enhanced Thermal Conductivity of Nanofluids: A Renovated Hamilton-Crosser Model," *J. Nanoparticle Research*, Vol. 6, pp. 355–361, 2004.

Xue, L., P. Keblinski, S.R. Phillpot, S.U.S. Choi, and J.A. Eastman, "Effect of Liquid Layering at the Liquid-Solid Interface on Thermal Transport," *Int. Journal of Heat and Mass Transfer*, 47, 4277–4284, 2004.

Chon, C.H., K.D. Kihm, S.P. Lee and S.U.S. Choi, "Empirical Correlation Finding the Role of Temperature and Particle Size for Nanofluid (Al2O3) Thermal Conductivity Enhancement," *Applied Physics Letters*, Vol. 87, 153107, 2005.

Yu, W., and S.U.S. Choi, "An Effective Thermal Conductivity Model of Nanofluids with a Cubical Arrangement of Spherical Particles," *J. Nanoscience and Nanotechnology*, Vol. 5, pp. 580–586, 2005.

Lockwood, F.E., Z.G. Zhang, T.R. Forbus, S.U.S. Choi, Y. Yang, and E.A. Grulke, "The Current Development of Nanofluid Research," Presented at the 2005 SAE World Congress,

April 11–14, 2005, Detroit, MI, Paper No. 2005-01-1929.

## Future Directions

Future work will focus on the following five major tasks.

- Produce and characterize nanofluids containing nanoparticles less than 10 nm.
- Conduct nanofluid flow and heat transfer experiments in laminar and turbulent flow.
- Modify the one-step nanofluid production system for a larger quantity of nanofluids.
- Refine models of nanostructure-enhanced and nanoparticle-mobility-enhanced thermal conductivity of nanofluids.
- Initiate a new CRADA with a commercial truck company, a radiator manufacturer and a coolant manufacturer which is aimed at radiator and full vehicle cooling tests through 2009.

### Produce and characterize nanofluids containing nanoparticles less than 10 nm.

Our experimental and theoretical studies show that particle size is of primary importance in the development of stable and high conductivity nanofluids. Size matters for achieving suspension stability (gravity is negligible) and dynamic thermal interactions.

Because the thermal conductivity of nanofluids increases much more dramatically with decreasing particle size, particularly when the particle diameter is on the order of 1 nm, it should be possible to design nanofluids at the molecular and nanoscale level to create unprecedented thermal properties at the macroscopic level. For this technology to become a reality, new techniques are needed for manufacturing nanoparticles smaller than 10 nm. We will produce nanofluids containing nanoparticles less than 10 nm using one-step physical and chemical methods and characterize them.

### Conduct nanofluid flow and heat transfer experiments in laminar and turbulent flow.

We will explore the flow characteristic and measure the heat transfer coefficient of nanofluids in tubes. We will then relate enhanced thermal conductivity and flow characteristic to enhanced heat transfer coefficient of nanofluids. Control tests will be completed with water as the test fluid. Subsequently, nanofluid flow and heat transfer experiments will be conducted. The flow and heat transfer data for nanofluids will be used to determine whether the flow and heat transfer correlations developed for homogeneous fluids could be applied to nanoparticle dispersions with aspect ratios different from one.

### Modify the one-step nanofluid production system for a larger quantity of nanofluids.

Nanofluids hold significant potential for revolutionizing industries that are dependent on the performance of heat transfer fluids. However, there is one big barrier to commercialization of nanofluids: production scale-up methods to produce nanofluids in volume and at low cost. Finding a way to produce small (1-10 nm) nanoparticles cheaply and disperse them without agglomeration is the key hurdle to commercialization. As a first step toward production scale-up, we will modify ANL's one-step process to produce more nanofluids.

### Refine models of nanostructure-enhanced and nanoparticle-mobility-enhanced thermal conductivity of nanofluids.

We have developed simple models of nanostructure-enhanced [5] and nanoparticle-mobility-enhanced thermal conductivity of nanofluids [3]. However, much is still unknown about the mechanisms of the anomalous thermal behavior of nanofluids. Therefore, we need to understand the fundamentals of energy transport in nanofluids. As we discover new energy transport mechanisms that are missing in existing theories, we will refine the simple models or develop a new model of energy transport in nanofluids integrating new mechanisms. A better understanding of the mechanisms behind the thermal-conductivity enhancement will likely lead to recommendations for nanofluid design and engineering for transportation applications.

### Initiate a new CRADA.

We will initiate, during FY2006, a new CRADA with a commercial truck company, a radiator

manufacturer and a coolant manufacturer which is aimed at conducting radiator and full vehicle cooling tests through 2009.

## Summary

These are the highlights of the progress during FY2005:

1. Developed new capabilities to measure the heat transfer coefficient of nanofluids by completing the construction of the test facility for nanofluid convective heat transfer.
2. Developed new capabilities to measure the thermal conductivity of nanofluids from room temperature to 100°C.
3. Measured the thermal conductivity of $Al_2O_3$ nanofluids as a function of temperature and particle size and experimentally validated the theoretical conjecture (Jang and Choi 2004) that the Brownian motion of nanoparticles is a key mechanism of the thermal conductivity enhancement with increasing temperature and decreasing nanoparticle size.
4. Developed and improved nanofluid models which account for the structure and arrangement of nanoparticles.

## Conclusions

Argonne scientists have created nanotechnology-based, next-generation fluids that may revolutionize heat transfer. By suspending nanophase materials like copper or carbon nanotubes in liquids such as water, ethylene glycol (radiator fluid) or engine oil, researchers can improve by up to 100% its ability to transfer heat. Improved oils and coolants would make possible more efficient engines and smaller and lighter cooling systems. Such engines and cooling systems would reduce aerodynamic drag and parasitic energy losses, improve fuel savings, and reduce damage to the environment.

## References

Choi, S.U.S., "Enhancing Thermal Conductivity of Fluids with Nanoparticles," *Developments and Applications of Non-Newtonian Flows*, eds. D.A. Siginer and H.P. Wang, The American Society of Mechanical Engineers, New York, FED–Vol. 231/MD-Vol. 66, pp. 99–105 (Nov. 1995).

Maxwell, J.C., 1881, *A Treatise on Electricity and Magnetism*, 2nd ed., 1, 435, Clarendon Press.

Jang, S.P., and S.U.S. Choi, "Role of Brownian Motion in the Enhanced Thermal Conductivity of Nanofluids," *Appl. Phys. Lett*. **84**, pp. 4316–4318, 2004.

Chon, C.H., K.D. Kihm, S.P. Lee and S.U.S. Choi, "Empirical Correlation Finding the Role of Temperature and Particle Size for Nanofluid ($Al_2O_3$) Thermal Conductivity Enhancement," *Applied Physics Letters*, Vol. 87, 153107, 2005.

Yu, W., and S.U.S. Choi, "An Effective Thermal Conductivity Model of Nanofluids with a Cubical Arrangement of Spherical Particles," *J. Nanoscience and Nanotechnology*, Vol. 5, pp. 580–586, 2005.

# II.D. Evaporative Cooling

*Principal Investigator: S.U.S. Choi*
*Argonne National Laboratory*
*Argonne, IL 60439*
*(630) 252-6439, fax: (630) 252-5568, e-mail: choi@anl.gov*

*Technology Development Managers: Sid Diamond and Lee Slezak*
*(202) 586-2335, fax: (202) 586-2476, e-mail: Lee.Slezak@hq.doe.gov*

---

*Contractor: Argonne National Laboratory*
*Contract No.: W-31-109-Eng-38*

---

## Objectives

- Improve air-side heat transfer of the radiator.
- Reduce the size and weight of the radiator by >10%.
- Design system to use water condensate from the air-conditioning system for use in evaporative cooling.
- Calculate the water balance requirements of a system under different driving conditions.

## Approach

- Conduct evaporative cooling tests on flat and cylindrical heaters.
- Characterize evaporative cooling with microporous surfaces.
- Develop improved techniques for making micro- and nano-porous coated surfaces.
- Conduct evaporative cooling tests on prototype radiators.
- Conduct full vehicle cooling tests.

## Accomplishments

- Designed and fabricated an experimental facility to study evaporative cooling with plain and coated surfaces.
- Demonstrated that evaporative cooling on microporous surface enhances the heat transfer coefficient by up to ~400% relative to uncoated, dry surface.
- Investigated the effects of coating particle sizes and coating thicknesses on evaporative cooling performance.
- Initiated the development of an improved coating technique called thermally conductive microporous coating (TCMC) technique.
- Identified technical barriers to the practical use of evaporative cooling.

## Future Directions

- Address the issue of water management including the source and minimum consumption of water for evaporative cooling.
- Develop improved techniques for making micro- and nano-porous coated surfaces including the TCMC technique.

- Develop new nozzle technology to minimize water consumption.
- Conduct evaporative cooling tests on prototype radiators.
- Conduct full vehicle cooling tests in collaboration with truck companies, radiator manufacturers, and coolant manufacturers.

## Introduction

Evaporative cooling is an effective and economical method to cool heated objects requiring comparatively high heat flux dissipation for numerous industrial applications. Since evaporative cooling involves liquid-vapor phase change, the increase of heat transfer is significant compared to single-phase forced convection of air. The heat of vaporization augments heat transfer when the tiny water droplets encounter and evaporate from the heated surface. In previous research, we successfully designed, fabricated, and operated an experimental facility to study evaporative cooling with plain and coated surfaces for flat and cylindrical heaters. The experimental apparatus is shown in Figure 1. Figure 2 shows one of our key findings that the combination of evaporative cooling and microporous coating on a flat heater enhances the heat transfer coefficient by up to 400% relative to the reference case (dry air cooling with uncoated, plain surface). Furthermore, the microporous coating extended the dryout heat flux significantly (~21 kilowatts per square meter [kW/m$^2$]) over the plain surface (15 kW/m$^2$). These findings clearly show that the performance on the air side of the radiator could be improved if evaporative heat transfer could be used. Therefore, one of the general strategies for improving the thermal control performance in heavy vehicles is to make better use of evaporative cooling. Furthermore, we investigated the effects of water flow rates, coating particle sizes, and coating thicknesses on evaporative cooling performance. In addition, we initiated the development of an improved coating technique called thermally conductive microporous coating (TCMC).

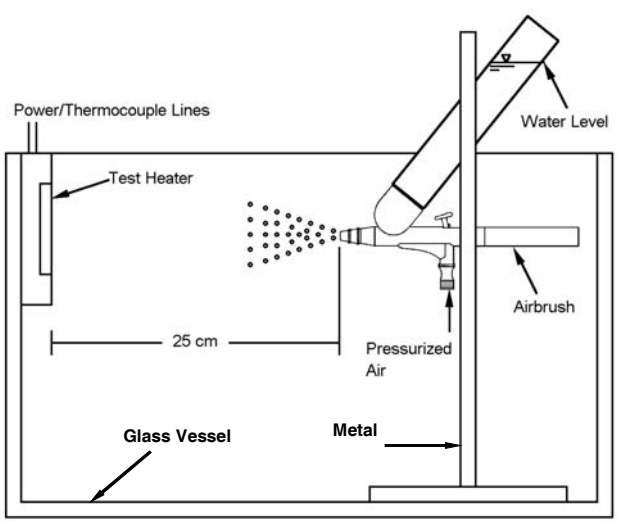


**Figure 1.** Schematic view of the experimental apparatus

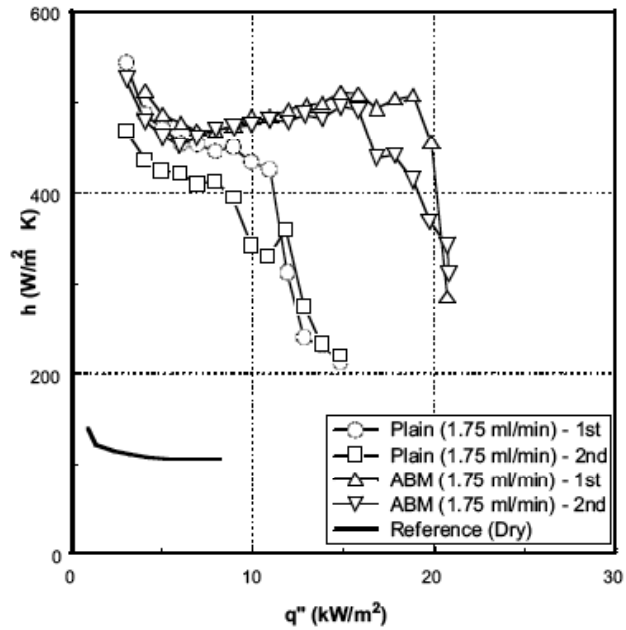


**Figure 2.** Heat transfer coefficient versus heat flux for plain and microporous surfaces with flat heater. The heat transfer coefficient of the evaporative cooling with the microporous surface was approximately 500 W/m$^2$K up to a heat flux of almost 20 kW/m$^2$, which is about a 400% increase compared to the reference case (dry air cooling with uncoated, plain surface).

## Results and Discussion

### Effect of Microporous Coating Thicknesses

The effect of microporous coating thickness was investigated using the smallest particle size (8–12 micrometers [μm]). Figure 3 shows the heat transfer performance with coating thicknesses of 50, 100, 150, and 200 μm on the flat heater during tests with spray cooling and a water flow rate of 1.75 milliliters per minute (ml/min). Microporous coatings with 150 and 200 μm thicknesses showed smaller enhancement in spray heat transfer than coatings with 50 and 100 μm thicknesses. The 100 μm coating thickness attained the highest heat transfer coefficient among the tested thicknesses. This thickness produced up to ~50% increase in evaporative heat transfer coefficient over the 200 μm thickness. The thicker microporous coating retains more water droplets as the coating thickness increases due to the larger number of microporous cavities. However, the evaporative heat transfer coefficient degrades extensively due to the additional thermal resistance to conduction as the thickness exceeds 100 μm.

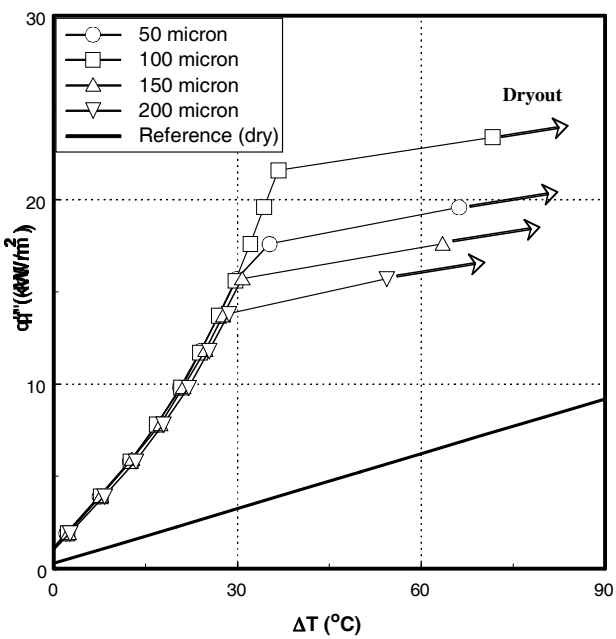


**Figure 3.** Effect of microporous coating thickness on heat transfer performance of flat heater (Water flow rate: 1.75 ml/min). The 100-μm coating thickness gives the maximum heat transfer performance among the tested thicknesses.

### ABM Coating Technique

The University of Texas at Arlington (UTA) has been collaborating with Argonne in the conduct of basic research on the effects of microporous coatings and other techniques on evaporative cooling. The ABM coating technique, named from the initial letters of the three components of the microporous coating: **A**luminum/**B**rushable Ceramic/**M**ethyl-Ethyl-Ketone, is one of the microporous coating methods previously developed to make a porous structure on heat transfer surfaces. After the carrier (methyl-ethyl-ketone [M.E.K.]) evaporates, the resulting coated layer consists of microporous structures with aluminum particles (8 to 12 μm) and a binder (Devcon Brushable Ceramic) having a thickness of ~50 and 100 μm, which was shown to be an optimum thickness for FC-72 and water, respectively.

The previous study on evaporative cooling was achieved by the ABM coating technique. The ABM coating enhances heat transfer coefficient of evaporative cooling mainly due to the capillary pumping action within the microporous structures. However, the epoxy component of the microporous structure has a poor thermal conductivity and thus potentially increases the conduction thermal resistance through the layer especially when the coating becomes thick. Also, use of epoxy appears to prohibit the porosity variation within the microporous structures even if the aluminum particle size was changed. In order to overcome these inferior thermal characteristics in evaporative cooling, a new innovative conductive microporous coating method needs to be developed.

### TCMC Coating Technique

We have therefore developed a TCMC technique that consists of metal particles with various micron sizes and the thermally conducting binding materials that bond the metal particles to produce numerous microporous cavities on a target surface. The new TCMC technique is similar in concept to the ABM coating (many small metal powders jointed by a thin bonding layer around the particles). However, a thermally conductive layer will be used for the TCMC technique instead of the epoxy layer used for the ABM technique to form the microporous coating. Different particle materials are being tested

for this current technique considering corrosion and compatibility with various fluids. The microporous coating methods — including the ABM technique — are inexpensive and easy processes compared to sintering/machining methods. However, the coating methods are inferior to sintering/machining methods due to the low thermal conductivity of binders (epoxy). The main advantage of this improved coating technique is to combine the inexpensive and easy coating process and low thermal resistance of thermally conductive binding materials. Another advantage is that heat transfer is insensitive to coating thickness due to the high thermal conductivity of binding structures. In addition, the coating technique is applicable to various working liquids, highly wetting to poorly wetting, simply by changing the size of metal particles since the surface tension of liquids determines the size of porous cavities to optimize heat transfer performance.

Figure 4 shows the SEM image of a TCMC-coated surface with aluminum particles (8 to 12 µm). As shown in the figure, the coating produced numerous microporous cavities. Figure 5 shows the boiling performance comparison between TCMC and ABM with 30–50 µm particles. It is clearly shown that TCMC generates higher boiling heat transfer over ABM. This boiling enhancement could be possibly achieved due to the thermally conducting binder

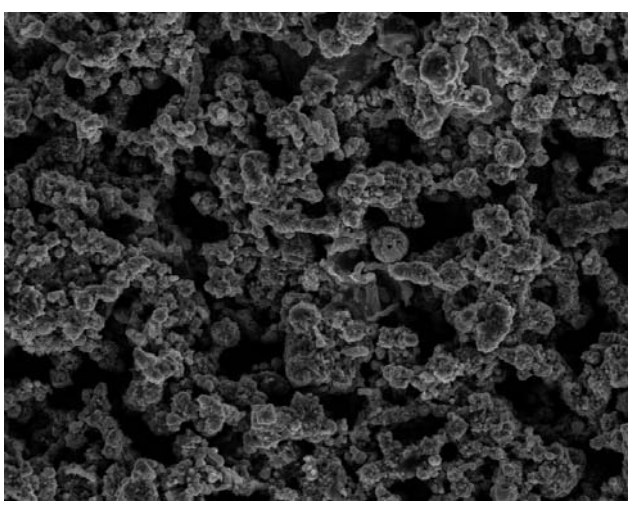

**Figure 4.** Scanning electron microscope image of thermally conductive microporous coated surface with aluminum particles of 8 to 12 µm diameter.

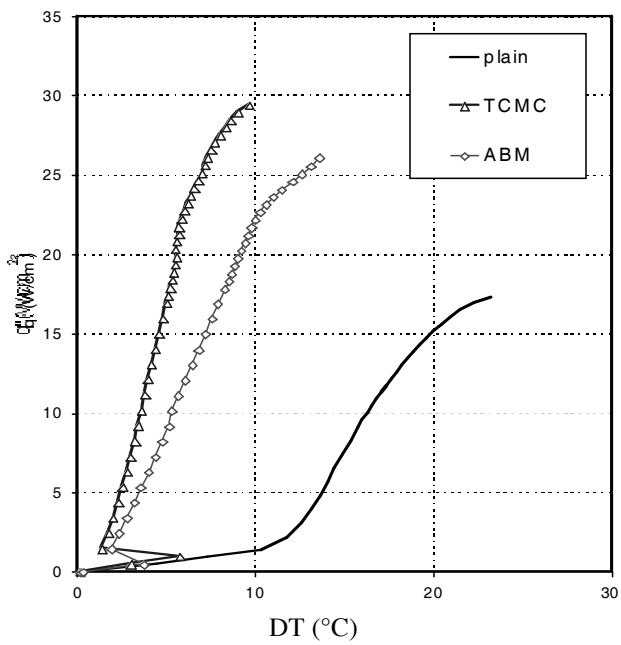


**Figure 5.** Comparison of heat transfer performance between previous ABM coating and new TCMC coating with 30–50 µm aluminum particles. It clearly shows that TCMC generates higher boiling heat transfer over ABM.

option, which generates very low thermal resistance at high heat flux compared to non-conducting binders.

The TCMC technique using the thermally conductive binder has significant advantages compared to the ABM method, specifically:

- ~100 times higher thermal conductivity of bonding layer than the epoxy binder.
- Thicker coating with higher porosity is possible to strengthen the capillary pumping through the coating without degrading thermal performance.

Therefore, the TCMC technique is believed to perform better than that of the microporous plate in the evaporative cooling heat transfer.

## Technical Barriers Have Been Identified

Argonne National Laboratory has already proved in a lab facility the feasibility of the concept of evaporative cooled ultra-high performance radiators. However, one of the most serious technical barriers to the practical use of evaporative cooled ultra-high performance radiators is the issue of water

management including the source and minimum consumption of water for evaporative cooling. This issue will be addressed as one of the major tasks in FY2006. Once this issue is resolved, the Heavy Vehicles Systems Optimization (HVSO) technical target of "by 2010, reducing cooling system size for a Class 7–8 truck by 8%" and 21st Century Truck Partnership goal of "increasing heat load rejected by thermal management systems by 20%" are well within reach.

## Future Directions

Future work will focus on the following major tasks and subtasks:

1. Show calculationally that use of evaporative cooling on the radiator surface during peak cooling can reduce the overall radiator size by at least 10%. Quantify the amount of water use required to accomplish this end.
2. Design system to use water condensate from the air-conditioning system for use in evaporative cooling.
3. Calculate the water balance requirements of a system under different driving conditions.
4. Develop new nozzle technology to minimize water consumption.
5. Develop improved techniques for making micro- and nano-porous coated surfaces including the TCMC technique.
6. Conduct evaporative cooling tests on prototype radiators.
7. Conduct full-vehicle cooling tests in collaboration with truck companies, radiator manufacturers, and coolant manufacturers.

## Summary

Technical accomplishments to date with respect to achieving objectives are as follows:

1. Designed and fabricated an experimental facility to study evaporative cooling with plain and coated surfaces.
2. Demonstrated that evaporative cooling on microporous surface enhances the heat transfer coefficient **by up to ~400%** relative to uncoated, dry surface.
3. Investigated the effects of coating thicknesses on evaporative cooling performance.
4. Initiated the development of an improved coating technique called thermally conductive microporous coating (TCMC) technique.
5. Identified technical barriers to the practical use of evaporative cooling.

## Conclusions

Argonne National Laboratory has developed the concept of evaporative cooled ultra-high performance radiators with three key ideas: (1) Use evaporative cooling to increase air-side heat transfer in contrast to air cooling alone in conventional radiators, (2) Use evaporative cooling primarily at peak heat loads, and (3) Develop evaporative cooling technology for ultra-high performance radiators with minimum water consumption. Argonne has already proved in a lab facility the feasibility of the concept of evaporative cooled ultra-high performance radiators. Argonne study clearly shows that the performance on the air side of the radiator could be dramatically improved when evaporative cooling is used. This finding could lead to a substantial downsizing of truck radiators. Even a 10% reduction in radiator size would have a significant impact on the fuel economy of trucks. However, one of the most serious technical barriers to the practical use of evaporative cooled ultra-high performance radiators is the issue of water management, including the source and minimum consumption of water for evaporative cooling. This issue will be addressed as one of the major tasks in FY2006. Once this issue is resolved, the HVSO technical target of "by 2010, reducing cooling system size for a Class 7–8 truck by 8%" and 21st Century Truck Partnership goal of "increasing heat load rejected by thermal management systems by 20%" are well within reach.

# II.E. Erosion of Materials in Nanofluids

*Principal Investigator: J.L. Routbort (co-worker: D. Singh)*
*Argonne National Laboratory*
*9700 S. Cass Avenue, Argonne, IL 60439-4838*
*(630) 252-5065, e-mail: routbort@anl.gov*

*Technology Development Managers: Sid Diamond and Lee Slezak*
*(202) 586-2335, e-mail: Lee.Slezak@hq.doe.gov*

---

*Contractor: Argonne National Laboratory*
*Contract No.: W-31-109-Eng-38*

---

## Objectives

- Determine if the use of fluids containing a variety of nanoparticles and nanotubes results in erosive damage to radiator materials.
- Develop models to predict the erosive damage.

## Approach

- Develop an experimental apparatus to measure erosive loss.
- Conduct experiments to study erosive damage of fluids on typical radiator materials.
- Develop methods to analyze the results.

## Accomplishments

- Built apparatus to study liquid erosion.
- Completed calibration of sample impact area as a function of fluid velocity.
- Obtained baseline data with ethylene glycol and water solutions.
- Conducted preliminary experiments with nanofluids.

## Future Directions

- Pumping problems to be solved.
- Fluids containing a variety of nanoparticles and nanotubes will be tested on typical radiator materials, varying both the angle and velocity of impact, volume percent of nanoparticles, and temperature.

---

## Introduction

Many industrial technologies face the challenge of thermal management. With ever-increasing thermal loads due to trends toward greater power output for engines and exhaust gas recirculation for diesel engines, cooling is a crucial issue in transportation. The conventional approach for increasing cooling rates is use of extended surfaces such as fins and microchannels. Reducing radiator size will reduce the frontal area and hence the aerodynamic drag. However, current designs have already stretched this approach to its limits. Therefore, an urgent need exists for new and innovative concepts to achieve ultra-high-performance cooling. Nanofluids seem to show enormous potentials as a coolant for radiators.

Eastman and Choi et al. have shown that fluids containing 1 vol.% Cu nanoparticles increases thermal conductivity by 40% (Eastman et al. 2001) while 1 vol.% carbon nanotubes increase thermal conductivity by 250% (Choi et al. 2001).

In order for the enhanced thermal conductivity to be utilized it must be shown that liquid erosion of typical radiator materials will be tolerable. Hence, the FreedomCar and Vehicle Technologies Program funded research on liquid erosion of radiator materials using nanofluids.

## Results and Discussion

An apparatus was designed and constructed to allow the erosion rates of fluids containing various nanoparticles and nanotubes to be determined, ranging from approximately 1 millisecond (m/s), velocities used in heavy vehicle radiators to about 15 m/s. Angle of impacts can be varied from 30° to 90° and temperatures up to approximately 95° Celsius (C) can be obtained. A photograph of the apparatus is shown in Figure 1. Figure 2 is a view of the specimen chamber with the cover removed showing the specimen and the nozzle. The experimentally determined variables are (1) pump revolutions per minute (RPM), (2) temperature, (3) pressure, and (4) weight loss. The velocity is determined by measuring the amount of fluid for a given time at a fixed RPM using a given nozzle diameter. Such a calibration is shown in Figure 3.

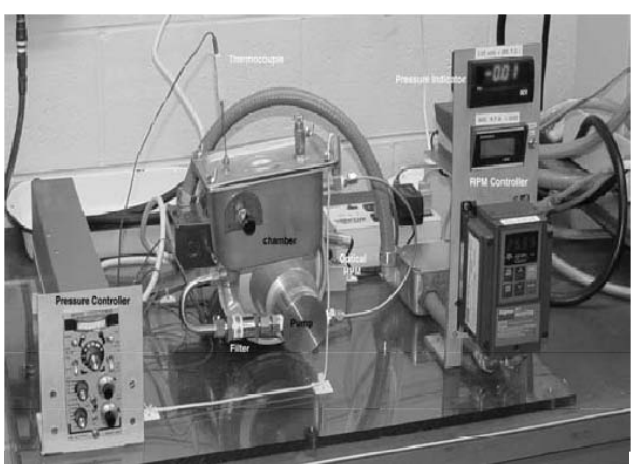


**Figure 1.** Photograph of the liquid erosion apparatus with various components labeled

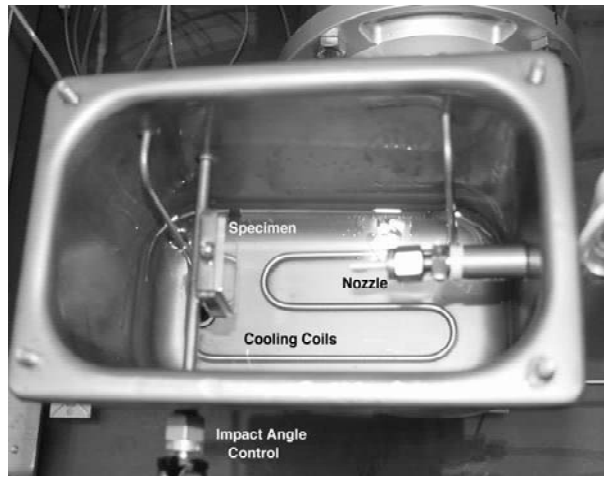


**Figure 2.** Close-up view of experimental chamber with the cover removed showing the specimen and the nozzle

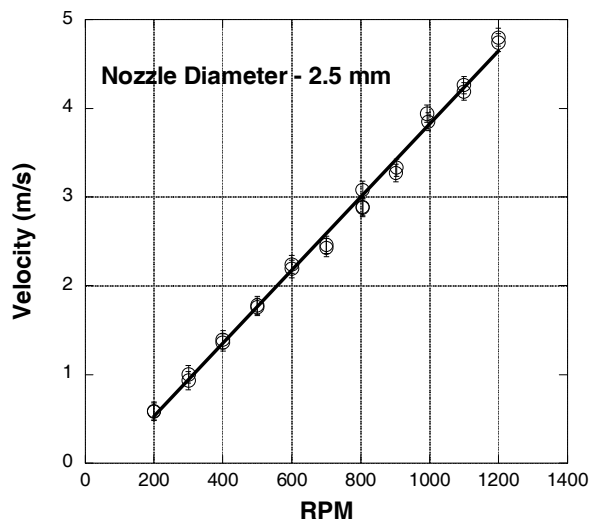


**Figure 3.** Plot of velocity, determined by measuring the volume of fluid (ethylene glycol/water, in this case) for a fixed time, as a function of pump RPM

During experimentation over the past year, it was determined that velocity at a fixed RPM during the course of an experiment is dependent on several factors such as wear of pump gears and clogging of the mesh filter placed in the fluid, etc. To ensure that velocity-RPM behavior remains consistent, modifications were made to the erosion set-up. These modifications included additional pressure gauges placed at the pump exit and before the nozzle (Figure 4). Stability of the pressure readings at these locations ensured the constant fluid velocity at a fixed pump RPM per the calibration profiles developed.

**Figure 4.** Newly installed pressure gauges to ensure appropriate pressures and velocities in the erosion system

As discussed in the 2004 report, it is well known that Al 3003 is susceptible to corrosion in presence of ethylene glycol/water solutions (Wong et al. 1979). In the presence of small amounts of impurities, Al metal can corrode in ethylene glycol solutions by localized pitting. It is believed that there is a possibility that a galvanic couple can form between the sample holder (steel) and the sample (Figure 5). To prevent this, a plastic sheet was used to isolate the sample from the sample holder.

Tests were conducted on equi-volume solution of ethylene glycol and water with no nanoparticles to establish a baseline data. In addition to varying the fluid velocity, impact angle was also varied from 90° to 30°. Tests were conducted as long as 293 hours at temperatures of 50°C. Reservoir temperature was maintained by using a heating tape.

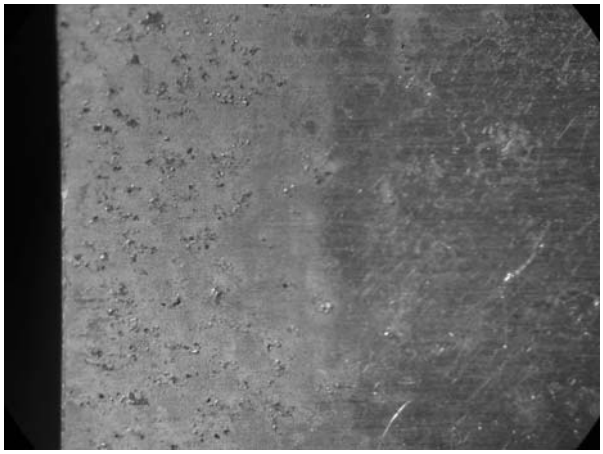

**Figure 5.** Galvanic pitting observed in Al3003

Table 1 summarizes the experimental data. No appreciable weight loss was measured at any of the velocities and impact angles tested.

Subsequent to establishing baseline erosion behavior, preliminary experiments using nanofluids containing carbon nanotubes (CNT) was initiated. S. Choi (Argonne National Laboratory) provided nanofluid containing 0.25 vol.% CNT in water. Initial tests were conducted at 8 m/s at 90° impact angle.

Several problems were encountered during the erosion tests with CNT nanofluid. The velocity of the fluid was not steady and dropped steadily with time. In addition, CNT particles not only eroded the sample, but also the polymeric gears of the pump and the stainless steel nozzle. Table 2 shows the weight loss measured on the Al 3003 sample and various components of the test set-up for an experiment conducted for a relatively short period of time (48 hours). Further, CNT did not remain in suspension in fluid and agglomerated (Figure 6). It is the agglomeration of CNT that caused clogging of the system and drop in the velocity. Results of this study clearly suggested that nanofluids with CNT are not suited for the current liquid erosion test set-up.

**Table 1.** Al 3003 Erosion Using Ethylene Glycol-Water (50:50 vol. %) Solutions

| Impact Angle (degrees [°]) | Velocity (milliseconds [m/s]) | Time (hours [h]) | Wt. Loss (milligrams [mg]) |
|---|---|---|---|
| 90 | 8.0 | 236 | 0 ± 0.2 |
| 90 | 10.5 | 211 | 0 ± 0.2 |
| 50 | 6.0 | 264 | 0 ± 0.2 |
| 50 | 10.0 | 244 | 0 ± 0.2 |
| 30 | 8.0 | 283 | 0 ± 0.2 |
| 30 | 10.5 | 293 | 0 ± 0.2 |

**Table 2.** Weight Loss of Various Components During Erosion Test with CNT

| Material | Weight Loss (mg) |
|---|---|
| Al 3003 | 2.4 |
| SS 316 — nozzle | 11.0 |
| Polymer — small pump gear | 9.4 |
| Polymer — large pump gear | 13.4 |

**Figure 6.** Agglomerated CNT in nozzle of the erosion test set-up

To avoid the agglomeration issues, a second set of nanofluid, 0.25 vol.% alumina (40 nanometers [nm]) in water, was attempted in the erosion study. This nanofluid was also supplied by S. Choi at Argonne. Tests were conducted at a velocity of 5 m/s at 90° and 30° impact angles. Interestingly, as shown in Table 3, at the end of >260 hours (h) test, there was a net weight increase observed on the target sample at both impact angles. It is believed that increase in weight of the sample could be due to several factors, including adhesion of alumina nanoparticles as well as material eroded from the polymeric pump gears on the sample surface. This adhesion of particles precluded the determination of actual sample weight loss (and erosion rate) from the impinging nanofluid. At the end of the experiment, weight measurement of pump gears revealed about 10% weight loss.

**Table 3.** Al 3003 Erosion Test Data Using Alumina Nanofluid

| Impact Angle (°) | Velocity (m/s) | Time (h) | Wt. Gain (mg) |
|---|---|---|---|
| 90 | 5.0 | 308 | 3.3± 0.2 |
| 30 | 5.0 | 260 | 4.0± 0.2 |

## Issues & Future Directions

Understanding mechanism(s) of weight loss of target metal is vital to developing predictive models to describe the erosion behavior from nanofluids. At the present time, it appears that erosion behavior by nanofluids is not severe. However, it is not conclusive because of the experimental issues discussed above. It is believed that the difficulty associated with repeatability of experiments is related to experimental challenge of pumping at stable requisite velocities. In this regard, several approaches are being undertaken: (a) use of Cu nanofluids (which are softer than ceramic nanoparticles and will not damage the pump components) and (b) use pump gears made of hardened steel or ceramic.

Furthermore, a parallel study to investigate the wear properties using nanofluids will be explored. Friction and wear behavior using base radiator fluid composition and a nanofluid will be studied using a ball-on-disk test set-up. This study will help in understanding the role nanoparticles play in introducing damage in the target radiator material.

## Conclusions

An apparatus to measure the erosion of radiator materials using nanofluids has been constructed. Baseline data indicates that no erosion of Al 3003 occurs using ethylene glycol/water solution for 90°–30° impact angles with velocities as high as 10 m/s. Erosion tests using CNT and alumina nanofluids did not conclusively show any erosion for Al 3003. Experimentation using Cu nanofluids and/or hardened pump gear material has been initiated. Wear properties of nanofluids will be explored.

## References

Eastman, J.A., S.U.S. Choi, S. Li, W. Yu, and L.J. Thompson, "Anomalously Increased Effective Thermal Conductivities of Ethylene Glycol-Based Nano-Fluids Containing Copper Nano-Particles," *Applied Physics Letters*, 78, 718–720 (2001).

Choi, S.U.S., Z.G. Zhang, W. Yu, F.E. Lockwood, and E.A. Grulke, "Anomalous Thermal Conductivity Enhancement in Nano-tube Suspensions," *Applied Physics Letters*, 79, 2252–2254 (2001).

Wong, D., L. Swette, and F.H. Cocks, "Aluminum Corrosion in Uninhibited Ethylene Glycol-water Solutions," J. Electrochem. Soc., 126, 11–15 (1979).

# II.F. Thermal Analysis of an Off-Road Machine Engine with Combined Use of 1-D Network Flow and 3-D CFD Simulation Techniques

*Principal Investigators: Tanju Sofu and Jimmy Chang*
*Argonne National Laboratory*
*9700 S. Cass Avenue, Argonne, Illinois 60439*
*(630) 252-9673, fax: (630) 252-4500, e-mail: tsofu@anl.gov, chang@anl.gov*

*Field Project Manager: John Hull*
*Argonne National Laboratory*
*9700 S. Cass Avenue, Argonne, Illinois 60439*
*(630) 252-8580, fax: (630) 252-5568, e-mail: jhull@anl.gov*

*Technology Development Managers: Sid Diamond and Lee Slezak*
*(202) 586-2335, fax: (202) 586-2476, e-mail: Lee.Slezak@hq.doe.gov*

---

*Contractor: Argonne National Laboratory*
*Contract No.: W-31-109-ENG-38*

---

## Objective

Assessment of a novel simulation technique based on combined use of three-dimensional (3-D) computational fluid dynamics (CFD) and one-dimensional (1-D) network flow models for predicting underhood air flow and temperatures and identification of possible hot-spots in separated engine compartment of an off-road machine.

## Approach

A prototypical test-rig that includes an engine and other installation hardware was built by the engineers at Caterpillar and the experiments were conducted with controlled ventilation air inlet locations and flow rates as part of a Cooperative Research and Development Agreement (CRADA) between Argonne National Laboratory and Caterpillar, Inc. Analytical efforts focused on combined use of a 1-D network flow model with three loops and engine structure to simulate the engine thermal system, and a 3-D CFD model for the ventilation air circulation in the test rig. The end product was a validated integrated analysis capability that needs only flow rates and inlet temperatures to study the effects of ventilation on heat rejection and component temperatures.

## Accomplishments

Five different inlet configurations were studied for various ventilation flow rates, and the corresponding flow field and temperature distributions were calculated. The results were used to determine the pressure drop through the test-rig, the flow splits around the engine, the heat-transfer coefficients on the engine and other heat-generating component surfaces, convection heat with the ventilation air, and the air and surface temperatures on various thermocouple locations. Using the data from Caterpillar experiments, the calculated temperatures using the 1-D network flow and the CFD models are compared with the measured temperatures.

## Future Direction

The model developed as part of this effort is proposed to be applied to other heavy-vehicle configurations through a CRADA with Cummins, Inc., on thermal analysis of diesel engines with exhaust-gas recirculation systems.

---

## Introduction

Mostly due to sound reduction requirements, modern off-road machines are designed with separate engine and cooling system compartments. Since high underhood temperatures can reduce component durability and life, the assessment of component temperatures in a relatively well-sealed engine enclosure is important. The main thermal management challenge for such a configuration is to determine the ventilation needs in the engine enclosure and its effect on the thermal balance.

To provide insight, a prototypical test-rig that includes an engine and other installation hardware for a typical medium size off-highway machine was built by the engineers at Caterpillar, Inc. Small doors installed at five sides of the enclosure (front, back, intake side, exhaust side, and bottom) served as ventilation air inlet locations. An external blower installed in the outlet pipe at the top was used to control the ventilation air flow rate. This combination of fixed outlet and varying inlet locations helped understand the effect of inlet location on critical component temperatures. The engine coolant temperature and the compressed air temperature at the intake manifold were maintained by laboratory heat exchangers and instrumented to account for the heat rejection closely. The ventilation air and component surface temperatures were measured at various locations.

An assessment of various simulation methods was performed at Argonne National Laboratory (ANL) for predicting underhood ventilation air flow field and temperatures in the test-rig. The analytical effort consisted of combined use of a 1-D network flow model to simulate the engine and the cooling systems, and a 3-D CFD model for the ventilation air circulation in the test rig. The goal was to provide an integrated analysis capability that needs only the flow rates and inlet temperatures as boundary conditions to assure adequate air cooling and to help identify potential hot-spots.

## Model Development

A computer-aided design (CAD) model of the test rig, provided by Caterpillar, was used to develop a 3-D CFD model of the test rig using the commercial CFD code STAR-CD. The CFD model consisted of approximately 1.34 million fluid cells with 8-millimeter (mm) resolution to capture the geometric details of the engine and other installation hardware inside the enclosure. The ventilation air flow field was simulated as a steady incompressible flow, decoupled from the energy equation using constant thermo-physical properties. This allowed a two-step analysis in which first the flow field is established inside the enclosure and then the temperature distributions were obtained for a given set of thermal boundary conditions. The simulations were performed using the high-Reynolds number k-ε turbulence model with logarithmic wall functions.

Each inlet configuration was analyzed for various ventilation air flow rates using the measured gauge pressure in the outlet pipe to specify the inlet and outlet pressure boundary conditions. This pressure-difference driven flow between the inlet plenum and outlet pipe provides more consistent flow distributions and improves the CFD model predictions to better account for the heat rejected through the ventilation air in the engine compartment. To scale the results for different engine configurations, the ventilation air flow rate is expressed relative to the engine combustion air flow rate. This air flow ratio was varied from 0.5 to 3.75 during the experiments and 0.5–2.5 in calculations. In traditional underhood compartment with no service wall to separate engine from cooling systems, the airflow ratio is close to ten.

As part of the analytical efforts, a 1-D thermal-fluid network model was also developed using the commercial software FLOWMASTER. In the 1-D model, the air, coolant, and oil loops were represented as separate thermal subsystems interacting with each other and the engine structure through discrete heat transfer paths. Through integration of these separate subsystems, the thermal interactions of the engine structure with the air, coolant and oil loops were simulated to predict pressure, temperature, heat, and fluid flow distributions in reduced dimensions.

In both the 1-D network and 3-D CFD models, the engine structure and muffler dump the heat into ventilation air through convective heat transfer. In 1-D model, the ventilation air entering the enclosure was considered to split around the engine block at

proportions specified by the CFD model and gain heat as it passes through individual surface points on the engine based on known contact surface area and the specified heat transfer coefficient. The radiative heat transfer is not included in the analysis. The ongoing simulation efforts at Caterpillar for design of next-generation vehicles using this integrated analysis approach will include radiative heat transfer and provide an estimation for the uncertainty caused by the neglecting the radiative heat transfer with the current model.

In the lubrication oil loop of the 1-D network model, the oil is supplied in three separate branches as follows: (1) to the turbo and back to the sump, (2) to the cylinder head where the oil gains heat from the valve cover, the cylinder head, and the upper engine block and then returns to the sump, and (3) to the engine block where it gains heat from the piston rings and the lower engine block and then returns to the sump. The oil circuit does not remove heat but redistributes it in the system. In the coolant loop, the water flows at a specified rate through the oil cooler in the lubrication circuit, circulates inside the upper engine block, and then flows back through the cylinder head. The radiator is simply modeled as an infinite heat and mass source/sink providing a steady flow of coolant with constant temperature.

This 1-D model serves as a tool to analyze the interactions of the engine with the air, coolant, and oil loops for predicting the complete thermal system performance, and to account for overall energy balance. The combustion process is included as a heat source with known heat rejection to the cylinder head, liner and piston. The exhaust gases are treated as the flows through the muffler assuming that they are at the same temperature.

The surface heat flux boundary conditions for the CFD model were deduced from the calculated surface and bulk ventilation air temperatures. In return, the results of the 3-D CFD analysis were used to provide the 1-D model with improved ventilation air flow paths and the resulting heat transfer coefficients between the heat generating components and the ventilation air. Since the 3-D CFD model requires component heat fluxes from the 1-D network flow model while the 1-D model requires accurate estimates of heat transfer coefficient, an iterative procedure was employed between the two models to obtain consistent solutions. The iterations between the CFD and network models continued until the difference in heat transfer coefficients between two subsequent steps were negligible (about 1% on average).

## Results

The ventilation air flow paths and temperatures as well as the surface temperatures in the test-rig are calculated for all five inlet configurations and five different air-flow ratios. In agreement with the experimental observations, the CFD results indicate a well mixed flow inside the enclosure with no significant difference in flow field and temperature distributions for different inlet locations. The flow field suggests significant turbulence inside the enclosure since the average "*turbulent viscosity*" is two orders of magnitude greater than the molecular viscosity of air even with such low flow.

To provide the 1-D thermal-fluid network model with an accurate measure of ventilation air flow paths around the engine for different inlet configurations, the computational domain is considered in six interconnected zones around the engine and the flow splits are determined from the flow rates through the surfaces separating these zones. When normalized with respect to the inlet flow rate, the calculated splits for each inlet configuration are found to be generally independent of the inlet flow rate. When the CFD results indicate counter flow patterns on one side of the engine, the calculated flow splits based on net flux across that side underestimate the near-surface flow rates. Therefore, the flow splits used in the 1-D network flow model were adjusted to better account for the influence of near surface jets after comparing the analytical predictions with the experimental data.

Using the flow rates reported in the experiments, the CFD model generally under-predicts the pressure drop based on the current geometric definition of the test rig. This is perhaps due in part to omitted details in the model (various hoses and instrument wires). Since the estimated total heat convected via the ventilation air is also under-predicted, an error in flow rate measurements were assumed and an alternative approach was implemented based on

calculating the convective heat transfer using the experimentally obtained inlet/outlet pressures as the boundary conditions.

With that modification, the estimations for the convected heat with the ventilation air and the area averaged outlet temperatures exhibit trends consistent with the experiments for all inlet configurations. The convected heat from the engine enclosure increases proportionally with the increase in ventilation air flow rate. However, the area-averaged outlet temperatures in the outlet pipe decrease non-linearly with flow rate and stabilize at the air-flow ratio of 2.0. For all inlet configurations, the temperatures are significantly higher on the exhaust side of the engine, particularly near the muffler and turbo charger.

In order to predict the temperature distributions in the test rig using only the coolant and air inlet temperatures and flow rates, the thermal calculations are performed using the surface heat fluxes as the boundary conditions based on the results of the 1-D simulations. Consistent with the nodalization of the 1-D model, the constant heat flux values are specified for the entire surface of a heat generating components. The portions of the enclosure wall near the muffler are also considered as heat transfer surfaces to account for their radiative heating from much higher muffler and tutbo-charger temperatures. The final set of heat transfer coefficients, as estimated by the CFD model and used in 1-D simulations, follow a predictable trend and increase almost proportionally with air flow ratio within the studied range.

In FY05, the coupled calculations are performed for all five inlet configurations, each for five different ventilation flow rates. The final CRADA reports documenting the details of 3-D CFD and 1-D network flow models are prepared and distributed. The reports include the full set of results including the heat-transfer coefficients on the engine and other heat-generating component surfaces, estimates for the convected heat with the ventilation air as part of the overall energy balance, and the temperatures on various thermocouple locations in the test rig.

Using the data from Caterpillar experiments, the calculated temperatures using the 1-D network flow and the CFD models are also compared with the measured component and fluid temperatures. As an example, the comparisons of measured and calculated ventilation air, coolant water, and oil temperatures for air-flow ratio of 1.5 are shown in Figures 1–5 for different air inlet locations. Figure 6 displays the comparison of calculated outlet temperatures for all five inlet configurations for the same air flow rate. Most of the predictions with the 1-D network model (including surface temperatures) are within 10% of the experimental values. For a complex network of engine and its thermal subsystems of coolant, oil, and ventilation air, these small discrepancies are considered satisfactory.

## Conclusions

An assessment of combined 1-D and 3-D simulation methods was completed for predicting ventilation air flow and underhood temperatures in a separated engine compartment of an off-road machine. The 1-D network flow model was built to simulate the thermal interactions between air, coolant and oil circuits through the engine structure, and to account for overall energy balance. The CFD model was built to determine the 3-D flow field and the rate of heat transfer between engine and ventilation air inside the enclosure. Consistency between the results of 3-D and 1-D models was achieved through an iterative co-simulation scheme in which the surface and ventilation air temperatures are calculated with the network flow model and used to deduce the heat flux boundary conditions for the CFD model. In return, the heat transfer coefficients are revised by the CFD model for the next round of 1-D calculations.

The coupled calculations were performed for five different inlet configurations (front, bottom, rear, intake-side, and exhaust-side of enclosure) each for a broad range of ventilation air flow rates. Consistent with the experimental observations, the results indicate a well-mixed flow inside the enclosure with no significant difference in flow field and temperature distributions for different ventilation inlet locations. The comparisons with experimental data indicate that the temperatures and distributed heat rejection rates can be estimated with a good accuracy when 3-D and 1-D models are used in combination.

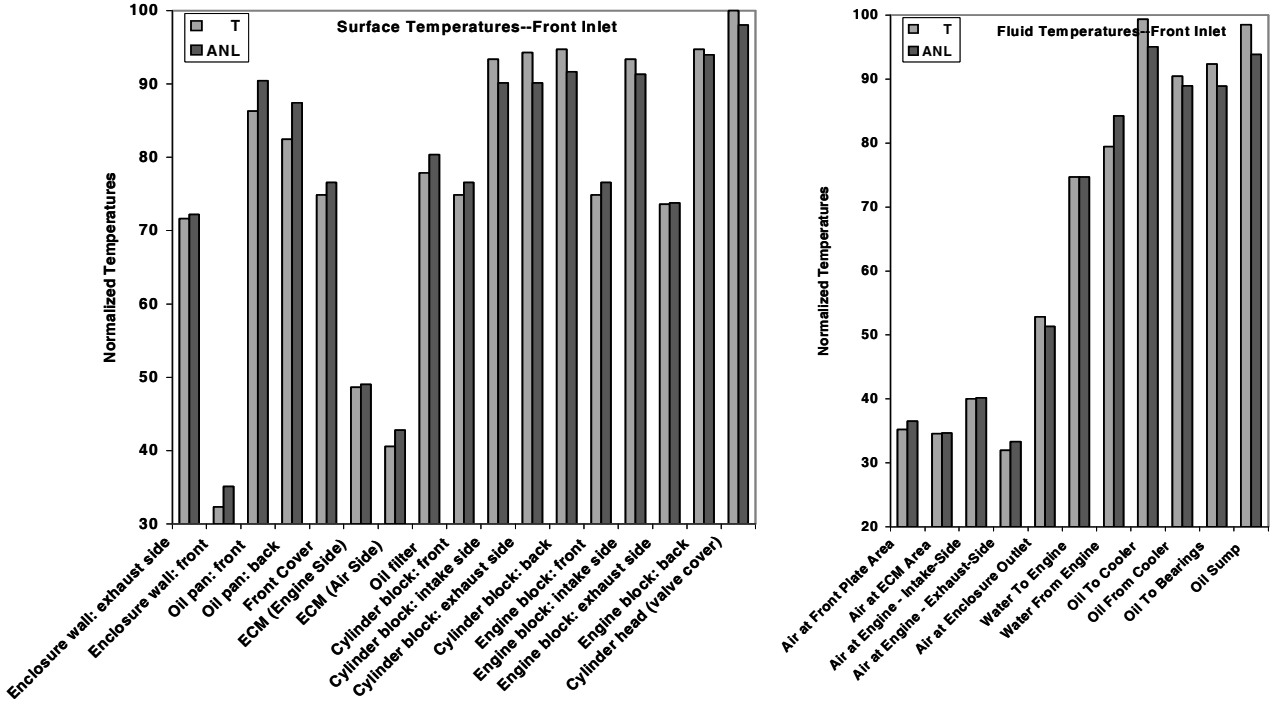


(a) (b)

**Figure 1.** Comparison of temperatures between measured data and model predictions for front inlet with airflow ratio 1.5: (a) surface temperatures and (b) fluid temperatures

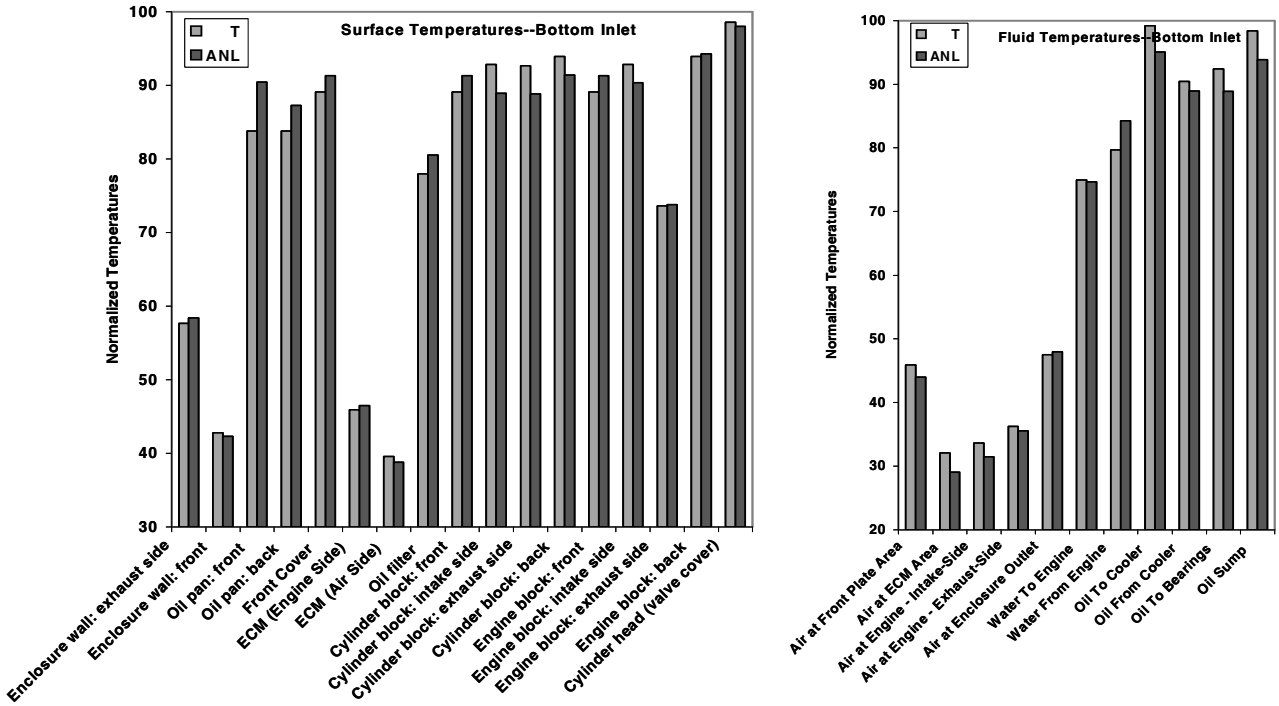


(a) (b)

**Figure 2.** Comparison of temperatures between measured data and model predictions for bottom inlet with airflow ratio 1.5: (a) surface temperatures and (b) fluid temperatures

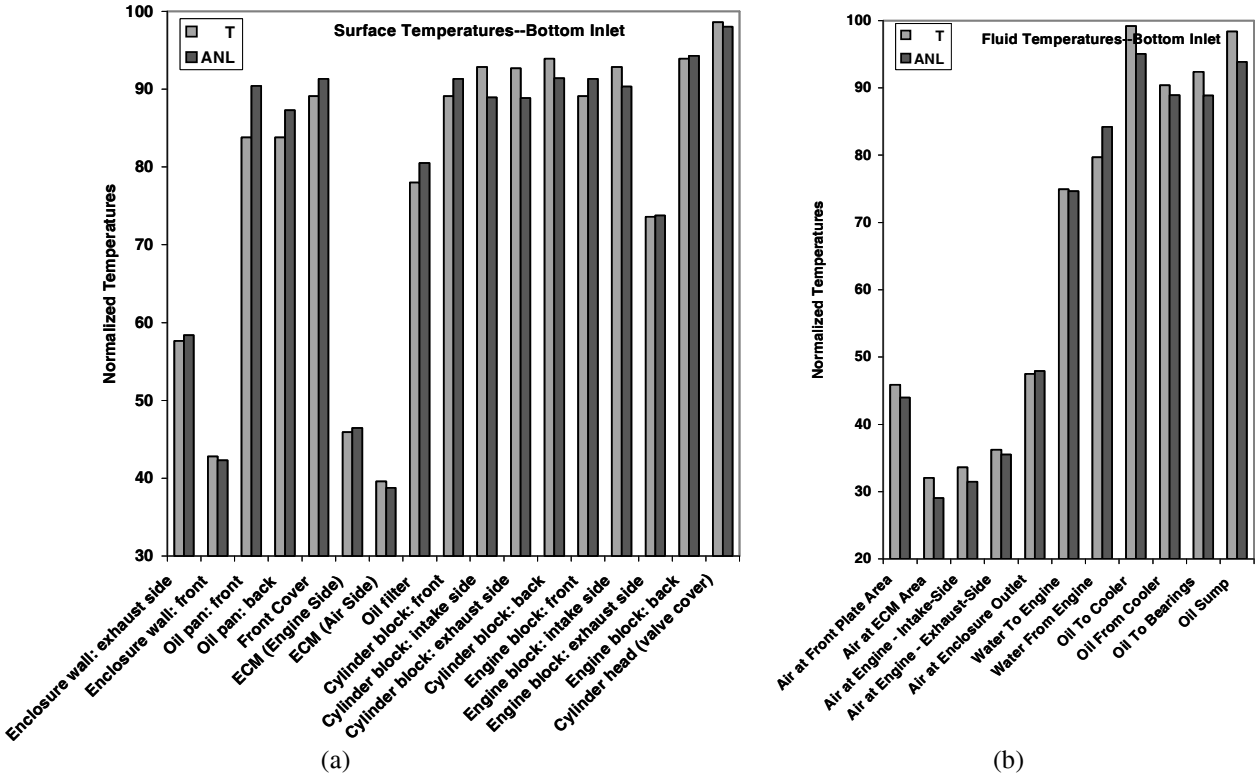


**Figure 3.** Comparison of temperatures between measured data and model predictions for rear inlet with airflow ratio 1.5: (a) surface temperatures and (b) fluid temperatures

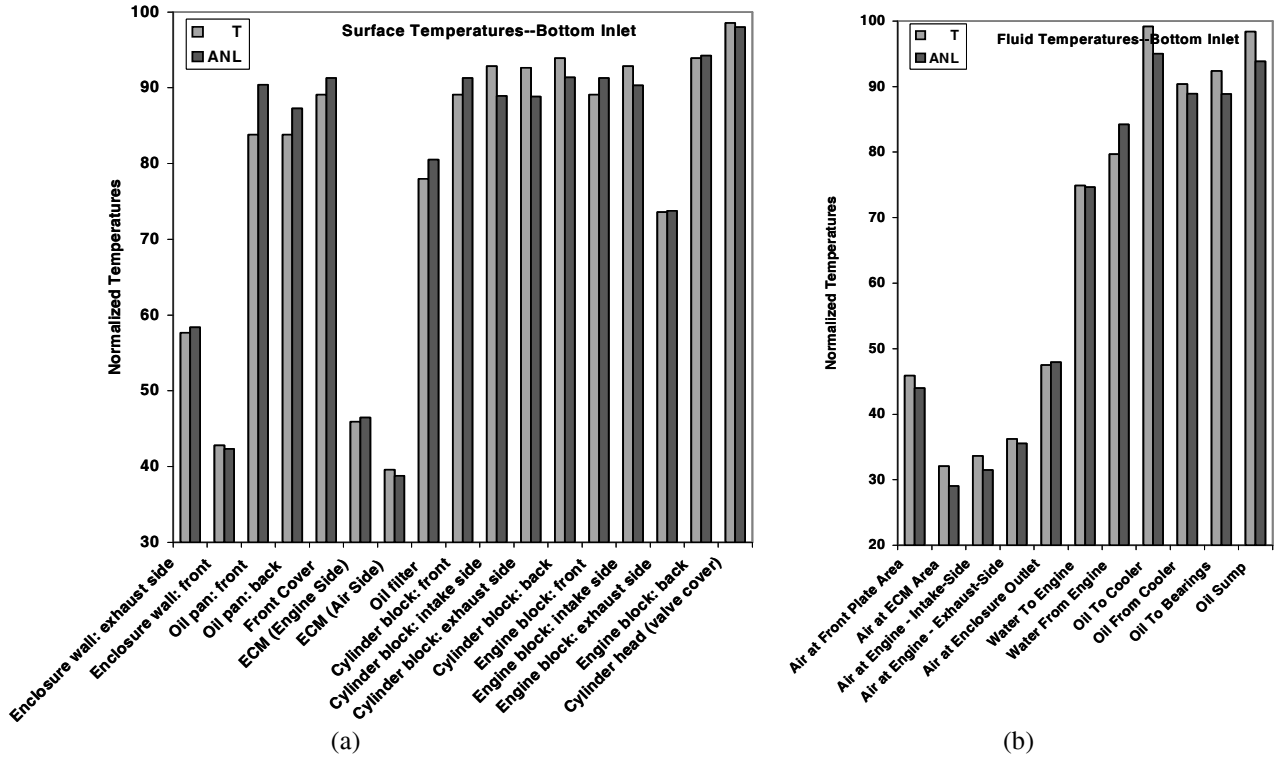


**Figure 4.** Comparison of temperatures between measured data and model predictions for intake-side inlet with airflow ratio 1.5: (a) surface temperatures and (b) fluid temperatures

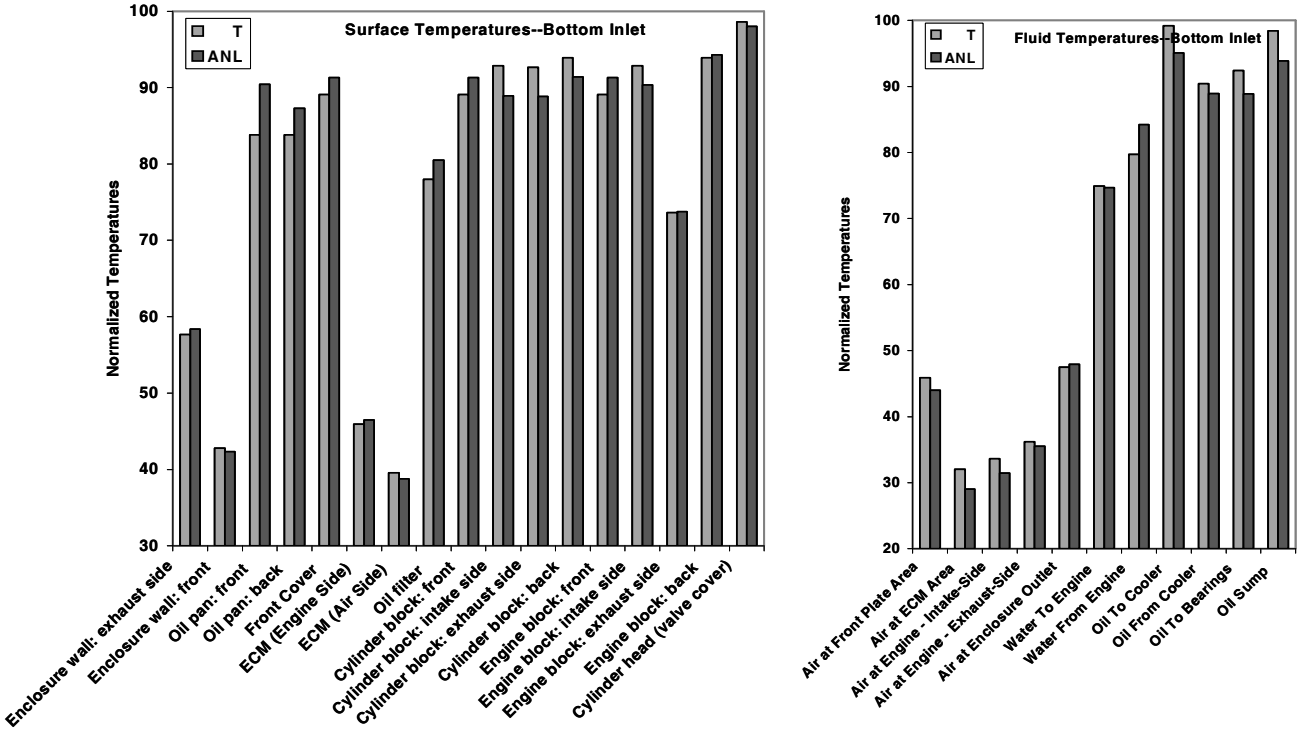


(a) (b)

**Figure 5.** Comparison of temperatures between measured data and model predictions for exhaust-side inlet with airflow ratio 1.5: (a) surface temperatures and (b) fluid temperatures

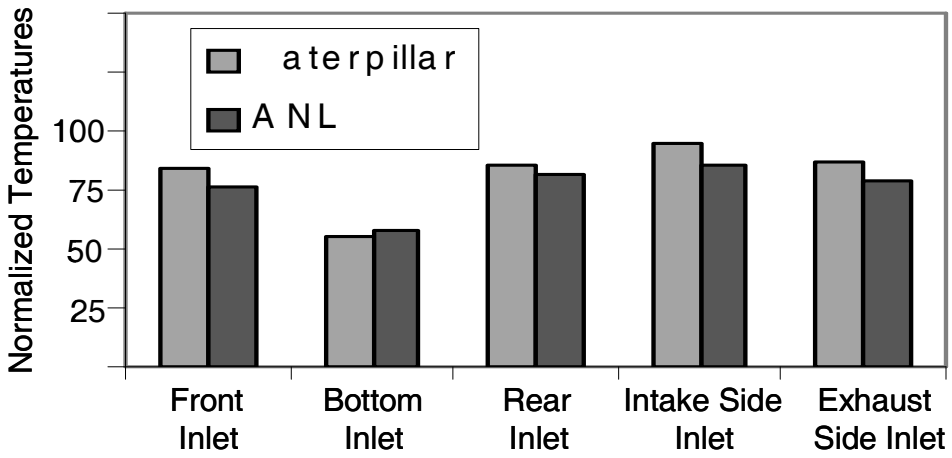


**Figure 6.** Enclosure outlet air temperature (normalized) as a function of inlet locations (airflow ratio 1.5)

# III. FRICTION AND WEAR

## III.A. Boundary Lubrication Mechanisms

*Principal Investigators: O.O. Ajayi, J.G. Hershberger, and G.R. Fenske*
*Argonne National Laboratory*
*9700 South Cass Avenue, Argonne, IL 60439*
*(630) 252-9021, fax: (630) 252-4798, e-mail: ajayi@anl.gov*

*Technology Development Managers: Sid Diamond and Lee Slezak*
*(202) 586-2335, e-mail: Lee.Slezak@hq.doe.gov*
*Technical Program Manager: Jules Routbort*
*(630) 252-5065, e-mail: routbort@anl.gov*

---

*Contractor: Argonne National Laboratory, Argonne, Illinois*
*Prime Contract No.: W-31-109-Eng-38.*

---

### Objectives

Develop a better understanding of the mechanisms and reactions that occur on component surfaces under boundary lubrication regimes with the ultimate goal of friction and wear reduction in oil-lubricated components and systems in heavy vehicles. Specific objectives are:

- Determine the basic mechanisms of catastrophic failure in lubricated surfaces in terms of materials behavior. This will facilitate the design of higher power density components and systems.
- Determine the basic mechanisms of chemical boundary lubrication. This will facilitate lubricant and surface design for minimum frictional properties.
- Establish and validate methodologies for predicting performance and failure of lubricated components and systems.
- Integrate coating and lubrication technologies for maximum enhancement of lubricated-surface performance.
- Transfer the technology developed to original equipment manufacturers (OEMs) of diesel engine and vehicle components and systems.

### Approach

- Characterize the dynamic changes in the near-surface material during scuffing. Formulate a material-behavior-based scuffing mechanism.
- Determine the chemical kinetics of boundary film formation and loss rate by *in situ* X-ray characterization of tribological interfaces at the Advanced Photon Source (APS) of Argonne National Laboratory (ANL).
- Characterize the physical, mechanical, and tribological properties of tribochemical films, including the failure mechanisms.
- Integrate the performance and failure mechanisms of all the structural elements of a lubricated interface to formulate a method for predicting performance and/or failure; this task will include incorporation of surface coatings.

- Maintain continuous collaboration with OEMs of heavy vehicle systems to facilitate effective technology transfer.

## Accomplishments

- Conducted extensive characterization of microstructural changes during scuffing of 4340 steel, using scanning electron microscopy (SEM) and X-ray analysis.
- Developed a model of scuffing initiation based on an adiabatic shear instability mechanism.
- Formulated a preliminary model of scuffing propagation based on a balance between heat generation and heat dissipation rates.
- Characterized the mechanical properties and scuffing resistance of a graded nanocrystalline surface layer produced by the scuffing process.
- Using X-ray fluorescence, reflectivity, and diffraction at the APS, demonstrated the ability to characterize tribochemical films generated from model oil additives.
- Designed and constructed an X-ray accessible tribo-tester for *in situ* study of boundary film formation and loss rates.

## Future Directions

- Experimentally validate the comprehensive scuffing theory for various engineering materials, including ceramics.
- Develop and evaluate methods and technologies to prevent scuffing in heavily loaded oil-lubricated components and systems.
- Using X-ray-based and other surface analytical techniques, continue to characterize tribochemical films formed by model lubricant additives.
- Characterize the physical, mechanical, and failure mechanisms of tribochemical films with nano-contact probe devices.
- Evaluate the impact of various surface technologies, such as coating and laser texturing, on boundary lubrication mechanisms.

---

## Introduction

Many critical components in diesel engines and transportation vehicle subsystems are oil-lubricated. Satisfactory performance of these components and systems is achieved through the integration of materials, surface finish, and lubricant oil formulation technologies. To that end, an Edisonian trial-and-error approach is often followed. Indeed, experience is likely the sole basis for new design and solutions to failure problems in lubricated components. With more severe operating conditions expected for component surfaces in advanced engines and vehicle systems, the trial-and-error approach to effective lubrication is inadequate and certainly inefficient. Departure from this approach will require a better understanding of the fundamentals of both boundary lubrication and surface failure mechanisms.

A major area of focus for the Department of Energy in the development of diesel engine technology for heavy vehicles is emission reduction. Some essential oil lubricants and diesel-fuel additives, such as sulfur, phosphorus, and chlorine, are known to poison the catalysts in emission-reducing after-treatment devices. Although reduction or elimination of these additives will make emission aftertreatment devices more effective and durable, it will also render the surfaces of many lubricated components vulnerable to catastrophic failure. Many of the methods used to reduce diesel engine emissions may also render critical-component surfaces vulnerable to catastrophic failure, thereby compromising their reliability.

Increases in vehicle efficiency will require friction reduction and increase in power density in the engine and powertrain systems. Higher power density translates to increased severity of contact between many components. This, again, will compromise the reliability of various critical components, unless they are effectively lubricated. The efficacy of oil additives in reducing friction and in protecting component surfaces depends on the nature and extent of the chemical interactions between the component surface and the oil additives.

In addition to reliability issues, the durability of lubricated components also depends on the effectiveness of oil lubrication mechanisms. Components will eventually fail or wear out by various mechanisms and contact fatigue. Wear is the gradual removal of material from contacting surfaces, and it can occur by various mechanisms, such as abrasion, adhesion, and corrosion. Also, the repeated contact stress cycles to which component contact surfaces are subjected can initiate and propagate fatigue cracks and, ultimately, lead to the loss of a chunk of material from the surface. This damage mode is often referred to as "pitting." Wear and contact fatigue are both closely related to boundary lubrication mechanisms. Antiwear additives in lubricants are designed to form a wear-resistant protective layer on the surface. The role of lubricant additives on contact fatigue failure is not fully understood, although it is clear that the lubricant chemistry significantly affects contact fatigue. Again, lack of a comprehensive understanding of basic mechanisms of boundary lubrication is a major obstacle to a reasonable prediction of lubricated component and system durability.

Significant benefits would accrue by extending the drain interval for diesel engine oil, with an ultimate goal of a fill-for-life system. Successful implementation of the fill-for-life concept for the various lubricated systems in heavy vehicles requires optimization of surface lubrication through the integration of materials, lubricant, and, perhaps, coating technologies. Such an effort will require an adequate fundamental understanding of surface material behavior, chemical interactions between the material surface and the lubricant, and the behavior of material and lubricant over time.

Some common threads run through all of the challenges and problems in the area of surface lubrication of engine components and systems briefly described above. The two key ones are lack of adequate basic and quantitative understanding of the failure mechanisms of component surfaces, and lack of understanding of basic mechanisms of boundary lubrication, i.e., how lubricant chemistry and additives interact with rubbing surfaces, and how this affects performance in terms of friction and wear. To progress beyond the empirical trial-and-error approach for predicting lubricated component performance, a better understanding is required of the basic mechanisms regarding the events that occur on lubricated surfaces. Consequently, the primary objective of the present project is to determine the fundamental mechanisms of boundary lubrication and failure processes of lubricated surfaces. The technical approach taken in this study differs from the usual one of post-test characterization of lubricated surfaces — rather, it will involve developing and applying *in situ* characterization techniques for lubricated interfaces that will use the X-ray beam at the APS located at ANL. Using a combination of X-ray fluorescence, reflectivity, and diffraction techniques, we will study, in real time, the interactions between oil lubricants and their additives and the surfaces they lubricate. Such study will provide the basic mechanisms of boundary lubrication. In addition to surface chemical changes, materials aspects of various tribological failure mechanisms will be studied.

## Results and Discussion

Efforts during the past year (FY 2005) involved validation of the scuffing model for nonferrous materials and ceramics and refinement of the X-ray characterization of tribochemical boundary films.

### Scuffing Model Validation

In the last year, a scuffing theory based on adiabatic shear instability was developed to include both the initiation and the propagation stages. Scuffing initiation occurs when the rate of thermal softening as a result of heat generated by plastic deformation

exceeds the rate of work hardening due to increase in dislocation density associated with plastic deformation. Under such conditions, the plastic deformation process becomes unstable and a severe localized plasticity ensues, accompanied by a large amount of heat generation — scuffing initiation. Progression of scuffing to a catastrophic stage is dependent on whether its propagation occurs or not. Management of the heat generated by the initiation process guides the propagation stage. If the rate of heat dissipation from the initiation site exceeds the rate of heat generation from continued deformation, then scuffing does not propagate. If the rate of heat generation exceeds the rate of heat dissipation, scuffing will propagate into a runaway thermal process, ultimately resulting in a catastrophic failure. Both the rate of heat generation and the rate of heat dissipation are dependent on the thermal properties of the materials in sliding contact — notably, the heat capacity and the thermal conductivity.

For the validation of the model, scuffing tests using materials with significantly different thermal properties should show different scuffing behavior. Scuffing may initiate but not propagate easily in materials with high thermal conductivity. Similarly, scuffing may not initiate easily in materials with resistance to thermal softening. Scuffing tests were conducted with three materials having very different plastic and thermal properties. These materials are magnesium oxide (MgO), which is a ceramic with low thermal conductivity and high resistance to thermal softening; H-13 tool steel, which has moderate thermal conductivity and thermal softening; and aluminum alloy, which has high thermal conductivity and can thermally soften easily. Figure 1a shows the result of a typical scuffing test for single-crystal MgO ceramic. In this material, the scuffing propagation stage was very short, as indicated by only a single friction spike at the scuffing point. Scuffing in this material occurred by a combination of mechanisms involving dislocation motion and interactions during the scuffing test. Further work is ongoing to elucidate the details of the scuffing mechanism in this material. Knowledge gained in the study of this material will be part of the scheme to develop scuffing-resistant surfaces.

The result of the scuffing test with the H-13 tool steel is shown in Figure 1b. Here again, the scuffing process propagated to final failure after the initiation event. Apparently, the heat generated at the shear instability initiation site could not be dissipated fast enough to prevent scuffing propagation and the consequent catastrophic failure. In the tests with aluminum alloy, a series of scuffing initiation events was observed. Scuffing is indicated by the many friction spikes during the tests (Figure 1c). However, many of the initiated events did not propagate until one finally did, and the test

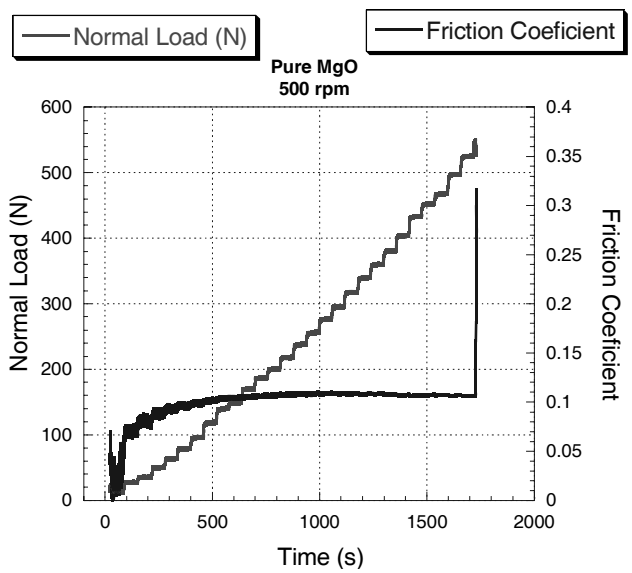


**Figure 1a.** Result of scuffing test with MgO single crystal showing friction coefficient as a function of step loading

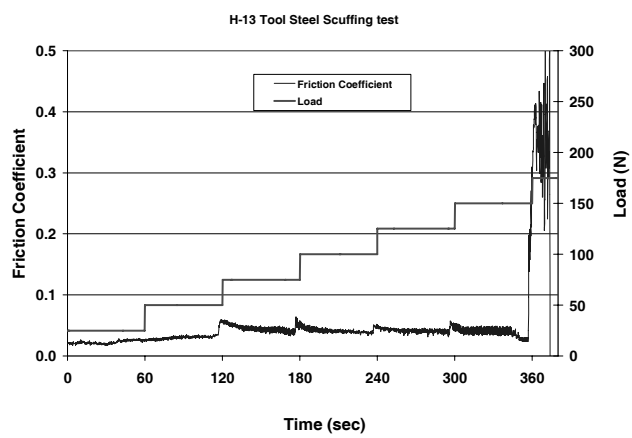


**Figure 1b.** Result of scuffing test with H-13 tool steel showing rapid propagation of scuffing once initiated. Scuffing is indicated by sudden and sustained rise in friction.

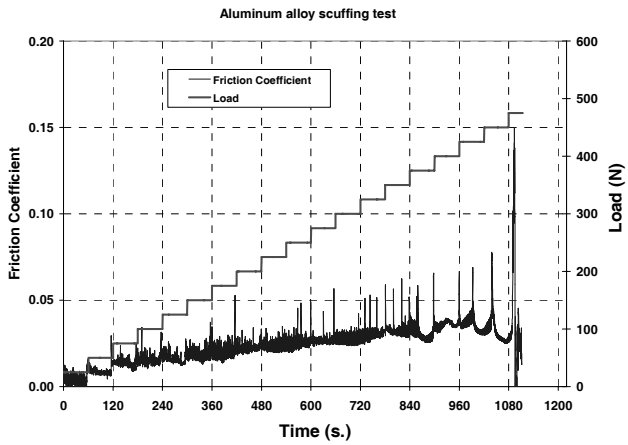


**Figure 1c.** Result of scuffing test with aluminum 6061 alloy showing series of scuffing initiation events, as indicated by the spikes in the friction coefficient, prior to the final scuffing failure

was terminated. The relatively high thermal conductivity of aluminum alloy allows quick dissipation of heat generated by the scuffing initiation process, thereby forestalling scuffing propagation until a point when the rate of heat generation finally exceeded the rate of heat dissipation.

Results from the scuffing tests with the three materials are all consistent with the predictions of our scuffing model based on adiabatic shear instability as the initiation mechanism and thermally driven plasticity as the propagation mechanism. This finding is quite significant. Mysteries surrounding the scuffing process are now solvable. Based on the model developed in this project, one can predict and perhaps control the occurrence of scuffing based on material properties.

## X-ray Characterization of Boundary Films

With the successful demonstration of X-ray-based surface analytical techniques to characterize boundary films, the main focus of this past year's effort in characterization of the tribochemical boundary film was the design and construction of an X-ray-accessible tribo-tester. Such a system will be needed for *in situ* characterization of boundary films. Because of the time availability constraint in a user facility such as the APS, the tribo-tester system will be developed and refined in a laboratory benchtop system. Once completed and performance assessment is satisfactory, the system will be used at APS with appropriate X-ray techniques.

Figure 2 shows a schematic diagram and picture of the new tribo-tester system. It uses an existing commercial pin-on-disc high-temperature test rig and an existing X-ray fluorescence (XRF) detector.

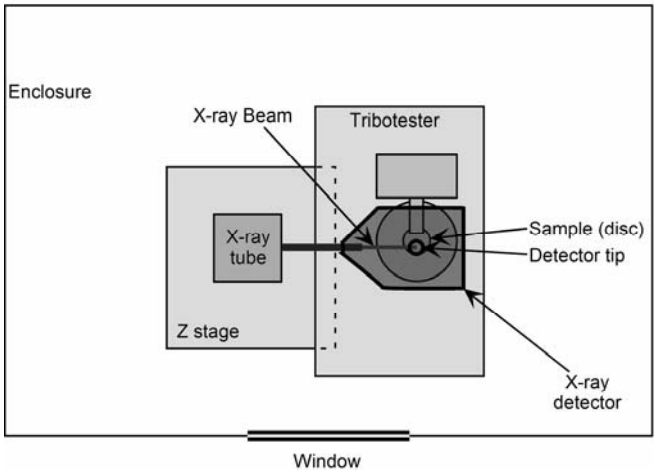


**Figure 2a.** Schematic diagram

**Figure 2b.** Photograph

**Figure 2.** Schematic diagram and photograph of the new X-ray-accessible tribo-tester system for *in situ* characterization of boundary film formation using XRF analysis.

A new 30-kV X-ray source was integrated with the system. XRF analysis can be conducted concurrently with friction and wear testing. Both the XRF analysis and the friction data collection are done by the same computer, making it possible to correlate friction behavior with surface chemical changes as indicated by XRF.

Figure 3 shows results of preliminary a test conducted with #1018 steel lubricated with commercial fully formulated oil. The variations of the Zn atom concentration on the disc surface and the friction coefficient with test time are shown. The Zn atoms are from the most used oil antiwear additive, zinc dialkylditniophosphate (ZDDP). Although preliminary, the results appear to indicate an inverse relationship between the Zn atom concentration (tribochemical film formation) and the friction coefficient.

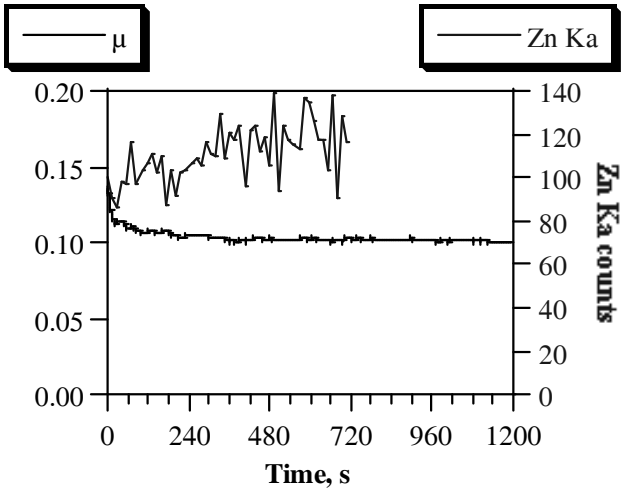


**Figure 3.** Preliminary test results from the X-ray-accessible tribo-tester showing the variation of Zn atom concentration and friction coefficient (μ) with time

## Conclusions

During FY2005, the efforts on this project were focused on the validation of the scuffing model. Using three materials with different pertinent properties, a two-step model of initiation and propagation stages for the scuffing mechanism was validated. MgO ceramic with high resistance to thermal softening and poor thermal conductivity exhibited the most resistance to scuffing initiation, but very rapid scuffing propagation. Similarly, H-13 tool steel had one initiation event, but slower propagation than MgO as a result of better thermal conductivity. Aluminum 6061 alloy, on the other hand, underwent a series of initiation events before final propagation. Higher thermal conductivity of aluminum facilitated faster dissipation of heat by the shear instability initiation mechanism. Observations from the three materials tested are all consistent with our scuffing model based on shear instability developed earlier in this project.

In the area of tribochemical film characterization, a new X-ray-accessible tribo-tester system was designed and constructed. In a preliminary test with the new rig, the variation of Zn atom concentration in the surface film as a function of test time was determined concurrently with the friction coefficient. This *in situ* test system will be used to determine the boundary film formation and loss rates during sliding contact of a lubricated surface.

## Publications

Ajayi, O.O., J. Hershberger, J. Zhang, H. Yoon, and G.R. Fenske, "Microstructural Evolution during Scuffing of 4340 Steel – Implication for Scuffing Mechanism," Tribology International 38 (2005) 277–282.

Hershberger, J., O.O. Ajayi, and G.R. Fenske, "Composition of ZDDP Films Formed Thermally and Mechanically," Tribology International 38 (2005) 299–303.

Hershberger, J., O.O. Ajayi, and G.R. Fenske, "Phase Transformation in Nickel during Tribotesting," Scripta Materialia, 53 (2005) 1449–1453.

# III.B. Parasitic Engine Loss

*Principal Investigators: George Fenske, Robert Erck, Ali Erdemir, and Layo Ajayi*
*Argonne National Laboratory*
*Argonne, IL 60439*
*(630) 252-5190, fax: (630) 252-4798, e-mail: gfenske@anl.gov*

*Technology Development Managers: Sid Diamond and Lee Slezak*
*(202) 586-2335, fax: (202) 586-2476, e-mail: Lee.Slezak@hq.doe.gov*
*Field Project Manager: Jules Routbort*
*(630) 252-5065, fax: (630) 252-4798, e-mail: routbort@anl.gov*

*Participants*
*Robert Erck, Argonne National Laboratory*
*Layo Ajayi, Argonne National Laboratory*
*Ali Erdemir, Argonne National Laboratory*
*James Kezerle, Ricardo Engineering*
*Isaac Fox, Ricardo Engineering (currently with Caterpillar, Inc.)*

---

*Contractor: Argonne National Laboratory*
*Contract No.: W-31-109-ENG-38*

---

## Objectives

- Develop and integrate mechanistic models of engine friction and wear to identify key sources of parasitic losses as functions of engine load, speed, and driving cycle.
- Develop advanced tribological systems (lubricants, surface metrology, and component materials/coatings) and model their impact on fuel efficiency with a goal to improve vehicle efficiency by 3% in FY 2012. Develop engine component maps to model impact for analytical system toolkits.
- Develop database of friction and wear properties required for mechanistic friction and wear models, baseline properties, and advanced systems (coatings, lubricant additives, engineered surface textures).
- Validate mechanistic models — perform instrumented, fired-engine tests on single- and multi-cylinder engine test stands to confirm system approaches to reduce friction and wear of key components.
- Integrate models into vehicle system codes — Powertrain System Analysis Toolkit (PSAT).

## Approach

- Predict fuel economy improvements over a wide range of oil viscosity using physics-based models of asperity and viscous losses.
- Model changes in contact severity loads on critical components that occur with low-viscosity lubricants.
- Develop and integrate advanced low-friction surface treatments (e.g., coatings, surface texturing, additives) into tribological systems.
- Measure friction and wear improvements on advanced lab rigs and fired engines to confirm model calculations.
- Develop component maps of parasitic energy losses for heavy vehicle system models.

## Accomplishments

- Modeled the impact of low-friction coatings and low-viscosity lubricants on fuel savings (up to 4%), and predicted the impact of low-viscosity lubricants on the wear/durability of critical engine components.
- Developed experimental protocols to evaluate the friction and wear performance of advanced engine materials, coatings, and surface treatments under prototypical piston/ring environments.
- Initiated lab testing of surface modified ring and liner components to optimize treatments for single-cylinder engine tests.

## Future Directions

- Apply superhard and low-friction coatings on actual engine components and demonstrate their usefulness in low-viscosity oils.
- Optimize coating composition, surface finish, thickness, and adhesion to achieve maximum fuel savings.
- Evaluate the impact of advanced lubricant additives on asperity friction.

## Introduction

Friction, wear, and lubrication impact energy efficiency, durability, and environmental soundness of critical transportation systems, including diesel engines. Total frictional losses in a typical diesel engine may alone account for more than 10% of the total fuel energy (depending on the engine size, driving conditions, etc.). The amount of emissions produced by diesel engines is related to each engine's fuel economy. In general, the higher the fuel economy, the lower the emissions. Higher fuel economy and lower emissions in future diesel engines may be achieved by the development and widespread use of novel materials, lubricants, and coatings. For example, with increased use of lower viscosity oils (which also contain the least amounts of sulfur and phosphorus-bearing additives), the fuel economy and environmental soundness of future engine systems can be dramatically improved. Furthermore, with the development and increased use of smart surface engineering and coating technologies, even higher fuel economy and better environmental soundness will be feasible.

Integration of advanced lubricant chemistries, textured/superfinished surfaces, and advanced component materials and coatings necessitates a systems approach. Changes in one system can readily change the performance of other system components. For example, application of a hard coating on a liner to improve its durability may negatively impact the durability of the mating rings. Lowering the viscous drag will cause certain components (e.g., bearings) to operate under boundary lubrication regimes not previously encountered resulting in accelerated degradation. It becomes clear that a systems approach is required to identify not only the critical components to address in terms of energy savings but also potential pitfalls and solutions.

The main goal of this project is to develop a suite of software packages that can predict the impact of smart surface engineering advanced coating technologies (e.g., laser dimpling, near-frictionless carbon, and superhard coatings), and energy-conserving lubricant additives on parasitic energy losses from diesel engine components. The project also aims to validate the predictions using experimental friction and wear studies at Argonne National Laboratory. Such information will help identify critical engine components that can benefit the most from the use of novel surface technologies, especially when low-viscosity engine oils are used to maximize the fuel economy of these engines by reducing churning and/or hydrodynamic losses. A longer-term objective is to develop a suite of computer codes capable of predicting the lifetime and durability of critical components exposed to low-viscosity lubricants.

Since FY 2003, Argonne and Ricardo, Inc., have collaborated to identify engine components that can benefit from low-friction coatings and/or surface treatments. The specific components considered included rings, piston skirt, piston pin bearings, crankshaft main and connecting rod bearings, and

cam bearings. Using computer codes, Ricardo quantified the impact of low-viscosity engine oils on fuel economy. Ricardo also identified conditions that can result in direct metal-to-metal contacts, which in turn can accelerate engine wear and asperity friction. Efforts were also initiated to identify approaches to validate the predictions under fired conditions.

Argonne also worked on the development and testing of a series of low-friction coatings under a wide range of sliding conditions using low- and high-viscosity engine oils. These coatings (such as near-frictionless carbon) as well as laser-textured surfaces were subjected to extensive tests using benchtop friction test rigs. The test conditions (i.e., speeds, loads, and temperatures) were selected to create conditions where direct metal-to-metal contacts will prevail as well as situations where mixed or hydrodynamic regimes will dominate. Using the ranges of frictional data generated by Argonne, Ricardo estimated the extent of potential energy savings in diesel engines and identified those components that can benefit the most from such low-friction coatings and/or surface treatments. Argonne developed a test rig to simulate engine conditions for piston rings sliding against cylinder liners — one of the major sources of parasitic energy losses identified in Ricardo's studies. Wear data generated by Argonne can be used to develop models and computer codes that predict the lifetime/durability of diesel engine components.

During FY 2005, Argonne worked with Ricardo to establish an instrumented, single-cylinder test bed (at the University of Michigan) capable of *in situ* friction force measurements between the cylinder liner and the piston/piston ring assembly — a major source of friction losses. Efforts also progressed on the development of a benchtop ring-on-liner test rig that will be used to the tribological conditions under which advanced surface treatments and additives optimally function.

## Results

The first two phases of this project with Ricardo focused on modeling the impact of low-friction surfaces and low-viscosity engine lubricants on friction losses and fuel economy. Figure 1 (Fox 2003) shows the friction losses (friction mean effective pressure [FMEP]) between the piston skirt and the cylinder liner for the engine modeled by Ricardo. Calculations performed for the rings, valvetrain components, and engine bearings were combined with the piston skirt calculations to determine their overall impact on FMEP and fuel consumption. The results predicted fuel savings up to 4–5% depending on lubricant viscosity grade and asperity friction.

Plans were established during FY 2005 for a Phase III activity to validate the calculations using a fired diesel engine. Several approaches were considered, including: (a) direct fuel consumption measurements in a running, mass-production, diesel engine; (b) friction force measurements in a running, mass-produced engine; and (c) friction force measurements in a running, single-cylinder test engine. The last approach (fired, single-cylinder test engine) was selected due to considerations of

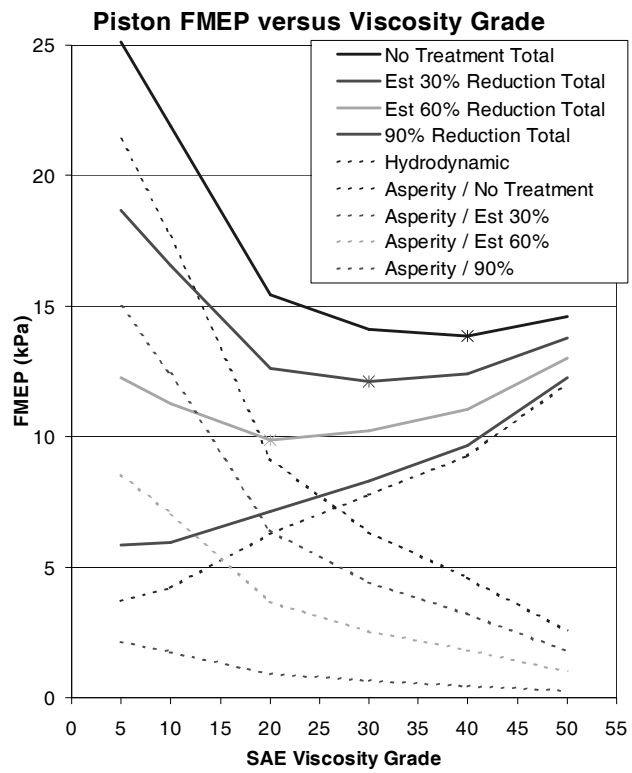


**Figure 1.** Friction mean effective pressure as a function of viscosity and asperity friction between the piston skirt and cylinder liner

simplicity and ability to accurately measure friction forces.

Three different concepts were considered to measure forces during operation. Force-difference methods based on cylinder-pressure and connecting rod strain measurements and floating liner methods based on load cell measurements of liner forces were ruled out due to large statistical errors associated with force-difference methods and gas leakage and structural vibration issues associated with floating liner methods. In the end, a fixed-sleeve method was chosen. The fixed-sleeve method employs strain gauges applied to a rigidly supported cylinder liner to measure the friction forces transmitted to the cylinder liner from the piston skirt and rings.

Figure 2 shows a schematic of the fixed-sleeve method. This concept will be used with a Ricardo Hydra test engine installed at the University of Michigan. With this method, a sliding sleeve is inserted inside a modified Hydra cylinder liner. The sleeve is fixed radially near its top by a supporting wire and is restrained axially by a locknut at its bottom. Axial forces on the sleeve are transmitted through the locknut joint to the liner. Friction forces are calculated from measured liner strain.

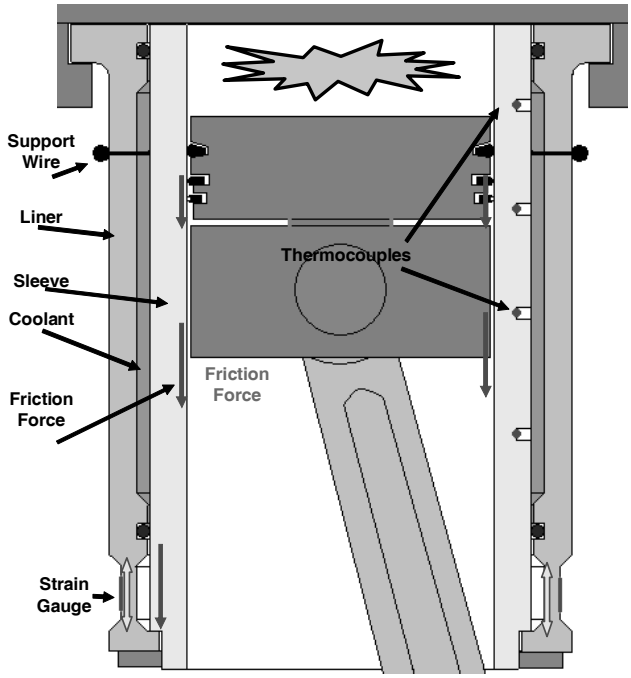


**Figure 2.** Schematic of the fixed-sleeve method that will be used to continuously monitor friction forces during fired operation of a single-cylinder diesel engine

Phase III activities are underway; the contract with Ricardo and the University of Michigan has been established. Plans for the first task of Phase III involve adapting the Hydra engine to accept fixed sleeve instruments for strain gauges and thermocouples. The second task will involve baselining the engine to obtain friction measurements at different engine conditions (speeds and loads) and lubricant viscosities. Subsequent tasks will concentrate on measurements using low-friction technologies (e.g., low-friction coatings, superfinishing, textured surfaces, and low-friction additives.

Experimental activities at Argonne concentrated on the development of a ring-on-liner rig to measure friction in an effort to confirm/validate asperity friction values used in the Ricardo models, to measure asperity friction of advanced low-friction technologies on prototype ring and liner components, and to integrate/optimize advanced technologies for rings, liners, and pistons.

Figures 3 shows a schematic of the test configuration used with the ring-on-liner rig. The system uses segments of rings and liners obtained from standard rings and liners, currently 137- and 145-millimeter (mm) diameter liners — comparable to those modeled by Ricardo. The system, shown in Figure 4 is capable of applying loads up to 2,000 Newtons (N), speeds up to 10 Hertz (Hz), strokes up to 37 mm, and temperatures to 300° Celsius (C). Data recorded

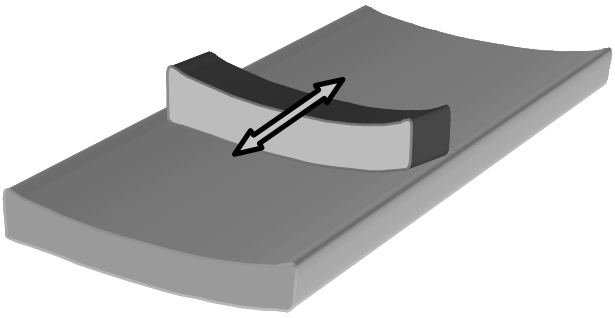

**Figure 3.** Schematic of the ring-on-liner test rig developed to measure friction under prototypic ring, piston, and liner conditions

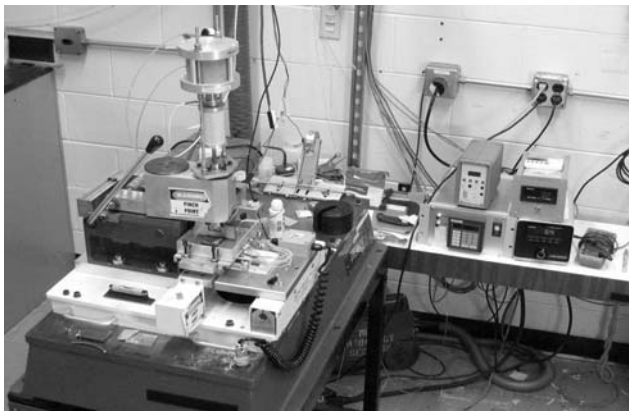

**Figure 4.** Photograph of the ring-on-liner test rig

during the tests include: friction forces, temperature, ring position, and contact resistance (between the ring and liner) at rates in excess of 2,000 Hz. High data acquisition rates (e.g., 2,000 Hz) are used to obtained flash shots of the friction, position, and contact resistance during each stroke. Such information provides detailed data required to determine which lubrication regime (boundary, mixed, or hydrodynamic) is dominant during the stroke.

For example, Figure 5 shows the friction as a function of time for a stock CrN-coated ring sliding against a stock liner, half of which was dimpled using an advanced laser texturing process developed by Technion University. This particular run was performed with a load of 100N at a reciprocating rate of 1 Hz (60 rpm). At the point of stroke reversal

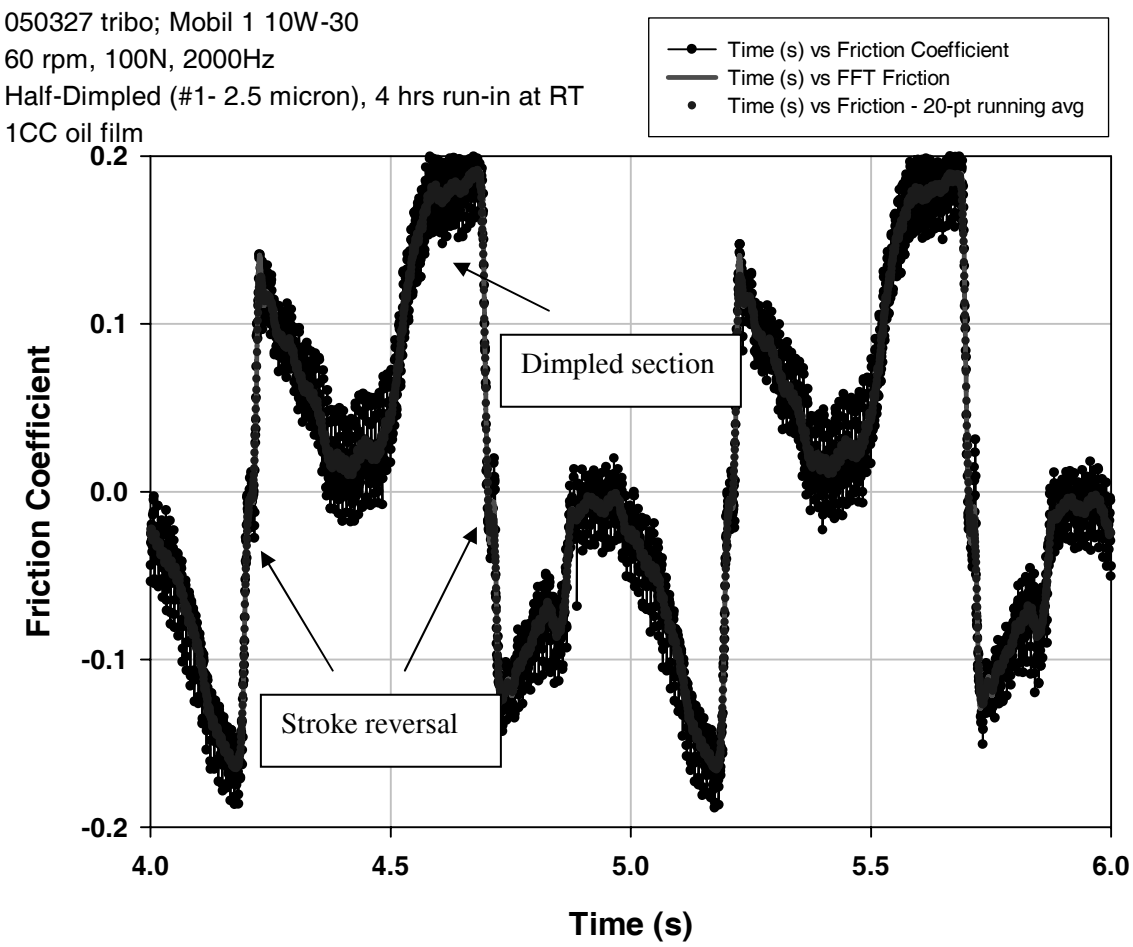


**Figure 5.** Friction as a function of time during a ring-on-liner test on a half-dimpled liner

where the speed is near zero, boundary lubrication is dominant with a friction coefficient around 0.12. As the velocity increases, the lubrication regime transitions to a mixed lubrication regime (indicated by a decrease in friction). At or near midstroke where the ring starts to ride on the dimpled surface, the friction increases suddenly — indicating a transition back to boundary lubrication. Closer examination of the dimpled surface after the ring-on-liner tests revealed the reason for the high boundary friction behavior (see Figure 6). In this case, the rims that are typically produced during the laser texturing process are still intact. The rims seen in Figure 6 are typically quite readily removed by gentle rubbing, however, in the current situation, it is evident that the rims are still present, and thus it is not unexpected to see the high friction. Indeed, friction measurements at the end of a 24-hour run revealed that the friction coefficient in the dimpled region had begun decrease indicative that the rims were being removed. Tests are planned for FY 2006 to develop polishing techniques to remove the rims and retest them.

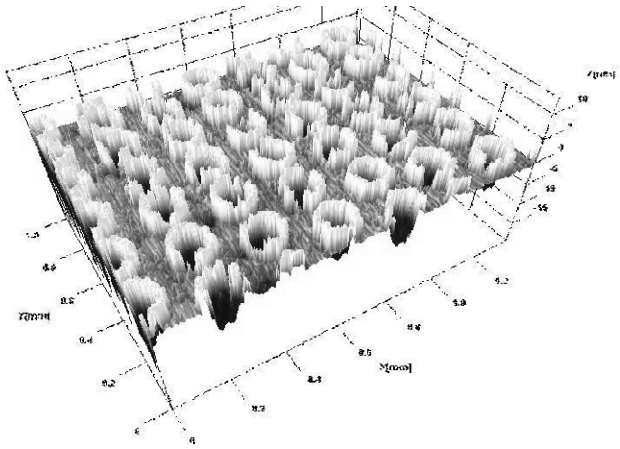

**Figure 6.** Three-dimensional micrograph of dimpled surface after ring-on-liner tests

Another example of the use of the ring-on-liner rig to evaluate potential friction-reducing technologies is shown in Figures 7a and 7b. Figure 7a shows the friction coefficient as a function of position for a ring-on-liner test performed using a stock CrN-coated ring sliding against a stock liner, while Figure 7b shows the same data with a friction-reducing additive (boric acid) added to the lubricant. Both cases in Figures 7a and 7b were performed at 60 rpm with a 250 N load at room temperature. The lubricant was a formulated 10W-30 synthetic lubricant. The only difference between the two was the addition of a boric acid solution to the lubricant. Figure 7a represents the untreated lubricant, while Figure 7b represents the friction after 5 to 10 minutes of operation with the boric acid additive. Both figures indicate the film is under boundary lubrication conditions. One can see that the friction for the curves in Figure 7b are lower than the friction for the nontreated case in Figure 7a. The straight, horizontal lines in both figures are the position-averaged friction coefficients. The non-treated case (Figure 7a) had an average friction coefficient of 0.12 while the treated case (Figure 7b) exhibited an average friction coefficient slightly less than 0.11 — an 8–9% decrease in friction.

## Summary

Computer simulation of parasitic energy losses in diesel engines indicate fuel savings up to 5% can be achieved through the use of low-viscosity engine lubricants and low-friction surface treatments. Work is currently underway to experimentally validate the models using a fired, single-cylinder diesel test rig outfitted with an instrumented fixed sleeve to measure the friction forces continuously as a function crank angle.

A ring-on-liner test rig was developed and brought online to validate the friction coefficient data used to model the parasitic friction losses, as well as to optimize advanced surface modification technologies for engine applications. Examples were given for two technologies: a boric acid-based lubricant additive, and a surface texturing technique. Both technologies, in addition to the use of low-friction coatings will be further examined and optimized in FY 2006 in preparation for fired engine tests on the instrumented Hydra test engine in FY 2007.

## Reference

Fox, I., "Numerical Evaluation of the Potential for Fuel Economy Improvement due to Boundary Friction Reduction within Heavy-Duty Diesel Engines," ECI International Conf. on Boundary Layer Lubrication, Copper Mountain, CO, Aug. 2003.

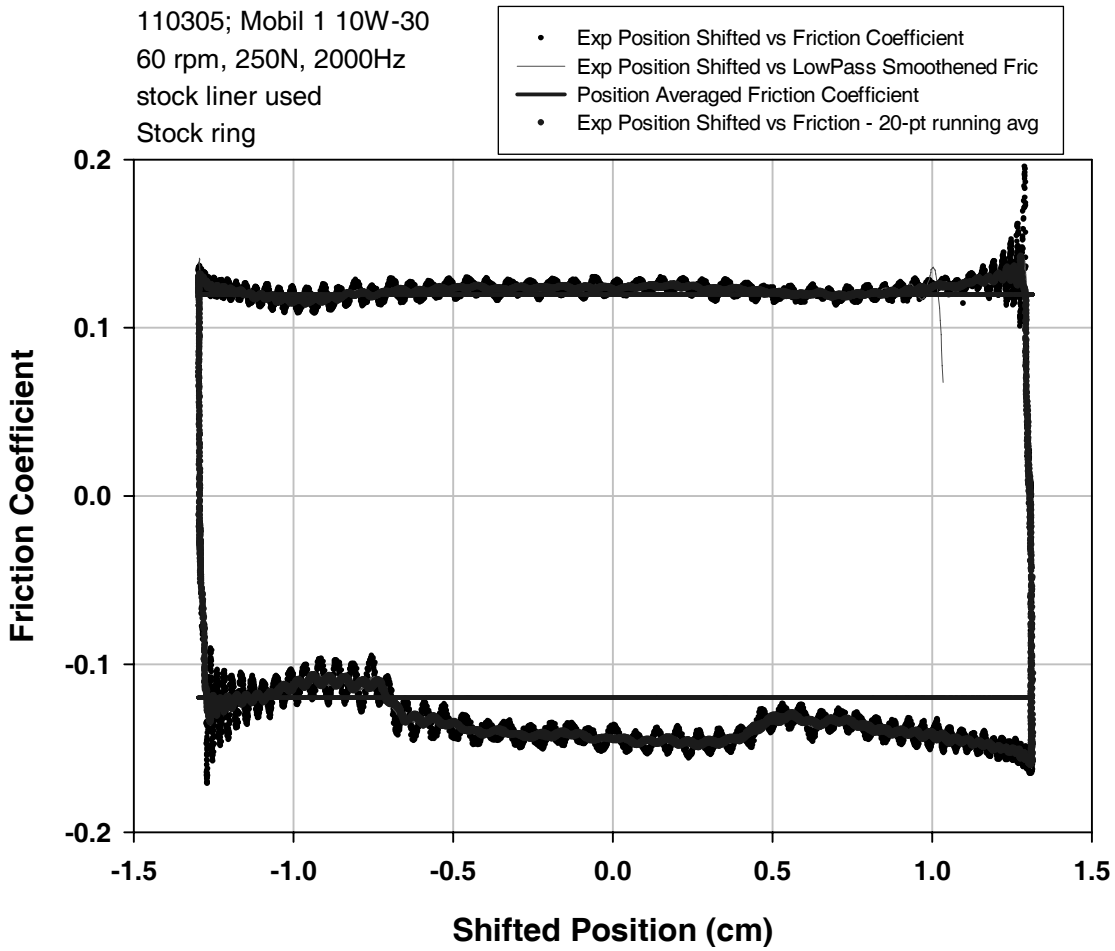


**Figure 7a.** Friction as a function of position for a CrN ring sliding against a stock liner segment in formulated 10W-30 synthetic oil

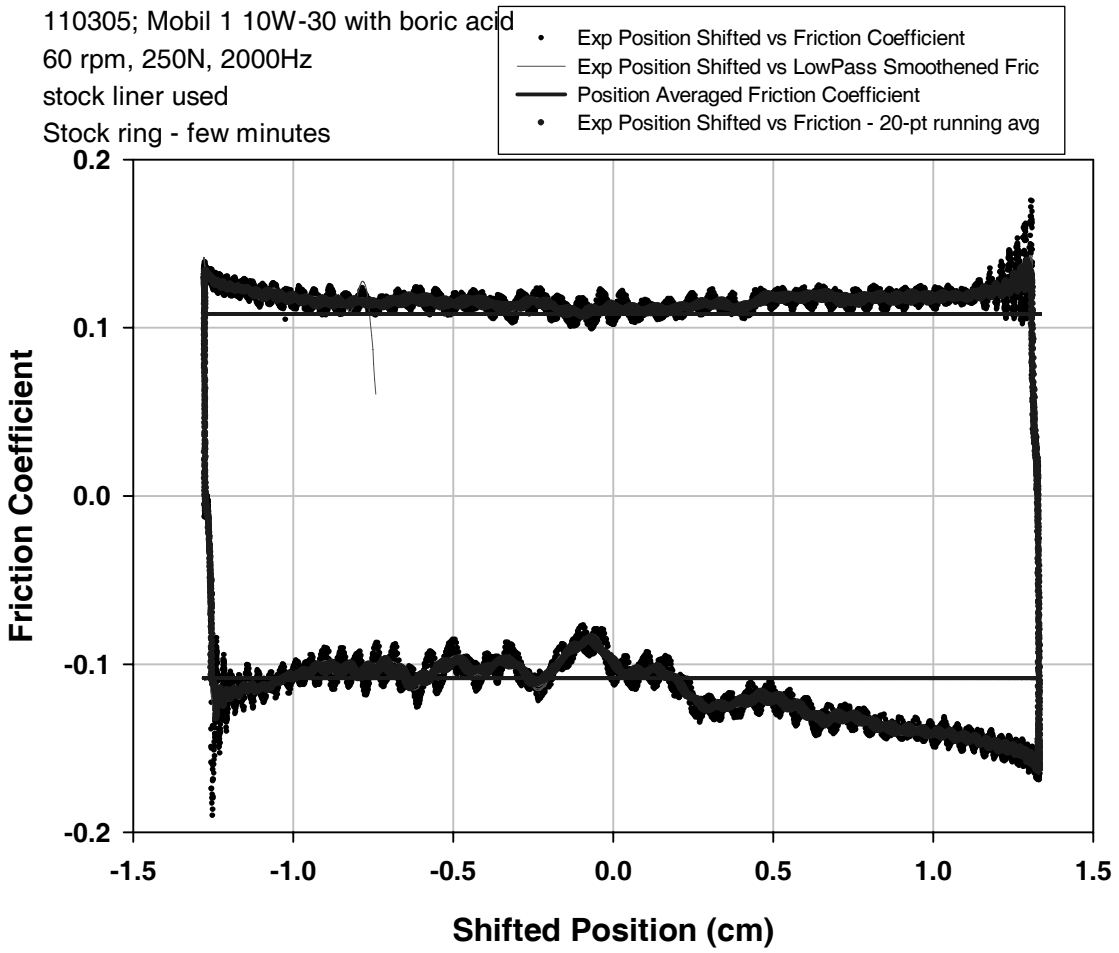


**Figure 7b.** Friction as a function of position for a CrN ring sliding against a stock liner segment in formulated 10W-30 synthetic oil with a boric acid additive

# III.C. Efficiency Improvement Through Reduction of Friction and Wear in Powertrain Systems

*Principal Investigator: Bohdan Lisowsky*
*Eaton Corporation*
*Innovation Center*
*26201 Northwestern Highway*
*Southfield, MI 48037*
*(248) 226-6219, fax: (248) 226-7166, e-mail: bohdanlisowsky@eaton.com*

*DOE Project Officer: Carl P. Maronde*
*National Energy Technology Laboratory*
*Pittsburgh, PA 15236-0940*
*(412) 386-6402, fax: (412) 386-4775, e-mail: carl.maronde@netl.doe.gov*

*Technology Development Managers: Sid Diamond and Lee A. Slezak*
*U.S. Department of Energy, FreedomCAR and Vehicle Technologies*
*(202) 586-2335, fax: (202) 586-2476, email: Lee.Slezak@hq.doe.gov*

*Technical Program Manager: Jules L. Routbort*
*(630) 252-5065, fax: (630) 252-4289, e-mail: jules.routbort@anl.gov*

*Participants*
*Jian Zhang, Diann Hua, Tom Beveridge, Caterpillar Inc.*
*Oyelayo Ajayi, George Fenske, Ali Erdemir, Jeff Hershberger, Argonne National Laboratory*
*Jane Wang, Leon Keer, Northwestern University*
*Dong Zhu, Zahedul Huq, Eaton Corporation, Innovation Center*

---

*Contractor: Eaton Corporation, 4201 North 27th Street, Milwaukee WI 53216*
*Contract No.: DE-FC26-04NT42263*

---

## Objectives

- Reduce friction and parasitic energy loss by 30–50% in truck transmissions and axles used in Class 3–8 trucks by conducting research and development resulting in an integrated procedure for component design and analysis for minimizing friction and oil churning losses without compromise in performance and durability.
  - During the first three years, develop computer simulation tools for various contact geometries to predict friction, interface temperatures, wear, and other performance parameters for gears, bearings, seals, and oil churning losses. These simulation tools will be calibrated and validated utilizing coupon fixture testing and component bench testing.
  - During the following two years, integrate the various simulation tools into a design procedure and prove its utility by designing specific components for transmissions and axles and conducting limited testing on dynamometers and vehicles.
- Identify potential commercialization strategies for efficiency improvement methods in transmissions and axles.

## Approach

- Reduce boundary friction through development of boundary film technologies, which involves low-friction materials, coatings, and lubricant additives. (Figure 1)
- Reduce hydrodynamic friction and churning loss via advanced lubrication technologies, improved system design, lubricant properties, and surface texturing.
- Optimize design parameters, operating conditions, and surface finish processes to minimize the severity of surface contact and maximize hydrodynamic lubrication effectiveness through next-generation integrated design and analysis tools.
- Develop surface failure analysis and prediction tools and their correlation with experimental data to improve the component design for longer life and higher reliability.

## Accomplishments

- Developed rough surface contact model for gears and verified it using both literature-reported data and laboratory experiments and coupon testing. The model can compute friction, interfacial temperatures, and contact stresses for specific operating conditions and oils.
- Using coupon bench testing, determined that significant reductions in friction could be achieved by improving surface roughness, generating specific texturing, and lubricant selection. Work continues on understanding the effect of coatings and their interaction with lubricants.
- Established a boundary film characterization capability at Argonne National Laboratory using an *in situ* real-time glancing X-ray diffraction technique, while a test was being performed.

## Future Directions

- Develop modeling capability for boundary lubrication and integrate all modeling modules into a design capability for prediction of friction and durability of contacting surfaces.
- Continue coupon testing and begin component testing to verify selection of specific surfaces, coatings, lubricants, and additives for friction reduction without adverse effects on durability.
- Conduct limited field tests to verify energy efficiency gains of a selected truck driveline and develop required durability data.
- Develop commercialization approaches for the best value surface treatments and lubricant conditions.

---

## Introduction

Truck powertrains typically utilize gear designs of spur, helical, spiral bevel, and hypoid geometry. Designs have been developed with single and multiple countershafts for considerations of load sharing, dynamics, weight, and packaging. Specific designs have been governed historically by material bulk strength and currently by noise and surface failure related issues. Typically, they have not been optimized for fuel efficiency. The ISO (International Standards Organization) and AGMA (American Gear Manufacturers Association) gear design and strength calculation standards currently used in industries, for example, mainly focus on simplified design methods for tooth bending and pitting strength.

Considerable heat generation and temperature increase in oil sumps indicate that they all have significant frictional losses during operation, although nominally those geared devices are supposed to have high efficiency under highway cruising conditions. In heavy-duty transmissions and axles, sources for parasitic losses typically include:

| | |
|---|---|
| Gear tooth contact friction: | 25–70% |
| Oil churning: | 15–35% |
| Bearings and thrust washers: | 10–25% |
| Seals/other parts (as shift yoke/shaft): | 10–20% |

The actual percentage breakdown in a specific case depends on the duty cycle, speed, torque, lubrication condition, design, and manufacturing processes as well as the number of pairs of gears engaged.

For most gears, the surface average roughness after machining is in the range of 70–150 micro (μ)-inches after shaving (40–60 μ-inches) while some critical gears may be ground (20–40 μ-inches), lapped (20–60 μ-inches), or honed (10–30 μ-inches) at significantly increased costs. These levels of roughness are still too high for standard lubricants to prevent significant surface asperity contacts, high friction, wear, and energy losses. Transmissions and axles use splash lubrication systems for most applications. This has been proven to be adequate for most power levels. However, the sump level optimization has been an issue, because a low sump level may result in poor lubricant supply and increased contact friction/surface failure in components, but a high sump level would result in more significant churning loss.

The most commonly used surface treatments for gears, shafts, and other powertrain components include carburizing, nitriding and shot-peening, which improve durability but do not reduce friction. Numerous low-friction coatings, solid lubricants, and advanced surface modifications such as ion beam and laser treatments have been intensively studied, but unsolved technical and cost difficulties prevent immediate commercialization. For instance, the interaction between coatings and lubricant additives has not been well understood.

Preliminary investigations have demonstrated, both experimentally and analytically, that improved surface finish and some advanced surface treatments could reduce friction and increase component life significantly. In addition, information has been published claiming that by careful formulation of low-viscosity lubricants, significant fuel economy improvements are possible. By creation of integrated computer-based modeling capability, optimization of the various parameters cited above,

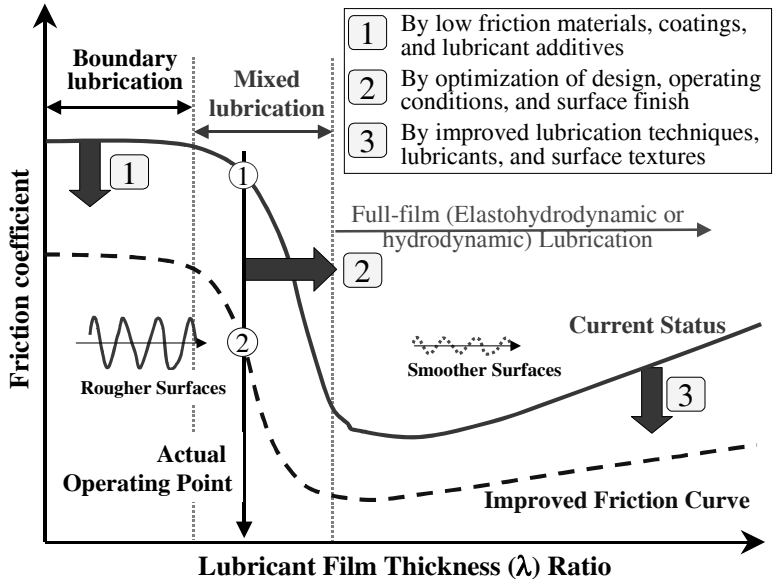


**Figure 1.** Strategy for friction reduction in truck drivelines — move the Stribeck curve down and to the right by reducing boundary friction [region 1] (through materials, oil additives, and coating selection), reducing boundary friction [region 2] (primarily through surface roughness optimization for given stress condition), and reducing hydrodynamic friction [region 3] (primarily by optimization of lubricants and surface texturing).

which affect friction and durability, will provide the optimum fuel savings at the best possible customer value leading to commercialization.

## Project Team

The project team integrates expertise in surface engineering, tribological testing, and modeling, as well as product development and manufacturing. Eaton Corporation, one of the largest truck and auto component suppliers in the world, is well qualified to be at the leading position for development and commercialization of the next-generation powertrain design and manufacturing technologies. Caterpillar Inc. is a leading diesel engine and off-highway truck producer having extensive knowledge and experience in tribology-related research and development (R&D) and product development. Northwestern University and Argonne National Laboratory (ANL) are well recognized as technology leaders in the areas of friction and lubrication modeling, testing, wear and pitting failure analysis, low-friction materials and coatings, and other surface modifications. The combined ability of the team establishes a strong research environment to tackle this technologically difficult project and provides a very good position for commercialization.

## Project Structure and Roles

The project structure is shown in Figure 2. The work conducted in this first year of a planned five-year project focused on Tasks 1–10, but excluded Task 9. Eaton leads Tasks 1, 7, and 10. Caterpillar leads Tasks 2 and 8. Argonne leads Tasks 3 and 4. Northwestern leads Tasks 5 and 6.

This progress report uses topical areas for progress presentation. Each topic combines theoretical and experimental work and results, as appropriate, generated under various tasks in the project structure. This approach is used to allow the reader for easier comprehension and integration of the project activities and results.

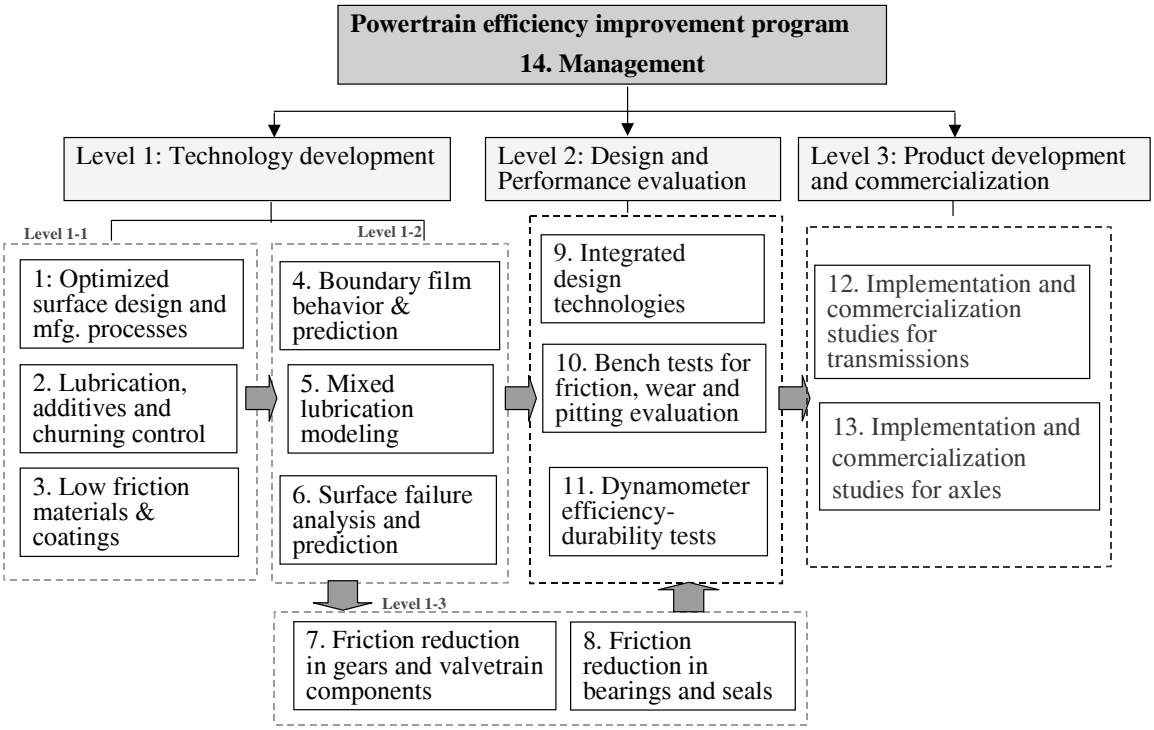


**Figure 2.** Project structure: three project levels, tasks, and information flow for project conduct

## Effect of Surface Topography on Friction

The effects of topography have been studied using bench testing and an improved computer model. Bench testing comprises of pin-on-ring and roller-on-roller rolling contact fatigue configurations. The computer model used for the analyses was calibrated and verified using smooth surface contact theory and experimental measurement. The comparison of the computed and measured traction (or friction) coefficient is shown in Figure 3 for two different oils. Utilizing computational modeling, friction results for various surfaces can be quickly computed. This calibrated computational capability allows rapid analysis of similar and dissimilar surfaces with different surface orientations and other topographical characteristics. Modeling results are shown Table 1. The surface conditions in Table 1 are shown in ascending average surface roughness. Depending on the surface finishing conditions, a similar process may generate different friction levels as well as seemingly better surface conditions (i.e., dimpled). In addition, it has been experimentally demonstrated that surface roughness may change as a function of test time. A coarse level of roughness will result either a pitting failure, if the contact loads are excessive, or smoother surfaces resulting in lower friction.

The model will be extended to accommodate surface changes as a function of running time and tribological conditions. This model is the first module for integrated design capability, a deliverable for future years.

**Table 1.** Friction Coefficient as a Function of Surface Condition at Constant Tribological Parameters

| Surface Contact Condition | Friction Coefficient |
|---|---|
| Theoretically Smooth | 0.026 |
| Polished - condition #1 | 0.035 |
| Polished - condition #2 | 0.059 |
| Turned | 0.042 |
| Honed - condition #1 | 0.049 |
| Honed - condition #2 | 0.0495 |
| Dimpled - Condition 31 | 0.06 |
| Hobbed & Shaved | 0.068 |
| CBN Ground | 0.073 |

Work has been initiated to develop a special technique for deterministic a computer-efficient analyses of journal-bearings in mixed lubrication conditions using a coarse mesh to determine their elastic deformation, while a local refined mesh is used for the effect of roughness.

## Effect of Surface Topography on Durability

In order to generate a commercially meaningful integrated model, surface durability must be incorporated so that optimization of the low friction and high durability can be achieved. To that end, a model for pitting life prediction is under development. A simple model for prediction of the

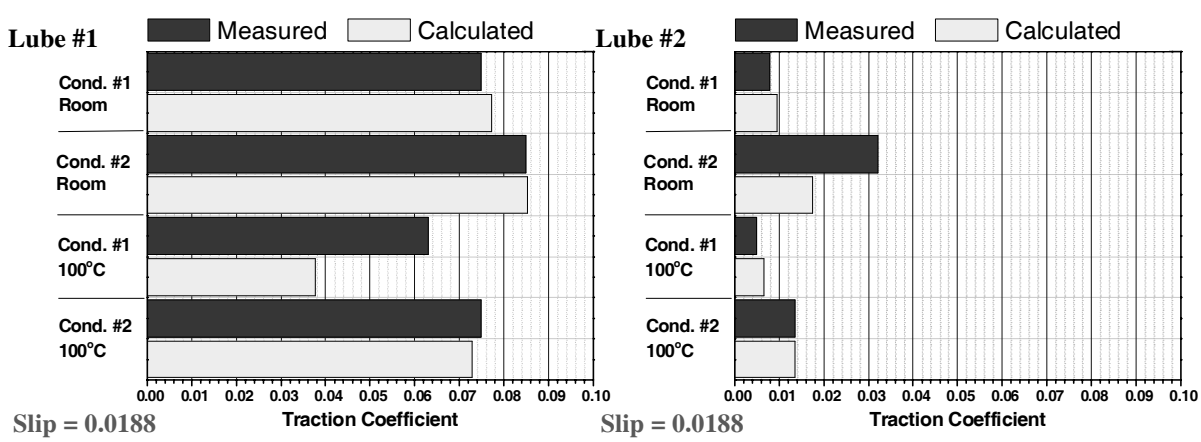


**Figure 3.** Comparison of the measured and calculated traction (friction) coefficient for two different lubricants under different tribological conditions. Condition #1 = Low Pressure / High Speed; Condition #2 = High Pressure / Low Speed. The other two permutations have also been modeled and agreement between computed and actual friction is quite good.

results of an elastic-perfectly plastic contact simulation was developed. The location and magnitude of the maximum stress was found to be a function of the size of the smallest significant asperity, material properties, and operating conditions. This model can be used as a tool for quick estimates of the upper bound of the maximum stress distribution in rough surface contact. The model is also capable of determining the transition load, for a given set of tibological conditions, required to maintain the maximum shear stress in the subsurface region for specific rough surface contact conditions. To obtain high durability, the stress level needs to be reasonably low and located below the surface.

Once the maximum stress location and magnitude is known, crack formation and growth need to be predicted, again to provide another necessary model for integration. An assessment was made that the FATG3D, previously developed at Northwestern University, can yield an accurate analysis of intensity factors, and it is capable of dealing with multiple cracks and their coalescence into larger cracks or one large crack.

## Lubricant Effect on Friction and Power Loss

There is a significant potential to reduce contact friction by developing new formulations. The automotive sector is leading this technology, which is now being expanded into the truck industry. The effect of lubricant on friction has been studied utilizing rotating ball-on-disk, "3 mailbox"-pins-on-ring (6.35 millimeter (mm) radius cylindrical line contact), and actual very limited dynamometer tests. The rotating-ball-on-disk, often known as the Wedevan test, has been used to evaluate hydrodynamic effects on different oils and the influence of operating conditions. Although additive, the hydrodynamic contribution to friction is relatively low in the mixed lubrication regime. Boundary friction strongly controls the friction performance of mixed lubrication. The reduction of the boundary friction coefficient from 0.1 down to 0.07–0.08 may reduce the total friction for hobbed/shaved to as low as about 0.05–0.06 and for isotropic polishing to 0.03–0.04, as computed by the use of the above-mentioned modeling capability. The computational results showed that when the boundary friction is reduced about 30%, the total friction reduction for the shaved surfaces is about

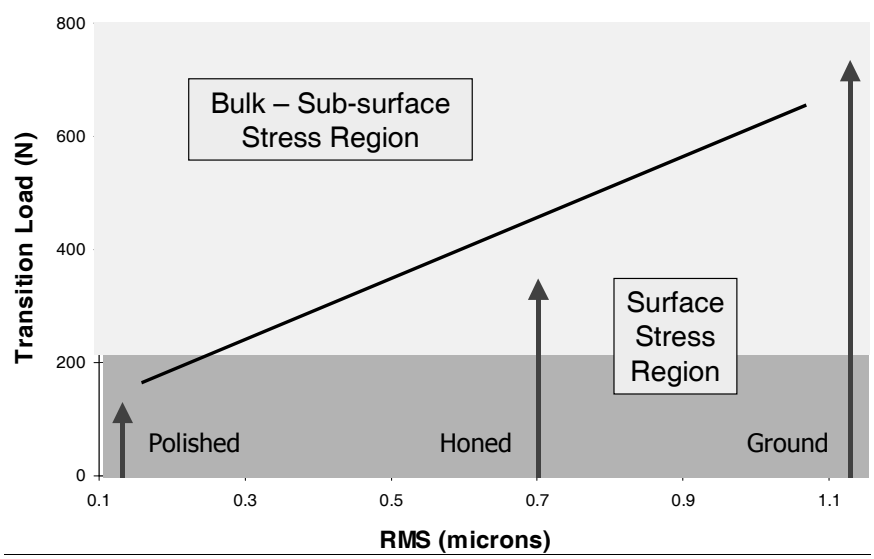


**Figure 4.** Computed "transition load" from surface to subsurface as a function of surface roughness for specific tribological conditions of rough surface contact (RMS = Root Mean Square)

25%. The total friction reduction is smaller for the polished surfaces because these surfaces are in stronger hydrodynamic lubrication. Clearly, boundary friction reduction should greatly help decrease the friction of surfaces in more severe mixed lubrication status. Figure 5 shows results obtained using "3 mailbox"-pins-on-ring coupon test configuration for existing and experimental oils. The observed reduction in friction is primarily due to boundary friction.

A series of additives having different chemistries were selected to study their effect on the boundary lubrication film formed on the worn surface. Four different lubricant blends were prepared by mixing 1.5 w/w% each of molybdenum phosphorodithioate and zinc diamyldithiocarbamate, equal weights of molybdenum phosphorodithioate plus zinc diamyldithiocarbamate and equal weights of Antimony phosphorodithioate plus zinc diamyldithiocarbamate so that the total percentage of the additive remains at 1.5 w/w% in polyalpha olefin-type synthetic base oil. The antiwear properties of the blends were evaluated using a four-ball test geometry generating a point contact under fully submerged lubricant conditions. The test consisted of rotating a 52100 extreme polish 0.5-inch steel ball on three identical stationary balls held tight in a lubricant filled cup at 75° Celsius (C). The top ball was rotated at a speed of 1200 revolutions per minute (rpm) and 196 Newtons (N) normal load was applied for 30 minutes. The tests resulted in a wear scar mark on each of the three stationary balls, which were later measured and analyzed for the presence of additive-initiated protective surface film using scanning electron microscopy (SEM), energy dispersive X-ray analysis (EDX), and Auger depth analysis. The following observations were made:

a. The Mo-containing additive resulted in the lowest wear scar followed by Zn, Mo+Zn, and Sb+Zn.
b. The higher Zn/Sb ratio as compared to Zn/Mo suggests the higher reactivity of Mo to form MoS2 on the surface as compared to Sb.
c. Auger depth analysis can provide insight into the boundary film elemental composition and provide information about its chemical nature when using various additive mixtures and their relative stability in multi-additive system.

An *in situ* boundary film analysis capability is being established at Argonne using a glancing X-ray

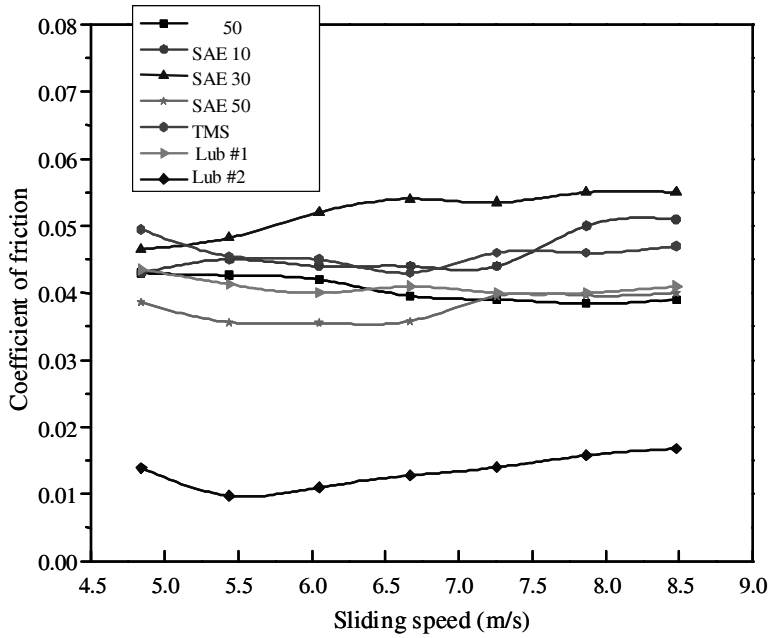


**Figure 5.** Friction performance of standard and experimental lubricants (Lub #1 and Lub #2)

analysis of a boundary layer as it is formed. That capability is essential for study of lubricant formulations reactivity with surfaces, especially coated surfaces, which may not be based on iron.

The effect of lubricants on drive axle power loss has been evaluated using standard ground gears. Three oils were used: transmission, mineral axle, and formulated synthetic axle oil. Table 2 shows that power loss of the axle can be reduced by selection of appropriate oils.

**Table 2.** Off-Highway Drive Axle Horsepower Loss as a Function of Oil Formulation

| Effective Grade (%) | Transmission Oil | Mineral Axle Oil | Synthetic Axle Oil |
|---|---|---|---|
| 8 | 15.9 | 14 | 12.8 |
| 10 | 17.7 | 15.9 | 14.5 |
| 12 | 17.9 | 16 | 14.6 |
| 14 | 19.1 | 16.9 | 15.8 |
| 15 | 19.3 | 17.1 | 15.7 |

## Low-Friction Coatings

Argonne leads this technological area as the expertise of the staff is perfectly suited to address the various issues related to coatings, such as coating integrity and adhesion, and ability to coat complex geometries, such as fine-mesh helical transmission gear teeth. The focus in the first year was to modify physical vapor deposition (PVD) coating parameters for superhard nanocoatings to develop a high-quality coating. Superhard coatings are classified as those in the range of 3000–6700 Vickers hardness number (Hv). Figure 6 shows how the PVD parameter studies improved the microstructure for superhard coating now under study at Argonne. Maximum substrate temperature is kept at 150°C. Several test coupons were coated and delivered to Eaton for tribological performance evaluation. Another batch of Eaton samples were also coated with ANL's low-friction amorphous carbon coating (NFC-2) for testing at Eaton in FY 2006.

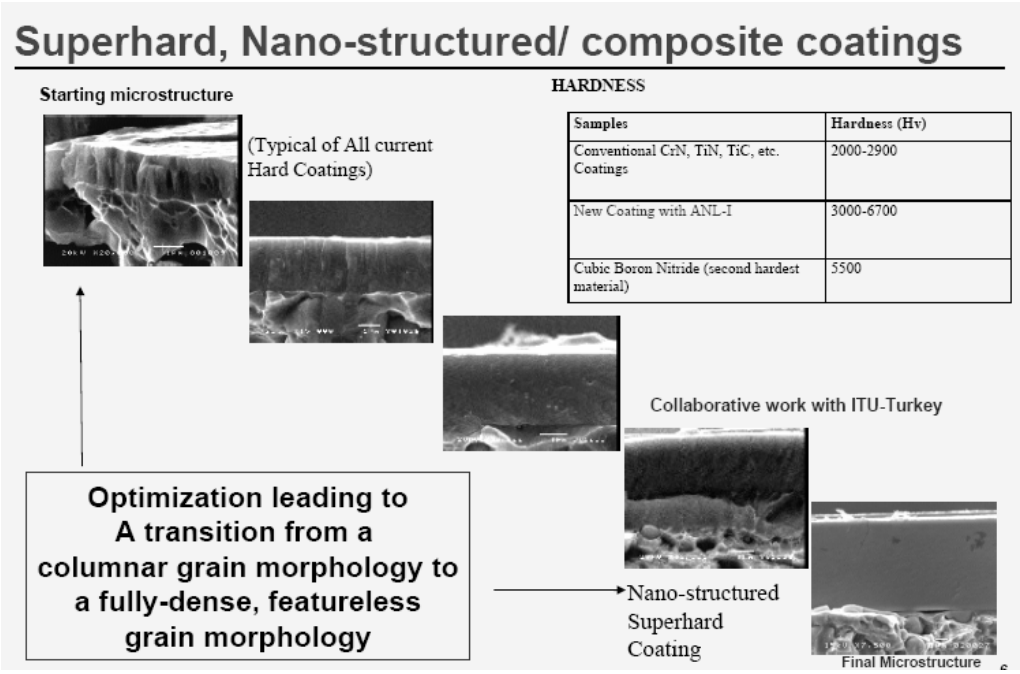


**Figure 6.** Result of chemical vapor deposition process parameter optimization to achieve desired microstructure for a new nanostructured superhard coating.

## Effect of Surface Texture on Friction

Surface texturing has been a very "hot" topic of discussion among many tribologists to reduce friction and improve efficiency of sliding/rotating components. Intuitively, texturing of gears and other surfaces should be controllable and repeatable. However, there are many parameters that define texturing. During this first year of the project, FY05, various textures have been experimentally evaluated using "mailbox" pin-on-disk coupon testing. Figure 7 shows the effect of textures on friction in that test. If texturing is not done correctly, it can lead not only to increased friction, but also to rapid surface deterioration and high wear rate. A separate study was initiated in the fourth quarter of FY 2005 to utilize virtually generated textured surfaces for analysis to better understand friction reduction. The rough surface contact computer analysis tool described under the section **Effect of Surface Topography on Friction** is being used for that analysis. The following parameters are being studied: texture geometries, sizes, distribution density, orientation with respect to the rolling/sliding direction, and various lubricating and loading conditions. Use of texturing seems to offer a high potential for friction and durability improvements beyond just lubricant formulation and coating technologies.

## Summary

Highlights of the progress during FY05 are:

1. Rough surface contact model improvements were made to model the effect of various tibological parameters on friction.
2. Experimental evaluations of frictional effects of standard and various surface textures were evaluated and potential for friction reduction demonstrated.
3. Study of boundary lubrication revealed competing chemical reactions depending on the specific lubricant formulations. *In situ* analysis capability is being developed at Argonne.
4. Process for superhard coatings has been improved to generate needed microstructure and limiting the substrate temperature during deposition to 150°C.
5. Four quarterly reports and two year-end deliverable reports have been issued on time.

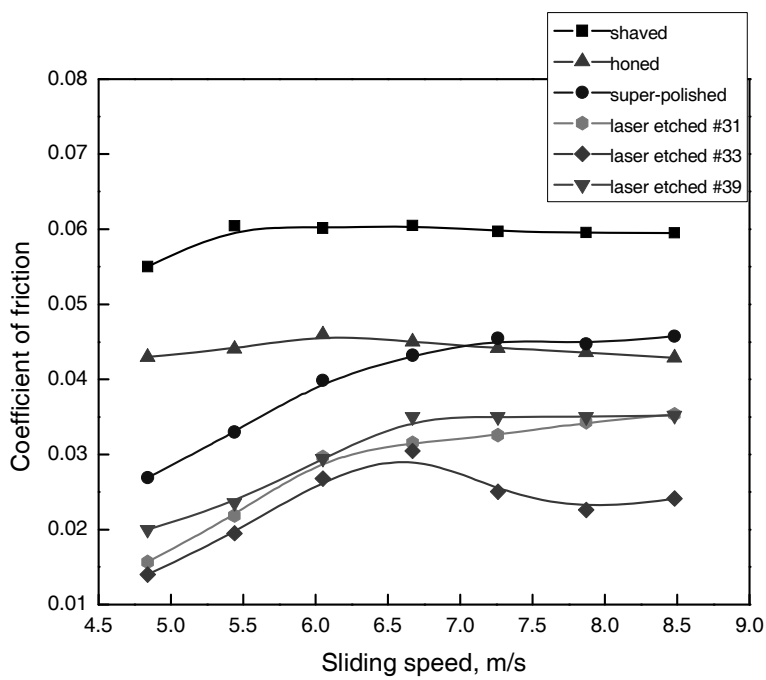


**Figure 7.** Effect of surface texturing on coefficient of friction as a function of relative sliding speed

## Conclusions

Modeling capability for realistic rough surface contact has been modified to rapidly assess the effect surface topography and oil viscosity and is being extended to assess effects of texturing, and resultant durability. The potential for significant reduction of parasitic losses in transmissions and drive axles due to friction has been demonstrated using specific coupon and limited bench testing. Improvements in generating desired coating microstructure has been demonstrated.

Future work in FY06 will focus on more in-depth understanding of boundary film development and its effect on friction, interactions of lubricant formulations with selected coatings and selection of the best driveline lubricant, and capability to model uncoated, texture, and coated surfaces under mixed lubrication regime. Surface durability will be included in the model as well.

## Publications

Publications and presentations, partially funded by this project, are identified below:

Wang Q., and D. Zhu, "Virtual Texturing: Modeling the Performance of Lubricated Contacts of Engineering Surfaces," accepted for publication in ASME Journal of Tribology.

Wang, W.Z., Y.Z. Hu, Y.C. Liu and D. Zhu, "Numerical Simulation of Mixed Lubrication in Point Contacts: A Comparative Study," submitted to the STLE for presentation at the 2005 Annual Meeting and publication in Tribology Transactions.

Liu, Y.C., Q. Wang, W.Z. Wang, Y.Z. Hu and D. Zhu, "Effects of Differential Scheme and Mesh Density on EHL Film Thickness in Point Contacts," submitted to the STLE for presentation at the 2005 Annual Meeting and publication in Tribology Transactions.

Xiong, S., Q.Wang, W.K. Liu, Q. Yang, K. Vaidyanathan, and D. Zhu, "On Mixed Elastohydrodynamic Lubrication of Smooth Journal-Bearing Systems with Low Viscosity and Rotating Speed," presentation at the 2005 Annual Meeting and publication in Tribology Transactions.

Xiong, S., Q. Wang, C. Lin, W. Liu, D. Zhu, B. Lisowsky, Q. Yang, and K. Vaidyanathan, "Local Enrichment Approaches for Deterministic Analyses of Conformal Contact and Lubrication," Submitted for presentation at the World Tribology Congress III.

Martini, A., Q. Wang, and R.Q. Snurr, "Hydrodynamic Lubrication at Multiple Length Scales," presentation at the 2005 STLE Annual Meeting, Las Vegas, Nevada.

# IV. FUEL REFORMER SYSTEMS

## IV.A. Diesel Fuel Reformer Technology

*Principal Investigator: M. Krumpelt*
*Argonne National Laboratory*
*9700 S Cass Ave., Argonne, IL 60439*
*(630) 252-8520, fax: (630) 252-4176, e-mail: krumpelt@anl.gov*

*Technology Development Managers: Sid Diamond and Lee Slezak*
*(202) 586-2335, fax: (202) 586-2476, e-mail: Lee.Slezak@hq.doe.gov*

*Field Technical Manager: Jules Routbort*
*(630) 252-5065, e-mail: routbort@anl.gov*

*Participants*
*Shuh-Haw Sheen, Argonne National Laboratory*
*Hual-Te Chien, Argonne National Laboratory*

---

*Contractor: Argonne National Laboratory*
*Contract No.: 49099*

---

### Objectives

- Develop an autothermal reforming process to convert diesel fuel into hydrogen-rich gas onboard a heavy-duty vehicle in a small fuel processor.
- Develop a diesel-fuel/air mixing device to achieve perfect mixing and thus reduce coke formation on the catalyst.
- Determine operating parameters for establishing "cool-flame" conditions and evaluate its effects on the reforming process.

### Approach

- Evaluate engineering issues that need to be better understood with regard to diesel fuel reforming. The main issues are how to avoid pre-ignition and coke formation and how to achieve catalyst stability.
- Construct a test facility for single-nozzle diesel fuel-reforming tests.
- Modify a typical diesel fuel injector with a steam/air injection and mixing system to achieve homogeneous mixing and stable cool flame conditions.
- Conduct diesel fuel-reforming tests to evaluate the catalytic autothermal reforming process.
- Develop a compact diesel fuel-reforming system that complies with industrial needs.
- Conduct field tests and document the results.

### Accomplishments

- Completed a series of fuel/air mixing tests.

- Analyzed temperature data of the mixing tests and determine the mixing quality.
- Conducted preliminary tests to demonstrate the cool-flame phenomenon.

### Future Directions

- Conduct fuel injection/mixing tests to determine the operating parameters for cool flame.
- Determine the cool-flame effects on fuel composition.
- Modify the facility for autothermal reforming tests.
- Conduct autothermal reforming tests.

---

## Introduction

The common practice in the trucking industry today is to keep diesel engines running to generate electricity for air conditioners and heaters for the cabin and the cargo space while the vehicle is parked. The fuel efficiency of diesel engines is only 9% in this idling mode. Significant fuel savings and emission reductions would be achieved if auxiliary power units (APUs) for trucks were available. One of the viable APU technologies is to convert diesel fuel into a hydrogen-rich gas that is subsequently fed into fuel cells for electrical power generation. Argonne National Laboratory has recently developed a catalytic autothermal reforming process that may be used as a compact and potentially cost-effective technology for diesel fuel reforming. However, because diesel fuel is more difficult to process due to high sulfur content and large aromatic molecules, the autothermal reforming process may encounter pre-ignition and coke formation problems causing catalyst instability. This project explores methods to mitigate the problems. Two approaches — homogeneous fuel/air mixing and cool-flame fuel treatment — will be examined.

## Diesel Fuel/Air Mixing Tests

A single diesel fuel injector test facility was constructed and used for fuel/air mixing tests. The facility's injector system is a commercially available G-2 fuel injector provided by the International Engine and Truck Company (ITEC). The injector is controlled by ITEC's Powertrain Control Module (PCM) simulator and operated under pulsed injection mode. The fuel injection rate can be varied by changing either the pulse rate or the fuel injection volume. Attached to the injector is a circular air chamber through which hot air is introduced. Figure 1 shows the injector and the air chamber with five slots for air to spray down onto the injected fuel. Both the airflow rate and air temperature can be controlled separately.

Each fuel/air mixing test involves injection of diesel fuel at ambient temperature into hot air. Thus, the effective way of determining the degree of mixing is to monitor the temperature changes downstream of the injector nozzle. Eight K-type thermocouples are distributed between one to four inches beneath the nozzle to measure the temperature profile.

Fuel/air mixing tests were conducted with a constant oxygen-to-carbon ($O_2$/C) ratio, 0.7 mol/mol, but with different injection rates. The injection variables examined in the tests involve fuel volume per injection, injection frequency, and injection pressure. The product of injection volume and injection frequency determines the injection rate. Figure 2 shows the temperature drops detected at three locations during the fuel injection. Less

**Figure 1.** Fuel injector and attached air chamber

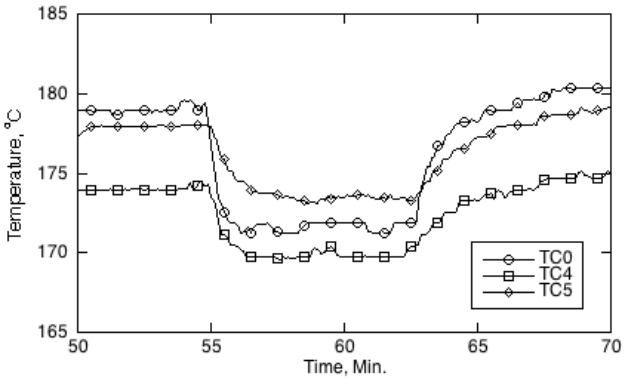


**Figure 2.** Temperature variations during fuel injection measured by three thermocouples, TC0 located at 1 inch below the injector, TC4 at 4 inches below and 1 inch to the side, and TC5 at 4 inches below. The injection rate is 78.80 cubic millimeters per second ($mm^3/s$) with injection frequency = 3.885 Hertz (Hz) and fuel injection volume = 20 cubic millimeters ($mm^3$)/injection.

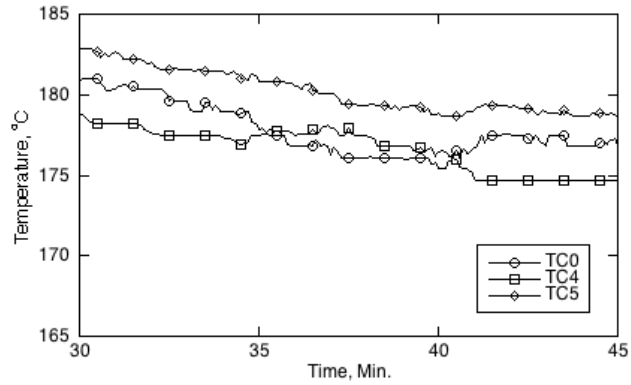


**Figure 3.** Temperature variations during fuel injection measured by three thermocouples, TC0 located at 1 inch below the injector, TC4 at 4 inches below and 1 inch to the side, and TC5 at 4 inches below. The injection rate is 78.80 $mm^3/s$ with injection frequency = 10.61 Hz and fuel injection volume = 7 $mm^3$/injection.

temperature drop is measured for farther locations from the injector, about 8° Celsius (C) at TC0 located at 1 inch below the injector and about 7°C at TC4 and TC5, which are 4 inches below the injector. However, the presence of temperature drop may indicate that total fuel evaporation and mixing have not been achieved. The better mixing and evaporation were observed by running the fuel injection at a higher injection frequency. Figure 3 shows the temperature variations of a test having the same injection rate but different injection frequency and volume as the one shown in Figure 2. Less than 1°C temperature drops at TC4 and TC5 were detected.

## Cool-flame Tests

Cool-flame phenomena were observed in a diesel-fuel/air mixing test. The test was conducted with a constant chamber temperature at 300°C and increasing air temperature from 300°C to 400°C. Both the airflow rate and fuel injection rate were kept constant with an estimated $O_2$/C ratio of 0.2.

Fuel was injected after the chamber reached the equilibrium temperature for each selected hot-air temperature. Eight thermocouples distributed on a plane 4 inches below the injector were used to measure the air/fuel mixture temperature. During each fuel injection, the downstream air/fuel mixture was also sampled for composition analysis. An off-line gas chromatography was used. Figure 4 shows the temperature variations of two thermocouples located at the center and edge of the thermocouple plane during the injection tests with the air temperature set at 360°C and 400°C. For air temperature at 360°C, the injection of diesel fuel lowered the equilibrium temperature slightly. But when the air temperature reached 400°C, a rapid temperature rise, approximately 100°C, was detected. The sudden temperature increase indicates the initiation of cool flame.

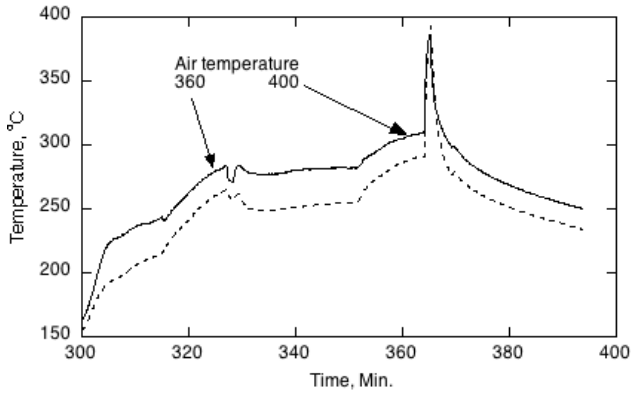


**Figure 4.** Temperature variations in the center (dash line) and 2 inches away from the centerline (solid line) during two fuel injections with different hot air temperatures

## Conclusions and Future Plan

We have conducted preliminary fuel/air mixing and cool-flame tests using the fuel/air mixing test facility established at Argonne. A circular air chamber with five injection slots is installed above the injector nozzle to deliver the hot air for fuel/air mixing. Results from mixing tests show that better mixing can be achieved by applying higher injector pressure and injecting the fuel at higher injection frequency but less fuel volume per injection. Cool-flame phenomena for diesel fuel were observed. The cool flame occurs when hot-air temperature reaches 400°C.

The future plan for this project includes three major tasks:

(1) Determine the effects of cool flame on diesel-fuel composition.
(2) Conduct fuel/air/steam mixing and cool-flame tests.
(3) Conduct diesel fuel autothermal reforming tests.

# IV.B. Onboard Plasmatron Hydrogen Production for Improved Vehicles

*Principal Investigators: Daniel R. Cohn, Leslie Bromberg*
*Plasma Science and Fusion Center, Massachusetts Institute of Technology*
*MIT PSFC NW16-104, 77 Massachusetts Avenue, Cambridge MA 02139*
*(617) 253-5524, fax: (617) 253-0700, e-mail: cohn@psfc.mit.edu*

*Technology Development Managers: Sid Diamond and James Eberhardt*
*(202) 586-9837, fax: (202) 586-1600, e-mail: james.eberhardt@ee.doe.gov*

*Field Technical Manager: Aaron Yocum*
*(304) 285-4852, fax: (304) 285-46383, e-mail: aaron.yocum@netl.doe.go*

---

*Contractor: Massachusetts Institute of Technology*
*Contract No.: DE-AC03-99EE50565*

---

## Objectives

- Conduct comparative study of plasmatron fuel conversion of alternative and conventional fuels.
- Investigate use of plasmatron fuel converter for potential use in reforming fuels on Energy Policy Act (EPAct) Alternative Fuels list for aftertreatment of engine exhaust and other vehicular applications.
- Prepare final technical report.

## Approach

- Optimize plasmatron fuel reformer configurations, including gas and fuel management, plasma geometry, and reactor chamber variations.
- Model plasmatron fuel reformer operation using computational studies of the chemistry of simple gaseous hydrocarbons (mainly methane) because of the complicated effects from liquid fuels, and computational fluid dynamics calculations of the flows upstream from the plasma discharge.

## Accomplishments

- Demonstrated efficient reforming of methane and propane at steady state and during transient regimes.
- Determined the effect of mixing through different fuel and air injection configurations into the plasmatron on the conversion of methane and propane.
- Demonstrated rapid response and effective conversion of ethanol and biodiesel into hydrogen and carbon monoxide.
- Developed a two-stage model for the homogeneous reforming of methane.

---

## Gaseous Fuels

Methane and propane were reformed using the low-current plasmatron at steady state and startup conditions. The experiments were carried out with propane or methane introduced in four different ways: (a) through the axial nozzle, similarly to what is done with liquid fuels, premixed with the wall air; (b) premixed with the plasma air; (c) premixed with the air, so that the air/propane distribution in the plasmatron and the reactor are homogeneous; and finally, (d) stoichiometric conditions in the swirl air, with the rest of the propane introduced with the wall

air. Downstream from the plasmatron head there is a 5-inch-long section of the reaction extension cylinder which is also included in the model. The volume of this section is approximately 1000 centimeters (cm).

In the case of propane, Table 1 shows a summary of the work performed. Conditions of optimal reforming (highest hydrogen concentration) are chosen. It is clear that the results are best when the propane is introduced through the swirl port (premixed plasma) with the highest values of hydrogen concentration with lowest values of $CO_2$ and temperature (a sign of combustion). Introducing a stoichiometric condition for the combustion mixture in the swirl gas is not better than when all the propane is introduced through the swirl port, but it is better than the other configurations. Some of the results from the fluid dynamic simulation suggest that premixing the propane with the swirl air results in the highest fraction of propane in stoichiometric combustion conditions in the plasma region. It is interesting to note that the worst configuration is that with the fuel injected through the axial port. Unfortunately, this is the configuration that is needed for injection of liquid fuels.

More detailed description of the specific experiments and results are given in Bromberg et al., PSFC-JA-05-15, 2005.

In the case of methane, it was determined that the hydrogen concentration and yields depended on the overall oxygen-to-carbon (O/C) ratio, and that the distribution of the air between swirl and wall had only a small effect.

The effect of the plasma power was investigated. It was determined that the need for the plasma depends on the O/C ratio. At high O/C ratios (O/C approximately 2.2) the dependence on plasma power is small, with an approximately 20% decrease in hydrogen concentration without the plasma. However, at O/C of approximately 2, the plasma is needed, and higher power is better. At even lower O/C ratios (O/C < 1.6), the reforming even in the presence of plasma, is poor.

More detailed description of the specific experiments and results are given in Bromberg et al., PSFC-JA-05-10, 2005.

Startup experiments were also performed for methane. The experiments indicated that when the plasmatron is used as an igniter, the hydrogen concentration is a function of O/C. Furthermore, the tests indicate that it is possible to increase the hydrogen concentration and the methane conversion by increasing the O/C to about 2.2. As the O/C for stoichiometric combustion of methane is O/C of approximately 4, the reformer is still operating at very fuel rich conditions.

When the plasmatron is used in continuous ignition mode, the use of the plasma at a given O/C ratio increases the hydrogen concentration and the methane conversion. Increasing the power increases the hydrogen concentration. Hydrogen concentration can be as high as 10 to 12% with O/C on the order of 2.2 with 300–400 watts (W).

**Table 1.** Summary of Propane Tests

| | O/C Ratio | Flow Dist | Efficiency | H2 Conc | Temp | Dependence on Power | Cold Start Up |
|---|---|---|---|---|---|---|---|
| Premixed | 1.7 | 140/60 | 60% | 12% | 850 | > 350 W | 8% in 1.5 s |
| Premixed plasma | 1.3 | 75/70 | 75% | 14.50% | 720 | > 100 W | 10% in 2 s Continues ~2% when plasma off |
| Axial | 1.8 | 160/65 | 65% | 12% | 790 | | 8% in 1.5 s |
| Premixed wall | 1.6 | 110/70 | 55% | 13% | 820 | Drops 20% when hot, plasma off | 8% in 1.5 s Power > 150 W |
| Combustion plasma air | 1.45 | 95/70 | 60% | 12% | 800 | Drops by 10-20% when plasma off | 10% in 1.5 s Power > 100 W |

More detailed description of the specific experiments and results are given in Bromberg et al., PSFC-JA-05-11, 2005.

## Bio Fuels

A series of experiments reforming biodiesel and ethanol renewable fuels was carried out using a plasmatron fuel converter. Conditions of good noncatalytic performance were investigated, with hydrogen concentration in the dry reformate > 10% and energy efficiency > 70%. Operation at relatively high O-to-C ratio is required. The ratio of free oxygen to carbon, however, is approximately 1.5 at the conditions of good performance. The plasma is required for the startup for both fuels until conditions near steady state are achieved. However, once steady state is achieved in ethanol, hydrogen concentration in the absence of plasma is maintained for all but the lowest value of O/C ratio, although with higher opacity than in the case with the plasma. For B-100, the plasma is needed throughout the O/C range explored. Detailed experimental setup and results are given in Bromberg et al., PSFC-JA-05-3, 2005.

## Modeling

A two-stage model has been developed for the homogeneous reforming of methane. The model was investigated using a simple Perfectly Stirred Reactor (PSR) with multiple inputs. It was determined that the reforming process ignited the overall O/C ratio is between 1.4 and 1.6. About 10–15% of the methane needs to be stoichiometrically combusted.

The actual composition of the reformate in the calculations underestimate the hydrogen concentration and the methane conversion. The Partially Stirred Reactor (PaSR) model does better in predicting the composition of the reformate. The results show a lack of sensitivity of the conversion to residence time. Increased conversion is difficult through the use of larger reactors. Instead, increased temperature is a more effective way to achieving high conversion of methane. The same results are obtained by increasing the reactor size by a factor of 8 or increasing the O/C ratio from 1.6 to 2. However, there is a minimum PSR size (defined as the section of the actual reactor with good mixing) for good reforming, and increased O/C ratio is needed to compensate for smaller well-mixed reactors.

A model of a plasmatron methane reformer where limited mixing is included has produced quantitative agreement with experimental results (Bromberg, PSFC-JA-05-13, 2005). The process uses only gas-phase chemistry, without the use of a catalyst. The model reproduces the hydrogen and other main components of the reformate, as well as the methane conversion.

The model also has been used to determine the effect of the plasma at steady state conditions. It has been shown that the plasma increases the hydrogen concentration by about 20%, but the reaction continues at lower temperatures even in the absence of the plasma. As the cold reagents are introduced into the hot reactor gas, they are heated and release sufficient energy to maintain the reaction, although at decreased temperature.

The composition of the reformate is accurately described by the model. However, there are regimes (low O/C, absence of plasma) where there is only qualitative agreement with the observations. Additional modeling is needed that includes losses or improved description of the fluid dynamics, mainly for the case without plasma.

## Documentation

Extensive documentation was undertaken during the month of August. Six papers were prepared and will be submitted for publications. The six papers will are preliminarily published as reports and are available on the web as PSFC reports. The six papers cover (1) steady-state reforming of methane; (2) transient experiments with methane; (3) CFD modeling of plasmatron methane reformers; (4) PSR model of methane; (5) PaSR model of methane; and (6) experimental results, both steady state and transient, on plasmatron propane reformers.

## Publications

Margarit Bel, N., J.B. Heywood, and L. Bromberg. Report PSFC-RR-05-1. “Simulation of Hydrogen Generation from Methane Partial Oxidation in a Plasma Fuel Reformer.” Plasma Science and Fusion Center, Massachusetts Institute of Technology,

Cambridge, MA. January 7, 2005. Available at http://www.psfc.mit.edu/library1/catalog/reports/2000/05rr/05rr001/05rr001_full.pdf.

Bromberg, L., D.R. Cohn, and V. Wong. Report PSFC-RR-05-002. "Regeneration Of Diesel Particulate Filters with Hydrogen Rich Gas." Plasma Science and Fusion Center, Massachusetts Institute of Technology, Cambridge, MA. January 25, 2005. Available at http://www.psfc.mit.edu/library1/catalog/reports/2000/05rr/05rr002/05rr002_full.pdf.

Bromberg, L., D.R. Cohn, K. Hadidi, J.B. Heywood, and A. Rabinovich. "Plasmatron Fuel Reformer Development and Internal Combustion Engine Vehicle Applications." Presented at the Diesel Engine Emission Reduction (DEER) Workshop, 2004, Coronado, CA, August 29–September 2, 2004.

Bromberg, L., K. Hadidi, and D.R. Cohn. Report PSFC-JA-05-10. "Experimental Investigation of Plasma Assisted Reforming of Methane I: Steady State Operation." Plasma Science and Fusion Center, Massachusetts Institute of Technology, Cambridge, MA. August 22, 2005. Available at http://www.psfc.mit.edu/library1/catalog/reports/2000/05ja/05ja010/05ja010_full.pdf.

Bromberg, L., K. Hadidi, and D.R. Cohn. Report PSFC-JA-05-11. "Experimental Investigation of Plasma Assisted Reforming of Methane II: Start-up." Plasma Science and Fusion Center, Massachusetts Institute of Technology, Cambridge, MA. August 25, 2005. Available at http://www.psfc.mit.edu/library1/catalog/reports/2000/05ja/05ja011/05ja011_full.pdf.

Bromberg, L. and N. Alexeev. Report PSFC-JA-05-12. "Plasma Assisted Reforming of Methane: Two Stage Perfectly Stirred Reactor (PSR) Simulation". Plasma Science and Fusion Center, Massachusetts Institute of Technology, Cambridge, MA. August 25, 2005. Available at http://www.psfc.mit.edu/library1/catalog/reports/2000/05ja/05ja012/05ja012_full.pdf.

Bromberg, L., Report PSFC-JA-05-13. "Modeling of Plasma Assisted Reforming of Methane II: Partially Stirred Reactor (PASR) Simulation." Plasma Science and Fusion Center, Massachusetts Institute of Technology, Cambridge, MA. August 26, 2005. Available at http://www.psfc.mit.edu/library1/catalog/reports/2000/05ja/05ja013/05ja013_full.pdf.

Bromberg. L. Report PSFC-JA-05-14. "CFD Modeling of Plasmatron Methane Reformers." Plasma Science and Fusion Center, Massachusetts Institute of Technology, Cambridge, MA. August 25, 2005. Available at http://www.psfc.mit.edu/library1/catalog/reports/2000/05ja/05ja014/05ja014_full.pdf.

Bromberg, L., K. Hadidi, and D.R. Cohn. Report PSFC-JA-05-15. "Experimental Investigation of Plasma Assisted Reforming of Propane." Plasma Science and Fusion Center, Massachusetts Institute of Technology, Cambridge, MA. August 25, 2005. Available at http://www.psfc.mit.edu/library1/catalog/reports/2000/05ja/05ja015/05ja015_full.pdf.

Bromberg, L., D.R. Cohn, K. Hadidi, J.B. Heywood, and A. Rabinovich. Report PSFC-JA-05-22. "Plasmatron Fuel reformer Development and Internal Conbustion Engine Vehicle Applications." Plasma Science and Fusion Center, Massachusetts Institute of Technology, Cambridge, MA. August 31, 2005. Available at http://www.psfc.mit.edu/library1/catalog/reports/2000/05ja/05ja022/05ja022_full.pdf.

## References

Bromberg L., K. Hadidi, and D.R. Cohn. Report PSFC-JA-05-15. "Experimental Investigation of Plasma Assisted Reforming of Propane." Plasma Science and Fusion Center, Massachusetts Institute of Technology, Cambridge, MA. August 12, 2005. Available at http://www.psfc.mit.edu/library1/catalog/reports/2000/05ja/05ja015/05ja015_full.pdf.

Bromberg L., K. Hadidi, and D.R. Cohn. Report PSFC-JA-05-10. "Experimental Investigation of Plasma Assisted Reforming of Methane I: Steady State Operations." Plasma Science and Fusion Center, Massachusetts Institute of Technology, Cambridge, MA. August 12, 2005. Available at http://www.psfc.mit.edu/library1/catalog/reports/2000/05ja/05ja010/05ja010_full.pdf.

Bromberg, L., K. Hadidi, and D.R. Cohn. Report PSFC-JA-05-11. "Experimental Investigation of Plasma Assisted Reforming of Methane II: Startup." Plasma Science and Fusion Center, Massachusetts Institute of Technology, Cambridge, MA. August 12, 2005. Available at http://www.psfc.mit.edu/library1/catalog/reports/2000/05ja/05ja011/05ja011_full.pdf

Bromberg, L., K. Hadidi, and D.R. Cohn. Report PSFC-JA-05-3. "Plasmatron Reformation of Renewable Fuels." Plasma Science and Fusion Center, Massachusetts Institute of Technology, Cambridge, MA. September 30, 2005. Available at http://www.psfc.mit.edu/library1/catalog/reports/2000/05ja/05ja003/05ja003_full.pdf.

Bromberg, L. and N. Alexeev. Report PSFC-JA-05-12. "Plasma Assisted Reforming of Methane: Two Stage Perfectly Stirred Reactor (PSR) Simulation." Plasma Science and Fusion Center, Massachusetts Institute of Technology, Cambridge, MA. August 25, 2005. Available at http://www.psfc.mit.edu/library1/catalog/reports/2000/05ja/05ja012/05ja012_full.pdf.

Bromberg, L. Report PSFC-JA-05-13. "Plasma Assisted Reforming of Methane II: Partially Stirred Reactor (PaSR) Simulation." Plasma Science and Fusion Center, Massachusetts Institute of Technology, Cambridge, MA. August 26, 2005. Available at http://www.psfc.mit.edu/library1/catalog/reports/2000/05ja/05ja013/05ja013_full.pdf.

# V. ELECTROMAGNETIC (EM) REGENERATIVE SHOCKS

## V.A. Regenerative Shock Absorbers and Tires

*Principal Investigator: J. Hull*
*Argonne National Laboratory*
*Argonne, Illinois 60439*
*(630) 252-8580, fax: (630) 252-5568, e-mail: jhull@anl.gov*

*Technology Development Managers: Sid Diamond and Lee Slezak*
*(201) 586-2335, e-mail: Lee.Slezak@hq.doe.gov*

*Technical Program Manager: Jules Routbort*
*(630) 252-5065, e-mail: routbort@anl.gov*

---

*Contractor: Argonne National Laboratory*
*Contract No.: W-31-109-ENG-38*

---

### Objectives

- Develop model to predict performance of regenerative shock absorbers and tires.
- Conduct experiment on a small-scale vehicle to verify the energy recovery from road-induced vehicle motion.
- Compare the experimental results with theoretical prediction.
- Develop road data to use as input to the model.

### Approach

- Mount regenerative shock on small vehicle and accrue test data.
- Instrument truck and run it over local roads to obtain data.
- Develop benchtop prototype of regenerative tire mechanism.

### Accomplishments

- Tested experimental electromagnetic shocks on all-terrain vehicle and used the data from it to verify model of regenerative shock performance.
- Instrumented truck and accumulated data on acceleration over local roads.
- Developed benchtop apparatus to test regenerative tire concepts.

### Future Directions

- More road data needs to be accumulated for a complete database.
- Incorporate road data in the regenerative shock model to predict expected performance.
- Explore potential of developing technologies for dynamic control of vehicle.

---

## Introduction

Approximately 30% of the losses in a heavy vehicle can be attributed to rolling friction. The two major components of rolling resistance arise from vertical motion of the vehicle due to road roughness and deformation of the tire as it rotates. Vertical motion is damped by shock absorbers, and the energy is presently dissipated as heat in the absorber. Deformation of the tire as it rotates results in a hysteretic energy loss, which also is presently dissipated as heat. The thesis of the present program is that most of the energy presently being dissipated as heat could instead be converted to electricity and used to help propel the vehicle or power its auxiliary systems. The concept is analogous to regenerative braking. Of the energy lost in rolling resistance, approximately 10–20% is lost in the shock, and most of the rest is lost in tire deformation.

## Regenerative Shock Testing

The up and down motion of a vehicle traversing a road is unwanted from a passenger comfort perspective. In present vehicles, where the motion is damped by shock absorbers, the energy provided by the prime power plant is diverted from its intended purpose and gets dissipated in heat. Prevention of this motion in the first place could be accomplished by construction and maintenance of smooth roads. However, in the absence of such a societal program, the energy diverted into the vertical motion can potentially be recovered by a regenerative shock absorber that converts the up and down motion into electrical energy. The goal of this project is to ascertain whether this can be accomplished in a cost-effective manner.

In order to estimate the power generated by the electromagnetic (EM) shocks, experimental regenerative shocks were mounted in an all-terrain vehicle (ATV), as shown in Figure 1. This vehicle was tested on local roads and on a specially constructed obstacle course to determine the performance of the experimental shock absorber.

In a separate series of experiments, the performance of experimental regenerative shocks has been obtained by subjecting them to forced oscillations of a shaker, as shown in Figure 2.

**Figure 1.** ATV used for EM shock testing

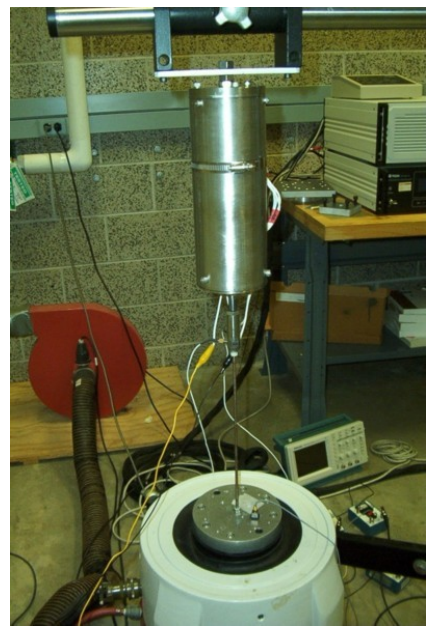

**Figure 2.** Shaker testing of Mark 1 EM shock

## Results on Prototype Shock

Using data from both experimental programs, a mathematical model of regenerative shock performance was established and verified. Sample data used in the model is shown in Figure 3. In this instance, the ATV was driven over a 4x4 beam.

In order to use the model to predict actual performance under real conditions, it is necessary to have the expected forcing function of a vehicle traveling of real roads. Examination of existing data bases suggested that the required data was not sufficient. Therefore, we instrumented a road vehicle to acquire the data.

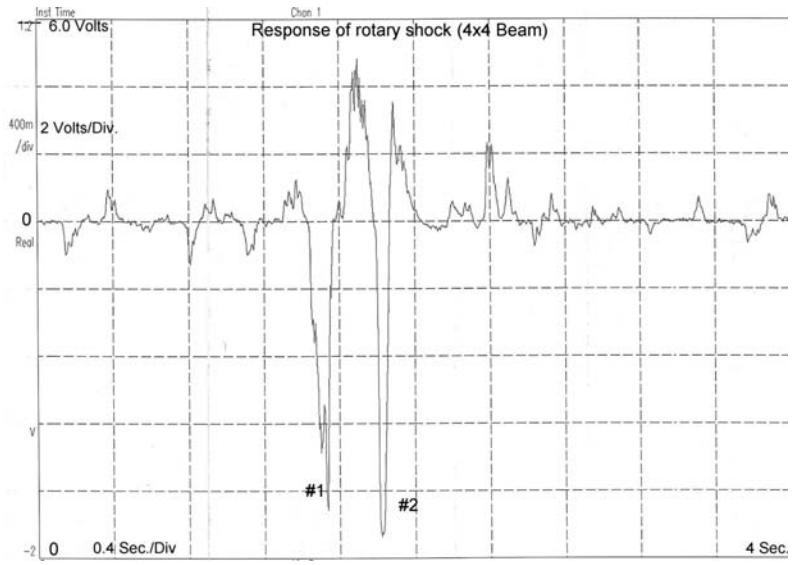


**Figure 3.** Response of Mark 2 (rotary) shock absorber transversing 4x4 beam

## Road Data

A linear vehicle displacement transducer (LVDT) was mounted in a dump truck between the axle and the chassis as shown in Figure 4. The purpose of this experiment was to record the suspension (conventional) relative displacement to get an estimate of the available energy.

The voltage output from the LVDT was sent to a tape deck onboard the truck cabin (as shown in Figure 5) as the truck was driven around a road inside Argonne National Laboratory.

The tape gain was set to 2 so that the actual voltage is twice the voltage shown in the graph (i.e., 2 volts peak in the graph implies 4 volt peak signal from LVDT). A segment of the time domain signal recorded is shown in Figure 6. It may be mentioned that the LVDT scale factor was 3.3 volts per inch (V/in). The frequency spectrum of the above signal is shown in Figure 7.

From Figure 7, a 0.374 millivolts (mv) at 4 Hertz (Hz) implies 0.226 in peak displacement at 4 Hz, which is approximately 5.6 inches per second (in/sec) or 0.142 meters per second (m/sec). Since the actual value of suspension damping constant of the dump truck is unavailable, a suspension damping constant of 89 kN.s/m which may be typical of a single-axle flatbed truck is assumed. This leads to power of 900 watts (W) at 4 Hz. However, if we

**Figure 4.** LVDT mounted in the truck

**Figure 5.** Tape recorder inside the truck

consider the time domain signal of Figure 6 (which accounts for contribution from all frequencies), it seems maximum velocity (after considering 2:1 factor of tape and LVDT scale factor of

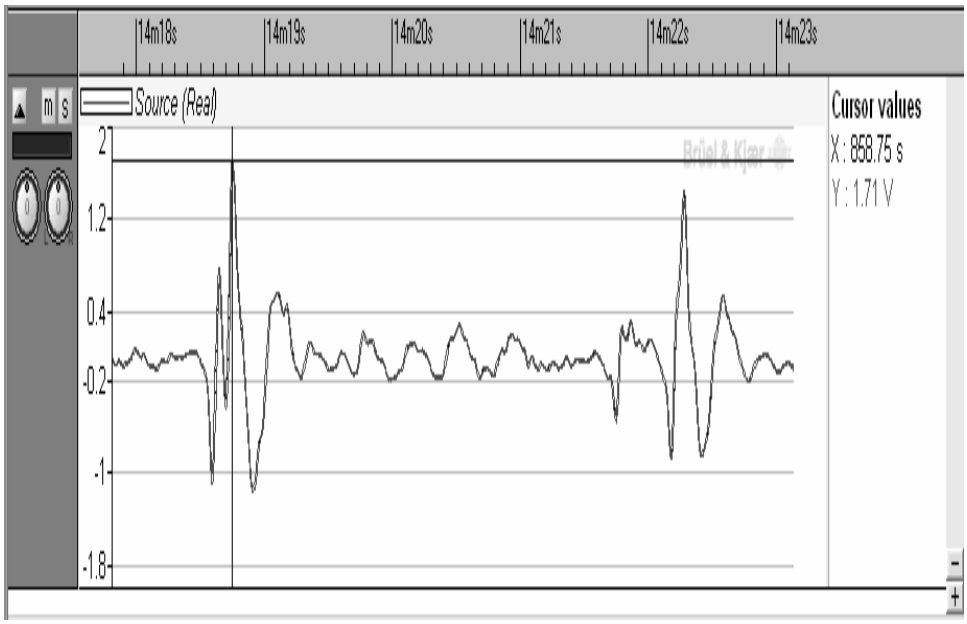


**Figure 6.** Time domain signal (with 2:1 reduction)

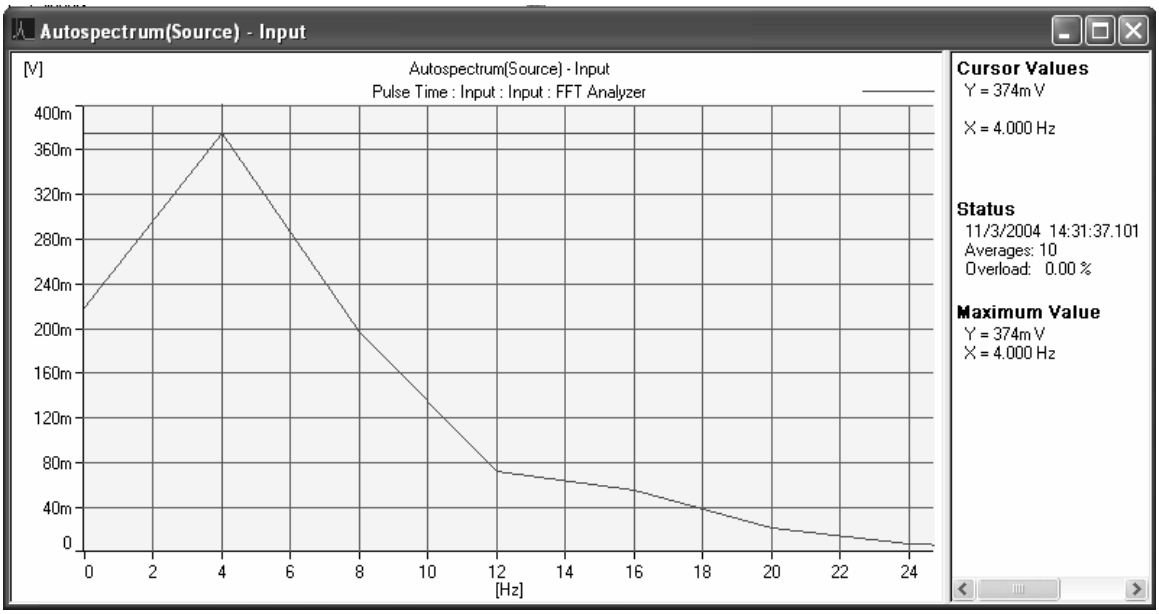


**Figure 7.** Frequency spectrum of the signal

3.3 V/in) is approximately 13.3 in/sec (0.338 m/sec). Again assuming the same damping constant, it leads to a peak power of approximately 5 kilowatts (kW). However, it may be cautioned that this 5-kW calculation is for peak power (when the truck hits a pothole) and not average power, and designing an electromagnetic shock with such damping constant may not be easy.

## Regenerative Tire

Building on the experience with regenerative shocks, an electromagnetic concept for a regenerative tire was chosen for initial experimentation. The basic idea is that the shock absorber and pneumatic tire will be replaced by an assembly of electromagnetic generators located in the tire. Vertical motion previously dissipated in the shock and tire deformation will instead be used to move the rotor in the electrical generator.

An apparatus was built (as shown in Figure 8) to study energy recovery from deformation of tires. The apparatus consists of a cam rotated by a variable-speed permanent magnet direct current (DC) motor. It was decided to use a cam follower mechanism because the cam profile can be changed to simulate large deformation only for part of rotational cycle, similar to a tire being deformed only when it is in contact with ground. Similarly a DC motor with speed control allows study of the effect of variation of tire rotational speed.

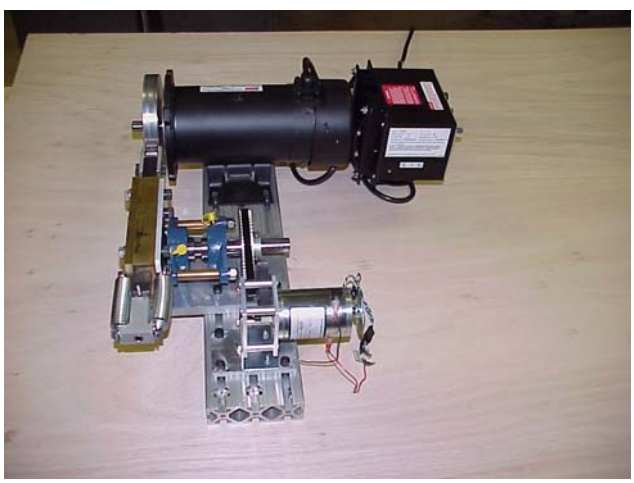

**Figure 8.** Top view of the apparatus

The cam follower was connected to a rack and pinion, which in turn was connected to a belt and pulley system to increase the rotational speed. The housing for the rack was loaded by a set of springs in order to ensure that the cam follower did not lose contact with the cam. The rotational speed was further magnified by a gear and pinion system. The pinion was then connected to a small permanent magnet DC motor used as a generator.

The voltage generated in the leads for the generator when the motor attached to the cam was rotated clockwise is shown in Figure 9. The large voltage peak (32.97 V) desirable for energy generation was causing overload for the data acquisition system. Hence, it was decided to use a voltage divider (two similar resistances in parallel and voltage measured across one resistor only) to divide the voltage approximately by half. Now the negative peak was measured as 15.16 V, and there was no overload or consequent clipping of signal. The resulting voltages are displayed in Figure 10, including cursor values for positive and negative peaks.

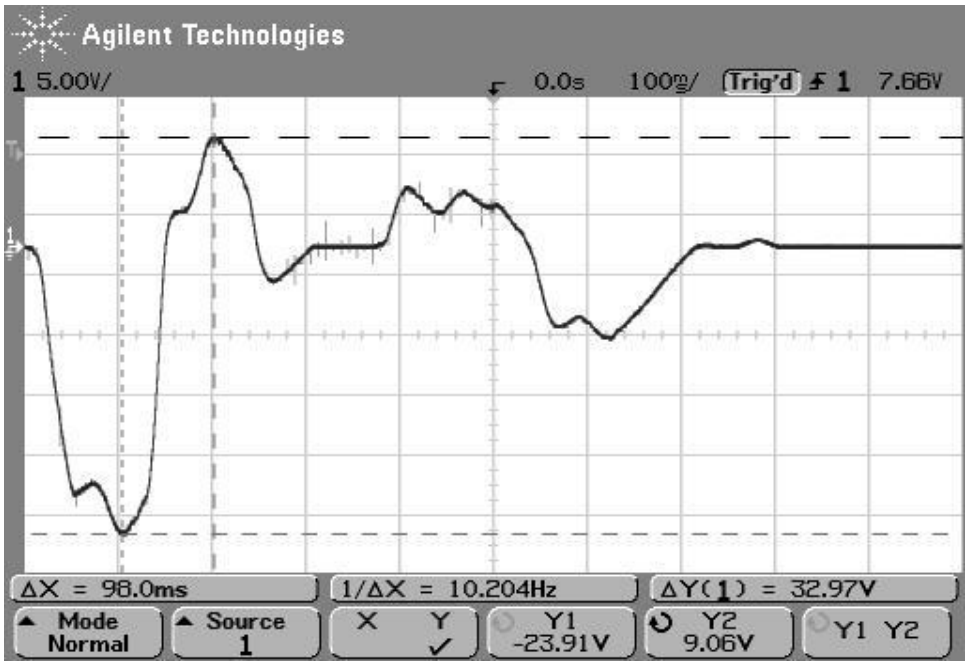


**Figure 9.** Voltage generated across leads of generator

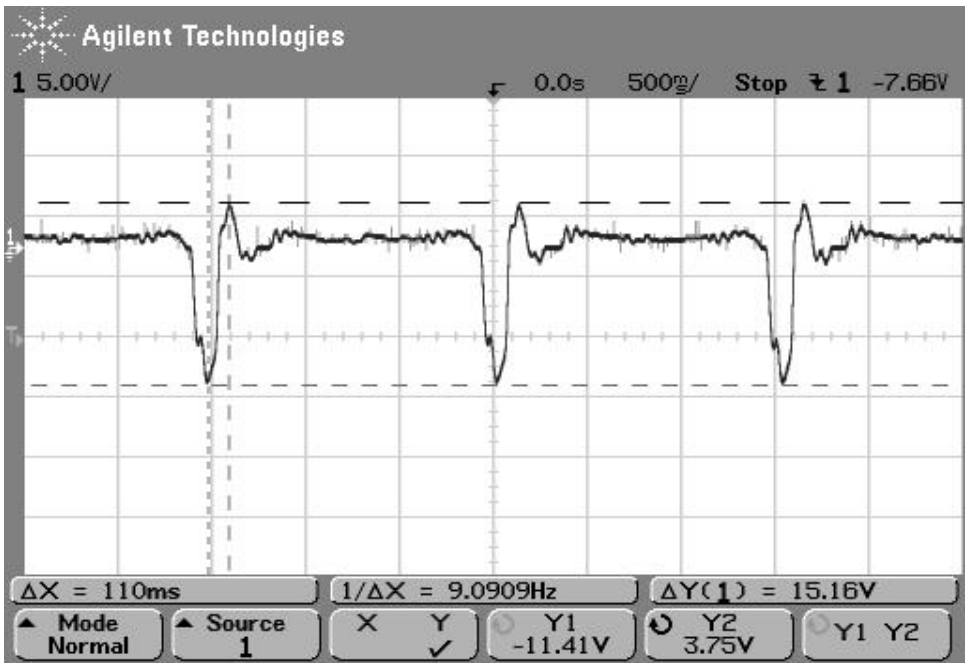


**Figure 10.** Output measured using voltage divider and cursors at negative-positive peak

# VI. ANALYSIS

## VI.A. Systems Analysis for Heavy Vehicles

*Principal Investigator: Linda Gaines*
*Argonne National Laboratory*
*Argonne, IL 60439*
*(630) 252-4919, fax: (630) 252-3443, e-mail: lgaines@anl.gov*

*Technology Development Managers: Sid Diamond and Lee Slezak*
*(202) 586-2335, fax: (202) 586-2476, e-mail: Lee.Slezak@hq.doe.gov*

---

*Contractor: Argonne National Laboratory*
*Contract No.: W-31-109-Eng-38*

---

### Objectives

- Analyze transportation technologies and fuel-efficiency measures objectively.
- Provide critical and unbiased evaluation of transportation or materials-related projects.
- Serve as a key idling-reduction resource for the U.S. Department of Energy (DOE).

### Approach

- Analyze technical and economic characteristics of competing technologies.
- Represent DOE at idling-reduction meetings.
- Coordinate efforts by DOE and other agencies.
- Supply technical input to policymakers.
- Maintain awareness about latest technical and political developments related to idling.

### Accomplishments

- Provided tutorials on idling reduction at numerous Clean Cities and other meetings.
- Completed and displayed poster on emissions from idling reduction technologies.
- Estimated diesel fuel use from workday idling of heavy trucks and wrote Transportation Research Board (TRB) paper.
- Led Technology Working Group (with Lee Slezak).
- Completed Technology Development section of National Idling Reduction Plan and one-page summaries.
- Managed contract to New West Technologies for analysis of wear due to idling.

### Future Directions

- Complete revised and expanded technical report.
- Complete worksheet for estimating idling reduction technology payback.
- Complete more detailed economic analysis of idling reduction (co-funded under other sponsorship).

- Continue to provide and analyze developing idling reduction information.
- Evaluate technology options for domestic liquid fuel production.

---

## Estimation of Fuel Use by Idling Commercial Trucks

We used the 2002 Vehicle Inventory and Use Survey (VIUS02 2004) to determine the number of commercial trucks in the categories that are most likely to idle for periods of more than half an hour at a time. Based on estimated numbers of hours for both overnight idling by sleepers and long-duration idling by all size classes during their workdays, the total fuel use by idling trucks is estimated to be over 2 billion gallons per year. Workday idling is determined to be a potentially much larger energy user than overnight idling, but data are required before any definitive conclusions can be reached. Existing technologies can reduce overnight idling, but development may be needed to reduce workday idling.

The type of truck idling that has received the most attention to date has been that of sleeper cabs, parked overnight at truck stops, rest areas, or by the side of the road, with the engine left on to keep the sleeping driver comfortable and to keep the engine fluids warm and the batteries charged. Of course, only sleepers, generally Class 8C trucks (see below) are likely to engage in this type of behavior. Several technical options, such as small heaters and auxiliary power units (APUs), as well as plug-in options, are available to provide the services needed when the main engine is shut off. These are described in Stodolsky et al. 2000 and listed on the EPA Smartway web site at http://www.epa.gov/ otaq/smartway/idlingtechnologies.htm.

Another type of idling is done by various vocational trucks during their workdays. These trucks are using their main engines to accomplish work other than moving the vehicle down the road. Examples include cement mixers that rotate and asphalt trucks that heat their loads to keep it from getting too viscous. The industry term for this kind of application is "power take-off" (or PTO). We do not include PTO in the accounting of truck idling because useful work is being accomplished.

The third type of idling is important but has not as yet been evaluated to see how much energy is being used. It is most succinctly described as "waiting," and can be divided into two categories, depending on whether the truck is simply parked or waiting in a queue, needing to move forward every few minutes to maintain its place in the line. The term for waiting in a line is "creep mode." Note that these categories exclude time during travel from place to place when the truck is stuck in traffic and must idle. The trucks that are simply parked could utilize the same devices as the overnight idlers if no comfortable waiting place were available for the drivers. Trucks in a line would require some alternative to restarting the engine frequently if this idling were to be avoided. Possibilities include scheduling, delicatessen-style numbers, and engineering to use APUs to power creep mode.

## Overnight Idling

Although there may be cases of trucks idling overnight for other reasons, by far the most common reason is that the driver is sleeping in the vehicle and requires heat or air conditioning and electricity to stay comfortable. Drivers remain in their sleeper compartments to sleep and relax during the off-duty periods required by the federal hours-of-service regulations. It is not yet known how recent changes in these regulations will affect total idling time. By definition, and by law, this type of idling is limited to those trucks that have sleeper compartments; almost all of these are Class 8C (combinations), but there are some in Classes 6 and 7 as well.

Even if the air temperature is moderate, the driver may leave the engine idling because open windows invite intrusions and let in polluted air and noises from other trucks. The number of hours varies greatly, from those drivers who get the truck warm, turn it off, and then curl up under heavy blankets for the night, to those who claim they never turn their trucks off for fear they won't start again. A survey at truck stops, by the University of California at Davis, showed a broad distribution from about

500 hours/year, up to over 3,500 (see Figure 1), in which the horizontal axis is hours per year idled, and the vertical axis is number of trucks.

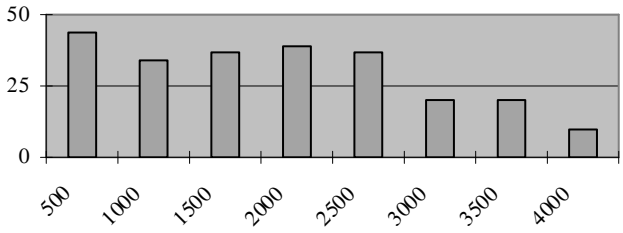


**Figure 1.** Range of idling times reported (*4*)

So truckers report idling from 1 to 10 hours per day. This is consistent with the typical 6 hours per day estimated by the American Trucking Associations, and the 1,800 hours/year estimated by Caterpillar as the result of an informal survey it performed (Orr 2003). However, although overnight idling has been discussed often, no good statistical data exist, and we performed a sensitivity analysis on this important parameter, around a baseline estimate of 6 hours per day, 300 days per year. Use of auxiliary power units and other idling-reduction devices could eliminate most of this overnight idling.

The 2002 VIUS reports over 665,000 sleepers in use, and almost 60% of these travel over 80,000 miles per year (or 270 miles per day for 300 days). The trucks that travel the longest distances in a year travel the furthest each day, and are most likely to be idling overnight, but if a truck's route is short but includes several stops each day, the driver can run out of hours far enough from home to have to rest in the truck. We therefore estimated overnight idling hours for a conservative case by assuming that trucks going over 80,000 miles annually idled 6 hours/day, 300 days/year, and those traveling 60–80,000 miles 70% of that, 40–60,000 miles 40%, and under 40,000 miles 10%. Trucks without sleepers are assumed not to idle overnight, and idling fuel use was assumed to be 0.8 gallons per hour. This gives a total fuel use for idling overnight of about 685 million gallons. Table 1 shows the breakout of fuel use by distance classes and trailer type. Class 6 and 7 sleepers are seen to be negligible.

Note that team drivers can drive through the night, so a more detailed analysis should include information on teams, and exclude overnight idling for them. Because no comprehensive data exist on idling hours, we performed a simple sensitivity analysis to several parameters. To get an upper bound on the fuel used by overnight idling, we considered all sleepers idling 10 hours/day at 1 gal/h. This triples the conservative estimated fuel use to almost two billion gallons, and is clearly unrealistic. However, the high degree of uncertainty to assumptions highlights the need to get better data on actual overnight idling practice. On-board computers could be utilized to collect these data.

## Idling as Part of the Working Day

Although it is well known that trucks often idle in the course of the workday, no detailed analysis exists. We will give some examples of situations in which trucks generally idle for extended periods, either at rest or in creep mode, and provide rough estimates of the time and energy use for these examples. Again, we will perform sensitivity analysis to get some insight into whether this workday idling is a significant contributor to total energy use by idling trucks.

It is necessary to disaggregate trucks into categories based on the type of service they perform and to examine their daily operations. First look at the large trucks that move raw materials, intermediate products, and final consumer goods around the country to and from ports and production plants to distribution centers, retail outlets, and construction sites. These trucks may need to park and find the right person to process paperwork, obtain a dock assignment, wait in line for their turn at the loading dock, then wait again while goods are unloaded from or loaded onto their trucks, check the load, and get more paperwork filled out when they are done. The time involved varies by location, time-of-day, and type of operation, but can be from one-half hour to as long as six hours for a single stop. Similarly, trucks can be delayed in queues at border crossings for as long as four hours.

**Table 1.** Fuel Used While Idling for Sleeper Trucks, by Selected Body Types and Miles Driven Category

| Class 8C w/sleeper body type | Miles driven category (mi/y) | Number of trucks | Total fuel used (gal / y) | Idle time per truck (h/y) | Fuel used to idle (gal/y)/trk | Fuel used to idle (gal/y) | Idle % of total fuel used |
|---|---|---|---|---|---|---|---|
| Dump | < 40,000 | 20,535 | 46,014,662 | 0 | 0 | 0 | 0.0% |
| | 40,000 - 60,000 | 3,797 | 35,481,756 | 720 | 576 | 2,187,072 | 6.2% |
| | 60,001 - 80,000 | 4,872 | 65,079,191 | 1,260 | 1,008 | 4,910,976 | 7.5% |
| | > 80,000 | 7,233 | 145,494,922 | 1,800 | 1,440 | 10,415,520 | 7.2% |
| Flatbed / platform | < 40,000 | 31,666 | 91,204,132 | 0 | 0 | 0 | 0.0% |
| | 40,000 - 60,000 | 14,840 | 142,730,487 | 720 | 576 | 8,547,840 | 6.0% |
| | 60,001 - 80,000 | 15,105 | 205,347,095 | 1,260 | 1,008 | 15,225,840 | 7.4% |
| | > 80,000 | 41,132 | 852,593,119 | 1,800 | 1,440 | 59,230,080 | 6.9% |
| Tank - liguid / gas | < 40,000 | 6,724 | 24,066,861 | 0 | 0 | 0 | 0.0% |
| | 40,000 - 60,000 | 4,055 | 36,194,736 | 720 | 576 | 2,335,680 | 6.5% |
| | 60,001 - 80,000 | 4,523 | 53,669,123 | 1,260 | 1,008 | 4,559,184 | 8.5% |
| | > 80,000 | 20,916 | 392,994,386 | 1,800 | 1,440 | 30,119,040 | 7.7% |
| Basic enclosed van | < 40,000 | 34,239 | 129,082,598 | 0 | 0 | 0 | 0.0% |
| | 40,000 - 60,000 | 25,541 | 235,177,541 | 720 | 576 | 14,711,616 | 6.3% |
| | 60,001 - 80,000 | 33,500 | 400,281,941 | 1,260 | 1,008 | 33,768,000 | 8.4% |
| | > 80,000 | 213,425 | 4,225,423,766 | 1,800 | 1,440 | 307,332,000 | 7.3% |
| Insulated reefer | < 40,000 | 5,914 | 21,147,647 | 0 | 0 | 0 | 0.0% |
| | 40,000 - 60,000 | 5,458 | 53,092,054 | 720 | 576 | 3,143,808 | 5.9% |
| | 60,001 - 80,000 | 7,293 | 93,097,435 | 1,260 | 1,008 | 7,351,344 | 7.9% |
| | > 80,000 | 59,659 | 1,350,114,617 | 1,800 | 1,440 | 85,908,960 | 6.4% |
| Other* | < 40,000 | 42,166 | 101,965,371 | 0 | 0 | 0 | 0.0% |
| | 40,000 - 60,000 | 11,839 | 116,466,377 | 720 | 576 | 6,819,264 | 5.9% |
| | 60,001 - 80,000 | 10,257 | 145,308,684 | 1,260 | 1,008 | 10,339,056 | 7.1% |
| | > 80,000 | 34,917 | 747,101,232 | 1,800 | 1,440 | 50,280,480 | 6.7% |
| Class 8C w/sleeper totals | | 659,606 | 9,709,129,733 | | | 657,185,760 | 6.8% |
| Class 7C w/sleeper totals | | 4,802 | 45,830,198 | 1,800 | 1,440 | 6,914,880 | 15.1% |
| Class 6C w/sleeper totals | | 1,652 | 23,364,721 | 1,800 | 1,440 | 2,378,880 | 10.2% |

* Other includes beverage, curtainside, low boy, pole, dry bulk tank, insulated non-reefer, open top, car carrier, livestock, mobile home toter, drop frame, unknown.

There are several measures that are being used or could be developed to reduce this wasteful idling time. First of all, many companies (like Wal-Mart) use a technique known as “drop and hook” to avoid the delay caused by the need to wait while trailers are being loaded or unloaded. If the entire trailer load is going to this site, the truck can back the trailer into the loading dock and separate the tractor from the trailer, leaving the tractor free to pick up another trailer and proceed on its way. This type of operation requires more trailers than tractors. And if only part of the load is for the site, the driver must wait until that part is unloaded before proceeding to the next stop on his/her route.

Another technique that can be used is scheduled pick-up or delivery times. This technique is being tried at the Port of Long Beach. However, real-time electronic communication is required for this to work well. Otherwise, delays on route can cause drivers to miss their scheduled slots. For locations without scheduling, it would be possible to avoid queues of trucks in creep mode by instituting a take-a-number system, similar to that used in

delicatessens. Drivers could then park, turn off their engines, and wait in comfortable areas such as some shippers already provide, until their numbers were called. Even border crossings could provide this service.

Another situation in which long-duration (> one-half hour) idling occurs spans a wide class of vehicle service types. Almost all drivers have an hour off for lunch; during this time, the vehicle may be left idling, especially if the weather is warm. One expert writes, "Remember, the cab sits on top of a 500–800 pound (lb) heat sink that could be over 200° Fahrenheit (F). On a 50-60º day, the cab can be like an oven after sitting for 20-30 minutes." (Abelson 2005) This problem becomes less severe for smaller vehicles.

Another class of vehicles that idles for significant periods during the workday is dump trucks, which idle while being loaded, drive to the dump-site, dump, and return. Depending on the operation, it might be reasonable to shut the engine off during loading. This might require a climate control system independent of the main engine for operation in extreme weather.

Next we consider smaller vehicles. As a general rule, smaller vehicles are easier to start, warm up faster, and are more likely to be stolen, so they are less likely to be left idling when the driver is not in them. However, some types of trucks have been observed to idle for significant periods when making deliveries or performing other jobs. These include leased refrigerated straight trucks, bakery trucks, and linen-supply company trucks (often walk-in vans), which idle from 10 minutes to one hour at a time. Similarly, heavy vocational straight trucks, including refuse haulers, public works crew trucks, and newspaper delivery trucks may idle for 20–30 minutes at each stop (Winsor 2004). Utility trucks idle as well, sometimes most of the day, but at least in some cases, these are providing a useful service by creating a place for workers to warm up when they come down from utility poles or up out of manholes. For such situations, heaters or APUs could provide the same service with less energy use and emissions. Other than these utility vehicles, we have not identified instances where small trucks are idled for long periods of time. The owners of the many pickups and vans that perform household and commercial repairs and installations or transport produce from small farms all seem to recognize how much money they save by simply turning their vehicles off when not in use.

## Fuel Use for Workday Idling

Given these general observations and essentially no actual data, we did some simple modeling to determine to what extent extended workday idling could be an important problem. The short answer is that, given the large numbers of vehicles potentially involved, the fuel use for this type of idling could be much larger than that for overnight idling, and data should be obtained. This section details the assumptions made in order to scope out the energy use for extended workday idling.

First of all, it was necessary to estimate the per-hour fuel use for extended idling. The only data point we have is that idling large sleeper tractors use approximately 0.8 gal/h (or more depending on idle speed and accessory loads). We assumed that smaller trucks would use proportionately less fuel at idle; thus, if a vehicle class got twice the fuel economy as a Class 8 tractor, it would burn half as much fuel at idle (0.4 gal/h).

Then it was necessary to estimate the idling hours for different types of trucks. This was highly uncertain. We identified several classes of trucks that might idle for extended periods, and estimated possible extents. Our first attempt assumed that all vehicles of that type idled for the maximum time; these estimates did not seem reasonable, so we revised our numbers downward on the basis that only a subset of the vehicles were high idlers, or that the need was only present part of the year. In each case, we assumed that the vehicles that traveled the longest distances spent most of their time driving, and those that traveled under 40,000 miles per year drove less because much of the time, they were stopped waiting for something or someone, and were idled most. We assigned the maximum idling hours to the under-40,000 mile trucks, 75% of maximum to 40–60,000 milers, 50% to 60–80,000 milers, and 25% to 80,000+ milers. In each case, we assumed that the vehicle operated for 300 days per year, and estimated a typical number of

hours idled per day for the body type. Vans and dump trucks were assigned 2 hours/day, utility vehicles 3 hours/day, and platform trucks, tankers, and garbage trucks 1 hour/day, and all other trucks, 0.5 hour/day. As can be seen in Table 2, even these relatively conservative estimates yield a total fuel use of almost 2.5 billion gallons annually (7% of the fuel used by these trucks), leading us to the conclusion that idling during the workday is likely to be a very significant user of fuel, and should be examined in detail.

This table was constructed by identifying types of trucks that were likely to idle, and specifically adding hours for them over an assumed low baseline. However, the idling hours by some delivery vans could be underestimated, and accounting for increased idling by those numerous large trucks would significantly increase the total. Similarly, it would be appropriate to identify types of trucks, such as pickups, for which we could not identify any reason to idle routinely, and subtract these out entirely. Doing this for pickup trucks reduced the first estimate by almost 500 million gallons per year because of the large number of pickups in commercial service (over seven million). This illustrates the high degree of sensitivity of these results to individual inputs. It is clear that actual data on idling practices of trucks during the workday must be sought.

## Conclusions

Extended idling by commercial trucks represents a significant use of our petroleum resources, and much of this oil use could be avoided by installing idle-reduction technologies, adopting vehicle scheduling policies, or simply by turning the trucks off. Until now, attention has been focused on overnight idling by tractor-trailers with sleepers, which represent a very visible and obvious target for conservation and emission-reduction efforts. However, commercial trucks of all sizes idle for extended periods (one-half hour or more) during their workdays, for a variety of reasons, from waiting to pick up or drop a load to providing a warm haven for workers fixing utilities or roads in inclement weather. The quantity of petroleum used by such trucks may be far greater than that used by sleepers idling overnight. Although the length of time these vehicles idle is considerably shorter than the 6–10 hours that sleepers idle, the sheer number of vehicles more than makes up for it.

The sum of overnight and workday idling of trucks may consume well over two billion gallons of oil (mostly diesel) annually in the United States. Collection of data from vehicles and fleets in many industries would be required to develop an accurate estimate of idling fuel use. Cost-effective technologies exist for reducing overnight idling, but the fewer hours trucks idle per day while working will be somewhat of a barrier to their use in non-sleepers, because the payback period will be longer than the two-years that the trucking industry requires. Further, for those vehicles that idle in queues (creep mode), some technology development will be required to enable slow vehicle motion without use of the main engine. One possibility is use of the auxiliary power unit to supply minimal motive power. It will be a challenge to extend the realm of idle-reduction technologies to solve the problem of workday idling.

## References

VIUS02, *Vehicle Inventory and Use Survey: 2002 — Microdata file.* U.S. Department of Commerce, Bureau of the Census, Washington, D.C. (2004).

Stodolsky, F., L. Gaines, and A. Vyas. *Analysis of Technology Options to Reduce Fuel Consumption of Idling Trucks*. Argonne National Laboratory Report ANL/ESD-43 (June 2000).

EPA Smartway Website. http://www.epa.gov/otaq/smartway/idlingtechnologies.htm (last accessed 8/1/05).

Lutsey, N., C.J. Brodrick, D. Sperling, and C. Oglesby. *Heavy-Duty Truck Idling Characteristics — Results from a Nationwide Truck Survey*. TRB Annual Meeting (January 2004).

Orr, David. Caterpillar. Personal communication. (September 2003)

Abelson, Paul. LandLine Magazine. Personal communication. (July 2005)

Winsor, Jim. *Idle Thoughts on Engine Idling*, Heavy Duty Trucking (April 2004) http://www.heavydutytrucking.com/2004/04/120a0404.asp (accessed 7/25/05).

**Table 2.** Fuel Used by Commercial Trucks Idling on the Job by Selected Body Type and Miles Driven Category

| All Commercial Body Type | Miles Driven Category (mi/yr) | Number of Trucks | Total Fuel Used (gallons/y) | Avg. mpg | Idle Time (hr/y) | Idle Fuel Flow Rate (gal/h) | Fuel Used to Idle (gal/y)/trk | Fuel Used to Idle (gal/y) | Idle is x% of Total Fuel Used |
|---|---|---|---|---|---|---|---|---|---|
| Minivan | < 40,000 | 1,175,532 | 1,038,768,478 | 17.7 | 600 | 0.262 | 157 | 184,897,237 | 17.8% |
| | 40,000 - 60,000 | 65,009 | 178,620,070 | 17.7 | 450 | 0.262 | 118 | 7,668,858 | 4.3% |
| | 60,001 - 80,000 | 17,384 | 86,127,314 | 13.0 | 300 | 0.357 | 107 | 1,861,425 | 2.2% |
| Full-size (LD) van | < 40,000 | 2,040,986 | 2,040,445,188 | 13.2 | 600 | 0.352 | 211 | 430,462,502 | 21.1% |
| | 40,000 - 60,000 | 69,063 | 240,504,381 | 13.1 | 450 | 0.354 | 159 | 11,007,904 | 4.6% |
| | > 80,000 | 9,400 | 51,618,036 | 17.3 | 150 | 0.268 | 40 | 378,173 | 0.7% |
| Dump | < 40,000 | 724,547 | 1,019,392,773 | 5.8 | 600 | 0.800 | 480 | 347,782,560 | 34.1% |
| | 40,000 - 60,000 | 49,005 | 490,693,938 | 4.9 | 450 | 0.947 | 426 | 20,882,131 | 4.3% |
| | 60,001 - 80,000 | 23,529 | 326,154,539 | 5.1 | 300 | 0.910 | 273 | 6,422,033 | 2.0% |
| | > 80,000 | 23,977 | 483,093,921 | 5.3 | 150 | 0.875 | 131 | 3,148,678 | 0.7% |
| Flatbed/platform | < 40,000 | 939,658 | 1,217,696,747 | 7.4 | 300 | 0.627 | 188 | 176,757,289 | 14.5% |
| | 40,000 - 60,000 | 49,334 | 370,892,077 | 6.4 | 225 | 0.725 | 163 | 8,047,609 | 2.2% |
| | 60,001 - 80,000 | 25,770 | 321,901,976 | 5.7 | 150 | 0.814 | 122 | 3,146,653 | 1.0% |
| | > 80,000 | 50,924 | 1,012,165,598 | 5.6 | 75 | 0.829 | 62 | 3,164,563 | 0.3% |
| Service - utility | < 40,000 | 248,756 | 368,030,625 | 7.7 | 900 | 0.603 | 542 | 134,909,748 | 36.7% |
| | 40,000 - 60,000 | 4,924 | 28,084,098 | 8.2 | 675 | 0.566 | 382 | 1,880,728 | 6.7% |
| | 60,001 - 80,000 | 718 | 4,313,840 | 11.3 | 450 | 0.411 | 185 | 132,671 | 3.1% |
| | > 80,000 | 913 | 8,736,854 | 10.3 | 225 | 0.450 | 101 | 92,541 | 1.1% |
| Tank – liquid/gas | < 40,000 | 177,128 | 379,586,263 | 5.5 | 300 | 0.844 | 253 | 44,829,487 | 11.8% |
| | 40,000 - 60,000 | 16,329 | 143,096,007 | 5.7 | 225 | 0.814 | 183 | 2,990,785 | 2.1% |
| | 60,001 - 80,000 | 12,016 | 146,697,628 | 5.9 | 150 | 0.786 | 118 | 1,417,481 | 1.0% |
| | > 80,000 | 35,401 | 673,812,671 | 5.9 | 75 | 0.786 | 59 | 2,088,059 | 0.3% |
| Trash/garbage | < 40,000 | 77,520 | 305,197,033 | 4.4 | 300 | 1.055 | 316 | 24,524,509 | 8.0% |
| | 40,000 - 60,000 | 12,016 | 119,502,504 | 5.0 | 225 | 0.928 | 209 | 2,508,941 | 2.1% |
| | 60,001 - 80,000 | 2,733 | 35,901,942 | 5.2 | 150 | 0.892 | 134 | 365,802 | 1.0% |
| | > 80,000 | 949 | 18,234,173 | 5.9 | 75 | 0.786 | 59 | 55,975 | 0.3% |
| Basic enclosed van | < 40,000 | 650,517 | 1,469,253,265 | 7.3 | 600 | 0.636 | 381 | 248,087,579 | 16.9% |
| | 40,000 - 60,000 | 107,404 | 817,171,943 | 6.5 | 450 | 0.714 | 321 | 34,501,470 | 4.2% |
| | 60,001 - 80,000 | 94,550 | 1,052,739,306 | 6.3 | 300 | 0.737 | 221 | 20,891,048 | 2.0% |
| | > 80,000 | 302,672 | 5,873,032,985 | 6.1 | 150 | 0.761 | 114 | 34,534,379 | 0.6% |
| Insulated reefer | < 40,000 | 96,268 | 292,236,464 | 6.7 | 600 | 0.693 | 416 | 40,001,509 | 13.7% |
| | 40,000 - 60,000 | 20,414 | 161,964,407 | 6.2 | 450 | 0.748 | 337 | 6,874,908 | 4.2% |
| | 60,001 - 80,000 | 17,325 | 202,947,017 | 6.0 | 300 | 0.773 | 232 | 4,019,400 | 2.0% |
| | > 80,000 | 70,694 | 1,556,874,982 | 5.6 | 150 | 0.829 | 124 | 8,786,254 | 0.6% |

**Table 2.** Cont.

| All Commercial Body Type | Miles Driven Category (mi/yr) | Number of Trucks | Total Fuel Used (gallons/y) | Avg. mpg | Idle Time (hr/y) | Idle Fuel Flow Rate (gal/h) | Fuel Used to Idle (gal/y)/trk | Fuel Used to Idle (gal/y) | Idle is x% of Total Fuel Used |
|---|---|---|---|---|---|---|---|---|---|
| Multi-stop van | < 40,000 | 372,892 | 662,599,461 | 8.6 | 600 | 0.540 | 324 | 120,712,945 | 18.2% |
| | 40,000 - 60,000 | 17,268 | 84,280,278 | 9.6 | 450 | 0.483 | 218 | 3,755,790 | 4.5% |
| | 60,001 - 80,000 | 3,077 | 24,132,931 | 8.5 | 300 | 0.546 | 164 | 503,904 | 2.1% |
| | > 80,000 | 1,265 | 11,870,995 | 10.1 | 150 | 0.459 | 69 | 87,172 | 0.7% |
| Other van | < 40,000 | 54,471 | 77,343,236 | 8.8 | 600 | 0.527 | 316 | 17,232,644 | 22.3% |
| | 40,000 - 60,000 | 1,193 | 5,713,537 | 9.6 | 450 | 0.483 | 218 | 259,478 | 4.5% |
| | 60,001 - 80,000 | 513 | 3,062,867 | 11.2 | 300 | 0.414 | 124 | 63,759 | 2.1% |
| | > 80,000 | 377 | 3,480,504 | 10.9 | 150 | 0.426 | 64 | 24,073 | 0.7% |
| Drop frame | < 40,000 | 6,304 | 18,859,832 | 6.2 | 600 | 0.748 | 449 | 2,830,699 | 15.0% |
| | 40,000 - 60,000 | 1,810 | 14,755,498 | 5.9 | 450 | 0.786 | 354 | 640,556 | 4.3% |
| | 60,001 - 80,000 | 1,364 | 15,423,848 | 6.3 | 300 | 0.737 | 221 | 301,379 | 2.0% |
| | > 80,000 | 4,502 | 102,985,261 | 6.0 | 150 | 0.773 | 116 | 522,232 | 0.5% |
| Other | < 40,000 | 9,829,988 | 9,827,530,297 | 13.7 | 150 | 0.339 | 51 | 499,392,091 | 5.1% |
| | 40,000 - 60,000 | 503,006 | 1,842,295,205 | 12.5 | 112 | 0.371 | 42 | 20,912,173 | 1.1% |
| | 60,001 - 80,000 | 65,680 | 579,037,170 | 7.8 | 75 | 0.595 | 45 | 2,930,338 | 0.5% |
| | > 80,000 | 70,181 | 1,173,164,852 | 6.5 | 37 | 0.714 | 26 | 1,853,642 | 0.2% |
| All commercial body type totals | | 18,147,256 | 36,982,024,815 | 9.4 | | | | 2,491,143,761 | 6.7% |

Note: Other includes pickup, SUV, armored, concrete mixer, concrete pumper, crane, curtainside, low boy, pole, other service, street sweeper, tank (dry/bulk), Tow/wrecker, vacuum, insulated non-reefer, open top, car carrier, livestock, mobile home toter, and unknown.

# VII. OFF-HIGHWAY

## VII.A. Hybrid Energy Storage and Fuel Optimization

*Principal Investigator: Lembit Salasoo*
*General Electric Global Research*
*1 Research Circle, Niskayuna NY 12309*
*(518) 387 5000, fax: (518) 387 6675, e-mail: salasoo@crd.ge.com*

*Field Project Manager: Steve Cooke*
*National Energy Technology Laboratory*
*Morgantown, WV 26507-0880*
*(304) 285-5437, e-mail Steve.Cooke@netl.doe.go*

*Technology Development Managers: Sid Diamond and Lee Slezak*
*(202) 586-2335, e-mail: Lee.Slezak@hq.doe.gov*

*Participants*
*Paul K. Houpt, General Electric Global Research*

---

*Contractor: General Electric Global Research*
*Contract No.: DE-FC04-2002AL68284*

---

### Objectives

- Develop and demonstrate locomotive system technologies targeting gross fuel efficiency gains.
- Demonstrate a modular energy storage system for hybrid locomotive system on a hybrid locomotive platform.
- Develop optimization software for minimizing fuel consumption in both hybrid and non-hybrid locomotives, and demonstrate the consist optimizer on the test track.
- Demonstrate the combination of modular energy storage system and fuel optimizer on a hybrid locomotive with full-scale energy storage system.

### Approach

- Specify and develop advanced modular energy storage units and lab test prototype modules.
- Design and bench test advanced hybrid locomotive energy management system controls and demonstrate on a hybrid locomotive on a test track.
- Develop suitable models for dynamic optimization of fuel use.
- Develop practical, robust fuel-use optimization algorithms capable of locomotive implementation.
- Demonstrate fuel use optimization algorithms in off-line interactive simulation environment.
- Complete field demonstrations of selected fuel-saving algorithms.
- Fabricate and bench test full-scale energy storage modules and associated controls.
- Integrate full-scale energy storage modules to hybrid locomotive.

- Design, fabricate, and bench test hybrid fuel optimizer controls.
- Integrate fuel optimizer controls on hybrid locomotive and demonstrate on test track.
- Measure and verify fuel savings benefit.

## Accomplishments

- Conducted modular advanced battery system ripple current, cold energization, long-term cycling, and accelerated vibration testing.
- Developed modular advanced battery system thermal and high-voltage design.
- Demonstrated advanced hybrid locomotive energy management system controls.
- Refined greatly simplified near-optimal approaches to compute fuel-saving driving plans.
- Enhanced real-time Consist Manager and Trip Optimizer simulation platform with operator interface.

## Future Directions

- Fabricate and evaluate locomotive-worthy hybrid energy storage modules.
- Design the integration of hybrid energy storage system into the hybrid locomotive platform.
- Fabricate full locomotive set of hybrid energy storage modules, integrate system into the hybrid locomotive and track test.
- Complete on-locomotive test of hybrid fuel optimization controls.
- Measure and verify fuel performance of combined system.

---

## Introduction

General Electric's (GE's) vision is a 21st Century locomotive that intelligently controls an efficient power plant to optimize energy management while meeting legislated emissions levels. The 21st Century Locomotive Technology project was proposed to improve locomotive efficiency with energy management and optimization technologies and to develop advanced fuel injection and turbomachinery technologies for an emissions-compliant and fuel-efficient power plant. The energy management and optimization technologies are applied to the locomotive system outside the power plant and projected to produce a total 20% reduction in total fuel consumption. This annual report applies in particular to the progress for the two locomotive system technologies for hybrid energy storage and fuel optimization.

At this point, two successful railroad customer demonstrations have validated the Consist Manager fuel optimization technique and advanced hybrid battery management techniques. The design of locomotive-hardened sodium-nickel chloride battery modules is well in hand, and the trip optimizer fuel optimization technique has been developed. The team looks forward to successfully integrating these technology components and validating the combined fuel efficiency benefits on a hybrid locomotive.

## Benefits for Locomotives and Road Vehicles

The rail modality carries approximately 40% of U.S. freight on a ton-mile basis, and in 2003, the Class 1 railroads consumed 3.85 billion gallons of fuel to move this freight. Application of the energy management and optimization technologies developed in this project to the whole locomotive fleet will save approximately 770 million gallons of fuel annually. Further, as fuel prices rise and global oil supply tightens, increasing railroad fuel efficiency makes transfer of freight transportation mode from less fuel-efficient modalities to rail increasingly attractive on an economic basis, producing significant impact on the national strategic imperative to reduce dependence on foreign oil. That is, the increase in railroad fuel efficiency will naturally provide the market-based

signals to transfer freight transportation to rail from modalities with significantly lower fuel efficiency.

In addition, the energy storage system and optimization technologies developed in this project have significant potential for impact on-road transportation fuel efficiency. At the start of the project it was anticipated that either nickel-metal hydride or lithium ion battery technologies developed for hybrid automobiles would form the basis for a hybrid locomotive, but a detailed locomotive requirements assessment coupled with a survey of available technologies identified sodium-nickel chloride technology as a much better fit due to simplified cooling and control requirements and reduced footprint. In addition, a bottom-up price entitlement assessment (Galloway and Dustmann 2003) projects an ultimate price per energy kilowatt-hour that is significantly lower than either nickel-metal hydride or lithium ion battery technologies (Matheys and Van Autenboer 2005), and roughly comparable to advanced lead-acid battery technology. It is anticipated that adoption of this technology for hybrid locomotives will accelerate the achievement of economies of scale and hasten the availability of economically priced energy storage for heavy hybrid road vehicles and plug-in hybrid road vehicles. In addition, the fuel optimizer concept and implementation developed in this project could be applied to on-road vehicles, in particular for longer trips and heavy vehicles. Quantification of these opportunities to transfer technologies to road vehicles and their effects on national fuel consumption is well outside the scope of this particular project, but it is clear that percentage-point improvements in fuel consumption for instance for the heavy truck segment yield significant reduction in national requirements for foreign oil.

## Advanced Modular Energy Storage System

A hybrid locomotive will store otherwise-wasted locomotive braking energy and reuse this energy for traction, thereby reducing fuel consumption 10–15%. The energy storage system (ESS) and energy management system (EMS) are complementary and critical parts of the overall hybrid locomotive system. The EMS controls and coordinates the storage and release of ESS energy, in order to maximize the fuel benefit, and avoid premature damage to the ESS due to exceeding operational limits. In previous years, multiple energy storage technologies were evaluated and sodium nickel chloride technology was selected for the hybrid locomotive, in particular due to its simplified cooling and control requirements and smaller footprint.

Existing sodium nickel chloride energy storage battery designs had been developed by the vendor in sizes up to 40 kWh to meet hybrid and pure-electric automobile and bus application requirements and had a history of good performance. However, the locomotive requirements are significantly more demanding, in particular for a higher operating voltage, more intense cycling, and harsher shock and vibration duty. It was expected that redesign based on the existing designs would be required. The vendor agreed to produce redesigned evaluation modules for evaluation by the 21st Century Locomotive Technology team, GE Rail, or the vendor, depending on the availability of necessary evaluation apparatus. In the past year, the vendor upgraded the battery module cooling system design and developed a 1224-V battery design.

The design approach to meet shock and vibration requirements was to identify failure modes of the existing design through test and then address these failure modes through design modifications. Such an approach has been used successfully for most locomotive subsystems. Typically, the first iteration results in system failure but subsequent redesign to address failure modes is successful. Two exploratory accelerated vibration tests were performed, followed up with a third test with more detailed internal instrumentation of the test battery. Analysis of data from the third test is in progress, but initial results show insulation abrasion as the most significant failure mode.

Electrical testing was performed to determine the battery interaction with the locomotive electrical transients and long-term cycling performance. Aging trends have been quantified based on long-term test results using subscale cell assemblies, and a test sequence is in process to quantify the effects of connecting a cold battery to the locomotive system.

## Advanced Energy Management System

GE proof-of-principle hybrid demonstrator locomotive experience showed that a backup method to estimate battery internal state of charge (SOC) was required, to maintain long-term accuracy in battery control by the EMS. Accurate EMS knowledge of SOC is required to avoid degradation to the battery, while obtaining maximum fuel-saving value. Previously, a successful method utilizing temperature and a combination of static and dynamic battery terminal current and voltage measurements was developed. The enhanced EMS with SOC backup algorithm was installed on the GE proof-of-principle hybrid demonstrator locomotive, and successfully track tested in the period November 2004–January 2005. Resulting statistics showed that the battery SOC was estimated within 8% of true value with 95% confidence. The method was shown to be robust enough to operate on a locomotive with noisy sensor data.

## Develop Fuel Optimizer Systems and Demonstrate Consist Fuel Optimizer

The goal was to develop and demonstrate control strategies to save fuel initially in freight trains using conventional (non-hybrid) diesel-electric locomotives for propulsion. A methodology was developed to bring benefit to non-hybrid locomotives, and then extended to hybrid locomotives. The key systems developed in the effort are referred to as Consist Manager and Trip Optimizer. Focus has been to develop the required algorithms to compute fuel optimal trips in numerically robust ways — including new ways to simplify a complex optimization problem; to develop a means to follow the optimal plans in a coaching or closed loop fashion; to provide for a means to re-plan a partially completed trip in an efficient fashion; to develop a simulation means to prototype a real-time interactive system to demonstrate the concepts; and finally, to demonstrate the system on a revenue service locomotive.

The Consist Manager has been described in detail previously; it saves fuel by distributing power requested by the driver among the locomotives in the most fuel-efficient fashion. This system was shown to be simple to implement and is transparent to operations, and was demonstrated to save 1–3% fuel when used in typical duty cycles.

Trip Optimizer provides an integrating framework for energy management in completing a freight haul from a mission perspective. Information provided by dispatch on the logistics of the load to be carried, starting point and destination, route to follow, power (locomotive) configuration, together with models and parameter values of associated models, are together used to synthesize the best way to drive the train to arrive at a specified time with the least fuel consumption. Trip Optimizer synthesizes the optimal speed to drive and the associated throttle setting, which minimizes fuel and satisfies speed restrictions (limits) along the route. The optimal "recipe" or plan for driving the train can be provided as coaching cues to the driver or executed closed-loop with feedback of certain locomotive variables plus GPS-derived track location coordinates. With Trip Optimizer, the onboard crew has a tool to manage the journey in a completely novel way, by allowing explicit tradeoffs between journey completion time and the fuel used as opposed to operating at or near the speed limit all the time when given a track authority. For this increase in mission complexity, a crew with suitable incentives can save more than 4% fuel in a typical mission, for the same travel time, compared to manual operation, and where even a small amount of slack time is available, fuel savings exceeding 8% are feasible.

## Efficient Computation of Optimal Trip Plans

Previously, the computation for a typical route segment of 100–200 miles of track might take several hours of computer time. This has been speeded up to take only 30–60 seconds by effective integration of all computations into a unified environment. Consequently it is now feasible to carry out calculation of a new plan (1) in a near interactive fashion and (2) onboard the locomotive as necessary to correct a driving plan for the numerous and inevitable changes that occur over the course of a trip. Various case studies consistently show potential fuel savings (compared to the performance of observed driver not running optimized) exceeding 4%.

A key element of the architecture is the partition of any trip into segments. Boundaries of segments are arbitrary, but can be formed at natural spatial locations such as stations, sidings or speed restrictions. On each segment, solutions can be pre-computed then pieced together later to meet required travel time.

A simple optimization formulation allocates travel-time among segments for minimum total fuel. Then the corresponding detailed plan can be looked up and pieced together to create the overall plan. It has been found that such plans, while strictly speaking suboptimal, achieve >99.5% of the performance of a fully optimized plan. If trip parameters change, e.g., a speed limit on a segment, the full-blown optimization must be repeated, but only for that segment, greatly simplifying the calculations that must be carried out online. This has enormous value when a plan is changed en route. For example, if at the end of the first segment it was necessary to change the travel time (up or down) for the remaining route, the 'new' travel time could be allocated to the remaining segments in a near-optimal fashion, and the driver could switch to the new plan.

## Planning Architecture

Trip Optimizer planning is the process that builds on the driving recipe of throttle and speed to carry out a typical trip. In particular, it provides the analysis and decision framework to start a journey, adjust a plan for changes that occur in route, and when required, to develop a completely new plan when conditions preclude a simple fix.

This architecture has been implemented, including the following elements:

- Data structures to represent the plan elements and system parameters
- An "engine" to compute a plan based on parameters and objectives
- An algorithm to break the plan into single or multiple parts (segments)
- A means to execute the plan in both an advisory (i.e., operator controls throttle) and closed loop (system controls the throttle)
- A means to track projected arrival times and performance compared to the plan

## Engineer Human-Machine Trip Optimizer Interface

An important functionality for the trip plan architecture is the interface between the engineer and the trip planning and its associated execution system. A prototype interactive, real-time planning and locomotive simulation environment system was implemented in a low cost PC-class workstation, to have the capability to perform all the required Trip Optimizer functions plus a realistic driver cab emulation environment. Software is able to display conventional elements of a locomotive display including throttle and brake status, speedometer, accelerometer, and tractive effort. The control console is illustrated in Figure 1. Enhancements for Trip Optimizer include a look-ahead strip-chart showing the current speed, speed limit, and optimal planned speed together with the current and optimal throttle (notch) setting. This "loco cab" display also shows a palette of data regarding the trip status, distance to go, and performance statistics. The simulation is interfaced to an AAR-105 full-scale control panel, which allows manual operator control with a standard control panel configuration. To add realism, the computed locomotive states are displayed in special analog gauges, and a pseudo-three-dimensional display is projected to provide a sense of motion during a simulation run. Numerous interactive features have been provided to examine and manage the data needed for a plan, carry out optimization over segments using the optimal control software, launch and execute a plan, and re-plan along the route. For training purposes, features were also included to zoom in on data, examine actual performance compared to plan (with driver manual control), and "fast forward" and "rewind" to interesting sections of the trip. While this interface is strictly for an engineering demonstration, it allows all the features of a potential commercial product to be demonstrated and evaluated, and will serve as the basis for future on-locomotive demonstrations.

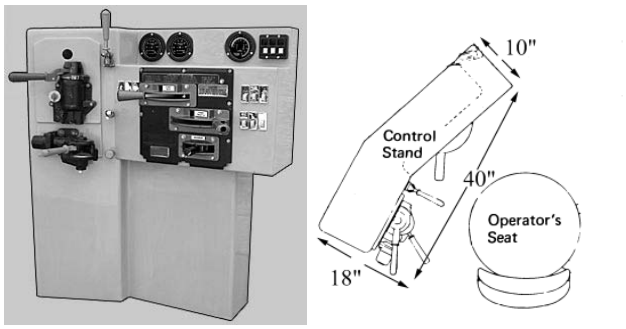


**Figure 1.** AAR 105 simulation control interface for Trip Optimizer

## Conclusions

In FY 2005, the locomotive track demonstration of advanced battery energy management was completed, and much of the fundamental electrical and mechanical testing of the baseline sodium-nickel chloride battery systems was completed as well. Accelerated vibration tests have clearly identified the necessary battery module design modification areas. The development of non-hybrid fuel optimization techniques (Consist Manager and Trip Optimizer) has been carried out, and the extension of these techniques to utilize the extra degrees of freedom offered by a hybrid locomotive has been initiated.

The GE project team looks forward in FY 2006 to integrating both the advanced energy storage module technology and hybrid optimizer technology onto a new GE prototype hybrid locomotive. The project will culminate with the validation of double-digit percentage reduction in fuel usage in freight haulage applications, a significant benefit to one of the dominant U.S. freight transportation modalities.

## References

Galloway, R.C., and C.-H. Dustmann, "ZEBRA Battery — Material Cost, Availability and Recycling," 20th International Electric Vehicle Symposium and Exposition (EVS20), Long Beach CA, 15–19 November 2003.

Matheys, J., and W. Van Autenboer, "SUBAT: sustainable batteries, Work Package 5: Overall Assessment, Final Public Report," SUBAT EU project no. 502490, 2005. Available at http://www.battery-electric.com/documents.php.

# VII.B. Advanced Hybrid Propulsion and Energy Management System for High-Efficiency, Off-Highway, 320-Ton-Class, Diesel Electric Haul Trucks

*Principal Investigator: Tim Richter*
*GE Global Research, 1 Research Circle, EP110C, Niskayuna, NY 12309*
*(518) 387-5670, fax: (518) 387-6675, e-mail: tim.richter@ge.com*

*Technology Development Managers: Sid Diamond and Lee Slezak*
*(202) 586-2335; e-mail: Lee.Slezak@hq.doe.gov*

*Field Project Manager: Sam Taylor*
*(304) 285-4681, fax (304) 285-4469, e-mail: samuel.taylor@netl.doe.gov*

*Participants*
*Sean Huang, GE Global Research*
*Kevin Gavel, GE Global Research*
*Gary Kilinski, GE Global Research*
*Dwight McCormick, GE Global Research*
*Henry Young, GE Rail*
*Allen Randolph, GE Rail*
*Rafael Santana, GE Rail*
*Tim Brown, GE Rail*
*Joe Currie, GE Rail*
*Kim Byard, Komatsu America Corp.*
*Cord Dustmann, MES-DEA*

---

*Contractor: GE Global Research*
*Contract No.: DE-FC04-2002AL68080*

---

## Objective

The objective of this project is to reduce the fuel consumption of off-highway vehicles, specifically large tonnage mine haul trucks, as shown in Figure 1. A hybrid energy storage and management system will be added to a conventional diesel-electric truck that will allow capture of braking energy normally dissipated in grid resistors as heat. The captured energy will be used during acceleration and motoring, reducing the diesel engine load, thus conserving fuel.

## Approach

The project will work toward a system validation of the hybrid system by first selecting an energy storage subsystem and energy management subsystem. Laboratory testing at a subscale level will evaluate these selections and then a full-scale laboratory test will be performed. After the subsystems have been proven at the full-scale lab, equipment will be mounted on a mine haul truck and integrated with the vehicle systems. The integrated hybrid components will be exercised to show functionality, capability, and fuel economy impacts in a mine setting.

## Accomplishments

- Confirmed operation of battery cells for system validation operations in subscale battery testing.

- Verified over one year of battery life with subscale testing for nameplate-rated cycles.
- Completed initial battery vibration testing.
- Readied full-scale prototype testing for power-up.
- Fabricated and populated several on-vehicle hybrid component systems with electrical components.
- Completed battery enclosure design and vibration mounting.

## Future Directions

All major modeling and system design has been completed. In FY 2006, the project will focus on hardware implementation, testing, and vehicle system validation. Full-scale testing of hybrid components will be performed at GE Rail in Erie, PA. On-vehicle hybrid equipment will be fabricated, populated, and installed on the test vehicle in Arizona. System validation will be performed and results compared with system modeling and baseline performance.

Following the on-truck system validation and pending Department of Energy (DOE) approval, battery performance and life can be investigated. General Electric (GE) plans to request additional scope, to be performed at no additional program cost, to characterize battery performance after the on-truck validation. While great care has been taken to evaluate and select batteries with regard to performance characteristics, it is also necessary to better understand the mechanical life of the battery systems in high-vibration installations. The batteries used in the system validation testing will be electrically characterized to measure resistance rise, one primary indication of service life. Several of these batteries will be torn down and analyzed for excessive wear and mechanical damage. Other batteries will be further exercised electrically and mechanically to better understand failure modes and performance characteristics.

Beyond the current program, work could continue to better investigate the primary commercialization paths and next generation energy storage systems. Beyond improving fuel economy, hybrid technology could also be used to reduce emissions. Through improved design of systems and related hybrid components the next-generation hybrid mine haul truck will provide increased benefits in many aspects of mining operations.

---

## Introduction

The conventional mine haul truck, also referred to as an off-highway vehicle (OHV), uses a diesel engine to turn an alternator that generates alternating current (AC) electricity. The electricity is rectified to direct current (DC) voltage that is applied to the main electrical bus called the DC link. Power electronics convert the DC link voltage to variable frequency, three-phase AC that drives the wheel motors during motoring. When braking is required, the wheel motors function as generators and electrical power is directed to the braking grid resistors, also known as the "grid box," to be dissipated as heat.

**Figure 1.** Komatsu 830E-AC

In addition to traction motors, the diesel engine must power auxiliary loads such as radiator cooling fans, operator air conditioning, steering, hydraulics, and control circuits. These auxiliary loads are powered by mechanical means and with a smaller, second alternator connected to the vehicle's 24-volt (V) battery system.

Figure 2 shows a block diagram of the planned hybrid vehicle system. Three primary components will be added to the conventional OHV: hybrid

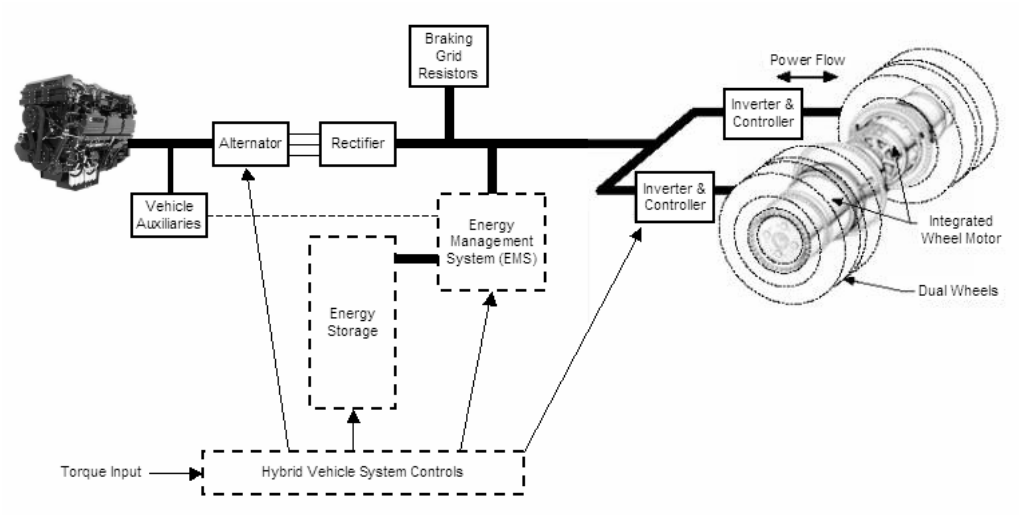


**Figure 2.** Hybrid electric system block diagram

vehicle system controls, energy management system, and energy storage system. Each component plays a specific role in the recovery of braking energy.

The hybrid vehicle system controls perform the high-level supervisory functions of the hybrid vehicle, primarily controlling the balance of engine power, grid dissipation, and battery charging or discharging. Performing these functions requires intimate connections to all of the truck systems.

The energy management system (EMS) acts to convert electrical power on the DC link into levels compatible with the energy storage system. The EMS is essentially a high-power DC-DC converter.

The energy storage system (ESS) consists of the batteries and manual disconnects, fuses, and related safety and protective components.

The hybrid system can enable additional power to be supplied as additional motoring power available at the wheels resulting in a faster speed-on-grade. The higher speed-on-grade is important when considering the impact of hybrid system weight on productivity. Any hybrid system weight must be subtracted from the working payload of the truck to maintain the same gross vehicle weight (GVW). Because the truck is already moving downhill as fast as possible, productivity, expressed in tons/hour, can only be maintained by decreasing the uphill haul time. The hybrid system enables this improvement while saving fuel.

## Subscale Battery Testing

The bulk of subscale testing has been completed prior to FY 2005; however, the complexity of battery chemistries makes it difficult to perform accelerated life tests. To address the uncertainties of accelerated life testing, MES-DEA, the manufacturer of the batteries selected for the hybrid system, has been supporting real-time life testing using their subscale test capability.

When running the subscale tests, the proper charge and discharge powers are applied at the cell level. At two points in the cycle, a resistance measurement is calculated, one to represent charging resistance and the other to represent discharging resistance. Over the term of the test, these resistance measurements are plotted to disclose trends in resistance change.

Cells can “fail” in two ways: complete failure or degraded performance. GE is primarily concerned with degraded performance in the form of increased resistance of cells. As a cells ages, the resistance generally increases, requiring higher voltages to drive charging current. For all chemical cells, there are voltage limits that, when exceeded, greatly reduce the life of the cell.

For the hybrid OHV application, the most demanding operating point is peak charging. Truck speeds are usually high (>20 miles per hour [mph]), and the wheel motors generate megawatts of power. To create an effective hybrid system, the batteries must capture as much of this generated power as possible.

Two life tests are being performed. The first test, a nameplate-rated power test, utilizes the battery system at nameplate ratings. GE expects to see minimal resistance rise and long battery life. The second test pushes charging power to 150% of the nameplate rating to investigate the capability of the battery. Power profiles were generated using GE Global Research's hybrid OHV simulation tool.

The nameplate-rated test has logged over one year of hybrid OHV cycles, and the cells are still performing well. Average cell resistance has increased approximately 50%. While this increases resistive losses and round-trip efficiency, this is not a large concern as most of the regenerative power is dissipated in the braking grid — the batteries cannot accept full wheel motor generation. The energy captured when resistance increases still remains the same. Air-cooling is capable of removing the additional $I^2R$ heat losses due to the increased resistance.

When the cell resistance is twice the original value, voltage limits are exceeded, so charge current must be reduced, resulting in decreased energy storage. Assuming an 80% reduction in energy recovered to indicate end-of-life and a linear resistance growth trend indicated by the first year of testing, battery life is estimated between two and three years for the specific test cycle. Testing will continue until failure is reached.

The high-power test was conceived to investigate the feasibility of applying high charge rates to increase the power density of the system. As noted in the next section, weight of the hybrid system has a significant and direct effect on the system benefits. The high-power test was aborted when the resistance rise trend began rapidly increasing. This "failure" was observed after only 90 days of testing. Research and development of alternative cell chemistries and geometries will be required to increase the power density of the cells.

A second concern of the OHV team was that of vibration. Heavy-duty diesel-powered vehicles are known for vibrations and resonance points. The impact of truck vibration on the life of the battery was unknown. The battery manufacturer provided a power spectral density (PSD) plot to define the United States Advanced Battery Consortium (USABC) vibration test to which the battery is qualified. That PSD was compared to several vibration measurements taken from existing equipment mounting points. The battery test was similar in shape and magnitude to the truck measurements, but further accelerated testing was desired.

A battery was identified for testing and an accelerated vibration test was performed. The battery brought up to temperature and vibration excitation was applied. Approximately 50 minutes into the test, a failure was observed. Internally, insulation had abraded and a cell had electrically shorted to the case creating an unintentional current path leading to failure of the battery.

The prime failure mechanism, movement of cells relative to the insulation, was identified and a means to isolate the vibration mode from the battery enclosures was designed into the battery enclosure frames and mounts. The batteries will also be installed into the frames using compliant material to further dampen the transmission of dangerous vibration to the battery.

Based on acceleration factors, the 50-minute test represents 180 hours at truck vibration levels. The target for vibration isolation is a 50% reduction that will extend life beyond 10,000 hours. Using vibration isolation measures, the team is confident the system validation system will survive the duration of testing easily.

## Full-scale Battery Testing

The full-scale system test is being performed at GE Transportation in Erie, PA. Facilities are available to emulate all vehicle systems in a controlled environment allowing instrumentation of the system

for analysis and troubleshooting. The entire battery system, with all control components and software, has been assembled for evaluation prior to the truck integration.

The full-scale battery test facility consists of twelve batteries connected with a controller area network (CAN) communication system. Each battery has a management controller on the CAN network and is capable of communicating status messages, such as temperature and state-of-charge (SOC), and receiving commands from the system controller.

The power electronics unit found on production trucks is used to provide wheel motor and braking grid power control, as well as perform some hybrid power management. The standard propulsion system controller has been adapted to interface with the hybrid controller to enable smooth response of diesel engine and battery power to the wheels based on driver commands.

The test facility is ready to start up, pending final environmental, health and safety reviews. Testing and results will be available by calendar year-end.

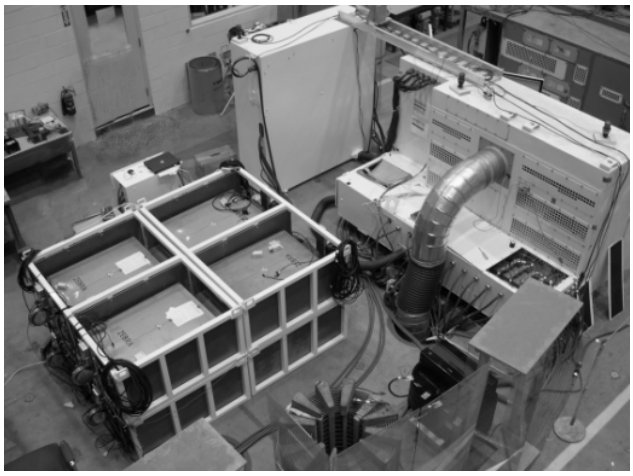

**Figure 3.** Full-scale test configuration

## Vehicle Integration

The final phase of the project is to validate system performance on an OHV in actual mine conditions. To realize this goal, integration of the hybrid equipment onto the truck is required.

The location of hybrid equipment on the vehicle and layout of hybrid components has been finalized and the primary interfaces between the hybrid equipment and truck are defined. Four primary hybrid equipment groups are to be mounted, as shown in Figure 4: two battery enclosures (boxes 2 and 3), one hybrid control group (box 1), and one inductor group (box 4).

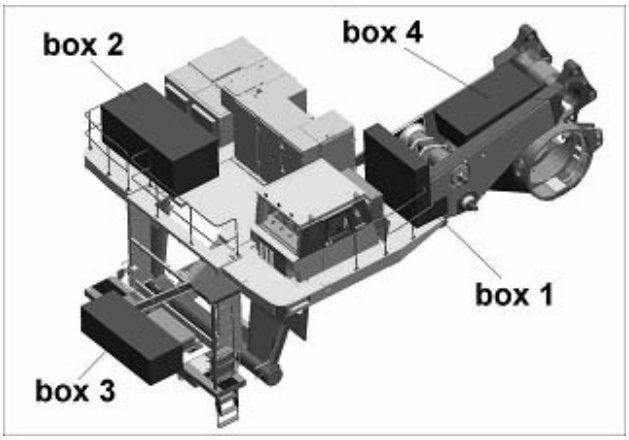


**Figure 4.** Hybrid equipment group

The batteries will be mounted in two separate enclosures. These enclosures will mount on the right-front upper deck and front bumper. The front bumper enclosure will include receptacles for off-truck battery charging and monitoring, when needed. Each enclosure will have appropriate vibration isolation to minimize the risk of mechanical battery failure. The battery enclosures also host appropriate support components, such as fuses, disconnect switches, and cooling fans.

The battery enclosures are designed to be compact, reducing weight overhead and affording visibility for the driver when possible. Visibility is certainly a concern for the enclosure on the upper right-front deck. Two visual aids, additional mirrors and a camera system, are planned to compensate for obstruction caused by the battery enclosure. The enclosures are air-cooled using filtered air and include means to quickly charge one or more batteries using off-board factory chargers to verify SOC and other diagnostic features.

The hybrid control group contains support and interface components for hybrid equipment. Power supplies (DC-DC converters), fuses, contactors, and

other auxiliary equipment will be located behind the operator's cab.

Smoothing reactors will be mounted between the frame rails in the rear of the vehicle. Two iron-core inductors have been procured and a simple cross-member type mounting structure will be welded or bolted to the frame to provide support for the inductors. A sheet metal cover will provide protection from water and excessive dirt.

In order to accommodate the extra weight of the hybrid equipment, the truck will be modified with support materials to stiffen mounting locations and provide a platform on the front bumper for one of the battery enclosures.

## On-vehicle System Test Plan

After integration, system debug, and initial testing, the vehicle will be demonstrated and performance metrics presented. Measured fuel savings and productivity benefits for the hybrid system will be presented and demonstrated with on-vehicle demonstrations at Komatsu's Proving Grounds near Tucson, AZ.

## Conclusions

FY 2005 efforts have focused on moving from paper and modeling design work to hardware design and fabrication. Final designs for all hybrid components are complete and some components have been fabricated. Integration of hybrid components with the vehicle has been defined and vehicle modifications design is underway. The full-scale test stand is assembled and ready to run.

Subscale laboratory testing by MES-DEA and battery vibration testing has provided added confidence that the selected battery systems will survive the on-vehicle system validation. This work also contributes to a better understanding of battery life and performance degradation.

GE and Komatsu will soon begin making modifications to the truck and detailing cable routes and other specifics preparing for the hybrid equipment installation. Hybrid equipment is expected to be installed during the first quarter of calendar year 2006 with demonstration in mid-2006.

# VIII. BRAKE SYSTEMS

## VIII.A. Advanced Brake Systems for Heavy-Duty Vehicles

*Project Manager: Glenn J. Grant*
*Pacific Northwest National Laboratory*
*P.O. Box 999, Richland, WA 99352*
*(509) 375-6890, e-mail: glenn.grant@pnl.gov*

*Technology Development Managers: Sid Diamond and Lee Slezak*
*(202) 586-2335, e-mail: Lee.Slezak@hq.doe.gov*

*Field Technical Manager: Jules Routbort*
*(630) 252-5065, fax: (630) 252-4798; e-mail: routbort@anl.gov*

*Participants: Yngve Naerheim*
*Tribomaterials LLC*
*(805) 496 837, e-mail: ynaerheim@verizon.net*

---

*Contractor: Pacific Northwest National Laboratory*
*Contract No.: DE-AC06-76RL01830*

---

### Objective

The objective of this project is to assess the potential of alternate disc brake designs and technology concepts to achieve the goals of increased energy efficiency, higher performance, and an increased level of safety and system control in heavy vehicle braking systems. System and material optimization will lead to increased energy efficiency, reduced environmental impact, and improved life-cycle costs.

### Approach

- Develop a new high-efficiency, low-inertia, and lightweight braking system for heavy vehicles and future heavy hybrids that will meet performance, durability, and economic metrics, as well as assisting in achieving 21st Century Truck Partnership (21CT) and FreedomCAR and Vehicle Technology (FCVT) energy efficiency program goals.
- Develop numerical computational tools to evaluate new brake designs and novel vehicle speed attenuation concepts, as well as wheel-well airflow that impacts braking cooling and vehicle performance. The intent is to develop these computational tools so that they can be incorporated into a module for the Powertrain System Analysis Toolkit (PSAT) model and enhance the vehicle performance simulations capability.
- Explore new friction materials and brake designs that will:
  - Facilitate energy efficiency (lightweight)
  - Increase safety, decreased stopping distance, and increase controllability (high and stable friction coefficient)
  - Increase operational efficiency (low life-cycle cost by high wear resistance)
- In conjunction with truck original equipment manufacturers (OEMs) and a Tier 1 brake supplier, use the computational tools to design and implement a full-scale lightweight brake system and initiate instrumented truck field trials to validate designs and generate wheel-well pressure field data. The application of a

lightweight disc brake system would impact vehicle fuel economy by reducing fuel consumption an estimated 0.8% for vocational Class 6–8 vehicles, and 0.5% for line-haul trucks.[1] If fully implemented across Class 6–8 vehicles, the energy savings are estimated to be $3 \times 10^{13}$ BTU/yr, or roughly equivalent to 5.3 million barrels of oil per year.[2]

## Accomplishments

- Computational fluid dynamics (CFD) and finite-element analysis (FEA) models have been developed that track braking energy transients and heat generation and convective cooling in a conventional heavy vehicle brake design. The model can input material properties and system geometries, allowing it to be used to predict the effects of materials and designs on the brake surface temperature and resulting heat transfer through the entire vehicle corner module.
- Five candidate new and innovative brake material friction pairs were evaluated for friction, wear, mechanical, and thermal performance at Pacific Northwest National Laboratory (PNNL), Tribo Materials LLC, and Rockwell Scientific. These materials include cermets, novel SiC-C-Cu composites, and friction stir-processed materials.

## Future Directions

- Initiate design study with brake system suppliers with the goal of developing a full-scale rotor/pad system that can be tested for performance and durability.
- Investigate multidisc brake rotor arrangements and other new design concepts and determine benefits and sensitivity of each to braking performance, energy efficiency, reduced mass, and barriers to implementation.
- Identify alternate energy absorption/conversion and heat management/rejection methods for potential system concept redesign.
- Evaluate system response to noise-vibration-harshness (NVH) for friction pair combinations.
- Select friction materials based on wear rate, thermal stability, friction characteristics, NVH, and cost.

---

## Introduction

The objective of this project is to assess the potential of alternate disc brake designs and technology concepts to increase the performance, energy-efficiency, and safety of heavy vehicle braking systems. For the last 50 years, heavy vehicle braking systems have remained largely unchanged; they rely on heavy, cast iron drum brakes actuated by air or hydraulic systems. These brakes have been refined over the years by changes in actuator geometry, and with the addition of automatic slack adjusters and ABS, but in terms of overall stopping efficiency and system design, cast iron/phenolic pad drum brakes have reached a technological plateau. In the last decade, a strong pull to increase the efficiency and performance of these systems has emerged both from the regulatory side (FMVSS 121 decreased stopping distance and control) and from the operational cost side, including the need for decreased life-cycle costs and increased energy efficiency. In addition to the pulls from the economic and regulatory side, the current braking systems are being subjected to increasing demands from:

- Higher speeds
- Higher gross vehicle weight (GVW)
- 30% decrease in the vehicle drag from parasitic loss (aerodynamics and other)[1]
- 19% reduction in engine braking force[3]

These trends will eventually push the current cast iron/phenolic pad systems beyond their capabilities to shed the energy required to stop efficiently and safely. The consequence of using current designs and materials in future heavy vehicles will be poor and unreliable performance, excessive wear, increased wear debris, and increased energy consumption on the manufacturing side for required replacement materials. This leads to increased environmental impact, higher maintenance costs, and ultimately, lower safety and productivity.

Optimizing and improving the current braking system will lead to a completely different paradigm (lightweight, high-temperature systems, electromechanical actuation, electrification of existing mechanical and compressed air-based systems, small-diameter multidisc, etc.).

Current braking systems are also heavy. A typical cast iron drum weighs 112 pounds (lbs) (50.8 kilograms [kg]). Weight reduction alone has a demonstrable effect on fuel consumption for a heavy vehicle, especially those with severe stop-and-go duty cycles, like urban delivery and transit buses (due to high rotational inertia in a heavy vehicle brake). It has been estimated that these high-duty-cycle heavy vehicles will see a 3.4% reduction in fuel consumption per 2,204 lb weight reduction.[1] The new materials proposed in this study, in a disc brake configuration, are estimated to be in the 25- to 30-lb range, representing a savings of up to 87 lbs per brake for the braking surface component alone (not including other scaled-down components such as lighter weight calipers and hubs). For a typical six-brake urban delivery or bus (Class 6–8) this is a potential weight savings of 522 lbs, leading to a projected fuel consumption reduction of about 0.8%. In 2002, these vehicles accounted for 10,305 million gallons of fuel.[1]

Although the fuel saving from weight reduction has less of an effect on long-haul Class 8 trucks (1.2% change in consumption per 2,200-lb weight reduction[1]), their total energy consumption is much higher than that of buses: 2.13 million barrels per day oil equivalent. Energy savings (reduction in fuel consumption) due to weight reduction in the braking system for a typical 10-brake Class 8 could be as high as 0.5%. In 2002, Class 8 long-haul tractor trailers consumed 26,451 million gallons of fuel. The 2002 U.S. energy consumption for commercial light trucks, transit buses, and Class 8 trucks (urban delivery and long-haul) was 5.21 Quads (quadrillion BTUs).[2] Energy savings due to brake system optimization could be as high as (0.0058)(5.21) = 0.0302 Quads or $3 \times 10^{13}$ BTUs (about 5.3 million barrels per year oil equivalent).

Next-generation, lightweight brake systems will have an opportunity to contribute to the goals of increased energy efficiency, performance, and safety. The challenge is integrating new systems and designs into the current truck platforms. A major concern of both truck manufacturers and customers is how new brake systems will interface with existing systems. Of particular concern is the balance between potential new tractor brakes and older legacy air-based systems on trailers. Concern also exists about upsetting the stability and balance that has been achieved over the last 10 years with automotive skid control (ASC) and antilock brake systems (ABS). Any new system envisioned by this program must take a systems optimization approach, and not one that simply seeks to replace cast iron with something new.

With the need to improve braking performance and durability beyond the 500,000 mile minimum expected life of the vehicle, new friction materials will be required. However, direct material substitution is not likely to be effective from current drum brake systems to advanced disc brake geometries. As such, disc brake design and system packaging is critical to achieving the project objectives.

## Approach

The project approach is to develop tools that can help identify new brake system designs and materials. A primary problem being investigated is thermal management. The trend in advanced braking systems is toward higher temperature operation. New brake materials being considered include cermets and high-temperature surface modified materials that deviate greatly in their thermal properties from conventional phenolic pad/cast iron braking systems. These materials may require fundamentally different ways to deal with heat rejection or conduction. For this reason, a primary focus of the project is on developing a generalized thermal/mechanical predictive models to describe heat flow and heat rejection in an advanced braking system. This focus uses linked computational fluid dynamics and solid mechanical modeling to predict how heat will be managed in a potentially higher temperature braking system. The models developed in the last two years are currently being calibrated by experimental testing of new material friction pairs, and will be validated by field trials and on-

vehicle testing in conjunction with project partners including truck OEMs and Tier 1 brake suppliers during the coming year.

The approach can be broken into three main task areas:

***Task 1 — Development of Thermal/Structural Models and Brake System Design***

This task focuses on developing and evaluating innovative disc brake designs, with the emphasis on enhanced thermal management. Modeling tools in development include computational fluid dynamic approaches (StarCD and RadTherm) and coupled stress analysis. These tools are used to assist in the design and evaluation of novel disc geometries and system components. The goal of the modeling is to develop a functional solid model and utilize predictive tools to simulate the performance (thermal and fluid profiles, as well as stress analysis) of the proposed disc brake systems.

Some of the brake system design concepts that will be explored include, but are not limited to, floating single or twin rotors, full phase pads/rotors, and mechanical/electric actuation.

***Task 2 — Friction Pair Development***

This task involves experimental testing and characterization of the five candidate friction materials outlined in FY 2004. Candidate materials are evaluated for wear and durability in conditions that simulate typical braking scenarios for on-highway and vocational heavy-duty vehicles. Testing includes thermomechanical tests on the bulk materials (coefficient of thermal expansion [CTE], Cp, emissivity, conductivity, as well as compressive strength and modulus), tests of the friction, wear, and durability characteristics (on instrumented subscale rotor/pad test equipment), and surface characterization (scanning electron microscopy [SEM], SEM-Auger, optical profilometry) of the tested pairs to establish the chemical and physical nature of the transfer layer, an important surface layer that determines friction coefficient, heat generation, wear performance, and noise, vibration, and harshness (NVH) characteristics.

Bulk thermomechanical testing and surface characterization is done at PNNL, and the subscale friction testing is done by Tribomaterials at Rockwell Scientific Company (RSC). This data helps to delineate the safe operating envelope of the materials and is needed by the brake designers to determine where and how the new materials can be employed for current and next-generation braking systems.

The outcome of this task will provide the thermal modelers and the brake designers with relevant data on new materials to enable them to explore new brake concepts, which until now have not been possible with currently available cast iron and phenolic-binder friction materials.

***Task 3 — Concept Feasibility of Alternate Braking Technologies***

The third task is generally focused on analyzing specific concepts that may be employable for brake systems to (1) enhance braking efficiency, (2) improve thermal management of friction surfaces, or (3) recover and store waste heat that can be utilized at a later time to drive an electrical loads.

Task objectives will be achieved through evaluation of emerging braking system concepts to scrub kinetic energy from a moving vehicle, such as the use of inductive/regenerative braking or mechanical (hydraulic) energy recovery. In addition, thermal management is critical in brake system durability and maintaining adequate friction performance. Waste heat is available throughout the braking cycle and is possibly recoverable through energy management devices or energy harvesting methods such as thermoelectrics or piezioelectic generators attached to brake system components. Methods which show promise will be presented to brake suppliers and OEMs, and investigated further as appropriate.

## Results

***Task 1 — Development of Thermal/Structural Models and Brake System Design***

A model was developed for a simplified disc brake rotor geometry that consists of a solid disc and brake pad. This model was created to predict the

fluid distribution (airflow) around the brake assembly, and the thermal profile and stress analysis. This will be used to establish design limits (bounding loads) in new disc brake designs. The thermally induced stresses are proportional to spatial and temporal gradients in temperature that develop during braking and cooling.

The analysis and CFD simulation predicts disc temperatures and heat flux during a maximum braking stop from highway speed. This analysis includes essential features of the vehicle wheel well airflow that determine convective cooling rates at the disc surface. Full-vehicle CFD simulations from manufacturers and other FreedomCAR projects will be used, as available, as guidance for the convective cooling portion of this model. Radiation heat transfer is also expected to significantly affect disc cooling. Conduction from the rotating disc to the caliper, hub, and wheel components is also accounted for in this simulation. If brake temperatures in next-generation braking systems are significantly higher than current systems, then it will be very important to be able to predict the temperature effects on adjacent components like aluminum wheels and hub bearings.

The simulation utilizes a two-step approach, in order to minimize time and computing requirements. StarCD was selected for the CFD part of this application. This software has been used by Volvo for a similar disc brake cooling application. Since the CFD analysis is a time-consuming transient simulation, selected results from StarCD are used to form inputs to an additional thermal analysis tool that can be used efficiently for preliminary/scoping sensitivity analyses. The tool selected for this purpose is RadTherm, as it is widely used for brake thermal analysis by industry.

RadTherm is typically used to predict component temperature distributions during repetitive braking test sequences. This package is capable of simulating simple radiation heat transfer from surfaces and also includes the capability to simulate conduction through solids. The efficiency with this tool is realized by not solving for cooling airflow, but by applying convective heat transfer as surface heat transfer coefficients. These heat transfer coefficients are obtained from the preceding StarCD CFD simulation. Sensitivity to parameters such as disc thickness, thermal radiation emissivities, or thermal contact resistances can be investigated with this software to better define the bounding conditions for the stress analysis.
Computer models provide a means of evaluating response of new brake materials, from both a thermal and structural standpoint. Thermal stresses induced during a panic stop and hold or those due to repeated start-stop transients are the limiting performance measures for these components. Both of these events can be effectively modeled to provide, at a minimum, a qualitative comparison between possible materials, and in many cases, accurate estimates of peak temperatures and stress states. Accurate knowledge of material properties is a key to the modeling process. In this report, initial comparisons of the temperature rise during a braking transient for two rotor materials will be presented: a “reaction-processed” cermet material and the baseline gray cast iron.

Calculations were performed with Adapco’s StarCCM+ code to compare thermal behavior of two heavy truck disc materials during braking. A simplified model is used for this comparison, consisting of a rotating solid disc and hub in air. The wheel, brake caliper, and pads are left out, as is the dust shield. The solid mesh is shown in Figure 1. Because the hub and disc model lacks the airflow blockage imposed by the wheel and the dust shield, predicted temperatures are not quantitatively accurate; however, they are useful for relative values and trends and in particular, when comparing between candidate rotor materials. Actual

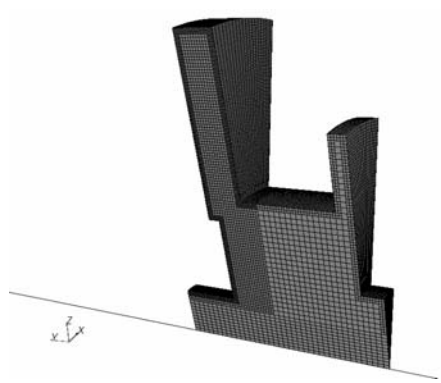

**Figure 1.** Solid mesh for modeled section of disc and hub

temperatures and rates of temperature increase would be slightly higher.

The two materials being compared are grey cast iron typical of current commercial truck brakes and an innovative cermet material. Thermal conductivity of the cermet is roughly 1/10 that of the cast iron, while density and heat capacity are half and twice that of cast iron, respectively. A 300 Kelvin (K) (27° Celsius [C]) ambient is assumed for the calculations.

Predicted temperatures are shown in Figures 2 and 3 for a steady-state calculation with a low heat-generation rate typical of continuous light braking to maintain speed (45 miles per hour [mph]) on gentle descent (1 degree grade). For the cast iron disc and hub, the maximum temperature on the friction faces are roughly 25°C lower than the peak for the cermet. The model also predicts that although the rotor face temperatures are higher for the cermet, the hub temperatures are lower for these materials, a logical effect of the lower conductivity of the cermet.

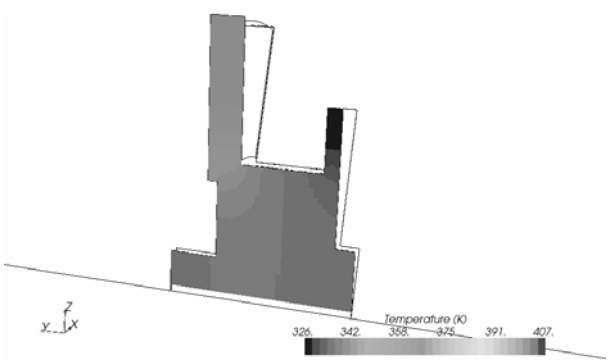


**Figure 2.** Steady-state temperature for cast iron during constant descent

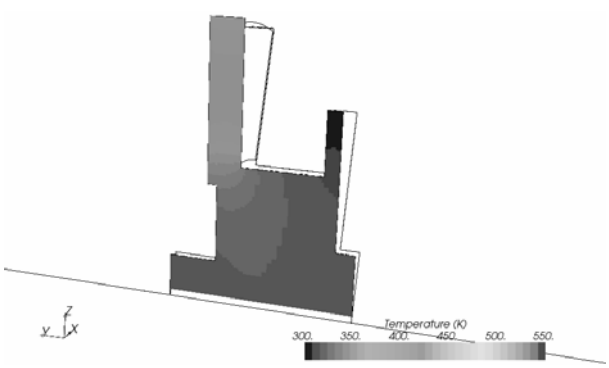


**Figure 3.** Steady-state temperature for low-k material during constant descent

The stopping transient simulation predicts temperature rise following an instantaneous increase in braking force. The constant rate descent steady state is used as the starting point with frictional heating increased by 100 times. This heating rate is typical of what would occur under a constant deceleration stop from 45 mph in 6 seconds. Temperatures are compared after the first three seconds of this transient in Figures 4 and 5. The peak temperature in the cast iron case is roughly 100°C, while the peak in the Excera material is 250°C over ambient. The temperature gradients across the Excera material are noticeably higher. Hub temperatures, however, are significantly lower in the cermet rotor simulation.

Although we again emphasize that these temperature magnitudes are dependent upon the simplifying assumptions, the difference in the peak temperature and temperature gradient is significant. In particular,

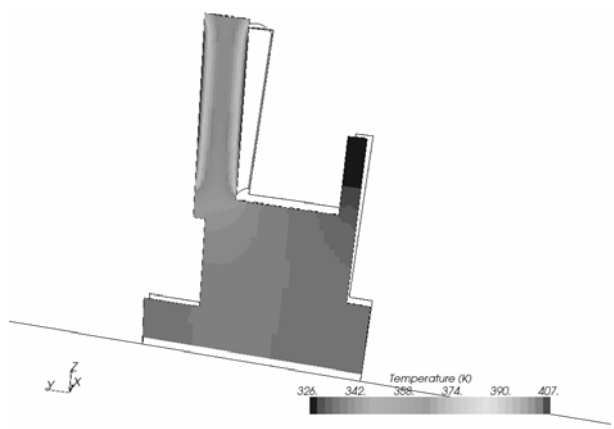


**Figure 4.** Temperatures at 3 s in stopping transient for cast iron

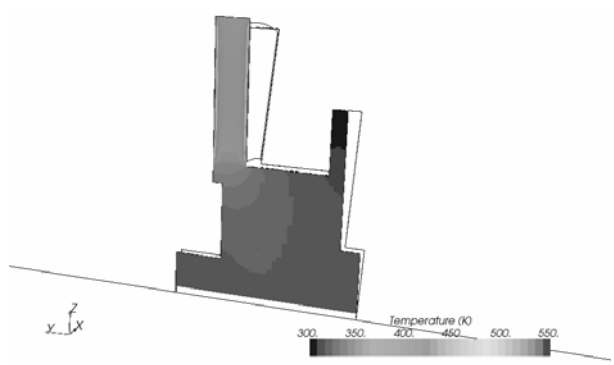


**Figure 5.** Temperatures at 3 s during stopping transient for low-k material

the temperature gradient will result in a high local stress state due to differential thermal expansion. However, this also leads to a situation where the rotor face is hotter but the temperatures in the hub and bearings will be lower than cast iron, a feature that could be important if the brake friction surface is to go to higher temperatures in future designs. Heat generation and flow could be very different in new brake designs — low-conductivity rotors may force changes in heat rejection that will be beneficial to some components and detrimental to others. Modeling and simulation tools like the one being developed in this program will be necessary to systems design and optimization.

A detailed FEA model, using the general finite element code ANSYS® 9.0, is currently being developed to explore the structural response of the brake rotor materials and designs to the potentially new thermal environments. The system geometry is shown in Figure 6 with an example finite-element mesh. A detailed view without the tire and caliper head is shown in Figure 7. The model currently features a standard diameter tire (43.4 inches [in.]), Alcoa® style wheel (24.5 in.), and a proportionately sized rotor (15.1 in.). However, the model was constructed such that geometric modifications can be rapidly implemented by simply altering relative dimensions and rebuilding. By using this approach, parametric sensitivity evaluations will be simple to perform.

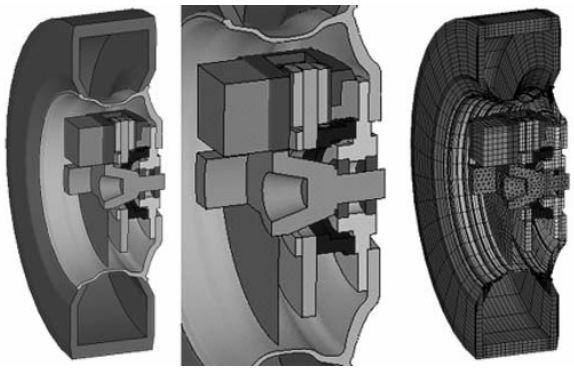

**Figure 6.** System geometry and sample mesh for detailed thermal-structural evaluation

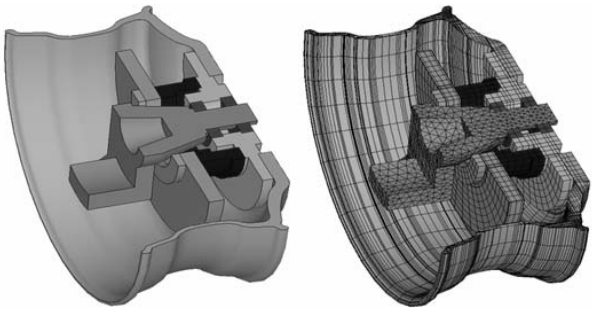

**Figure 7.** Model and mesh detail without tire and caliper head

When the model is complete, two possible approaches will be available for performing the coupled thermal-structural evaluations of a cyclic stopping transient and heat soak. Our favored approach is to perform all thermal evaluations within ANSYS using contact, conductive, convective, and radiative heat transfer elements as well as superposition and nodal coupling to determine the thermal transient data, perform a thermal-to-structural element conversion, and then compute the resulting stresses in the rotor material and any subcomponent of interest. An alternate approach is to utilize the temperature transient data and effective convective coefficients stemming from the StarCCM+ CFD analysis to compute the resulting stresses using the ANSYS FEA model. Both approaches could be used to compare thermal predictions, providing additional confidence in the time dependent temperature distribution results.

The time-dependent stress distribution determination will include the heat generation and expansion due to friction heat, rotor torsion-induced between the rotor attachment and the caliper friction loading combination, caliper clamping pressure, rotor attachment loading, rotational velocity ($\omega$), and rotational deceleration ($\alpha$), and will incorporate current properties of new brake materials being tested at PNNL.

### *Task 2 — Friction Pair Development*

An integral part of the development of new braking systems is the development of new friction pair materials. It is probable that future demands on the breaking system and the needs for increased operational and energy efficiency will drive the brake friction pair materials away from cast iron and phenolic pad systems. Friction pair development is a rich research area with data available from numerous sources including commercial material suppliers as well as government funded research.[4]

For this study, a survey of was conducted of friction pair materials, which included commercial and emerging materials options, as well as those still in the research and development phase by various vendors. Over twenty friction material options and vendors were surveyed. Based on the technology readiness level and cursory economic considerations, four were selected. These four friction materials were tested along with a baseline cast iron rotor material. Friction pairs were assembled from various combinations of these basic materials as the rotor and either these same materials as the pad or other pad materials. The baseline system was a well-optimized cast iron with an Arvin Meritor disc brake pad: R705. The four candidate new materials are outlined below, and described more fully in the FY04 DOE FreedomCAR and Vehicle Technology Program's Heavy Vehicle Systems Optimization Annual Report.[5] The friction materials include examples of C/SiC, reaction-processed cermets, and friction stir-processed surface-engineered materials.

1. Reaction processed cermet from Excera Materials Group — 50SiC/35$Al_2O_3$/W1461-XBr
2. C-SiC from Starfire Systems polymer-based ceramic reinforced with chopped polyacrylonitrile (PAN) carbon fibers.
3. C-SiC-copper composite from MER Corp. of pitch-based graphite cloth in SiC matrix, *in situ* attached to high-temperature copper core.
4. Surface engineered cast iron with TiB2 particles incorporated into the surface by friction stir-processing, designed by PNNL/South Dakota School of Mines and Technology (SDSMT).

All the brake materials selected are currently more expensive than the baseline cast iron, but all are fabricated by methods that could be translated to bulk processing and reduced part cost at high volume. Current estimates of market conditions suggest that 20% of the heavy vehicle market is very sensitive to weight reduction. It has been estimated that in this specialty market, the premium paid for weight reduction could be as high as 3$/lb.[6] In the mass truck market, this number may be closer to $1.50/lb, indicating any new material proposed will be subjected to very stringent demands on cost differential if weight reduction alone is the only consideration. However, another factor that may play heavily into the economics of looking at advanced material replacements of cast iron is the life-cycle cost and performance. Many materials provide combinations of high friction coefficient, particular heat transfer characteristics, or increased wear life that can favorably affect system life-cycle cost. A 50% increase in wear life, for instance, will double the interval between rotor change-outs and can affect the economics for those vehicles sensitive to downtime.

Experimental investigations into the performance of new brake materials included studies of the friction pair wear performance and durability, thermo-mechanical testing, and surface characterization. Friction pair testing was done at Tribomaterials LLC and Rockwell Scientific. Four-inch-diameter discs of each selected rotor material were fabricated and tested for wear performance in an instrumented test apparatus (Figure 8). The tests were run at constant torque for a fixed time, and rotor temperatures were maintained by a water-cooled backing plate. Pads of different manufacture and composition were tested against each rotor material, and loads required to maintain torque were measured. From this data, the friction coefficient can be calculated. Post-test weights were taken of the rotor and pads material to determine wear rate and wear performance. Two conditions were tested in this program. Condition 1 is designed to simulate light braking as might be needed in a gradual descent or in a light snub from freeway speeds. These tests were conducted at a 60-mph equivalent

**Figure 8.** Subscale wear/durability tester at Rockwell Scientific

rotational speed, 100-psi rotor/pad contact pressure, and a constant temperature of 200°C. The second condition was more aggressive and designed to simulate slow speed braking at high brake pressure as might be expected in a mountain descent. These conditions were 30-mph equivalent, 700-psi rotor pad contact pressure, and 600°C rotor temperature.

Figures 9 and 10 illustrate a subset of the tested materials and show the wide range of wear rates and friction coefficients that are possible with the selected friction pairs. Friction pair development and optimization is an iterative process. One pad material may show high wear rates against one rotor material, but might cause the rotor to wear when run against another rotor. Optimization of the friction pairs is not in the scope of this program, so data in Figures 9 and 10 is generated only to expose the basic frictional and thermal conduction characteristics of these new materials. Several new material pairs performed very well against the baseline cast iron/phenolic pad showing friction coefficients as high or higher (0.31–0.37 on subscale tester) than the optimized cast iron rotor running a current commercial Arvin Meritor pad (R705). Some rotor materials (like the C-SiC at low load condition 1 and the reaction processed cermet rotor at conditions 1 and 2) showed wear rates far below cast iron, suggesting that these materials may show very low life-cycle cost (potentially life of vehicle parts).

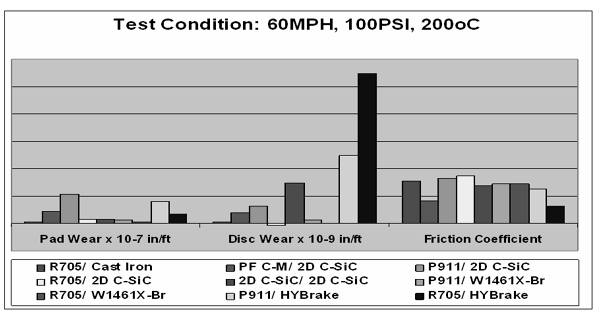


**Figure 9.** Friction pair performance at low load snubs

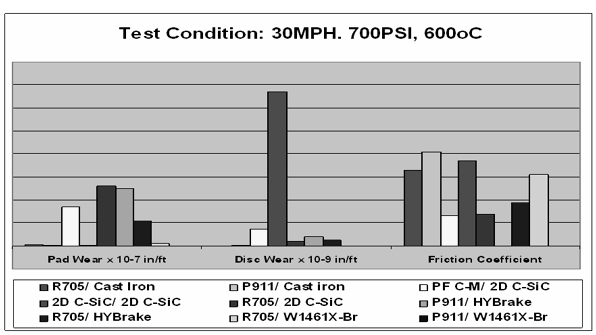


**Figure 10.** Friction pair performance at high load transient

Wear rate, friction coefficient, and to some extent, thermal properties of a friction pair are strongly dependent on the nature of the transfer layer, a very thin layer that develops between the rotor and the pad during braking. This layer is constantly sheared and redeposited during braking and is important to characterize in the process of optimizing the friction pair performance. Baseline studies of this transfer layer were done on several of the friction pairs used in this program in an effort to quantify wear rate better and to understand the mechanical and chemical/physical nature of the transfer layer. These studies used a combination of optical surface profilometry and SEM in conjunction with electron dispersive spectroscopy (EDS) to characterize the surface of the brake rotors and pads, and to determine whether material was transferring from one surface onto another in the wear track. Figure 11 shows several typical wear tracks observed in different rotor materials.

An optical surface profilometer was used as a tool to quantify the amount of wear on the brake rotor surfaces investigated in this study. Optical profilometery allows quantification of surface profile, roughness, wear features and extent. Figure 12(a) is a typical three-dimensional (3-D) plot created from the surface profilometry measurements illustrating the topography of a tested rotor surface.

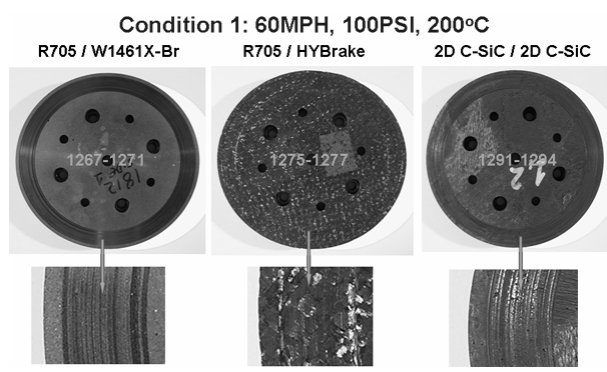


**Figure 11.** Typical wear tracks for cermets and C-SiC rotor materials

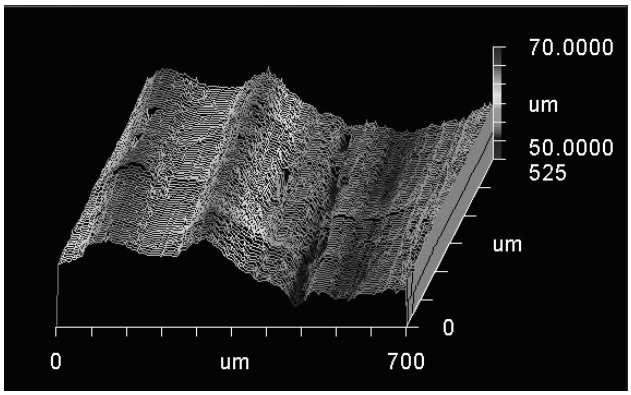


(a)

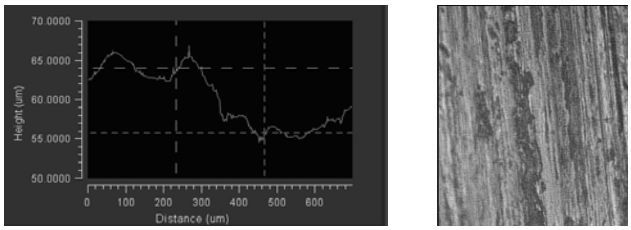


(b)

**Figure 12.** Typical 3-D plot from the surface profilometry measurements illustrating the topography of a tested W1461x-Br rotor surface.

Surface roughness ($R_a$ ) is an average roughness or deviation of all points from a plane fit to the average surface and can be a good indication of the development of a transfer layer. On some materials, such as the C-SiC rotors, $R_a$ was drastically reduced when transfer layers were developed. Table 1 shows that the surface of a C-SiC rotor had a $R_a$ of 3.88. The $R_a$ value on the part of the rotor in contact with the pads after testing showed a smoother surface in condition 1 (low load snubs) and a very smooth surface after a high-load, high-temperature test ($R_a$ around 1).

Scanning electron microscopy in conjunction with EDS was utilized to determine whether material was transferring from one surface onto another during performance testing of the brake rotors and pads. EDS was conducted on both the pads and rotors. Figure 13 is a backscatter image of a C-SiC rotor test surface where a transfer layer is developed. The EDS results show iron and other elements present on the surface that are not in the original chemistry of the C-SiC rotor. The chemical character of the transfer layer when correlated to the wear performance and friction coefficient can be used to optimize the friction pair later in the program.

**Table 1.** $R_a$ Values (μm) Determined for Two-Dimensional (2-D) C-SiC Rotors

| Rotor Type | Non-Tested Surface | Tested Surface | | | |
|---|---|---|---|---|---|
| | | R705 Pad | | PFC-M Pad | |
| | | *Cond. 1* | *Cond. 2* | *Cond. 1* | *Cond. 2* |
| 2D C-SiC | 3.88 | 3.91 | 0.87 | 3.47 | 1.16 |

In addition to wear-testing, a wide range of thermomechanical tests and characterization work was done on each new material. Mechanical properties (modulus, compressive strength, and ductility) were measured as well as thermal

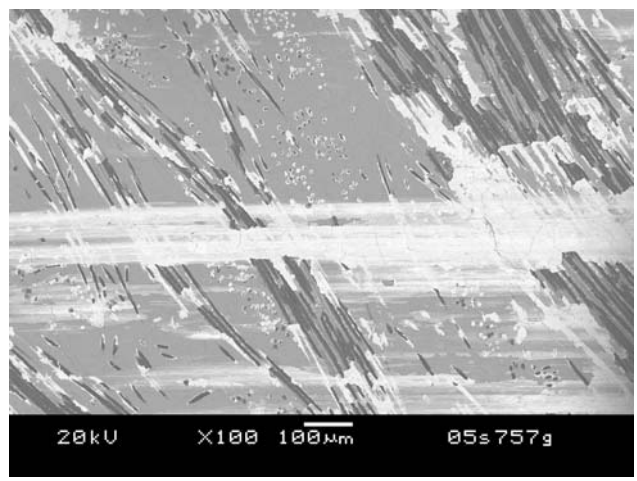


(a)

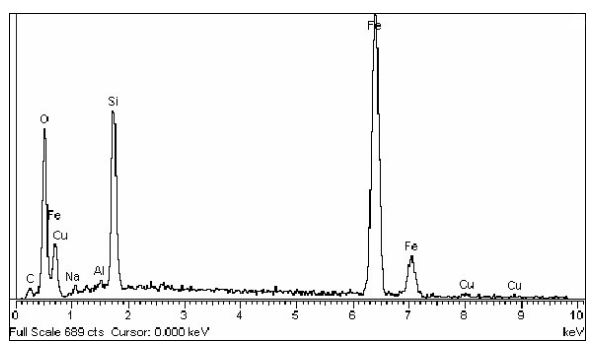


(b)

**Figure 13.** (a) Photo representative of a tested 2-D C-SiC rotor with transfer layers from a Performance Friction Carbon Metallic pad present. (b) The EDS results of the transfer layer shown in (a) indicating high amounts of iron present that have been transferred from the pad.

properties including CTE, conductivity/diffusivity, and emissivity. For most materials in this study, these properties were found to be highly anisotropic. Anisotropy in heat conduction, for instance, may be a feature that can be used in design to affect cooling or heat management. The data generated from thermomechanical characterization feeds directly into the input for the thermal/mechanical model being developed and is a necessary package of information needed to design an advanced braking system.

## Conclusions

System modeling tools developed during this program will help to define if some of these wear-resistant, high-temperature friction pairs can be applied to the specific demands of heavy vehicle brake systems.

The primary scope of work for FY 2006 will focus predominately on brake rotor geometry design, thermal management, and model simulation activates in support of system design considerations. Multidisc brake rotor geometries will be investigated for thermal and braking performance. Other new design concepts will be investigated to determine what benefits they may provide, as well as the sensitivity of each on braking performance. The modeling task will continue to investigate heat generation, fluid flow, and the resulting surface temperature of the brake system components. These properties will be determined, along with the evaluation of system response to NVH for the various friction pair combinations. In addition, alternate energy absorption/conversion and heat management/rejection methods will be investigated for their potential as primary or secondary methods to control vehicle speed.

A critical focus of FY 2006 will be on model calibration and validation. During FY 2006, full-scale testing will be initiated with the collaboration of a truck OEM/Tier 1 brake supplier. These efforts will be directed toward instrumented on-vehicle tests of heat generation and rejection in current braking systems to help refine the current models predictions on heat generation and wheel well airflow. As new friction pairs and brake designs are developed, full-scale testing (dyno and on-vehicle testing) will be required to verify new material durability, designs, and concepts.

Brake system and material optimization will lead to increased energy efficiency, reduced environmental impact, and improved life cycle costs. Lightweight, high-performance braking systems have an opportunity to contribute directly to the 21CT and Vehicle Systems Team goals of increased energy efficiency, decreased parasitic losses through mass reductions, improved knowledge of vehicle undercarriage and wheel-well aerodynamic flow, and improving truck safety through the development and optimization of technologies for better stability, control, and braking performance.

## Acknowledgments

The principal investigators would like to acknowledge the valuable contributions of James Fort and Harold Adkins of the Pacific Northwest National Laboratory for their work associated with the developing the brake model and simulations.

## Endnotes

1. US DOT FHA Highway Statistics, www.ops.fhwa.dot.gov/freight/freight_analysis
2. Annual Energy Outlook 2005, DOE/EIA-0383, 2005
3. NRC-CNRC Technical Report, TP 13892E, 2002
4. P.J. Blau, Advanced Materials for Friction Brakes, DOE OFCVT 2004 HSWR Annual Report, http://www.eere.energy.gov/vehiclesandfuels/pdfs/hswr_2004/fy04_hswr_6.pdf
5. http://www.eere.energy.gov/vehiclesandfuels/pdfs/program/2004_hv_optimization.pdf
6. NRC-CNRC Technical Report, TP 13892E, 2002

# IX. EFFICIENCY IMPROVEMENTS FOR HEAVY VEHICLES

## IX.A. Truck Essential Power Systems Efficiency Improvements for Medium-Duty Trucks

*Principal Investigator/Technical Manager: Larry M. Slone*
*Caterpillar Inc., Technical Services Division*
*(309) 578-0243, fax: (309) 578-4277, e-mail: Slone_Larry_M@Cat.com*

*Program Manager: William H. Lane*
*Caterpillar Inc., Technical Services Division*
*(309) 578-8643, fax: (309) 578-4277, e-mail: bill.lane@Cat.com*

*Assistant Contract Administrator: Pamela J. Breen*
*Caterpillar Inc., New Technology Division*
*(309) 578-9955, fax: (309) 578-2834, e-mail: Breen_Pamela_J@Cat.com*

*Technology Development Managers: Sid Diamond and Lee Slezak*
*(202) 586-2335, fax: (202) 586-2476, e-mail: Lee.Slezak@hq.doe.gov*

---

*Contractor: National Energy Technology Laboratory*
*Contract No.: DE-FC26-04NT42258*

---

### Objectives

The goals of the Truck Essential Power Systems Efficiency Improvements for Medium-Duty Trucks (TEPS) are:

1. Develop a medium-duty generator package and energy storage system for sales to a broad, medium-duty (Class 4–7) truck market.
2. Develop electrical alternatives to the use of the belts and gears in the medium truck engine compartment.
3. Develop a computer supervisory controller and algorithms to establish fuel savings by taking advantage of electrification.
4. Demonstrate reduced fuel consumption during idle conditions and evaluate the possibility of charging the energy system during vehicle braking.
5. Provide electricity for auxiliary equipment used in the field.

### Approach

During the previous year, the team has tackled the design work outlined in Task 101 (Specifications, Concepts, and Designs) of the original contract. The team continues to design to the truck specifications cited in earlier reports. The market input from the original equipment manufacturer (OEM) truck company and simulation results continue to indicate that the utility truck will provide a solid platform for demonstrating the TEPS technologies. The target truck comprises the following key elements:

- 300-horsepower Caterpillar C7 engine
- A medium-duty chassis equipped as follows:
  - 12,000-pound (lb) front axle
  - 23,000-lb rear axle

- Utility truck body
- Automatic transmission

## Accomplishments

- Selected quality function deployment completed with OEM truck company.
- Selected "Best" application (utility truck).
- Produced starter/generator controller board.
- Successfully downsized the starter/generator converter design.
- Completed design of the electrohydraulic power steering unit.
- Selected a control platform.
- Chose an energy storage technology.
- Finalized a powertrain configuration.

## Future Directions

- Obtain truck chassis and perform baseline testing.
- Procure and bench test new components.
- Perform vehicle integration and testing.

---

## Introduction

During this year, the TEPS project has focused on Task 101 as detailed in the contract proposal. Task 101 — Specifications, Concepts, and Design — comprises the bulk of the background research and design work as the name implies.

Early in the year, the team, including the members from Caterpillar as well as the partner companies, was assembled. Engineering Machined Products (EMP) is committed to delivering a more efficient cooling package capable of capitalizing on the electrified chassis. Dana will provide an electro-hydraulic power steering (EHPS) unit to further utilize the efficiency enhancements allowed by the electrified chassis. Switched Reluctance Drives (SRD), a division of Emerson Electric, is providing the integrated starter/generator (ISG) that will power the high-voltage bus. Additionally, support from an OEM truck company was enlisted to furnish chassis details and market information. During the first quarter of 2005, the Consortium Agreement among the partners and the National Energy Technology Laboratory (NETL) Cooperative Agreement were signed and returned.

With the team assembled, the group further embarked on design details. Caterpillar and the OEM truck company employed Six Sigma methodology to develop a quality function deployment (QFD). The QFD paved the road to determining the best application in the medium-duty market for demonstrating the TEPS technologies. Meanwhile, the team partners began work on a first concept. For the first concept, team members assumed the vehicle to be a beverage delivery truck. Team members used specifications for an "average" medium-duty beverage delivery truck to initiate their design work. The first concept idea provided team members with a design target and facilitated a smooth transition to the final, "Best" application when one emerged from the QFD work.

Selection of the "Best" concept in the second quarter of 2005 freed designers up to finalize their initial concepts. While a few components may have been tailored to the "Best" application, the team strives to develop products that can be readily applied to the broad medium-duty truck market.

## Design Efforts

*"Best" Application* — As previously mentioned, the team began designing for a target of a beverage delivery truck. This first concept never referred to a specific vehicle or any particular hardware. It merely served as a design target for all of the partners while Caterpillar and the OEM truck company were working through the QFD data to select the "Best" application.

The work with the OEM truck company led to the selection of the "Best" vehicle application, a utility truck. Members of the team recently traveled to an industry trade show to gather a variety of information about the utility market. Team members learned more about current and future offerings in the market and had opportunities to gather additional end-user feedback. Furthermore, the exhibition featured an array of suppliers to the market, some of who may be tasked with contributing specific components or services to the TEPS effort.

*Transmission* — While the choice of an automatic transmission was made early on, the team considered multiple configurations for packaging the ISG, transmission, and engine. Connecting these components in different manners yields different topologies, each with unique advantages. Caterpillar Six Sigma tools such as the Pugh matrix and others were invoked to compare the competing configurations against design goals and criteria. Selection of the transmission configuration is a key enabler for finishing the mechanical design of the ISG/engine/transmission interface.

*Control Platform* — The team performed an in-depth examination of available control hardware platforms. An analysis similar to that performed for the transmission configuration confirmed that there are multiple tools available that are comparable, while offering unique features. Subtle differences distinguished the competitors, and any of them could perform the tasks necessary to manage the functions of the vehicle. Nevertheless, one platform has been selected and vendor quotes have been received.

*ISG Controller Electronics* — The printed circuit board (PCB) design became a manufactured component recently. The blank PCB was produced and then populated by SRD. The finished product (Figure 1) employs a new microprocessor chip and digital signal processing technology, yielding a flexible controller that could quickly be adapted to a variety of applications in a production scenario.

The basic electrical testing of the populated PCB has been successfully carried out. SRD has also commenced on the writing of the software for the PCB.

*ISG Converter* — SRD completed the design of the power electronics. Additionally, all of the major components have been selected. As shown in Figure 2, packaging exercises for the power electronics components are underway.

With the components selected, ordering has also begun. Orders for long lead-time items have been placed, while some, more readily available materials have already been received. One key element of the design was to downsize the components from the unit previously produced for the Class 8 vehicle of an earlier DOE project with Caterpillar. The new

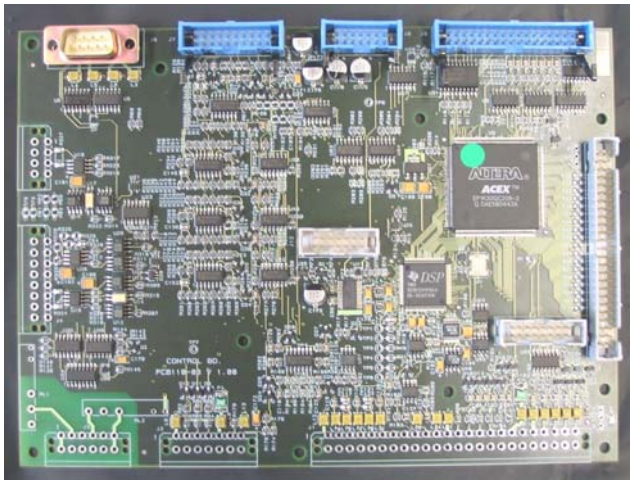


**Figure 1.** DSP-based ISG controller PCB

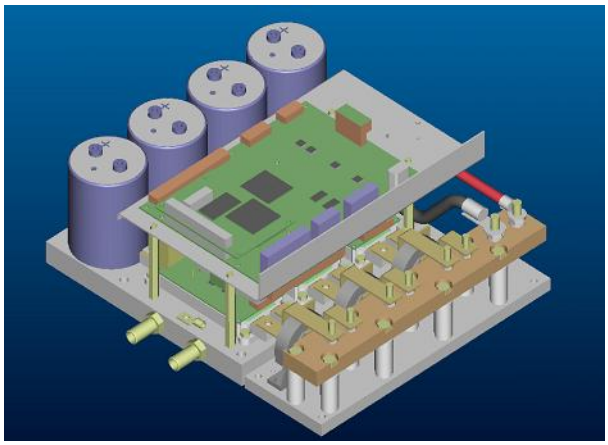

**Figure 2.** Preliminary solid model rendering of ISG converter

design represents a nearly 40% reduction in size when compared to the previous controller.

*Control Algorithms* — Simulation and analysis have continued throughout the year. Plant and control models are refined as more information becomes available. An apparent lack of a standard utility operating cycle led team members to develop one aimed at exercising all of the vehicle systems in a challenging fashion. Meanwhile, the operating modes for the ISG have been defined and the coding has begun. The results of these simulations are encouraging, suggesting that the 10% fuel savings originally targeted by the TEPS project are achievable.

*Electrical Architecture* — The team has made strides in the design of the electrical architecture. Wiring diagrams are nearly complete. Controller area network (CAN) has been adopted as the communication standard for the vehicle. The proposed CAN architecture has been presented to the team and approved.

*Electrified Power Steering* — The mechanical design work is complete. The model shown in Figure 3 reflects the final design. Recent advances in the equipment available in the medium-duty market have also been considered in the present design.

Components for the unit have been ordered and some have been received. Initial assembly has begun, with final assembly anticipated during the coming quarter. Meanwhile, the motor/drive design is also nearing completion.

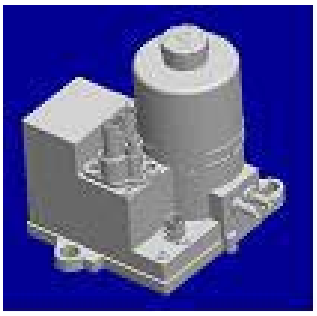

**Figure 3.** Solid model rendering of the power steering package

*Truck Frame* — Solid modeling work for the chassis continues. Project partners have supplied sufficient models and space claim requirements to initiate packaging concepts. The modeling work will continue as more details come in from the partners and final component selection occurs.

## Results

The team continues to design around the "Best" vehicle application. Several designs are complete or nearly complete. Procurement of parts has begun and some long-lead items have been ordered. In some cases, such as the ISG converter, assembly is complete and initial checks have even been performed.

Caterpillar team members have continued to employ Six Sigma tools such as the QFD and Pugh matrix to facilitate design decisions. During this period, these tools proved particularly useful for the selection of a transmission configuration and control hardware platform. In both instances, these tools helped drive decisions between similar and often equally capable components and arrangements.

Simulations aimed at converging on a battery technology have proven successful. The team has selected nickel metal hydride as the chemistry of choice and is actively soliciting quotations. These simulations have also provided insight into the fuel savings potential associated with different technologies and operating strategies.

Details of the electrical architecture are coming together. The first step of control algorithm development, defining operating modes for the ISG, is complete. The partners are designing components to reside on the CAN. Wiring diagrams are nearly complete and many of the component connections have been specified.

Caterpillar and SRD have agreed to the ISG specifications. SRD has initiated the mechanical design after having successfully downsized the converter electronics. Additionally, the selection of the transmission configuration provides Caterpillar's mechanical designers with the necessary information to complete the design of the ISG/engine/transmission interface.

During the month of October, team members participated in an all-day review. The review meeting was held in conjunction with a hybrid truck conference, providing an opportunity for team members to come together for TEPS while benchmarking other vehicles and components under development.

## Conclusions

All design work is proceeding well. Some of the component and subcomponent design is complete. Completed designs have paved the way for parts ordering. The weekly team meetings continue to provide a useful forum for information exchange among partners. The baseline Gantt chart was completed and progress against the project plan is examined and updated weekly. The plan has been distributed to all of the team members and a comprehensive review was recently completed.

The designs and concepts have been used to simulate the vehicle through a variety of scenarios. The results of these simulations continue to support the project's initial claim to deliver a fuel consumption reduction of 10%.

Per the 2002 Vehicle Inventory and Use Survey (VIUS), the current fleet of medium-duty vehicles in the United States stands at approximately three million. This report also cites 9–10.9 miles per gallon (mpg) as the most common fuel economy range for these vehicles. Likewise, 10,000 to 19,000 miles/year was the prevalent annual mileage noted as well. For illustrative purposes, if the three million vehicles are assumed to travel 15,000 miles annually at 10 mpg, they will consume 4.5 billion gallons of fuel. A 10% decrease in fuel consumption for this example translates to a $1 billion impact on annual fuel expenditures. Moreover, vocations with extended idle periods may likely see fuel economy improvements greater than 10%. In addition to the fuel economy gains, chassis enhancements such as available field power further add to the attractiveness of the TEPS architecture.

# IX.B. Advanced Electric Systems and Aerodynamics for Efficiency Improvements in Heavy-Duty Trucks

*Principle Investigator: Kris W. Johnson*
*Caterpillar Inc.*
*(309) 578-4890, fax (309) 578-4277, e-mail: johnson_kris_w@cat.com*

*Program Manager: William H. Lane*
*Caterpillar Inc.*
*(309) 578-8643, fax (309) 578-4277, e-mail: lane_william_h@cat.com*

*Project Manager: Ralph Nine*
*National Energy Technology Laboratory*
*(304) 285-2017, e-mail: Ralph.Nine@NETL.DOE.GOV*

*Technology Development Managers: Sid Diamond and Lee Slezak*
*U.S. Department of Energy*
*(202)586-2335, fax: (202) 586-2476, e-mail: Lee.Slezak@hq.doe.gov*

---

*Contractor: Caterpillar Inc*
*Contract No.: DE-FC26-04NT42189*

---

## Purpose

Through electrification of engine and vehicle accessory systems, this project aims to improve fuel efficiency of heavy-duty trucks via improvements in cooling system thermal performance, air system management, advanced power management, and aerodynamics. Prototype components will be developed and integrated for fuel economy, thermal, and functional performance testing on the Kenworth T-2000 More Electric Truck (MET) platform. Switched Reluctance Drives, Ltd., Division of Emerson Electric Co., and Engineered Machine Products (EMP) are participating partners. A Cooperative Research and Development Agreement (CRADA) with Argonne National Laboratory has been established for aerodynamic analysis.

## Objectives

- Analyze, design, build, and test a cooling system that provides a minimum of 10% greater heat rejection in the same frontal area, with no increase in parasitic fan load.
- Develop an intelligent vehicle air management system, whereby the vehicle air system compressor is decoupled from the engine and is incorporated into an air system supply module.
- Realize fuel savings with advanced power management and acceleration assist, utilizing the Integrated Starter Generator (ISG) and energy storage devices.
- Quantify the effect of aerodynamic drag due to the frontal shape mandated by the area required for the cooling system.

## Major Accomplishments

- Heavy-duty truck More Electric Initiative (MEI)/Driveline simulation model completed, along with analysis of drive cycles and advanced power management strategies.

- Electric thermostat valve and drive electronics design and fabrication completed and delivered to Caterpillar from EMP. Valve bench testing for operation and communications completed; electrical integration of valve to MET complete. Valve installation and initial testing in MET completed.
- Procurement of 2007 emissions-compliant C15 customer evaluation engine has been secured.
- Two prototype 20-kW electric cooling fan motors specified, designed, and fabricated. Fan motor dyno testing and characterization completed, motors onsite at Caterpillar, motor drive communication testing completed. Initial fan supervisory control algorithms completed.
- Integrated Motor Generator (IMG) sensorless algorithms and dyno testing completed, fully characterized for engine assist operation over 0 to 2,400 revolutions per minute (rpm) range. Initial IMG supervisory control algorithms completed.
- Nickel metal hydride energy storage specification sized for anticipated drive cycle and life cycling for hybrid operation of MET.
- Detailed work plan developed with Argonne National Laboratory for aerodynamic analysis.
- Specifications completed for electrically driven air compressor system.

---

## Introduction

This program effort is aimed at extending the concept of heavy-duty truck electrification. It focuses on areas that will primarily benefit fuel economy while driving over the road. The October 2002 emissions regulations have resulted in increased engine heat rejection, and the 2007 regulation will further this trend. Truck electrification offers technology solutions to mitigate or even neutralize the effects of this trend. Opportunities exist to reduce cooling system area and to benefit from aerodynamic drag affected by cooling system improvements. The Class 8 truck will benefit the greatest due to its higher average speed, the number of vehicles produced yearly, and the large number of miles per year accumulated by each vehicle. Better fuel economy can accompany emissions reduction, and will encourage customers to purchase the vehicles as an improved capital investment.

The research team has built upon the previous More Electric Truck (MET) project (see Figure 1), where the fundamental concept of electrically driven accessories replacing belt/gear-driven accessories was demonstrated on a Kenworth T2000 truck chassis. This technology is strategically important because it lowers fuel consumption, decreases gaseous emissions, reduces noise, and enables substantial reduction of main engine idling. The transition to broad commercial applications of these technologies in the trucking industry will lead to

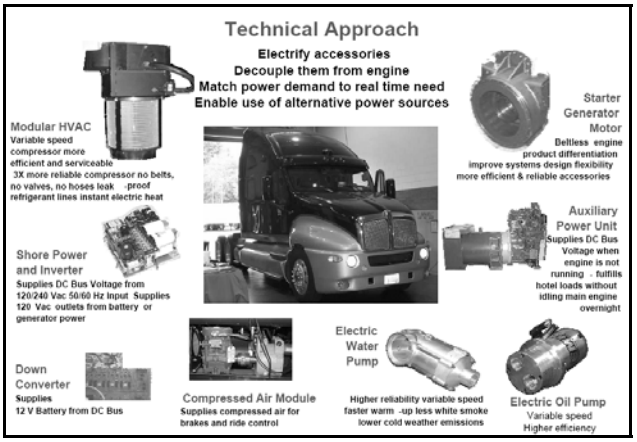


**Figure 1.** Key components of the More Electric Truck

significant gains in performance, reliability, serviceability, and system design flexibility. These technology enhancements are also directly beneficial to mobile construction equipment, a variety of commercial and marine engine markets, and powertrains used by a wide variety of U.S. military mobile equipment as well.

In alignment with the first project goal — cooling system design — the team has identified four subsystems to increase heat rejection and improve fuel economy: radiator fan electrification, charge air cooler, thermostat, and oil cooler.

Typical engine cooling fans on heavy-duty trucks range in size from about 28 to 32 inches in diameter and can consume up to 75 horsepower (hp) at full

engine speed. The fan is belt driven through an on-off clutch on the front of the engine. Average fan on-time as a percentage of truck operation is about 6%, with half of that time attributable to air conditioning demands. The cooling fan is typically sized to deliver adequate cooling air flow at peak torque engine speed of 1,200 rpm, resulting in excess air delivery at higher engine speeds, and cubic exponential increase in parasitic power draw from the engine. Electrification of the fan allows fan speed to be matched proportionately to cooling system load.

The high-performance cooling system module will incorporate a high-efficiency aftercooler, or charge air cooler, with material properties that will allow higher core temperatures. This drives more heat rejection due to the higher temperature differential between the core and ambient cooling air, as well as allowing for the elimination of a water-cooled charge air pre-cooler. Removal of the pre-cooler will reduce the pressure drop in the charge air-line, reducing parasitic pumping losses.

A remote engine oil cooler will allow current engine lube oil temperatures to be maintained under high engine load, while maximum engine coolant temperature may possibly be increased to drive more jacket water heat rejection from the radiator core.

An advanced, electronically controlled thermostat valve will be designed, developed, and demonstrated for more efficient cooling on the MET. Replacing the mechanical valves with electronically controlled valves is a paradigm shift. Mechanical thermostats have been used for almost 100 years. Current thermostats consist of a thermally actuated valve, which contains eutectic wax that changes phase when heated. The valve restricts coolant from flowing to the engine radiator and bypassing back to the engine until the coolant temperature has reached a predetermined temperature corresponding to the melting point of the wax. During cold ambient conditions, an electric valve can be used to raise the coolant temperature higher than with a conventional thermostat and still satisfy the engine needs at high thermal load situations. In this manner, the engine can run warmer than normal, which can help enhance combustion along the walls, improve heat flow return, and obtain higher combustion temperatures.

The increased heat rejection per unit of frontal area of the above cooling system designs may allow truck original equipment manufacturers (OEMs) the vehicle design option of reducing the frontal area of the engine hood. Computational fluid dynamics (CFD) analysis of parametric width and height deviations for hood frontal area from baseline geometry will result in drag coefficients that will be used to determine the fuel efficiency opportunity for a heavy-duty vehicle, made possible from proposed cooling system changes.

The potential for advanced power management of electrified accessories and hybrid operation with electric energy storage and integrated motor generator (IMG) is being explored in Class 7 and 8 short- and long-haul trucks. Vehicle acceleration and deceleration assist with IMG and regenerative storage of braking energy have potential to increase fuel economy significantly, depending on the drive cycle the vehicle undergoes. Power management during vehicle operation on hilly terrain, where energy is captured and stored during downhill runs and then utilized to power electric accessories on the uphill run, also has potential for fuel savings, again depending on the slope and length of the terrain.

An electrically driven air compressor was demonstrated for proof of concept purposes on the MET. Operation of a conventional gear-driven compressor in its unloaded condition results in a 0.8-kilowatt (kW) constant parasitic load on the engine. Electric-only operation of the air compressor results in power use only during compressor on-time, typically about 5% duty cycle. This project effort is furthering the design of this accessory by incorporating an integrated motor and compressor for smaller packaging and space claim, and increased reliability for this critical accessory from fewer moving parts.

Table 1 shows a breakdown of the fuel and heat rejection savings potential of this project's objectives. With 20 billion gallons per year of diesel fuel consumed by Class 7 and 8 trucks in the United States alone, a 3–10% increase in fuel economy

**Table 1.** Projected Fuel and Heat Rejection Savings

| Technical Approach | Annual Fuel Savings Range % | | Radiator Heat Rejection Improvement Range % | |
|---|---|---|---|---|
| | Low | High | Low | High |
| Aerodynamic Drag | 1 | 3.5 | | |
| Air Management System | 0.3 | 0.5 | 1.5 | 2.5 |
| Advanced Power Management | 1 | 4 | 1 | 5 |
| Cooling Cycle Management | 0.5 | 2 | | |
| Cooling System Fan Module | | | 5 | 7 |
| Cooling System Air to Oil Cooler | | | 5 | 15 |
| **Totals** | **3** | **10** | **13** | **30** |

would result in significant reduction in total fuel use, as well as a proportional reduction in gaseous engine emissions.

## Results

### Electric Cooling Fan

For the electric cooling fan, space constraint for installation in the current T-2000 platform was a determining factor in decision to use a puller-type fan, as hood profile and mounting considerations of truck frame rail ends would make for difficult redesign of major structural components. Fan motor power was specified to 20 kW continuous at 2,000 rpm. This matches 20 kW mechanical fan power at 1,800-rpm engine speed with 30 mph ram air and the conventional belt-driven fan of the MET. With a higher efficiency fan and shroud, the same fan power will give more airflow and higher heat rejection. Due to thermal issues, preliminary fan design dimensions from engine installation space claim constraints limited fan motor peak power to 20 kW.

The motor design uses switched reluctance technology, with 18/12-stator/rotor pole structure, and peak continuous power rating of 20 kW at 2,000 rpm. Motor operation allows for reversal of the fan. Motor physical size is approximately 12 inches in diameter by 8 inches axial length. A machined, keyed hub attaches to motor shaft and fan blades. Current commutation is provided by position sensors mounted to motor front, interfacing with tabs on fan hub. Primary motor stator winding cooling is with engine coolant, secondary rotor/stator cooling is provided by aft-to-fore air-cooling stream through open rotor design. Radial vanes on fan hub provide negative pressure zone at motor front. System controller/fan motor drive communications is J1939 spec CAN over proprietary data link.

Design, fabrication, characterization, and dyno testing of two 20-kW switched reluctance motors for the cooling fan at SRD was completed. The motors (Figure 2) and drive electronics have been delivered to Caterpillar, where low-voltage signal and communication tests were conducted.

Supervisory control algorithms for cooling fan motor speed control, in various operational modes, were developed. High-fidelity cooling system component models were developed, allowing for testing and tuning of fan control algorithms with interaction of other system components.

The space claim from the radiator-mounted fan motor required a redesign for the current crankshaft mounted engine damper and pulley. Since the pulley is not required to drive the fan, it will be removed, and a shorter damper spacer was designed to facilitate mounting the damper closer to the engine block, to reduce its length by 2.75 inches. This also required a redesign of the front engine to frame-mount to accommodate the diameter of the damper in its new aft location. The damper spacer fabrication was completed.

**Figure 2.** 20-kW switched reluctance fan motor

### Electric Thermostat Valve

The Electric Thermostat Valve (eStat) was delivered from EMP to Caterpillar for integration with the MET C-15. The valve consists of a linearly actuated flow diverter contained in a cylindrical nylon and aluminum housing, driven by a stepper motor. A small drive electronics box with controller area

network (CAN) communication and drivers for the valve motor/actuator, runs from 12 V power.

The 2.4-inch valve with 1-inch bypass will deliver 100 gallons per minute (gpm) with 1 pound per square inch (psi) pressure drop, 300 gpm with 5 psi pressure drop, and goes from closed to full open in 16 seconds. The valve drive electronics operates from 12 V. System controller to valve electronics communication is over CAN at SAE J1939 specs, with proprietary network IDs.

An adapter to deliver flow to the valve from the engine head and provide mounting for the valve was designed and fabricated, and the assembly installed in the MET. Initial control testing was performed during engine warm-up and low-power operation. Figure 3 shows the completed installation in MET with C-15.

**Figure 3.** Electric thermostat valve installation

## Electric Air Compressor

Functional specifications for the electric air compressor and system were determined. The function of the air compressor is to provide compressed air for vehicle brake systems and other vehicle accessories. Air pressure required for these applications vary but normally range from 120 to 150 psi. Future air pressure requirements may be even higher. The air compressor will provide free air delivery of 11 scfm (0-psi inlet, 120-psi outlet). Compressor inlet air capabilities will be compatible with charge air pressure and temperature extremes. A method of removing oil passing to the air system to less than 1.0 cubic centimeters per hour (cc/hr) will be required.

## Advanced Power Management

A Dynasty/Simulink model of the MEI truck was used in a comparative evaluation of a power-management control. In this scheme, the ISG, energy storage system, and engine operate as a mild parallel hybrid vehicle. The simulation showed to 4% fuel economy improvement at constant speed over hilly terrain.

Modeling and simulation with the objective of using the ISG for launch assist of the truck was undertaken. The truck's motion in terms of velocity, acceleration, and jerk at start-up in second, fourth, and sixth gears was evaluated. It was determined that with the engine at warm temperature (coolant above 70° Celsius [C]), the ISG does have the torque capability to launch the truck, even fully loaded, on level ground, with clutch engaged, while concurrently bringing the engine up to starting speed. Piston compression events may cause rapid acceleration changes, or jerk, which may be unacceptable to the operator. Further enhancement of torque control algorithms to ISG may result in attenuation of jerk. On-vehicle testing of launch assist will help provide further data and validation of modeling results. A major objective of developing launch assist is to further increase the overall value of an ISG to the end customer, in terms of increased functionality, while at the same time having the increased efficiency and high power characteristics of the ISG contribute to overall fuel savings opportunity.

Power management control algorithms for engine assist mode were developed and tested on the MET. Figure 4 shows a plot of an engine off stop/start operation with the ISG. Idle stop and launch assist for heavy-duty applications have potential to provide increased and smooth vehicle acceleration, and to reduce clutch wear. Collateral benefits such as these may increase the customer value of an ISG, stepping up acceptance of the technology, while also providing critical fuel savings.

Sensorless control algorithms for the ISG were developed by SRD for motoring operation over

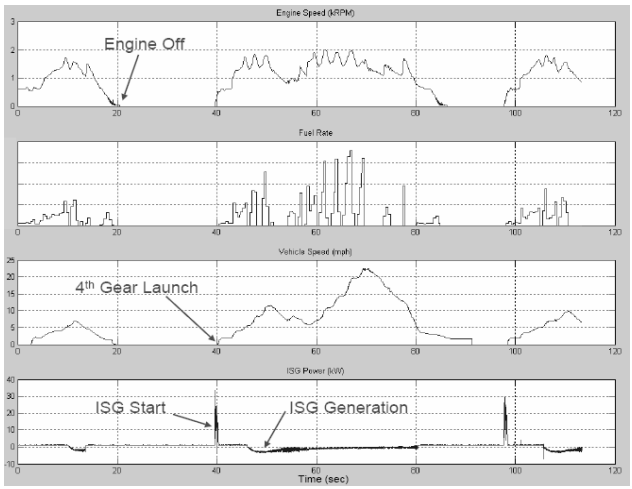


**Figure 4.** ISG plots showing engine stop/start assist

0–2,400 rpm. Peak torque of 1,200 Newton meters (Nm) was achieved from 0–160 rpm, and constant power of 25–26 kW was achieved from 500 to 2,400 rpm, with 84–90% efficiency. The ISG motoring functionality was developed to facilitate engine stop/start assist, acceleration assist, and highway cruise assist modes of MET operation.

An electrical energy storage system using nickel metal hydride (NiMH) chemistry was specified for typical heavy-duty over-the-road-drive cycles. Key factors of life cycle vs. depth of discharge, peak power delivery and absorption, and charge/discharge efficiency were used for system sizing.

## Engine Upgrade

Plans for procurement of a 2007 emissions-compliant C15 engine were made. This engine is part of a limited production run of customer evaluation engines made available to OEMs and internal Caterpillar divisions. The engine is ACERT C15 rated at 550 hp, 1,850 foot-pounds (ft-lb) torque, and includes a diesel particulate filter (DPF), with active regeneration device (ARD). It uses clean gas induction (CGI) for recirculation of clean exhaust gas from the downstream end of the DPF. This engine upgrade was made so the advanced cooling concepts being developed as part of this project are demonstrated with the latest Caterpillar engine technology and are subjected to the significantly higher heat loads induced by the CGI cooler.

## Future Work

Project plans call for control algorithm refinement and tuning of electric thermostat valve, during on road testing. The upgrade to the 2007 emissions-compliant engine will occur in early 2006, followed by baseline thermal and fuel economy performance testing. Integration of the existing electric accessory components from the MET will occur, followed by integration of the electric cooling fan, high-efficiency aftercooler, oil cooler, and air compressor. Subsequent thermal and fuel economy testing during 2007 will document the individual and combined performance improvements made possible by the project objectives.

Assessment of reliability and fail-safe fault protection of the air compressor and air system will be a high priority during the development effort. A Failure Mode and Effect Analysis, during and after the design phase, and performed with subject matter experts, will be one tool to formally assess these needs.

## Conclusions

After year one of this three-year program, the design specifications, and detailed design of most components are complete; a few components have even been fabricated, and integrated onto the test chassis of the MET. Plans are well underway to ensure compatibility and capability with an upgraded 2007 emissions-compliant engine, and subsequently integrate the Advanced Electric Systems put forth in the objectives of this project. These important objectives remain critical to developing technology to enable substantial fuel savings, heat rejection reduction, and increased functionality to the end customer. The technology and concepts being developed as part of this project are on track and continue to address key issues faced by the commercial trucking industry.

# X. ULTRALIGHT TRANSIT BUS SYSTEM

## X.A. The Vehicle System Optimization of a Lightweight Stainless Steel Bus

*Principal Investigator: J. Bruce Emmons*
*Autokinetics Inc.*
*1711 West Hamlin Road*
*Rochester Hills, MI 48309-3368*
*(248) 852-4450, fax: (248) 852-718 , e-mail: jbemmons@autokinetics.com*

*Technology Development Managers: Sid Diamond and Lee Slezak*
*(202) 586-2335, fax: (202) 586-2476, e-mail: Lee.Slezak@hq.doe.gov*

*Field Technical Manager: Jules Routbort*
*(630) 252-5065, fax: (630) 252-4798, e-mail: routbort@anl.gov*

---

*Contractor: Argonne National Laboratory*
*Contract No.: 4F-02161*

---

### Objectives

- The intent of this project is to perform the integration and optimization of a hybrid or battery/electric propulsion system, and various vehicle subsystems into a lightweight bus body.
- Autokinetics will use as much off-the-shelf technology as possible. The propulsion and vehicle systems will be optimized through careful selection of appropriately sized components.
- This project will result in a single "proof-of-concept" prototype bus, suitable for testing and evaluation of performance under controlled conditions.
- A further objective of the project is to identify one or more paths to rapid commercialization of the technology.

### Approach

- Conduct Advanced VehIcle SimulaTOR (ADVISOR) and Greenhouse gases, Regulated Emissions, and Energy Use in Transportation (GREET) computer simulations of a number of different types of propulsion systems to predict performance and energy efficiency.
- After identifying the most promising propulsion system architecture, use computer simulations to evaluate and select the individual components with the best combination of performance and affordability.
- Design, integrate, and install the propulsion system.
- Design or select optimized vehicle subsystems, such as seats, glass, air conditioning, etc.
- Purchase or fabricate and install all vehicle subsystems.
- Evaluate the performance and make modifications, if necessary.
- Perform initial testing.

## Accomplishments

- Completed the following design tasks:
  - Energy storage system design
  - Vehicle controller design
  - Low voltage system design
  - Diesel range extender design
  - Cooling system design
  - Hydraulic systems design
  - Driver's station design
- Completed the following selection tasks:
  - Select traction motor controller and regenerative braking
  - Select energy storage system
  - Select generator selection
  - Select vehicle controller
- Purchased the vehicle controller.
- Began integration of propulsion system components.
- Constructed mockup of driver's station.

## Future Directions

- Complete the integration of the propulsion system components.
- Install the propulsion system.
- Design, fabricate, and install vehicle subsystems.
- Install and test the propulsion system.
- Perform failure modes and effects analysis.
- Install the driver's station and controls.
- Perform limited testing and development of the complete vehicle.
- Continue efforts aimed at rapid commercialization.

---

## Introduction

The intent of this project is to perform the integration and optimization of a hybrid or battery/electric propulsion system and various vehicle subsystems into a lightweight bus body. Off-the-shelf technology will be used wherever possible. Optimization of the propulsion and vehicle systems will primarily be through careful selection of appropriately sized components.

This project will result in a single "proof-of-concept" prototype bus, suitable for testing and evaluation of performance under controlled conditions. The design will not necessarily be ready for mass production, nor will it include trim and appearance items.

The completed prototype will include the primary body structure, suspension, glazing, driver's station, electric wheel motors, inverters, and energy storage system. It will also include regenerative braking, limited lighting, bumpers, and full seating.

## Propulsion System Design

The Propulsion System simulations performed in FY04 using ADVISOR and GREET, and updated during FY05, concluded that a battery-electric version would have comparable "well-to-wheels"

energy efficiency compared to hybrid versions (see Figure 1). Since the battery electric vehicle (BEV) configuration is relatively simple and straightforward to implement using available component technology, it has been selected as the best choice of propulsion system for the prototype.

In this configuration, the energy storage system is one of the more critical components of the propulsion system. Since an objective of the Autokinetics bus is a lightweight design, the energy storage system should have the highest energy density that is practical in light of other requirements. Because of the large capacity of the battery pack, power density is not an important criterion for selection. One of the design tasks accomplished this year was the investigation of various energy storage technologies, such as chemical battery, ultracapacitor, flywheel, and hydraulic hybrid accumulator. The design team concluded that the most practical high-capacity energy storage technology currently available is the chemical battery. The selection process for the chemical battery energy storage system is discussed later in this report.

The Autokinetics bus has several subsystems: traction motor controllers, energy storage system, driver's station controls, and accessories. These subsystems must be interconnected and controlled by a top tier vehicle controller. The primary tasks required for the BEV Autokinetics bus vehicle control unit are regenerative braking control, driver instrumentation control, driver input control (brake and accelerator), accessory control, propulsion system supervision. The control system for the bus was designed during this reporting period. A block diagram of the Autokinetics bus control system is shown in Figure 2.

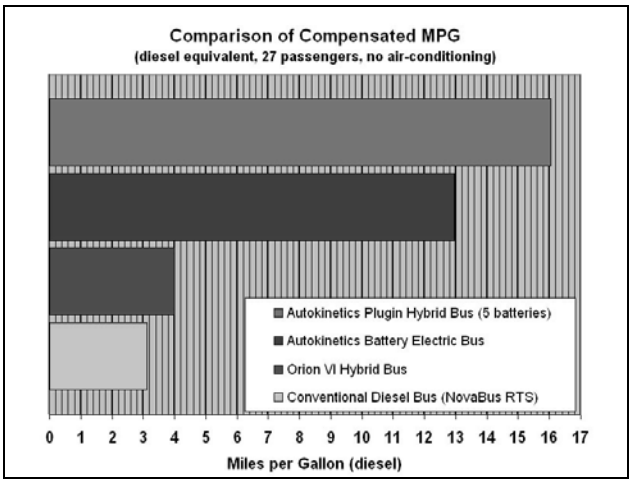


**Figure 1.** Comparison of predicted fuel economy

A minimum of two SAE J1939 controller area network (CAN) bus networks will be used for communications between the subsystems and the vehicle controller. Multiplexers convert discreet analog and digital input/output to the J1939 CAN bus and will be used at various locations on the Autokinetics bus. These will expand the I/O capacity and extend the range of the vehicle controller.

The energy storage system is a high-voltage system. However, the controllers and many of the accessories will require low voltage for power. A 24-volt (V) direct current (DC) low-voltage system has been designed consisting of a special high-power DC-to-DC converter that will provide 24 VDC power and will charge 24 VDC sealed lead acid batteries. The sealed lead acid batteries will provide power to critical controls and accessories when the high-voltage energy storage system is offline. Other standard DC-to-DC converters will power noncritical accessories.

The only drawback to the use of a BEV configuration is the limited range achievable with currently available battery technology. While the BEV configuration continues to hold great promise for energy efficiency and independence from

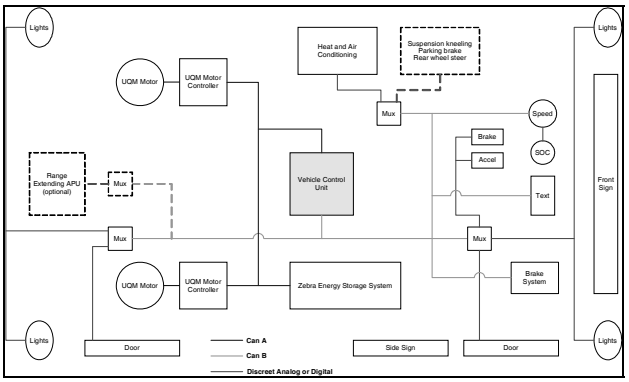


**Figure 2.** Block diagram of the Autokinetics bus control system

foreign oil, it is necessary to provide a practical near-term solution to the range issue. Autokinetics completed the conceptual design of a small auxiliary power unit (APU) to be used as an optional range extender in a plug-in hybrid configuration. Steps accomplished were performance simulation to quantify component outputs, packaging studies to identify size constraints, selection of commercially available components, and design of the APU system configuration. A computer-aided design (CAD) model of the APU is shown in Figure 3. This subsystem consists of a Hatz 1.4-liter diesel engine rated at 25 kW, mated to a generator.

A report was generated to select the generator for the APU in the optional plug-in hyrid electric vehicle (PHEV) configuration. Autokinetics has selected the UQM SR218N Brushless Permanent Magnet Motor/Generator with CD40-400L Inverter/Controller for the generator. This is the same unit that we are using for the two traction motors. It has ample torque at the intended operating speeds of the Hatz diesel (2,000 revolutions per minute (rpm), 2,500 rpm, and 3,600 rpm max continuous) and is reasonably small and light. It is also useful at this stage to have commonality with the traction motors and controllers.

Although the hardware implementation of this unit is not included in the budget for this project, Autokinetics will collaborate with Michigan State University's new Energy and Automotive Research Laboratories to develop and test the APU.

In the normal operation of a BEV propulsion system, unwanted heat is generated by the very substantial electric currents which flow through the internal resistances of the various components. This heat must be dissipated to avoid damage to certain components due to excessive internal temperatures. For the Autokinetics BEV, the components that require discreet cooling systems are the batteries, traction motors, and motor controllers. The design of the cooling systems for the Autokinetics BEV bus has been completed. The completed cooling system, ready for installation, is shown in Figure 4.

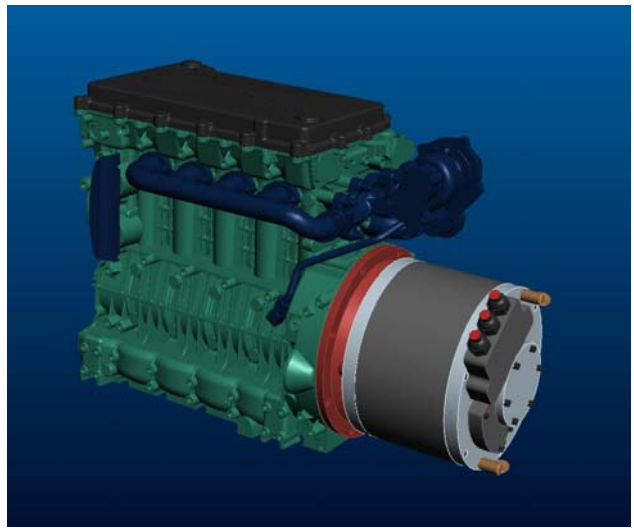

**Figure 3.** Diesel APU subsystem

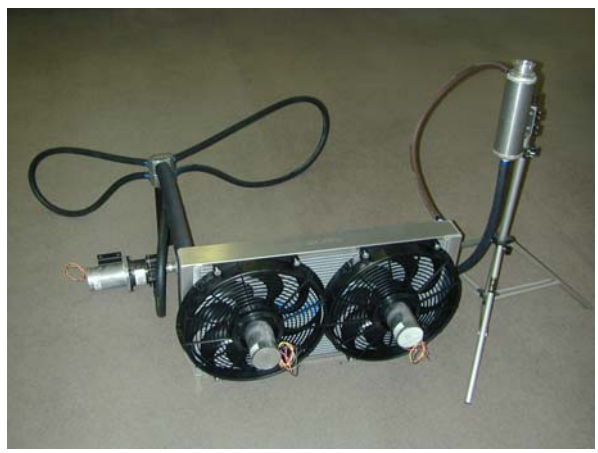

**Figure 4.** Motor and controller cooling system

To minimize parasitic losses, we have decided to eliminate the pneumatic system typically used on most heavy-duty buses to provide power to the brakes, suspension air springs, door openers, etc. Instead, electrically powered hydraulic subsystems will be used, allowing for on-demand operation. Three independent hydraulic subsystems have been configured and designed for use in the Autokinetics bus: suspension hydraulics, steering hydraulics, and brake hydraulics. Important vehicle dynamics parameters such as ride frequency, damping ratio, brake proportioning, etc., can be readily adjusted without making hardware changes. A schematic of the hydraulic brake circuit is shown in Figure 5.

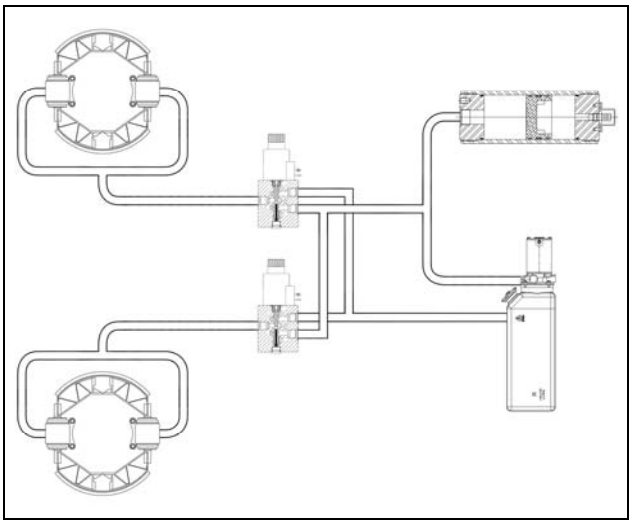

**Figure 5.** Hydraulic brake circuit (one of two)

The design of the driver's station was completed. This study involved the evaluation and selection of the seat, steering column, pedals, and instrument panel. A CAD model was built following well established Society of Automotive Engineers (SAE) procedures for visibility and human factors. A partially shaded image of the CAD model of the driver's station is shown in Figure 6.

The driver's seat and other components were acquired and assembled into a full scale mockup to confirm the seating position and visibility. A photo of this mockup is shown in Figure 7.

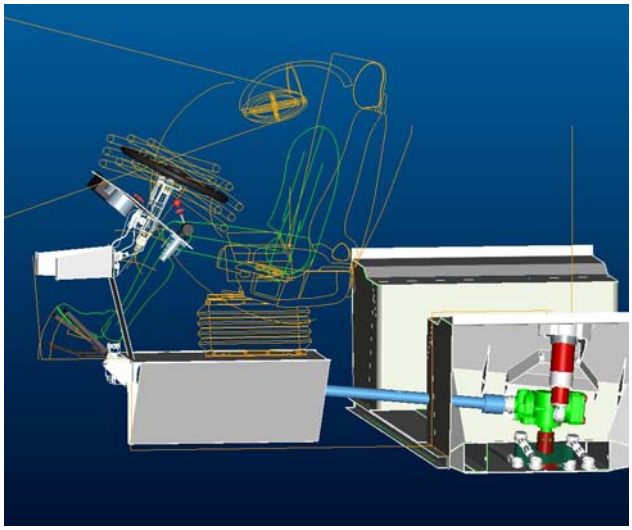

**Figure 6.** CAD model of the driver's station

**Figure 7.** Mockup of the driver's station

## Propulsion System Component Selection

Two UQM SR218N Brushless PM Motor/Generators and two UQM CD40-400L Inverter/Controllers were acquired as part of Autokinetics' High Strength Weight Reduction Materials project. UQM designates this motor/controller combination as "PowerPhase 75 Traction System." A report was generated that investigated the PowerPhase 75 Traction System for its suitability for this Heavy Vehicle Systems Optimization project. Other possible traction motors were also investigated and compared to the PowerPhase 75 Traction System (see Figure 8). The UQM Traction System was recommended because there is a clear upgrade path to a higher power system that would use the same packaging footprint.

An energy storage system selection report reviewed the following chemical battery technologies: advanced lead acid, nickel cadmium, nickel metal hydride, lithium-ion, lithium polymer, and sodium nickel chloride. Some of the key criteria compared in the report included specific power, specific energy, energy density, and cycle life. The Zebra Z37C sodium nickel chloride batteries and system (see Figures 9 and Figure 10) were selected for the Autokinetics BEV bus. The Z37C system is air-cooled and has a built in battery management interface, and MES-DEA can provide a multibattery server and chargers to make a complete energy storage system.

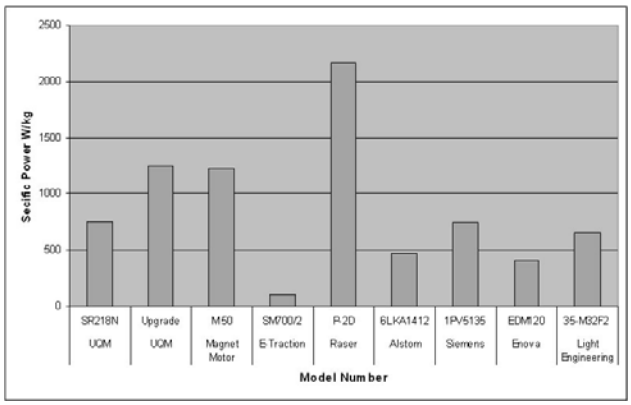


**Figure 8.** Comparison of specific power of several motors

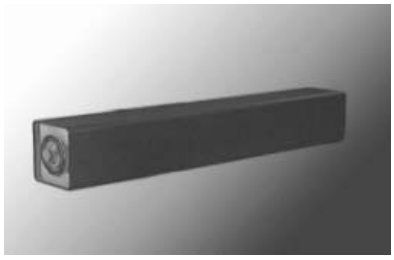

**Figure 9.** MES-DEA ML3 cell

**Figure 10.** Z37C Zebra battery system

Autokinetics has done an extensive search through the marketplace for the appropriate hardware, development tools, and engineering services for the vehicle control unit (VCU). The VCU must meet all technical requirements such as sufficient input/output capability, adequate throughput with real time operating system, adequate CAN bus capability, and rapid design development system. The Parker IQAN MDL Controller was selected for this application (see Figure 11). The input/output is flexible and can be configured from generic digital

**Figure 11.** Parker IQAN MDL Controller

to current-regulated hydraulic outputs, which will be used for the electro-hydraulic systems. The 6.5" color display will simplify the driver's station while adding control and integration. The IQAN design software is straightforward and robust, and programs can be easily downloaded to the controller.

## Conclusions

A significant number of system design and component selection tasks were accomplished for the system optimization of the Autokinetics bus during the 2005 interim period. The completion of these tasks further demonstrates the feasibility of a BEV propulsion system installed in a lightweight stainless steel body structure. Additionally, the work completed shows that the system is being constructed with current technology and commercially available components.

Simulations show the combination of this BEV propulsion system with the Autokinetics lightweight bus will provide a "well-to-wheels" equivalent mileage of 13 miles per gallon (CBD14 drive cycle, no air conditioning). This represents a 300% improvement over conventional diesel buses. It is hoped that this figure will be validated when the running prototype is completed.

This document highlights work sponsored by agencies of the U.S. Government. Neither the U.S. Government nor any agency thereof, nor any of their employees, makes any warranty, express or implied, or assumes any legal liability or responsibility for the accuracy, completeness, or usefulness of any information, apparatus, product, or process disclosed, or represents that its use would not infringe privately owned rights. Reference herein to any specific commercial product, process, or service by trade name, trademark, manufacturer, or otherwise does not necessarily constitute or imply its endorsement, recommendation, or favoring by the U.S. Government or any agency thereof. The views and opinions of authors expressed herein do not necessarily state or reflect those of the U.S. Government or any agency thereof.

Printed on recycled paper

**A Strong Energy Portfolio for a Strong America**

Energy efficiency and clean, renewable energy will mean a stronger economy, a cleaner environment, and greater energy independence for America. Working with a wide array of state, community, industry, and university partners, the U.S. Department of Energy's Office of Energy Efficiency and Renewable Energy invests in a diverse portfolio of energy technologies.

For more information contact:
EERE Information Center
1-877-EERE-INF (1-877-337-3463)
www.eere.energy.gov